A marine geophysical investigation of the continental margin of east Greenland (63(^o)n to 69(^o) n)

Armstrong, Thomas Leonard

A MARINE GEOPHYSICAL INVESTIGATION OF THE CONTINENTAL MARGIN OF EAST GREENLAND (63°N to 69°N)

by

Thomas Leonard Armstrong

A thesis submitted for the degree of
Doctor of Philosophy at the University of Durham

Grey College

June 1981

"He felt much like a man who had had a tooth pulled out that had been bothering him for a long time. After an excruciating pain and a sensation as if something enormous, something larger than the head itself had been torn out of his gum, the patient, scarcely believing his own happiness, feels that what has been poisoning his life for so long has ceased to exist and he can once more live, think and interest himself in something other than his tooth."

extract from Anna Karenina Vol. 1
by Leo N. Tolstoy
translated by Rochelle S. Townsend
Heron Books, London, 1958

ABSTRACT

During late July and August 1977, a marine geophysical investigation of the continental margin off East Greenland between latitudes 63°N and 69.1°N was undertaken by the University of Durham using the research vessel, R.R.S. Shackleton. Nearly 3500 km of continuously recorded bathymetric, magnetic and gravity data and approximately 2000 km of multi-channel seismic reflection data were recorded in a series of nearly parallel profiles perpendicular to the assumed strike of the continental margin. Disposable sonobuoy work was also carried out.

The reduction, processing and interpretation of the geophysical data are described. In particular, the application of the maximum entropy method (MEM) of spectral estimation (using Burg's algorithm) to the problem of estimating the depth to buried magnetic sources is assessed.

The principal geophysical results include:

1. The location of the ocean-continent boundary is inferred from seismic reflection data and the recognition of marine magnetic anomalies. Oceanic anomalies 22 through 24 are truncated by the continental margin. The marine anomaly sequence 13 through 21 is tentatively extrapolated northwards through the Denmark Straits and stops against the Denmark Straits fracture zone.

2. It is proposed that the Tertiary plateau basalts of the Blosseville coast do not terminate abruptly offshore but are down-faulted and continue eastwards, overlain by a prograded sequence of Tertiary sediments.

3. An interpretation of one processed, CDP stacked seismic section north of the Greenland-Iceland Ridge is presented. Several unconformities are recognised on the basis of seismic stratigraphic analysis. Two seismic horizons showing distinctive offlap against oceanic basement are tentatively dated at 30 Ma and 22 Ma respectively. No evidence is found for the presence of Mesozoic sediments offshore.

4. Gravity modelling indicates that the prograded wedge of Tertiary sediments observed north and south of the Greenland-Iceland Ridge is not isostatically compensated.

CONTENTS

CONTENTS

LIST OF FIGURES

LIST OF FIGURES

LIST OF FIGURES

LIST OF FIGURES

LIST OF FIGURES

LIST OF FIGURES

LIST OF FIGURES

LIST OF FIGURES

LIST OF TABLES

LIST OF ENCLOSURES

ACKNOWLEDGEMENTS

Firstly, and above all, it is my privilege to thank my Mum and Dad for their encouragement and loving support, without which this thesis may well have sunk without trace!

I thank Mr. J.H. Peacock for his supervision of my work whilst at Durham, for his hard work in installing and maintaining the shipborne seismic acquisition system and for his overall supervision as senior scientist during the 1977 East Greenland geophysical research cruise. I am extremely grateful to Professor M.H.P. Bott for provision of departmental facilities, for his sympathetic and helpful advice and for volunteering to read my manuscript after my departure from Durham.

My thanks go to the following: Dr. John Skilbeck for his friendship, advice and mathematical expertise; Dr. C.H. Emeleus for his provision of various papers, published and unpublished, relating to the geology of East Greenland; Drs. A.M. Faller and E.A. Hailwood for preprints and reprints relating to their work.

The success of the 1977 East Greenland research cruise is a tribute to the Captain, officers and crew of the R.R.S. Shackleton and to the unstinting efforts of the personnel of IOS Barry, in particular, Doriel Jones, Steve Jones and Stan Smith. Their conscientious, hard work is gratefully acknowledged.

My friends and colleagues have been a constant source of encouragement and inspiration to me. So many individuals have helped me to finish my thesis that it would fill a book to thank them all. However, I offer my special thanks to my friends Alan Nunns, Karl Gunnarsson and Mick Poulter whose genuine interest in my work, generous advice and priceless humour kept my head above the troubled waters of despair.

Thanks are due to Mr. B.R. Lander and all his staff at the Durham University Computer Unit for provision of excellent service and facilities.

I would also like to thank Mrs. H. Winn for her patience and loyalty during the typing of, what proved to be, a first draft of the first four chapters of this thesis.

The generous contribution of the British Petroleum Co. Ltd. to the success of this work is gratefully acknowledged. I thank BP for their processing of the multi-channel seismic reflection data of profile 11 and for their help in the reproduction of diagrams.

I thank the Natural Environment Research Council for the award of a Research Studentship which enabled me to carry out this work.

Finally, it is my pleasure to thank Luba Mumford and Barbara Hammond for typing my thesis so efficiently and for making every effort to meet my arbitrarily imposed deadline.

CHAPTER 1

INTRODUCTION

1.1 The survey and its scientific goals

A marine geophysical investigation of the continental margin off the east coast of Greenland between latitudes 63° and 69.1°N was carried out in August 1977 by the Department of Geological Sciences, Durham University. This was the third of a series of marine geophysical surveys undertaken by Durham University to study the nature and precise location of the passive continental margin of East Greenland. The two earlier cruises traversed the continental margin between latitudes 58° and 65° N (Featherstone, 1976; Featherstone, Bott and Peacock, 1977).

The location of the present survey and its relationship to the previously studied area to the south are shown in Figure 1.1.

The earlier studies of the East Greenland continental margin had reduced the element of speculation surrounding its structure and evolution, but there remained many unresolved problems. The aim of the present work was to extend the two previous marine geophysical surveys, off South East Greenland, northwards through the Denmark Straits and into the Norwegian Sea. In this way, it was hoped to accomplish several scientific goals, including

(1) the accurate definition of the ocean-continent boundary to the north;

(2) a geophysical study of the submerged Greenland-Iceland aseismic ridge and its immediate environs, and the location of the offshore termination of the Tertiary plateau basalts along the Blosseville coastline;

(3) the location of any major sedimentary sequences along the continental margin and the location of a possible southward continuation of the thick Mesozoic sedimentary succession of Jameson Land (north of Scoresby Sund);

and (4) having determined the precise location and structural framework of the continental margin, to draw the findings together into a

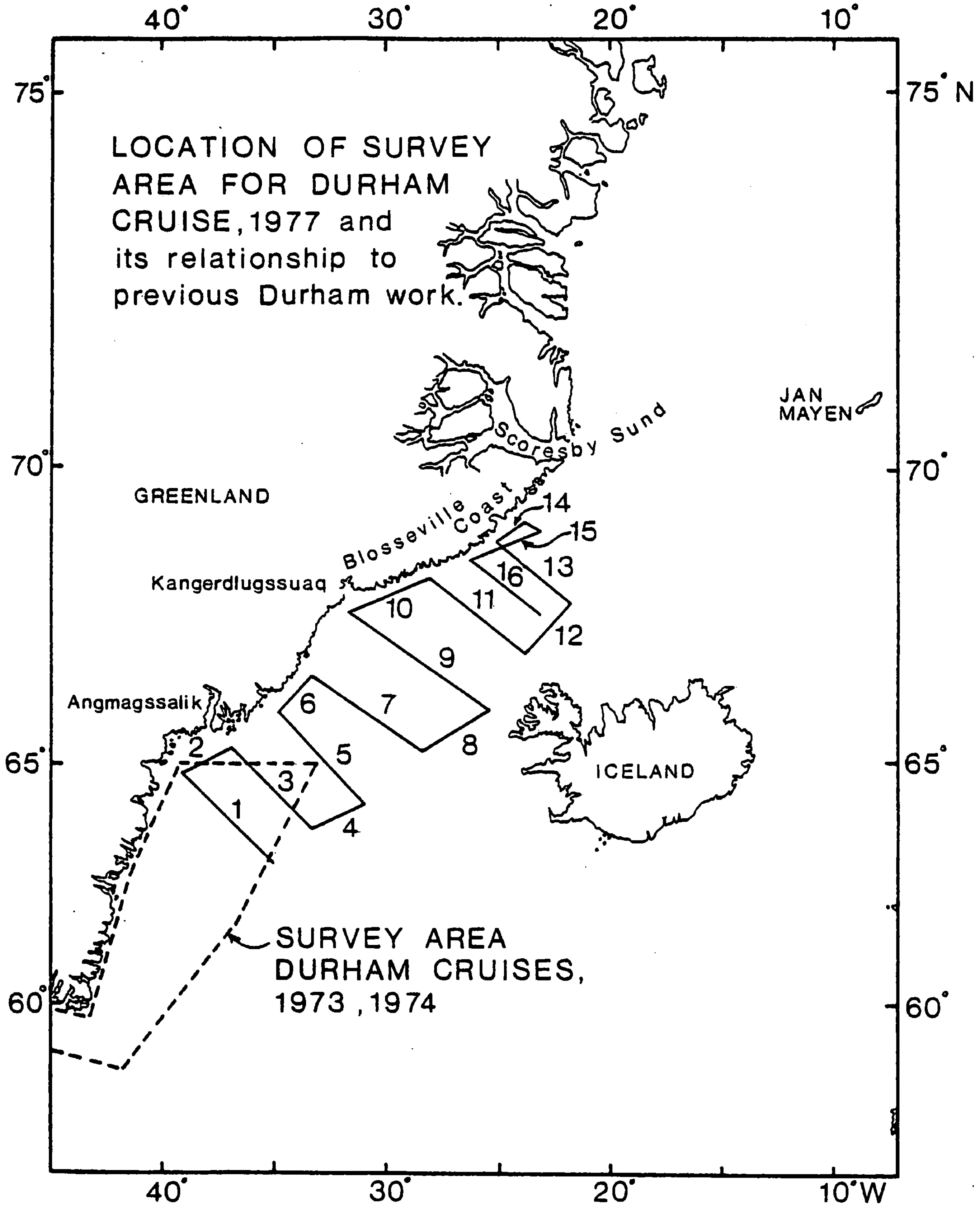

SIMPLIFIED SHIP'S TRACK
NUMBERS IDENTIFY INDIVIDUAL PROFILES

Figure 1.1 The location of the geophysical investigation of the continental margin of East Greenland (1977) and its relationship to previous Durham work.

tectonic synthesis consistent with constraints imposed by the overall geological evolution of the northern North Atlantic region.

Above all, the early history of continental break-up in the North Atlantic and the formation of the Greenland-Iceland-Faeroe aseismic ridge system are still not fully understood. Geophysical techniques were applied during the research cruise in an attempt to elucidate these fundamental problems associated with the East Greenland continental margin.

1.2 An outline of the geology of East Greenland

Any pre-drift configuration of continental land masses prior to the opening of the North Atlantic and the Norwegian-Greenland Seas presupposes an accurate knowledge of the ocean-continent boundary. Further speculation on the tectonic evolution of the ocean demands an insight into the geology and structural framework of the land masses contiguous to the area. A simplified geological map of East Greenland, modified from Haller (1970), is shown in Figure 1.2. The following synopsis of the geology of East Greenland is predominantly taken from Haller (1970), Birkelund et al (1974), and Escher and Watt (1976).

The geology of the South East Greenland coast is characterised by three old Precambrian units; the Archaean cratonic shield area bounded by two Proterozoic mobile belts - the Nagssugtoqidian to the north and the Ketilidian to the south. The Archaean craton consists predominantly of quartzo-feldspathic gneisses yielding ages around 2500 - 2700 Ma for the last regional metamorphism (Birkelund et al, 1974), although the earliest granitic rocks of the area have given isotopically determined geological ages between 3700 and 4000 Ma (Oxford Isotope Geology Laboratory and McGregor, 1971). This represents the oldest material yet discovered in the earth's crust. The Ketilidian mobile belt of South Greenland consists of reworked older gneisses and metamorphosed sediments and lavas into which granitic intrusions were emplaced. The major thermal event took place approximately 2500 - 1600 Ma ago, although tectonic and magmatic activity continued for about 800 Ma after completion of metamorphism during which E-W trending grabens accommodated continental sandstone deposition and basaltic volcanism. To the north, the reworked gneisses of the Nagssugtoqidian mobile belt exhibit a marked, though not universal, grain striking NW-SE in East Greenland and vary between amphibolite to granulite metamorphic facies. The major deformation probably began about 2500 Ma ago (Birkelund et al, 1974).

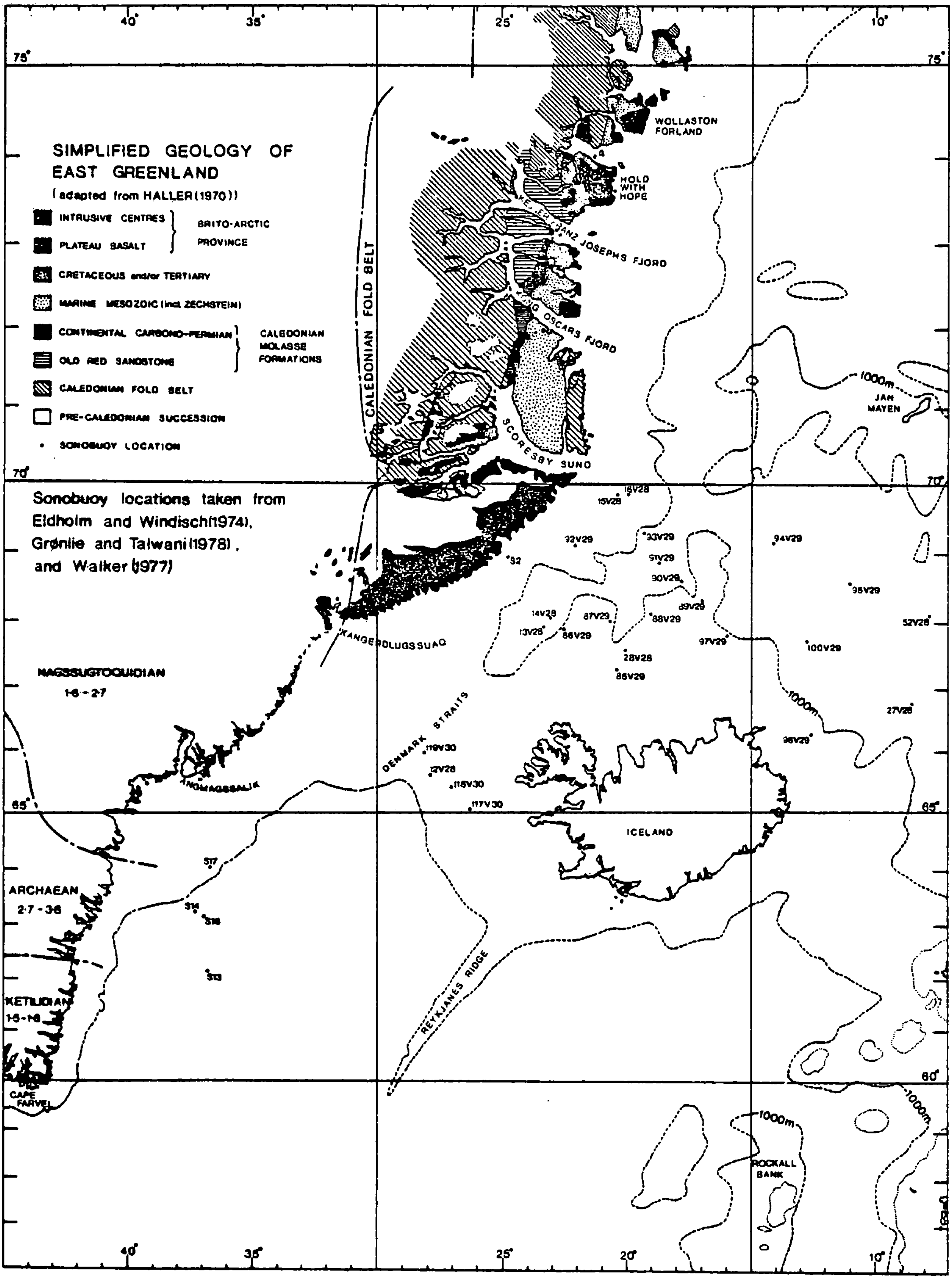

Figure 1.2 A simplified geological map of East Greenland, modified from Haller (1970) and Escher and Watt (1976). Sonobuoy locations are indicated for the Durham cruises (this survey and Walker, 1977) and for published VEMA work (Eldholm and Windisch, 1974; Gronlie and Talwani, 1979). Nominal bathymetry is shown by the 1000m depth contour.

A further metamorphic province, called the Rinkian mobile belt, appears to the north of the Nagssugtoqidian in West Greenland, but it is not known whether the Rinkian province extends into East Greenland. This is because the northern extent of the Nagssugtoqidian is covered by Tertiary basalts.

Between latitudes 70° and 82°N, the coastal geology is dominated by the Caledonian fold belt. Haller (1970, 1971) recognised three phases of orogenic development;

(1) the main orogeny due to deep-seated mobility occurred in latest Ordovician to earliest Silurian time (Henriksen and Higgins, 1976), but appears to have been a diachronous event, the main Caledonian movements of North East Greenland occurring between Upper Silurian and Lower Devonian time;

(2) Late Caledonian spasms, associated with regional compression producing folding and the injection of palingenetic intrusions, followed with the formation of a NW-trending intra-montane molasse basin comprising more than 7 km of Middle and Upper Devonian Red Beds;

(3) minor succeeding episodes, including minor folding and thrusting, persisting into the Lower Carboniferous.

In Central East Greenland, sediment deposition continued throughout Middle Carboniferous to Lower Permian times in a N-NE trending depressional zone formed by a new suite of fracture lines. A thickness of 5 - 6 km of molasse sediments accumulated in fault-bounded troughs as the folded Caledonian mountain chain underwent extensive peneplanation (Haller, 1970). The western boundary of the subsiding basin was formed by a faulted contact of "en echelon" faults (Surlyk, 1978) against the Caledonian mountain belt. The area to the east continued to subside as a series of westward-tilting, faulted blocks resulting from persistent tensional tectonics.

In the late Permian, a marine transgression took place from the north-east (Birkelund and Perch-Nielsen, 1976) and a maximum thickness of 300 m of marine Upper Permian deposits of neritic to littoral facies were laid down in a warm, shallow sea environment.

A fluctuating marginal sea persisted throughout the Mesozoic, the underlying basement continuing to subside as a complex of antithetic fault blocks. In Triassic times, fine clastic deposits with coarse intercalations were deposited in a shallow sea, open to the north (Callomon et al, 1972). However, as the sea retreated northwards, coarser clastic deposits were laid down and towards the central Jameson Land basin, flood-plain sandstones and shales appeared. A hot, arid climate coupled with a fluctuating shore-line persisted and resulted in evaporite formation (gypsum).

The Jurassic basin of East Greenland developed as a graben rifting from south to north in a series of steps. Surlyk (1977, 1978) postulated that NW-SE trending cross faults situated in the major fjords of Central East Greenland (Figure 1.3) subdivided the basin into a series of fault bounded blocks which were progressively transgressed from the south by an advancing sea. Basin evolution took place in a number of phases. The most important events (Surlyk, 1978) were:

(1) the initial marine transgression which invaded the southernmost block 1 in the Pliensbachian. The shallow marine sediments include foreshore and beach sandstones grading upwards into tidal, estuarine and shelf mudstones and sandstones. The advancing sea transgressed block 2 in Toarcian-Bathonian times;

(2) the major transgressive phase in East Greenland occurred in the Bathonian (or latest Bajocian) which produced fully marine conditions over blocks 1 and 2 and northern blocks 4 and 5 were inundated for the first time when Middle Jurassic sandstones were deposited directly onto deeply eroded Caledonian basement. However, the Middle Jurassic deposits, up to 600 m thick, are predominantly regressive, indicating a prograding shoreline;

(3) a major phase of fault-controlled subsidence, traceable all over East Greenland, occurred in the Late Oxfordian. This abrupt event is marked by a widespread change from shallow marine sandstones to relatively deep-water black mudstones;

(4) the most important phase of Mesozoic block-faulting subsidence took place in Middle Volgian times. Rejuvenated source areas in the south provided huge volumes of coarse shallow marine sandstones for deposition on block 1 and on Milne Land to the west in Middle Volgian-Valanginian times. This tectonic phase is hardly developed on block 2,

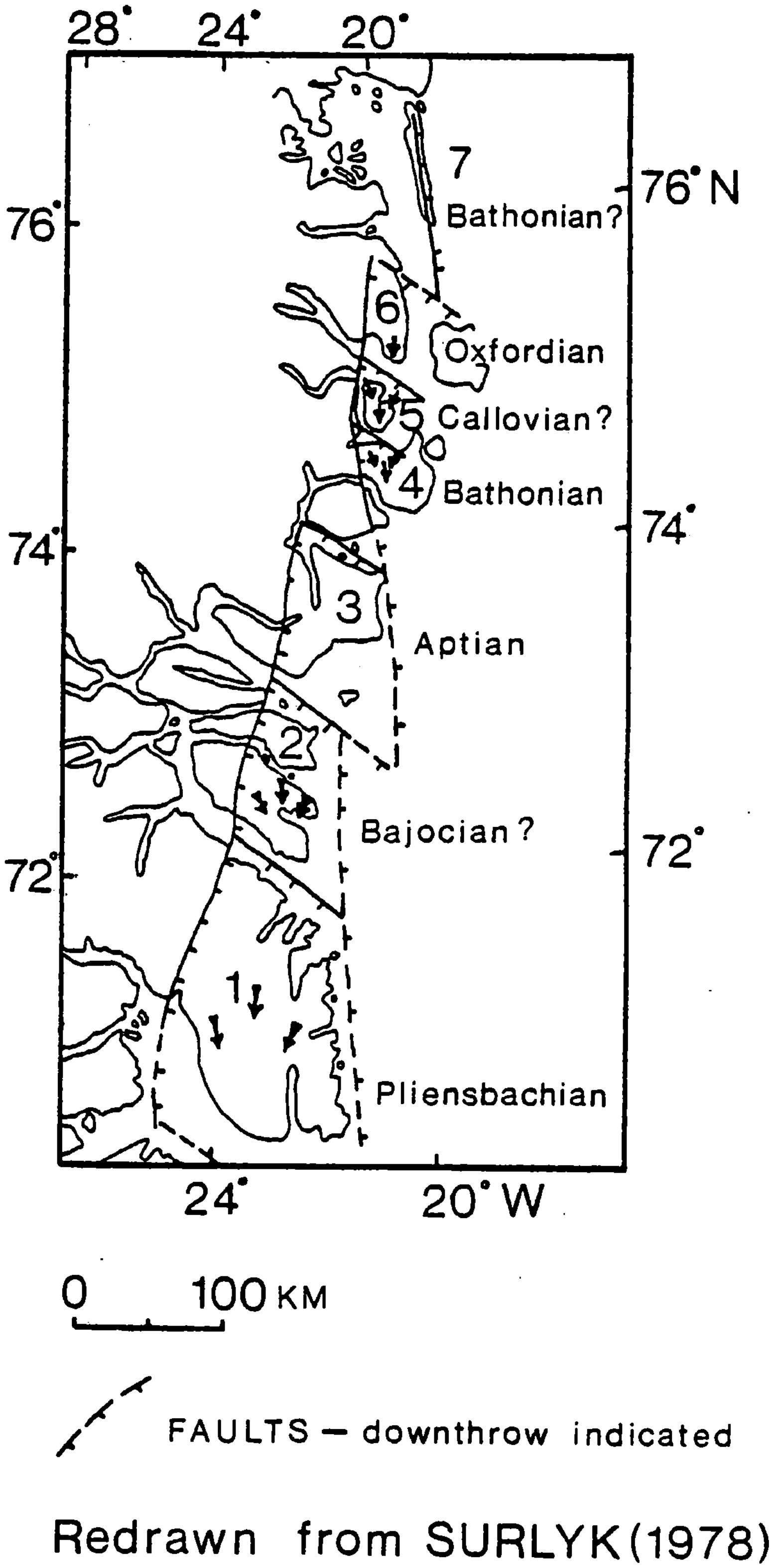

Figure 1.3 The location of the main Jurassic fault blocks of Central East Greenland proposed by Surlyk (1978). Arrows indicate the dominant direction of sediment transport. The time of the first post-Triassic transgression is shown alongside each block.

but thick syntectonic sequences appear on the other blocks. The blocks north of block 2 suffered strong antithetic rotation towards the continent (Surlyk, 1977) and the sediments accumulated in the marginal troughs indicate lateral basin fill, in marked contrast to the longitudinal basin fill indicated by all the other Jurassic sediments of the Central East Greenland basin.

Surlyk (1977) concludes that the faults responsible for the block-faulted subsidence of the Mesozoic sedimentary basin were controlled by structural trends in the Caledonian and older basement, although rifting itself was independent of earlier tectonic events.

The Cretaceous period was one of relative quiescence during which almost continuous basin subsidence accommodated marine shales, sandstones and conglomerates. The extent of Cretaceous outcrops in East Greenland to the north and to the south is greater than for any other Mesozoic succession. Gentle folding took place in earliest Cretaceous time in the south part of block 1, the fold axes plunging a few degrees to the south. This movement has been interpreted as due to left-lateral wrenching along a cross fault situated in Scoresby Sund, the fjord limiting the block to the south (Surlyk, 1978).

Tensional tectonics throughout the Mesozoic period have produced a major sedimentary basin some 800 km long, with a maximum width of 140 km in south Jameson Land and containing a maximum thickness of 5 km of sediments. In contrast, an isolated occurrence of Late Cretaceous to Early Tertiary sediments, overlying the metamorphic basement complex but predating the Tertiary basalt sequence, occurs to the north-east of Kangerdlugssuaq (Wager, 1947). These thin sediments make up the Kangerdlugssuaq Group, which comprises of the Sorgenfrei Formation and the Ryberg Formation (Deer, 1976). The Sorgenfrei Formation consists of 30 m marine shales, containing a dinoflagellate flora of Upper Albian age at its base and ammonites of Lower Cenomanian age above. The shallow marine sands and calcareous siltstones of the Ryberg Formation contain dinoflagellates of Maastrichtian and Danian age, including bivalves, gastropods and rich plant floras also. These sediments reach a thickness of up to 170 m. This sediment group represents shallow marine deposition in a basin whose probable south-western extent was situated in the Kangerdlugssuaq region.

A succession of basement-derived conglomerates, arkosic sandstones grading upwards into dark sandstones with an increasing proportion of volcanic debris lies unconformably on the Danian sediments. The Tertiary basalt sequence follows and thin marine shales containing Lower Sparnacian dinoflagellates are intercalated with the earliest volcanic breccias. This evidence dates the onset of effusive volcanic activity to latest Palaeocene time (Deer, 1976).

The plateau basalt series was outpoured during a major eruptive phase during which a thickness of up to 9 km of predominantly tholeiitic and transitional tholeiitic basalts was extruded over the Kangerdlugssuaq region and inland from the Blosseville Kyst, extending northwards as far as Scoresby Sund. Most of the lavas were erupted subaerially, although submarine pillow lavas grading upwards into subaerial flows have been recorded south of Scoresby Sund and lower basalts between Kangerdlugssuaq and I.C. Jacobsen Fjord were also extruded under water. Subsidence occurred contemporaneously with lava effusion. Individual flows may exhibit extensive lateral persistence and deeply eroded fjord exposures reveal flows which are approximately parallel to one another over long distances, indicating that the basalts accumulated in an approximately horizontal orientation.

At Kap Dalton ($69^{o}25'$N), about 40 m (Henderson, 1976) of marine sediments known as the "Kap Dalton Series" rest conformably over the basalt pile. These sediments were preserved on a down-faulted block (Wager, 1935) and marine fossils extracted from the sequence yield a Lower to Middle Eocene age (Deer, 1976). This marine series of about 130 m thickness (Henderson, 1976) is also found at Kap Brewster ($70^{o}10'$N), in conjunction with a basal conglomerate, overlying pillow lavas and brecciated volcanics (Hassan, 1953) which indicates marine transgression prior to the completion of volcanism. A separate post-basalt marine transgressive sequence called the "Kap Brewster Series" also occurs. These beds, 76 m thick, rest directly on basalt and consist of a basal conglomerate, overlain by sandstones and coarser clastics (Henderson, 1976) and are of probable Miocene age.

The important sediments of the Kangerdlugssuaq Group and the Kap Dalton Series, bracketing the major phase of basalt effusion, place the onset of volcanism in latest Palaeocene time and its apparent completion by Middle to Late Eocene time. However, Henderson (1976) draws attention to the fact that Hassan (1953) considered the marine fauna of the Kap Dalton Series to lie in the extended range from Eocene to Oligocene.

Further igneous activity took place in the form of basic intrusions (Skaergaard and Kap Edvard Holm) and minor intrusive sills and dykes. Several intrusive complexes occur to the north of Scoresby Sund. However, the coastal area of the Blosseville Kyst was subjected to a large-scale crustal flexure whereby subsidence to the east formed the submerged Iceland-Greenland aseismic ridge beneath the Denmark Straits and upwarping to the west formed the highest mountains in Greenland (up to 3700 m). This vertical differential movement of the order of 8 km was accompanied by a major swarm of coast parallel dyke intrusion. Later igneous activity included the emplacement of several syenite, granite and alkaline intrusions with minor dyke swarms.

Subsequent erosion and the extensive Pliocene-Quaternary glaciation have eroded deeply into the coastal geology of East Greenland, producing spectacular fjords and submarine ice-scoured troughs accommodating local sediment accumulations. Offshore scarps and submarine topography have been strongly influenced by ocean bottom currents (contourites).

1.3 The tectonic evolution of the northern North Atlantic Ocean

The recognition of marine magnetic lineations parallel to the mid-oceanic ridge systems of the world and their explanation via the hypothesis of seafloor spreading (Vine and Matthews, 1963) have enabled the details of ocean basin evolution to be worked out and have lent credence to the idea of continental migration.

There follows a review of current literature on the geological evolution of the North Atlantic ocean basin compiled predominantly from the following authors: Laughton (1975), Talwani and Eldholm (1977) and Srivastava (1978). The review is written from the standpoint of plate tectonics, since the chronology of marine magnetic anomalies is well established (Heirtzler et al, 1968) although subject to frequent review (Berggren et al, 1979; Kruczyk et al, 1977; LaBreque, Kent and Cande, 1977; Larson and Hilde, 1975; Odin, Curry and Hunziker, 1978; Tarling and Mitchell, 1976). The revised magnetic polarity time scale according to Hailwood et al (1979) has been adopted throughout this thesis, unless stated otherwise. This time scale, together with important tectonic events, is shown in Figure 1.4.

The present geographical distribution of continents, continental fragments and ocean basins in the northern North Atlantic Ocean is shown in Figure 1.5.

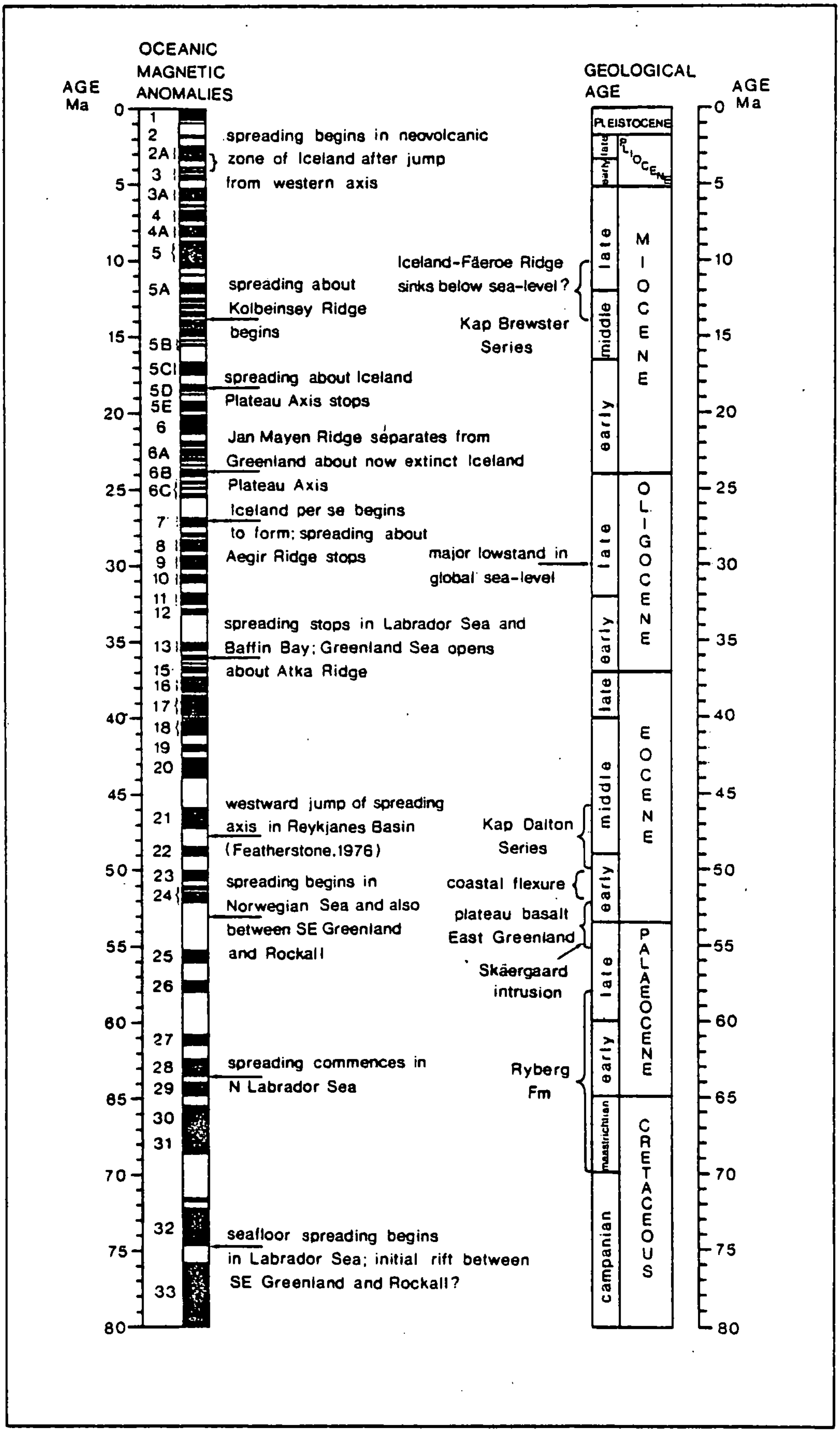

Figure 1.4 The revised magnetic polarity time scale according to Hailwood et al., (1979) with principal geologic and tectonic events annotated alongside. The major lowstand in global sea level indicated is after Vail et al., (1977b). Anomaly 33 was inferred from LaBreque et al., (1977). For further references, see text.

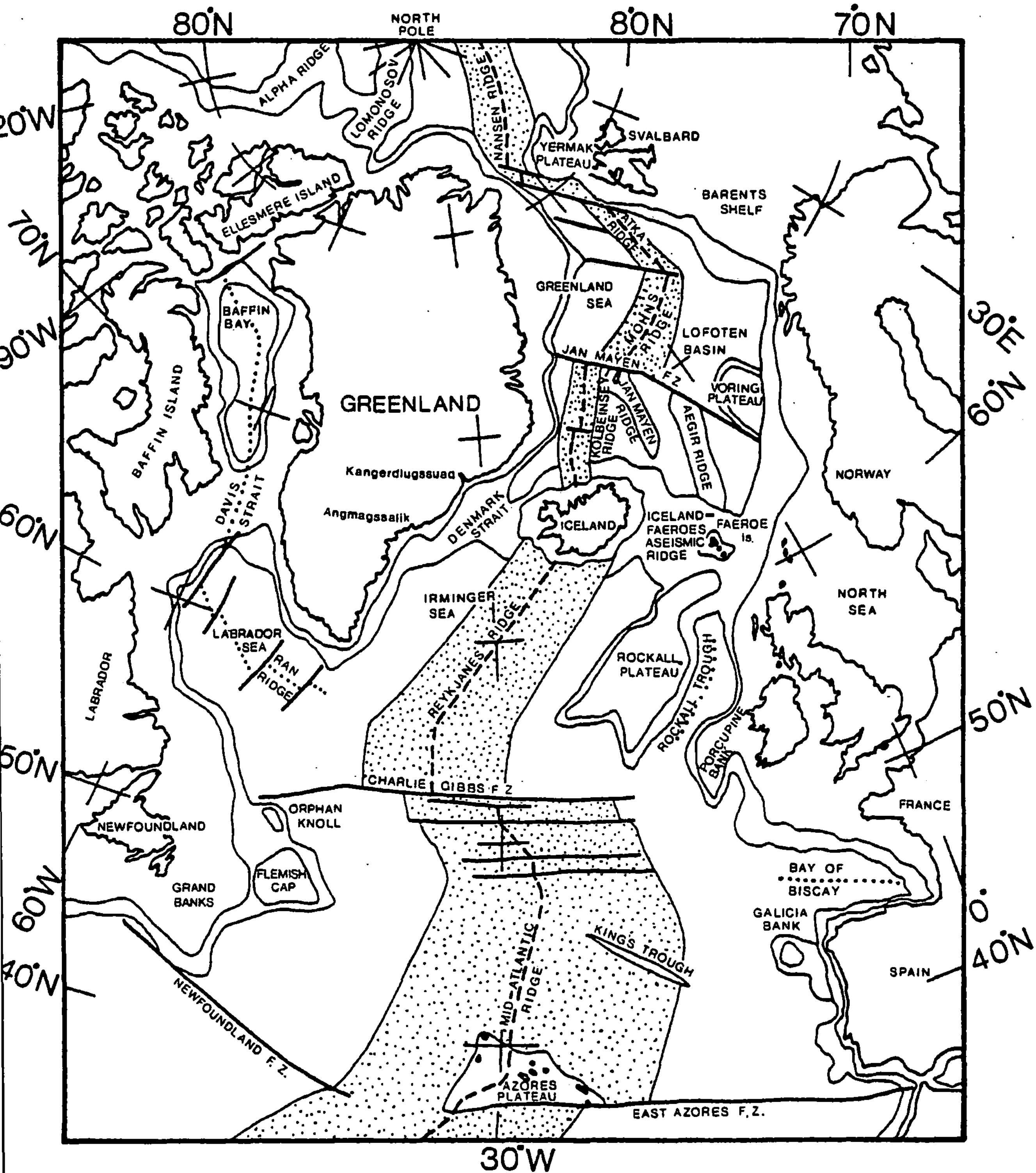

Figure 1.5 The present geographical distribution of continents, continental fragments and ocean basins in the northern North Atlantic Ocean redrawn from Laughton (1975). The two lines bordering the continents represent the top and bottom of the continental slope. The mid-ocean ridge system has been shaded.

Initial rifting between Africa and America began during Triassic times in the north (Morocco-Senegal) and during Late Jurassic to Early Cretaceous times in the south (Forster, 1978). The time of opening of the South Atlantic has been estimated as Early Cretaceous, probably Valanginian, about 125 - 130 Ma ago (Larson and Ladd, 1973), but recent palaeomagnetic results (Schult and Guerreiro, 1979) indicate a small separation of South America and Africa from the so-called "pre-drift configuration". This separation may reflect a pre-Triassic or Early Jurassic rifting phase which remained essentially static throughout the Mesozoic until the end of Lower Cretaceous time. The northern South Atlantic was completely open by Albian time, 100 - 105 Ma ago (Reyment, 1969), although it was bounded to the north by a sinistral transform fault running from south of Newfoundland to the south of the Iberian peninsula.

Before Late Cretaceous time, the continental landmass north of the Azores-Gibraltar Ridge remained intact but rifting between Portugal and the Grand Banks cannot be ruled out (Kristoffersen, 1978). The spreading phase between Europe and North America began at the end of the Late Cretaceous normal geomagnetic polarity interval, about 90 - 95 Ma ago (Kristoffersen, 1978). The oldest marine magnetic anomalies recognised in the North East Atlantic were originally anomalies 31 and 32 (Williams and McKenzie, 1971), but these have recently been re-identified as anomalies 33 and 34 by Cande and Kristoffersen (1977) with a subsequent revision of the relative widths of magnetic polarity intervals in the Late Cretaceous. However, the identification of anomaly 31 by Pitman and Talwani (1972) for the NW Atlantic and by Williams and McKenzie (1971) for the NE Atlantic was favoured by Srivastava (1978) as a result of geophysical investigations in the Labrador Sea.

The date of the initial rifting episode between Europe and North America has been estimated as Hauterivian (120 Ma ago) from geological considerations by Dewey et al (1973) who assumed a transform fault (North Pyrenean fault) bounding the Iberian peninsula to the north, as proposed by Le Pichon et al (1971a, 1971b). However, Ries (1978) concluded that the simple rotation model proposed by Carey (1958) and Williams (1975) for the opening of the Bay of Biscay was consistent with available geological and geophysical data.

Initial rifting in the Bay of Biscay probably began during the Late Triassic and Jurassic (Ries, 1978) and the phase of seafloor spreading coincided with opening between Iberia and the Grand Banks about 90 - 95 Ma ago (Kristoffersen, 1978). A ridge-ridge-ridge triple junction at the western end of the Bay of Biscay was proposed by Kristoffersen (1978), the initial opening extending northwards from the Azores-Gibraltar Ridge into Rockall Trough. During the interval 90 - 95 Ma to anomaly 34 (Late Santonian), opening took place in Rockall Trough, Newfoundland separated from Ireland and the Bay of Biscay opened as Spain rotated in an anticlockwise direction away from Europe. Towards the end of anomaly 34 time (Late Santonian), spreading ceased in Rockall Trough and the spreading axis jumped westwards, south of Rockall Bank. This jump initiated the Charlie Gibbs fracture zone and another transform set south of Hatton Bank. Relative motion took place between North America and Rockall Bank for the first time. During the reversed magnetic interval between anomaly 33 and 34 (Early Campanian), spreading ceased in the Bay of Biscay (83 Ma ago; Ries, 1978) and the triple junction west of Iberia became extinct (Kristoffersen, 1978). The westward migration of the spreading axis from Rockall Trough was interpreted by Srivastava (1978) as coinciding with the onset of seafloor spreading in the Labrador Sea about anomaly 32 time (75 Ma ago according to Hailwood et al, 1979).

Alternatively, the spreading phases in the Rockall Trough and Newfoundland basin, between the Grand Banks and Portugal, may have been connected by a NW-SE trending transform fault located eastwards of Orphan Knoll and Flemish Cap (Srivastava, 1978). Laughton (1975) further speculates that the transform fault may have extended to the north-west towards the Labrador Sea and that seafloor spreading may have occurred between SE Greenland and Hatton Bank contemporaneous with the opening of Rockall Trough to form a proto- Iceland basin. From geophysical studies of the continental margin off Labrador and NE Newfoundland, Grant (1972) proposed the existence of an "intracratonic" depression along the proto-Labrador Sea which was active since early Palaeozoic time and accommodated Mesozoic sediments in a trough formed by graben subsidence. Thick sedimentary sequences have been proved in offshore West Greenland in the Melville Bugt graben (Keen and Barrett, 1972) and although in situ sediments of pre-Cretaceous age have not been proved, their presence appears to be highly likely (Henderson, 1976).

The presence of Mesozoic sediments has been postulated in Rockall Trough, overlying oceanic crust (Scrutton and Roberts, 1971) and Mesozoic sediments may also be present on the continental margin of SE Greenland (Featherstone et al, 1977). These predictions require confirmation by drilling but, if proved, they may reflect an episode of major graben subsidence prior to rifting and seafloor spreading.

A Lower Permian age for seafloor spreading in the Rockall Trough has been proposed by Russell (1976) and Russell and Smythe (1978). These authors extend the zone of Permian spreading northwards, through the Faeroe-Shetland Trough, into the Norwegian-Greenland Seas, so that this proto-northern North Atlantic Ocean opened before the Bay of Biscay. Its extent was bounded to the north by the Greenland-Svalbard transform fault and to the south by the proto-Bay of Biscay fault. These transform faults are small circles with a common pole of rotation (Russell and Smythe, 1978). Russell (1976) interprets the foundered continental basement proposed by Talwani and Eldholm (1972) beneath the Vøring Plateau off western Norway as ocean floor basalt of Lower Permian age.

These conflicting hypotheses concerning the early evolutionary history of the northern North Atlantic remain unresolved. Deep borehole information is required to reduce the uncertainties remaining in the interpretation of this complex area.

The oldest marine magnetic anomaly recognised in the Labrador Sea was anomaly 32 (75 Ma old, Campanian; Srivastava, 1978). Extensive tensional and block-faulting tectonics preceded the onset of seafloor spreading and sediment accumulation in subsiding graben structures developed (cf. Grant, 1972). Active seafloor spreading started in the southern Labrador Sea first and only began in the northern Labrador Sea during anomaly 28 time, preceded by a phase of crustal thinning and stretching in response to tensional stresses. Srivastava (1978) places anomaly 28 in Maastrichtian time (about 68 Ma ago; Le Pichon et al, 1976) whereas Hailwood et al (1979) place anomaly 28 in the Early Palaeocene, about 63 Ma ago. No active spreading took place in Baffin Bay at this time.

Immediately before anomaly 24 time (about 53 Ma ago), there was a drastic change in the spreading direction in the Labrador Sea induced by the onset of spreading in Baffin Bay, the opening of the Norwegian Sea and spreading between SE Greenland and Rockall Plateau. At this time, a ridge-ridge-ridge triple junction was established south of Greenland (Kristoffersen and Talwani, 1977).

Laughton (1975) postulated that the new spreading axis between Rockall Plateau and Greenland was located to the east of the proposed proto-Iceland basin, adjacent to the foot of Hatton Bank. This implied that the pre-existing sea floor of Upper Cretaceous age was left adjoining the SE Greenland continental margin. However, Vann (1974) and Featherstone et al (1977) interpreted the gap of some 80 km between Rockall Plateau and Greenland observed in palaeogeographic reconstructions as caused by the subsidence of attenuated continental crust, giving rise to a magnetic smooth zone along the continental margin. In order to explain the observed discrepancy between the computed finite difference poles of rotation describing ocean floor spreading between anomalies 25 and 32 in the Labrador Sea and the North Atlantic respectively, Srivastava (1978) concluded that the old oceanic crust interpretation was the most favourable hypothesis. Although active seafloor spreading between SE Greenland and Rockall Plateau started at about anomaly 24 time, the earlier phase of rifting inferred from studies of the poles of rotation began as early as the Campanian (anomaly 32; about 75 Ma ago) and oceanic crust may have evolved between Greenland and Europe during this interval (about 63 km of oceanic crust at a spreading rate of 2.5 mm yr^{-1} between Greenland and Rockall Bank according to Srivastava (1978)). However, the subsidence of attenuated continental crust remains an equally valid solution to this problem.

Seafloor spreading has continued in the Reykjanes Basin to the south of Iceland since anomaly 24 time. Featherstone et al (1977) noted the pinch-out of marine magnetic anomalies 22 through 24 against their proposed ocean-continent boundary on the SE Greenland margin. A westward jump of the spreading axis just prior to anomaly 21 time (47 - 48 Ma ago) has been proposed by Featherstone (1976) to explain this phenomenon in relation to the segment of ocean floor older than anomaly 21 located just north of Hatton Bank (Roberts, 1975) which apparently doubles its expected width.

The spreading history to the north of Iceland was extremely complex. Seafloor spreading in the Norwegian Sea about the Aegir and Mohns Ridges started between anomaly 24 and 25 time (52 - 56 Ma ago) and until the cessation of spreading in the Labrador Sea and Baffin Bay just prior to anomaly 13 time (Lower Oligocene, about 35 - 36 Ma ago), Greenland migrated to the north-west relative to Europe. For this reason, only the Norwegian Sea opened up. This motion was accommodated by compression and shearing along a transform fault separating Greenland from Svalbard and the Barents shelf. When spreading stopped in the Labrador Sea, Greenland began to move with the North American plate in an almost westerly direction relative to Norway and separation of the transform margins took place due to seafloor spreading about the Atka Ridge (also called the Knipovich Ridge) to create the Greenland ocean basin. The time of extinction of the triple junction to the south of Greenland was accurately dated by Kristoffersen and Talwani (1977), who recognised anomaly 13 as the oldest marine magnetic anomaly in the NW Atlantic area to continue parallel to the Reykjanes Ridge without deviation into the Labrador Sea.

Spreading about the Mohns Ridge, between the Jan Mayen fracture zone to the south and the Greenland-Senja fracture zones to the north, has been relatively undisturbed since the time of initial opening. The oldest marine magnetic anomaly identified in the Lofoten Basin was anomaly 24 (Talwani and Eldholm, 1977). North of the Greenland-Senja fracture zone, the asymmetric disposition of the Atka Ridge relative to the margins of the Greenland Sea and the poorly developed magnetic anomalies in this basin were thought to indicate several eastward jumps of the axis location since the onset of spreading about anomaly 13 time (Talwani and Eldholm, 1977). However, Le Pichon et al (1977) considered the constraints imposed by seafloor spreading in the Eurasian Basin of the Arctic Ocean on any reconstruction of continental landmasses around the Atlantic Ocean. These authors concluded that the asymmetry of axial position shown by the Atka Ridge was a direct consequence of the spreading geometry proposed and asymmetrical spreading or jumps of the ridge axis were redundant hypotheses.

The Atka Ridge is offset to the west by the Spitzbergen fracture zone, a transform fault connecting the Atka Ridge to the Nansen Ridge in the Arctic Ocean.

However, the evolution of the Norwegian Sea between Iceland and the Jan Mayen fracture zone was less straightforward. The major phase of seafloor spreading took place about the Aegir Ridge (Figure 1.5).

The oldest marine magnetic anomaly identified in the Norway Basin was anomaly 23 (Talwani and Eldholm, 1977). The absence of older anomalies prompted Talwani and Eldholm to suggest that an earlier, short-lived, spreading axis was active in the Norway Basin shortly before anomaly 23 time and then, upon its extinction, the spreading activity migrated westward to the Aegir Ridge. These authors speculated that the magnetic anomalies generated during the brief spreading episode prior to anomaly 23 time lie adjacent to the Faeroe-Shetland escarpment.

However, in recent work relating to the Norwegian Basin, Nunns (1980) and Robinson (1980) have identified anomaly 24 after reappraisal of marine magnetic anomaly correlations about the Aegir Ridge.

The nature of the crust underlying the Faeroes is still the subject of controversy. Talwani and Eldholm (1972, 1977) considered the crust beneath the Faeroes to be of oceanic origin and they proposed the ocean-continent boundary to be situated along the eastern margin of the Faeroe block (that is, along the western margin ofthe Faeroe-Shetland channel). In contrast, Bott et al (1974) forwarded the continental nature of the crust beneath the Faeroes, the ocean-continent boundary being along an escarpment forming the western margin of this block. Unpublished multi-channel seismic reflection data and a reappraisal of magnetic anomalies to the west of the Faeroe-Shetland escarpment (Robinson, 1980) lend support to the continental nature of the crust beneath the Faeroes. The location of the ocean-continent boundary to the west of the Faeroes reduces the gap in the palaeogeographical reconstruction of the northern North Atlantic due to Talwani and Eldholm (1977). The fit of the continents around the North Atlantic Ocean as proposed by Le Pichon et al (1977) also indicates continental crust beneath the Faeroes.

The phase of seafloor spreading along the Aegir Ridge continued from anomaly 24 time (about 52 Ma ago) until about anomaly 7 time (about 27 Ma ago). The magnetic anomalies generated by this, now extinct, spreading axis between anomaly 20 time and anomaly 7 time form a fan-shaped pattern in the Norway Basin, some 300 km wide at its northern end narrowing to nearly 150 km width in the south. Talwani and Eldholm (1977) dismissed the hypothesis that these anomalies were caused by rotation about a pole close to the southern extremity of the extinct axis and proposed the existence of a further spreading axis active over the same period of time (between anomaly 7 and anomaly 20 time) during which the observed fan-shaped anomaly pattern was created.

When the Aegir Ridge became extinct, the spreading axis jumped westward and the continental fragment (Johnson and Heezen, 1967; Johnson et al, 1972) of the Jan Mayen Ridge was separated from Greenland by seafloor spreading. This spreading episode was relatively short-lived and the extinct axis of the Iceland Plateau was abandoned before anomaly 5 time (10 Ma ago) due to a further westward jump of spreading activity to form the presently active Kolbeinsey Ridge (also called the Iceland-Jan Mayen Ridge). Johnson et al (1972) proposed the existence of an intermediate spreading axis prior to the later phase associated with the Kolbeinsey Ridge but its position was relocated by Talwani and Eldholm (1977) on the basis of a re-identification of magnetic anomalies. The latter authors reported unpublished work by Chapman and Talwani which suggests that spreading about the intermediate Iceland Plateau axis took place between anomaly 6A time (23 Ma ago) and anomaly 5D time (18 Ma ago).

Vogt et al (1980) studied detailed low-level aeromagnetic data between Iceland and 70^{O}N and, after a revised correlation of marine magnetic anomalies about the Kolbeinsey Ridge, concluded that the intermediate Iceland Plateau axis does not exist.

Active seafloor spreading has continued along the Kolbeinsey Ridge since its initiation prior to anomaly 5 time (about 13 Ma ago; Talwani and Eldholm, 1977) to the present day. The asymmetric position of the ridge axis was recognised by Johnson and Heezen (1967) who suggested the possible existence of an extinct spreading axis in the Norway Basin. The discovery of the Aegir Ridge and its associated suite of magnetic anomalies vindicated their hypothesis.

The Kolbeinsey Ridge is bounded northwards by the Jan Mayen fracture zone, the transform fault connecting this spreading axis to the currently active Mohns Ridge in the northern Norwegian Sea. To the south, the Tjornes fracture zone offsets the spreading axis and provides a connection with the currently active spreading axis in the neovolcanic zone of eastern Iceland. However, Palmason (1974) and Saemundsson (1974) have both independently suggested that this axis has only been active for the past 3 or 4 Ma. Before this time, the western axis located approximately between the Reykjanes Peninsula and the Kolbeinsey Ridge was actively spreading. In their reconstruction and proposed spreading history for the Norwegian Sea, Talwani and Eldholm (1977) suggested that Iceland per se only came into existence subsequent to anomaly 7 time (about 27 Ma ago).

A number of geophysical surveys have been carried out over the Iceland-Faeroe Ridge (Bott, Browitt and Stacey, 1971 ; Fleischer, 1971; Johnson and Tanner, 1972; Bott et al, 1974; Fleischer et al, 1974; Zverev et al, 1977; Bott and Gunnarsson, 1980). It represents a narrow, upstanding bathymetric feature about 400 m deep along its smooth crest and it is separated from the Iceland Block to the NW and the Faeroe Block to the SE by narrow, abrupt bathymetric scarps. Sediments are thin or absent over much of the crestal region except where preserved in local troughs (for example, Bott et al, 1971).

The correlation of marine magnetic anomalies has not been possible over the Iceland-Faeroe Ridge but some large amplitude, circular magnetic anomalies probably indicate igneous intrusions of ring type associated with the eroded cores of ancient volcanoes (Ingles, 1971).

Bott (1974) emphasised the similarity of crustal structure beneath Iceland and the Iceland-Faeroe Ridge respectively and he referred to the crust beneath both regions as of Icelandic type. In both areas, variable upper crustal layers, most likely representing basaltic volcanics, are underlain by a well-defined main crustal layer of P-wave velocity 6.4 to 6.8 km s^{-1}. Along the Iceland-Faeroe Ridge, a 6.7 km s^{-1} refractor at 4 to 8 km depth represents the top of the main crustal layer (Bott and Gunnarsson, 1980). However, beneath Iceland the depth to the Moho varies between about 8 and 18 km (Bott, 1974) in contrast with the estimated depth to the Moho beneath the central and south-eastern part of the Iceland-Faeroe Ridge of 30 to 35 km, shallowing by a few kilometres to the NW approaching the Iceland Block (Bott and Gunnarsson, 1980). Also, an anomalously low velocity upper mantle of P-wave velocity about 7.2 km s^{-1} underlies Iceland whereas a more normal sub-Moho velocity of about 7.8 km s^{-1} represents the upper mantle beneath the Iceland-Faeroe Ridge (Bott, 1974; Bott and Gunnarsson, 1980).

Although the crustal structure beneath Iceland and the Iceland-Faeroe Ridge is similar, significant differences are apparent. Bott (1974) lists the principal differences as follows:

(1) layer 1 (3.2 - 4.6 km s^{-1} P-wave velocity and varying in thickness from 0 to 3 km) beneath the aseismic ridge representing localised basins filled by pyroclastics and possibly sediments is absent on Iceland;

(2) crustal thickness beneath the Iceland-Faeroe Ridge is significantly greater than beneath Iceland;

(3) anomalously low upper mantle P-wave velocities occur beneath Iceland in contrast with the fairly normal sub-Moho velocities beneath the Ridge;

(4) in general, corresponding layers beneath the Ridge exhibit higher

velocities than those beneath Iceland.

Evidence for the nature of the crust beneath the Faeroe Islands was presented by Bott et al (1974). These authors proposed that continental crust underlies the Faeroes because

(1) P_g velocities of 5.9 to 6.2 km s^{-1} and less, characteristic of the Faeroe Islands, have not been observed beneath Iceland;

(2) the main crustal layer of velocity 6.4 to 6.8 km s^{-1} within Icelandic type crust has not been observed at shallow depth beneath the Faeroes;

(3) an upper mantle velocity, P_n of 8.2 km s^{-1} is observed beneath the Faeroes but the anomalously low value of 7.2 km s^{-1} is observed below Iceland;

(4) the crustal thickness beneath the Faeroes, about 37 to 40 km (Bott and Gunnarsson, 1980), is substantially greater than beneath Iceland.

Further evidence for the ocean-continent boundary being located between Icelandic type crust of the Iceland-Faeroe Ridge and the proposed continental crust of the Faeroe Block was provided by the observation of converted P-waves originating at this continental margin (Bott et al, 1976).

The unusual thickness of the Icelandic type crust beneath the Iceland-Faeroe Ridge (normal oceanic crust has a thickness of order 7 km) has been attributed to vigorous differentiation of crustal material from an underlying upper mantle at an exceptionally high temperature (Bott, 1974). Oceanic crust to the north and south of the Iceland-Faeroe Ridge has been created by seafloor spreading over the last 53 Ma and it is likely that this ridge has been generated by processes related to the formation of the ocean basins contiguous to it.

No detailed geophysical surveys have been undertaken over the Greenland-Iceland Ridge but its structure and origin is probably similar to that of the Iceland-Faeroe Ridge.

The Greenland-Iceland-Faeroe aseismic ridge stood above sea level from Eocene to Middle Miocene times (Vogt, 1972; Grønlie, 1979) and provided a major barrier to water circulation in the North Atlantic Ocean (Vogt, 1972; Talwani and Udintsev, 1976). After subsidence of the ridge system, the overflow of cold water from the Norwegian Sea into the North Atlantic initiated fast-flowing bottom currents (Vogt, 1972) and erosion of the South East Greenland continental scarp by contour currents (Featherstone, 1976).

Seafloor spreading continues today, as indicated by earthquake epicentres, along the Reykjanes Ridge, the neovolcanic zone of Iceland, the Kolbeinsey Ridge, the Mohns Ridge and the Atka Ridge, which is offset by transform faulting from the Nansen Ridge in the Arctic Ocean.

1.4 The relationship between onshore geology of East Greenland and the evolution of the ocean basins in the northern North Atlantic

Embodied in the scientific rationale motivating the marine geophysical cruise off the East Greenland continental margin was an attempt to establish the relationship between the onshore field geology and the off-shore structure inferred from geophysical measurements.

From studies of the Mesozoic faulting in Central East Greenland, Surlyk (1977) proposed a model for the Mesozoic basin development of East Greenland which predicted the location of a triple junction in the area south of Scoresby Sund and the existence of "failed arm" sedimentary basins caused by crustal updoming. In his sketch map reconstruction of the northern North Atlantic prior to opening, shown in Figure 1.6, Surlyk (1977, 1978) emphasised the Jurassic relationship between the Mesozoic sedimentary basins of Central East Greenland and the Viking graben of the North Sea. He further postulated the existence of a third arm to the graben structure along the East Greenland coast south of Scoresby Sund.

Surlyk (1977) supported his hypothesis for a triple junction formed by crustal updoming with the following evidence:

(1) the arms of triple junctions so formed are widest at the centre of the dome and become narrower with increasing distance from the centre. The Jurassic basin of Central East Greenland narrows from about 140 km width in the south to only 10 - 20 km in the north;

(2) the ideal configuration of rifts radiating from a triple junction is a symmetric pattern of three graben at an angle of 120° to one another. The sharp change in direction of the coastline south of Scoresby Sund implies that a coast-parallel basin off the Blosseville coast would

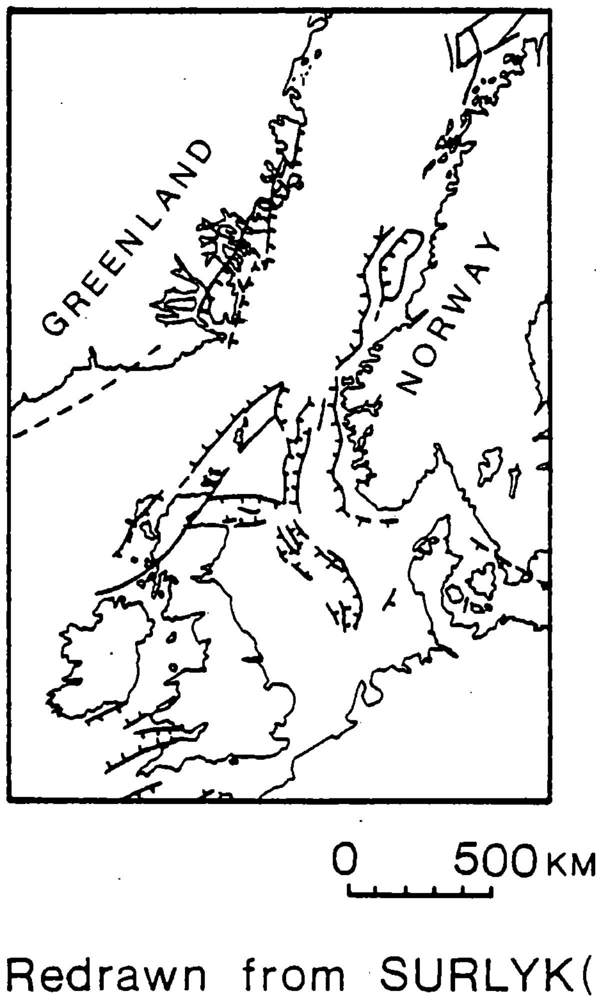

Figure 1.6 Sketch map showing basin formation related to the Mesozoic rift of East Greenland and contemporaneous rifts in the northern North Sea and North Atlantic Ocean. A postulated Jurassic triple junction south of Scoresby Sund is inferred.

form an angle of about 120^{o} with the coast-parallel Jurassic basin to the north;

(3) the direction of sediment transport in the fault-controlled Jurassic basins of Central East Greenland indicates longitudinal sediment fill towards the south. Longitudinal transport towards the centre of the triple junction is characteristic of many "failed arm" sedimentary basins.

This model proposed by Surlyk predicted a major sequence of Mesozoic sediments offshore along the East Greenland continental margin. To what degree the distribution of graben structures had been affected by subsequent episodes of seafloor spreading throughout the Tertiary or whether submarine erosion had removed any surviving remnants of the Mesozoic basin was a matter for speculation. Indeed, the very existence of such a sedimentary basin was entirely conjectural, although Henderson (1976) indicated the probable extent of major sedimentary units off the coast of Greenland based on the interpretation of aeromagnetic data.

It was the purpose of the 1977 geophysical cruise to East Greenland to try to find some answers to these questions.

CHAPTER 2

DATA ACQUISITION AND PRELIMINARY PROCESSING

2.1 Introduction

The continental margin of South East Greenland between latitudes 58° and 65°N was investigated by Durham University during two geophysical research cruises in 1973 and 1974 (Featherstone, 1976). During late July and August 1977, a further marine geophysical investigation of the East Greenland continental margin was carried out between latitudes 63° and 69.1°N, thereby extending the previous survey area into the Denmark Straits and beyond the submerged Greenland-Iceland aseismic ridge.

The 1977 survey was carried out by the research vessel RRS Shackleton. The ship was allocated and financially supported by the Natural Environment Research Council.

Provisional ship's track for the survey was drawn up on the basis of an offshore ice-limit indicated by ice synopsis charts provided by the Meteorological Office, Bracknell. Actual ship's track was updated during the cruise consistent with prevailing ice and weather conditions, and the inexorable demands of time.

Bathymetric, magnetic, gravity and multi-channel seismic reflection data were recorded along predominantly NW-SE profiles approximately perpendicular to the anticipated strike of the continental margin. The geophysical data were augmented by two disposal sonobuoy seismic refraction/wide-angle reflection experiments. The survey area and the ship's track are shown in Figure 1.1.

The senior scientist responsible for the conduct of the research cruise was Mr J.H. Peacock.

The ship was at sea for a total of 16 days (28 July until 13 August), out of which 12 days were spent in active data acquisition in the survey area. With the exception of heavy storms at the beginning and end of the survey, good weather prevailed throughout the cruise. The northern limit of the geophysical investigation was dictated by extensive offshore ice conditions at latitude 69°N. Despite this, nearly 3500 km of continuously recorded bathymetric, magnetic and gravity data were collected in the survey area and approximately 2000 km of multi-channel seismic reflection data were gathered in a series of nearly parallel profiles traversing the continental margin.

2.2 Equipment and data acquisition

The instrumentation for measurement and recording of geophysical and essential related data is outlined below. Other important acquisition considerations are included under the relevant section.

Bathymetry:

IOS Precision Echo Sounder - Mark 3 (analogue)
Digitrak Precision Depth Recorder (digital)

Gravity:

La Coste and Romberg shipboard gravity meter mounted on a gyroscopically controlled stable platform
instrument no. s - 4Ø
time constant = 4 minutes
calibration constant = Ø.9915 mgals/division

The La Coste and Romberg stabilised platform shipboard gravity meter, with its attendant computer and servo-mechanisms, was located just forward of amidships, and at approximate sea level, in the gravimeter room of the RRS Shackleton. The overall length of the ship was 61 metres and its displacement was 1685 tonnes.

The theoretical and practical considerations of measuring gravity at sea are discussed at length by Worzel and Harrison (1963), La Coste (1967) and La Coste, Clarkson and Hamilton (1967).

The gravity meter provided analogue output of the gravity reading, the spring tension, the cross coupling correction and the total correction applied to the recorded gravity values.

Gravity corrections due to the ship's motion (the Eotvos correction) were made off-line on the IBM 1130 computer during subsequent data reduction (see section 2.3).

The absence of track intersection points in order to assess discrepancies in gravity values resulting from navigational inaccuracies and instrument drift was unfortunate. Stormy weather towards the end of the survey precluded a return to Reykjavik along a track intersecting the profiles already surveyed. However, one track intersection point was achieved at 68.7063°N, 24.6067°W and the discrepancy between gravity values on the two profiles at their common point was found to be 0.7 mgal. Valliant et al (1967) reported on sea-gravimeter trials carried out on the Halifax Test Range in 1972. The test consisted of a total of 33 traverses over precisely located and calibrated test profiles. They defined their errors as the difference between surface and underwater measured gravity values reduced to a common datum. The mean observed error for the La Coste and Romberg S-39 gravity meter was 1.8 $\pm$ 1.0 mgal and the spread of errors was observed to be a nearly normal Gaussian distribution.

Taking into account instrument drift considerations (see details of the gravity tie-ins, section 2.4), the survey gravity measurements were probably accurate to within $\pm$ 2.0 mgals at worst.

Magnetics:

Varian proton precession magnetometer
model no. 14937; serial no. 105
6 second polarisation period

The proton precession magnetometer measured the total magnetic field of the earth. The details of its operation are well known (for example, Dobrin, 1976). The sensor bottle was encapsulated in a robust waterproof container and towed behind the ship by a low-noise towing cable. The length of cable played out was approximately 183 metres, about 3 times the length of the ship, in order to minimise the unpredictable magnetic effect of the vessel. Provided that the sensor bottle is more than 2 ship's lengths astern of the ship, the magnetic disturbance induced by most ships does not exceed 3γ and can normally be neglected (Bullard and Mason, 1963).

Navigation:

LORAN Type C Receiver
Magnavox Satellite Navigator
Micro-Technica Sirius Gyro Compass
Weather facsimile receiver (ice synopsis charts)

Grenway crystal clock and timing system
Two-component electromagnetic velocity log

The primary navigation method was provided by TRANSIT, the U.S. Navy Navigation Satellite system, which employs six satellites in circular, polar orbits circling the earth every 107 minutes approximately (Stansell, 1978). The interval between position fixes varies from about 35 to 100 minutes depending on the navigator's latitude but at typical survey latitudes of 60^{o} - 70^{o}, the average fix interval is approximately 30 to 50 minutes.

Satellite navigation employs the Doppler shift of a signal transmitted by the satellite and received by the observer. For a moving observer, the motion must be recorded before an accurate position fix can be computed.

The shipboard HP2100 computer took ship's speed from the two-component electromagnetic velocity log and ship's heading from the gyro compass in order to compute an approximate fix by dead reckoning. During a satellite pass, the Doppler count on the incoming signal was used to update the initial estimate to provide accurate fix solutions at the beginning and end of each Doppler count interval. When the fix solution had converged, delta-latitude and delta-longitude values were applied to the current position and so the accumulated dead reckoning error was eliminated.

A complete discussion of fix accuracy is given by Stansell (1978). Position fixes computed from satellites with elevations between 10^{o} and 70^{o} were chosen, since passes falling outside these limits were more likely to suffer degraded accuracy. Furthermore, fix solutions requiring only 3 or 4 iterations to converge on to the final fix were selected in preference to other satellite fixes. Subject to these criteria, specific satellite fixes were transferred from the satellite logger paper roll and input manually or on paper tape into a navigation file on the mobile IBM 1130 computer.

Stansell (1978) estimated that for a stationary observer, fix accuracy was of the order of 50 metres root mean square radial error. However, a velocity-north solution for a moving observer was subject to greater error and it may be optimistic to claim absolute fix accuracies to within 100 metres rms radial error for the cruise data. The single track intersection point result showing a discrepancy of only 0.7 mgal between the gravity values recorded at the common point along two independent profiles may indicate good relative fix accuracy for the survey but on the basis of only one cross-over point, this is a tentative conclusion.

LORAN-C navigation data were also recorded at 10 minute intervals by the scientific watchkeepers. The basic principle of LORAN navigation was the use of time-difference readings representative of the relative positions of the receiver and three fixed location transmitters, comprising two master/slave pairs. The master transmitter station was located on Eysturoy in the Faeroe Islands and the two slave stations on the Snaefellsnes peninsular of Iceland (lane SL3-Y) and Jan Mayen Island (lane SL3-Z) respectively (see LORAN-C Position Plotting Chart No. 7404, U.S. Defence Mapping Agency). Fix accuracy was a function of the distance from each transmitter and the correct use of area correction factors on the LORAN-C charts. Accuracies of approximately 50 to 200 metres were to be expected in areas of good ground wave cover.

However, the angle of intersection of the hyperbolic lines of position corresponding to the available master/slave pairs in the survey area was so acute as to be unfavourable for accurate fix determination. Therefore, it was decided not to use the LORAN-C navigation data, but to rely solely on satellite navigation for updating position estimated by dead reckoning.

Data logger:

The output from the gravimeter, magnetometer, Digitrack depth recorder, gyro compass, crystal clock and electromagnetic velocity log (fore-aft and athwart velocities respectively) were sampled at 1 second intervals and recorded in multiplexed form on magnetic tape by a modified Decca data logger (Stacey et al, 1972). The digitally recorded data were supplemented by analogue output from the gravimeter, magnetometer and precision echo sounder, the analogue records being annotated at 10 minute intervals by the scientific watchkeepers.

A scientific log was continually updated at 10 minute intervals and this provided back-up data for the other parameters in the event of data logger failure or tape malfunction. Parameters included compass heading, fore-aft and athwart velocities, pairs of LORAN-C readings, details of satellite navigation fixes and general comments relating to instrument performance and details of experimental status.

Seismic source:

3 Bolt airguns, synchronised to fire simultaneously
chamber capacity: 1 @ 4.92 litre and 2 @ 2.62 litre
normal working air pressure = 10.3 - 12.4 MPa
nominal source depth = 6.7 m

The ideal seismic energy source consists of a delta function impulse whose frequency spectrum is constant over all frequencies. All frequencies are equally represented. A single airgun seismic source provides a sharp impulsive primary pulse but much of its energy remains to generate an extended series of secondary pulses. This bubble oscillation is very troublesome because if the downgoing signal consists of the primary event plus a series of secondary pulses, any "single" event from a sub-surface reflecting horizon will appear on the reflection record as the primary plus a train of secondary arrivals. In this way, the bubble oscillations can completely swamp real events on the seismic record.

Bubble oscillation can be removed by the data processing technique of deconvolution or an attempt to suppress the train of bubble pulses can be made by design of a suitable airgun array. Modern seismic reflection surveys use a combination of both methods.

The airgun is a reliable and powerful seismic energy source producing a signature with a broadband energy spectrum (Brandsaeter, Farestveit and Ursin, 1979). The objective of both deep penetration and high resolution can result in a compromise between their conflicting design requirements. High resolution demands a signal with a broad frequency spectrum. Deep penetration requires enhanced source strength within the low frequency components of the source spectrum (Brandsaeter et al, 1979). In designing a seismic acquisition system, Giles and Johnston (1973) stress the inter-dependence of source, receiver and recording systems. In particular, the far-field signature of the seismic pulse depends on the airgun array depth, the streamer depth and the impulse response of the recording system.

The output pressure waveform from a single airgun has been derived theoretically by Ziolkowski (1970). The form of the radiated pressure and the oscillation of bubble radius from a single airgun are shown in Figure 2.1. The period of oscillation of the bubble pulses for a single airgun is given approximately (Giles and Johnston, 1973) by:

$$T = \frac{1}{109} \frac{(PV)^{1/3}}{P_o^{5/6}} \qquad 2.1$$

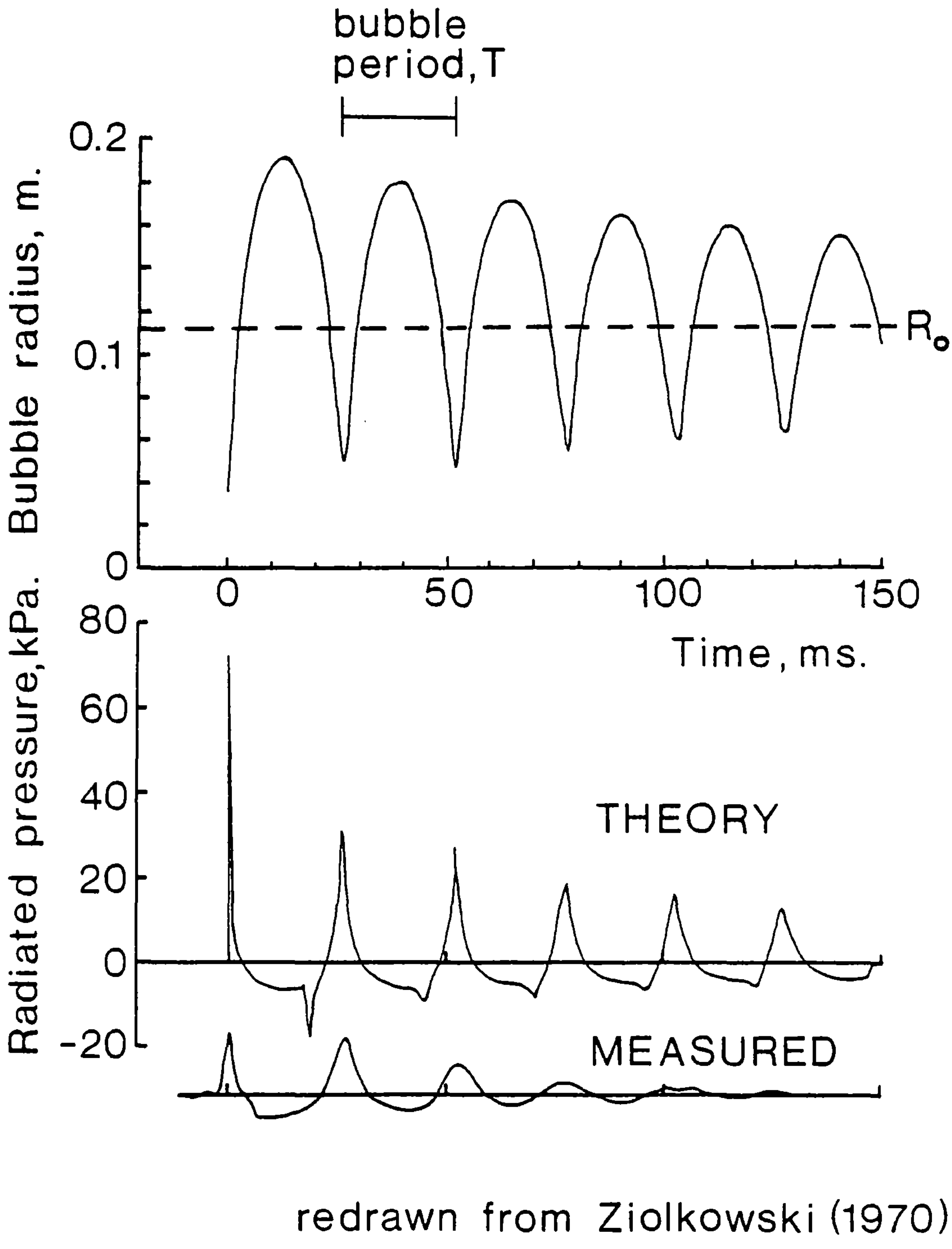

Figure 2.1 The radiated pressure and oscillation of bubble radius from a single airgun of capacity 0.155 l, operating at depth 14m and air pressure 13.3 MPa. Ro is the radius of the bubble at which the internal pressure and hydrostatic pressure are equal (redrawn from Ziolkowski, 1970).

where T = the bubble period (seconds)

P = the absolute gun chamber pressure (bars)

V = the gun chamber volume (litres)

P_o = the absolute hydrostatic pressure (bars).

This equation does not take into account the perturbing effects of the sea/air interface and the proximity of other airguns on the bubble period estimated. These effects are discussed at length by Giles and Johnston (1973) and Safar (1976a, 1976b), but see also Buchanan (1977), Ziolkowski (1977) and Safar (1978).

Equation 2.1 indicates that the frequency content of the airgun signature is controlled by the size of the initial bubble. Large gun chamber volumes and high compressed air pressures give long period bubble oscillations and enhance the low frequency content of the spectrum. Conversely, increasing the depth of the airgun reduces the bubble period and so increases the frequency of the pulse. However, Mayne and Quay (1971) carried out tests to determine the seismic signatures of large airguns and observed that at shallow depths, relative responses at high frequencies were enhanced relative to airgun signatures obtained at greater depth due to surface reflection from the sea/air interface. These authors also observed an increase in the low frequency content of the airgun signature at shallower depths. The results were obtained with a 16.39 ℓ divided-chamber airgun operating with an air pressure of 11.7 MPa at depths of 6.1 m and 12.2 m respectively.

The initial pressure of the compressed air in the gun chamber is not a crucial factor in determining the bubble oscillation frequency, especially at high pressures. Giles (1968) carried out tests with a 0.66 ℓ airgun at 9.8 m depth and observed a peak frequency change from 24 to 23 Hz for a pressure change from 10.3 to 13.8 MPa. He concluded that a fluctuation in air pressure of $\pm$ 0.68 MPa was easily tolerable and would still yield a reliable and reproducible seismic signature.

Therefore, by using several different guns with different chamber sizes synchronised to fire simultaneously, it is possible to generate a broad, flat frequency spectrum between reasonably specified limits and so shape the output spectrum in order to approach the broadband characteristic of the ideal seismic signature (Giles, 1968).

The far-field signature of a single airgun represents the superposition of the primary pulse and ghost arrivals from the sea/air interface above the source and receiver respectively. The radiation pressure from the airgun propagates approximately as a spherical bubble. On reflection at the sea/air boundary, the up-going signal is reflected downwards with a phase change of $-\pi$. Therefore, an inverted, time-delayed waveform is superimposed on the down-going primary. Ziolkowski (1971) develops this theory for a single airgun and concludes that whenever the source depth, d_S and receiver depth, d_R are integer multiples of $\lambda/2$ (where λ = the fundamental wavelength of the bubble period), zeroes will appear in the frequency spectrum of the received signal at frequencies, f given by

$$f = \frac{V_w}{\lambda} \qquad 2.2$$

where λ = the wavelength associated with the bubble period

V_w = the velocity of the seismic pulse in water.

The airgun depth, d_S and streamer depth, d_R for the East Greenland survey were different ($d_R \approx 2d_S$) so that two sets of zeroes in the frequency spectrum of the recorded signal were generated due to ghost superposition on the primary signal. Ziolkowski (1971) proposed the elimination of zeroes in the frequency spectrum of the received signal by using several non-interacting airguns of different chamber capacities located at different depths. However, this theory was restricted to airguns sufficiently separated to ensure that each bubble acted independently of the other bubbles.

Nooteboom (1978) investigated airgun separation distances necessary to prevent bubble interaction and observed that it was the capacity of the larger of two airguns which determined the separation necessary to prevent interaction. Nooteboom gave the following relationship:

$$D = 5.1 \left(\frac{P}{P_o}\right)^{1/3} V^{1/3} \qquad 2.3$$

where D = the distance between the guns in metres

P = the absolute gun chamber pressure in Nm^{-2}

P_o = the absolute hydrostatic pressure in Nm^{-2}

V = the chamber volume of the large gun in m^3.

At a nominal depth of 6.7 m and an air pressure of 10.3 MPa, Nooteboom's

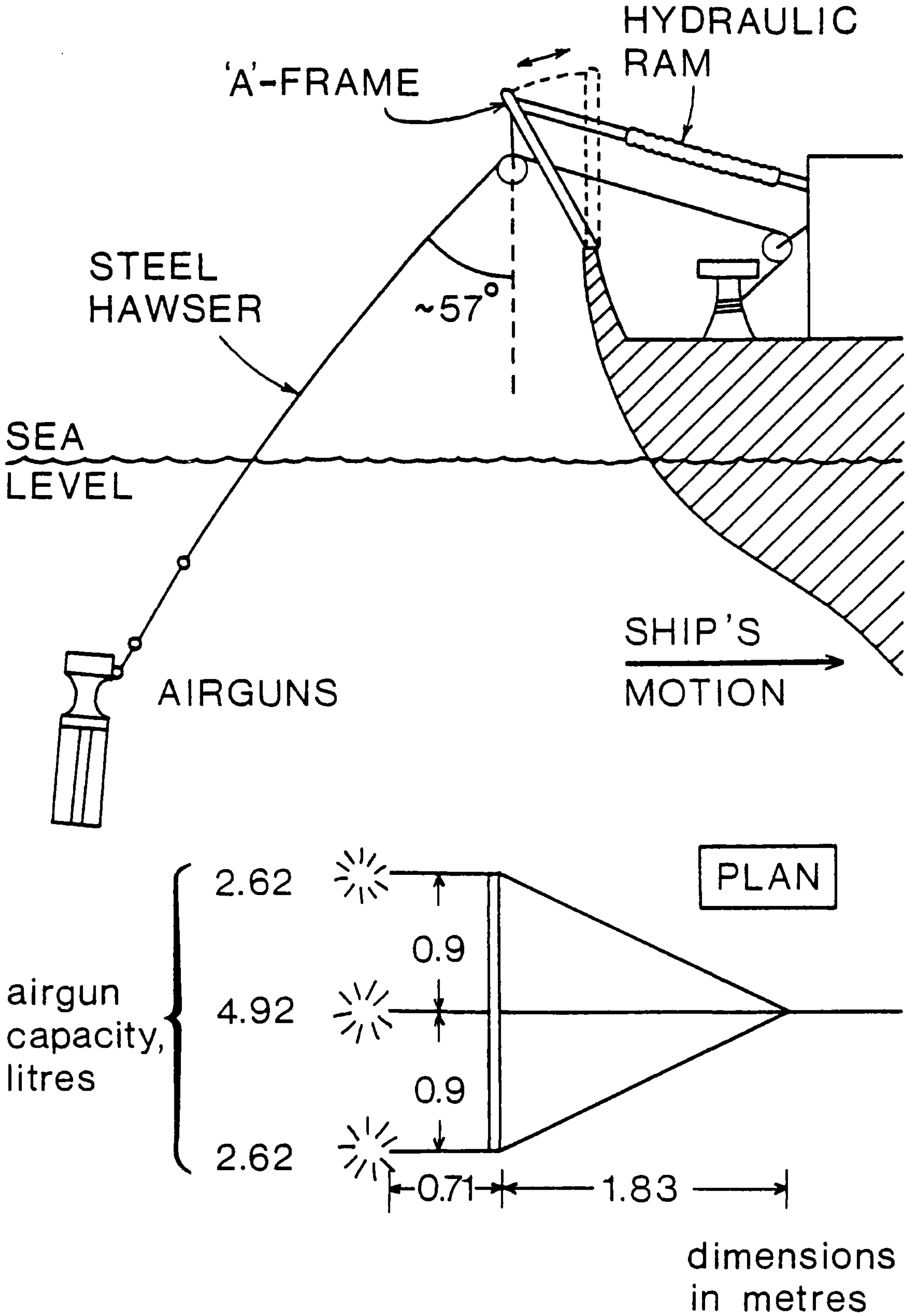

Figure 2.2 Schematic diagram illustrating the towing arrangement and airgun separation distances for the 3-airgun array used during the East Greenland marine geophysical survey, 1977.

criterion predicts a minimum separation distance of 4.6 m for the 4.92 ℓ airgun. The arrangement and dimensions of the 3 airgun array used for the marine survey are shown in Figure 2.2. The separation distance of 0.9 m suggests that the bubble pulses from each airgun were very strongly interacting.

A simple calculation is carried out retrospectively in order to assess the performance of the airgun array. Let us estimate the equilibrium bubble radius, R_O of each airgun when firing independently of one another. The extension of bubble theory, developed for a single airgun in the absence of boundaries, to an array of 3 airguns whose bubble pulses were strongly interactive represents a crude, first-order approximation but it does provide a working model for the operation of the airgun array.

The equilibrium bubble radius, R_O is the radius of the bubble at which the partial pressure of air inside the bubble is equal to the hydrostatic pressure outside the bubble and at an infinite distance away from it. Assuming a perfectly adiabatic bubble oscillation, the equation of state for a fixed mass of gas is given (Ziolkowski, 1970) by:

$$PV^n = \text{CONSTANT} \tag{2.4}$$

where P = the pressure of gas

V = the volume of gas

$n = \gamma$ = the ratio of specific heats.

Using Equation 2.4 and assuming that the initial gas bubble is a sphere of volume equal to the airgun chamber, the equilibrium radius, R_O of the gas bubble is given by:

$$R_O = \left(\frac{3}{4\pi}\right)^{1/3} V_I^{1/3} \left(\frac{P_I}{P_O}\right)^{1/3n} \tag{2.5}$$

where P_I = the initial air pressure in the airgun chamber

V_I = the volume of the airgun chamber

P_O = the hydrostatic pressure outside the bubble.

The equilibrium radii for the 4.92 ℓ and 2.62 ℓ airguns respectively are tabulated, together with their respective bubble periods and associated data, in Table 2.1. The data are calculated for a nominal airgun pressure of 10.3 MPa, $n = 1.13$ and $P_o = 0.068$ MPa for water depth = 6.7m.

Table 2.1 Calculated airgun parameters for nominal airgun pressure of 10.3 MPa

AIRGUN CAPACITY litres	BUBBLE PERIOD $\times 10^{-3}$ seconds	BUBBLE FREQUENCY Hertz	EQUILIBRIUM BUBBLE RADIUS metres
2.62	82	12.2	0.38
4.92	101	9.9	0.46
10.16	129	7.8	-

It is interesting to note that Safar (1976b) deduced that the minimum distance, D necessary to prevent bubble interaction between any pair of identical guns is approximately given by:

$$D \simeq 10\, R_o \qquad 2.6$$

The value of $R_o = 0.46$ m for the 4.92 ℓ airgun yields a value for D = 4.6 m which agrees with the predicted separation distance given by Nooteboom (1978), Equation 2.3.

Inspection of Figure 2.1 shows that after the airgun has been fired, the initial pressure pulse peaks and falls to its equilibrium value, whilst the bubble radius increases and attains its equilibrium value, R_o for the first time. How long does it take for the bubble radius to expand to its equilibrium value? Table 2.2 gives approximate times taken for the initial bubble to expand to its equilibrium value. These data were taken from actually recorded pressure signatures observed by Mayne and Quay (1971) and Smith (1975).

The time taken for the bubble to attain its equilibrium volume appears to be approximately independent of airgun size for the 4.92 ℓ and 2.62 ℓ airguns, and an average time of 11 ms has been adopted. The geometry of the bubble pulses for the 3 airgun array, 11 ms after the shot instant, is shown in Figure 2.3. The simple theory predicts no overlap between bubbles until after the primary pressure pulse has been radiated. The bubble radii continue to increase through their respective equilibrium values and each bubble expands to a maximum radius typically of the order 1.8 R_o (Ziolkowski, 1970, 1977). Therefore, almost immediately after the primary pressure pulse has been radiated from each airgun, the bubbles overlap and coalesce to form one large bubble.

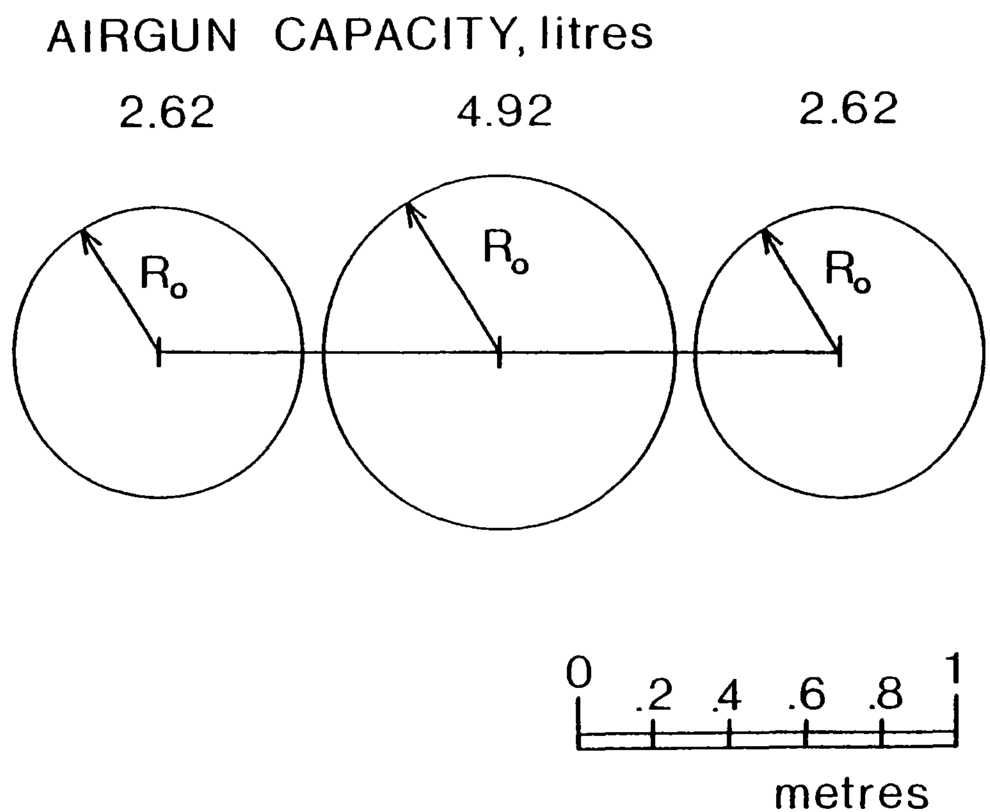

Figure 2.3 Schematic diagram to show the geometry of the 3 airgun bubble pulses 11ms after the shot instant. Ro represents the equilibrium radius of each respective airgun.

Table 2.2 Observed values for the time taken by the initial bubble to attain its equilibrium radius, R_o

TIME FOR BUBBLE TO ATTAIN R_o X 10^{-3} sec.	AIRGUN CAPACITY litres	AIR PRESSURE MPa	AIRGUN DEPTH metres	REFERENCE
13	4.92	9.0	7.9	Smith (1975)
10	4.92	11.7	6.1	Mayne and Quay (1971)
11	2.62	8.6 8.3	4.6 8.5	Smith (1975)

Safar (1976a) made two important points. Firstly, he estimated that 80% of the equilibrium volume of the air bubble for a single airgun is occupied by the gun. Secondly, the initial volume of the bubble is considerably less than that predicted by assuming a spherical source with initial volume equal to that of the airgun chamber. The first point indicates that the equilibrium radius, R_o estimated from the simple theory is probably too small since a fixed mass of gas will occupy a smaller volume than the actual gas plus airgun combination at the same external pressure. The second point means that the equilibrium radius estimated from Equation 2.5 is too large since V_I was overestimated.

Fortunately, although the relative magnitude of these opposing constraints cannot be estimated here, their effects tend to cancel one another and it probably indicates that the estimated equilibrium radius, R_o is approximately correct.

Giles and Johnston (1973) pointed out that using an array of small airguns placed close enough together so that their bubbles coalesce when fired simultaneously is a more effective method of obtaining the pulse of an equivalent volume large airgun. The initial pulses of each gun are not attenuated but reinforce each other to provide an enhanced primary pulse. The interaction of the coalesced bubbles tends to attenuate the bubble pulse compared with the output from a single large airgun of equivalent volume.

The bubble period of the coalesced guns is the same as the period of a single big airgun of the same total volume. The bubble period of the airgun array of total volume 10.16 ℓ is 129 ms compared with the periods of 101 ms for the 4.92 ℓ gun and 82 ms for the 2.62 ℓ gun (Table 2.1).

The presence of two different gun chamber volumes in the array provided a broader frequency spectrum in the far-field signal and the different bubble oscillation periods caused more effective bubble pulse attenuation in the coalesced bubble, therefore yielding a superior primary-to-bubble ratio relative to a single gun of the same total volume. The superposition of the 3 primary pressure pulses provided a higher amplitude primary signal than that obtained from an equivalent volume single airgun.

Unfortunately, the signature of the airgun array was not measured at sea by using a single hydrophone to record the far-field signal. The signature was not monitored throughout the survey either, although small variations of the emitted signal can occur due to airgun synchronisation errors, fluctuations in gun depths related to ship's speed and failures of single guns (Nooteboom, 1978). However, Nooteboom commented on the use of the constant monitoring of the airgun signature to provide data for the derivation of a deconvolution filter for each trace and concluded that it was ineffective for a signal with primary-to-bubble ratio better than 7.

Seismic streamer:

Geomechanique 'Flexotir' marine seismic streamer;
11 active sections, each active section 50 m in length,
48 hydrophones per section arranged in 3 in-series groups of
16 detectors connected in parallel;
50 m passive sections separating active sections
offset = 228 m
total length = 1345 m
depth of compensation = 12.2 m

The seismic streamer was towed behind the ship and its precise layout is shown in Figure 2.4. Each section of the seismic streamer consisted of an approximately neutrally buoyant, oil-filled neoprene tube containing stress members and mechanical and electrical connectors. The active sections contained, in addition, 48 equally-spaced hydrophones arranged in 3 groups, each group comprised of 16 hydrophones connected in parallel. The outputs from the three groups were summed in series to form an array and this signal formed the input to one channel of the shipborne recording system.

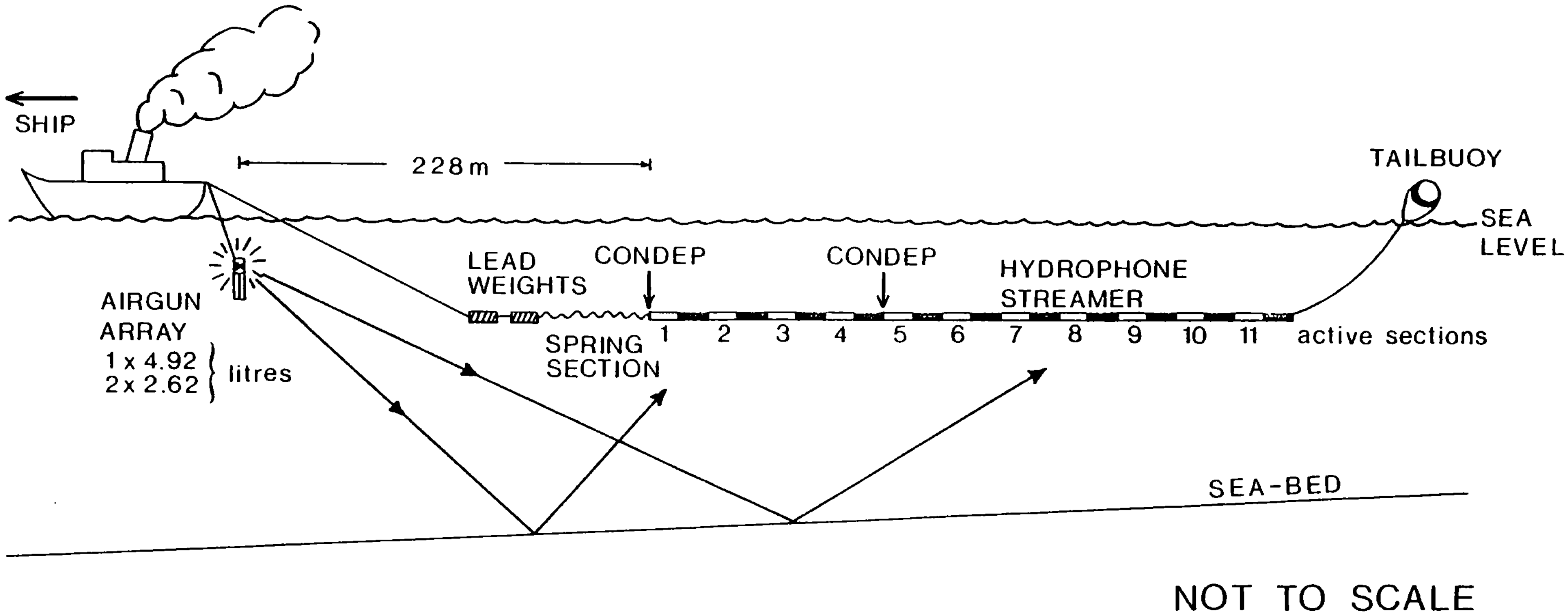

Figure 2.4 Towing arrangement of the hydrophone streamer and airgun array for the acquisition of multi-channel seismic reflection data, East Greenland marine survey, 1977.

The seismic streamer incorporated a limited number of noise-reduction features. In order to decouple the streamer from the motion of the ship, the streamer was attached to the towing cable through a 100 m long spring section. Two lead weights were attached to the tow cable in order to submerge the rest of the streamer to a suitable towing depth. Each active section of the streamer was separated from its neighbour by a passive section. The effect of the motion of the tailbuoy was suppressed by terminating the streamer with a passive section.

The tow-depth was controlled by two depth controllers, 'condeps' or 'birds', fitted immediately before active sections 1 and 5 respectively. The angle at which the fin of each controller moved through the water was governed by the pressure difference between compressed air in a tank in each bird and the hydrostatic pressure of the surrounding water. The depth of compensation was set at 12.2 m.

A complete discussion of hydrophone streamer noise is given by Bedenbender, Johnston and Neitzel (1970) and Schoenberger and Mifsud (1974). Reduction of the absolute tow-noise level is equivalent to increasing the depth of penetration of the seismic system, since the ultimate resolution of primary arrivals from deep reflecting horizons is governed by the noise level in the acquisition instrumentation.

Schoenberger and Mifsud (1974) carried out sea-going trials on a streamer already designed to incorporate several noise reduction features. Their conclusions and the implications for the seismic streamer used for the East Greenland survey are summarised here:

(1) The depth controller 'birds' were identified as significant discrete noise sources. The bird noise was local and symmetric, and its spectral characteristics were found to lie in the seismic band between 7 and 30 Hz. A minimum separation of about 3 m between bird and active section was recommended on the basis of noise level observations in hydrophone response adjacent to depth controllers. The noise level was found to be about 14 db above the ambient noise level at a distant hydrophone along the streamer at tow speeds around 9.8 km hr^{-1}. Hence, the location of depth controllers immediately preceding active sections 1 and 5 probably was a source of local noise on these seismic channels.

The ship, lead-in cable and tailbuoy were not considered to be significant discrete noise sources.

(2) The remaining non-bird noise was concentrated in the frequency range between 10 and 25 Hz. Random and coherent noise components were recognised.

The array of n hydrophones improved the signal to noise ratio for random noise by a factor of $\sqrt{n}$. The hydrophone separation in each active section was 1.0 m. Schoenberger and Mifsud found that the coherence distance for their streamer was less than 2.4 m (the coherence distance is the smallest separation of hydrophones for which the noise is still uncorrelated). Assuming that the 'random' noise was still uncorrelated for the array with detector spacing of 1.0 m, the signal to random noise improvement for n = 48 was a factor of 6.9 relative to that of a single hydrophone.

The array was less effective in reducing coherent noise. Since the main energy of the noise was in the seismic frequency range between 10 and 15 Hz, this was only to be expected. Savit, Brustad and Sider (1958) developed the following expression for the amplitude, A_M of the output from an array of M detectors evenly distributed over an aperture, S:

$$A_M = \frac{\sin\left[\frac{M}{M-1} \cdot \frac{\pi S}{\lambda}\right]}{M \sin\left[\frac{1}{M-1} \cdot \frac{\pi S}{\lambda}\right]} \qquad 2.7$$

where λ = the apparent wavelength of the incident waveform.

The effective aperture of each active section of the streamer was slightly less than its nominal length because the hydrophones were mounted away from the ends of the active section. The form of the array response for S = 47 m and M = 48, equal gain detectors is shown in Figure 2.5. Schoenberger and Mifsud (1974) observed that the dominant coherent noise was in the form of a wave travelling horizontally away from the boat with a velocity of 1524 m s^{-1}. For this velocity, each array of the "Flexotir" streamer acted as a low pass filter with cut-off frequency about 30 Hz, a 3 db point at 14 Hz and an attenuation rate of approximately 21 db/octave in the range between frequencies 14 and 30 Hz. Note that the direct water wave (with approximate velocity of 1460 m s^{-1}) from the airgun source

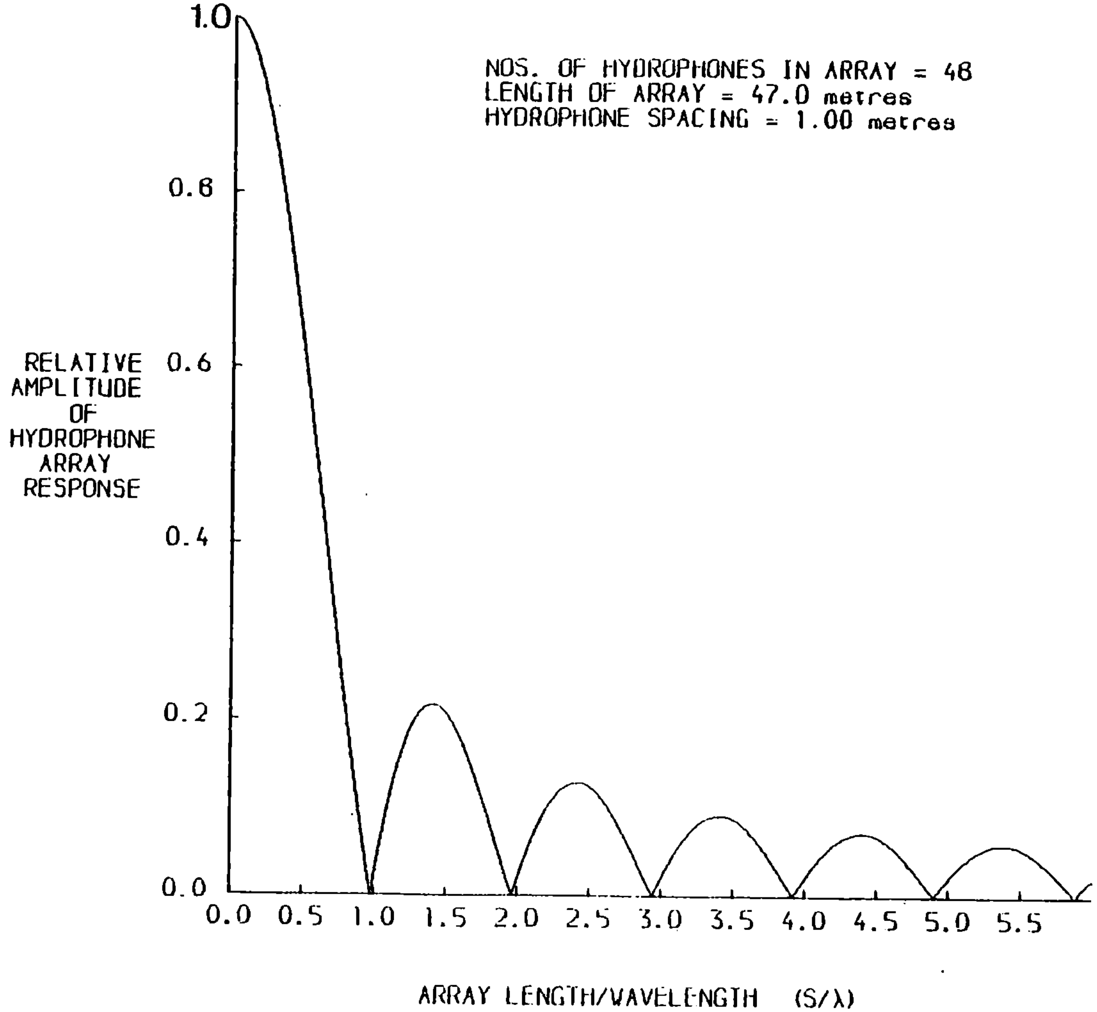

Figure 2.5 The array response for each active section of the hydrophone streamer, each section consisting of 48 equal gain hydrophones separated by a distance of 1m.

suffered a similar degree of attenuation.

What about the effect of each array on seismic arrivals? The apparent velocity, V_A' of an incident seismic event is given by:

$$V_A = \frac{V}{\cos\theta} \qquad 2.8$$

where V = the actual velocity of the incident wavefront (= the velocity in water, 1460 m s^{-1})

θ = the angle between the streamer and the ray path of the incident wave.

For $\theta = 70^{\circ}$ and a frequency of 30 Hz, the relative amplitude of the signal passed by one array of the "Flexotir" streamer was about 0.82. For lower frequency events and arrivals impinging on the streamer at steeper angles, the degree of attenuation was even smaller.

(3) The general conclusion regarding hydrophone streamer noise was that it was not induced by electrical noise or ambient sea conditions. The noise was locally generated. It was uniform along the cable but was not produced by cable strumming and vortex shedding. Pressure fluctuations along the cable were also considered to be unlikely sources. The nature of the noise source was not known.

The superposition of ghost arrivals on seismic signals incident on the streamer due to reflections from the air/sea interface has already been discussed in connection with the design of the airgun array.

No measurement of the feathering angle of the seismic streamer was made during the survey (the feathering angle is defined as the angle between the profile along which the ship is sailing and the line of the seismic streamer). Disregard of feathering resulted in a degraded resolution of the final stacked seismic reflection record because reflection points were no longer common as assumed in common depth point (CDP) stacking. However, since the survey program was primarily undertaken to define structural trends on a regional scale, no compensation for feathering was necessary (Renick, 1974).

<u>Seismic recording:</u>

Series 1010 Geophysical Digital Recording System manufactured by

SDS Data Systems (SDS 98 01 37A) comprising:

(1) signal conditioning cabinet including gain control and geophysical low-pass and high-pass filters;

(2) recorder cabinet with 2 magnetic tape transports (Model no. FT 152, Potter Instrument Co., Inc); digital data recorded on to 9 track, ½ inch, 800 bytes per inch, gapless magnetic tape (Memorex);

(3) power unit cabinet consisting of Lambda Electronics, Model LM, Regulated Power Packs;

(4) master control unit incorporating system control logic, analogue multiplexer and analogue to digital converter.

Seismic display:

(1) 2 EPC single-channel variable area display units using an electrically generated spark on heat sensitive paper;

(2) 1 Geospace Digital Seismic Monitor Recorder (Model no. MR-101A); a single-channel variable area display using galvanometer reflected beam trace on light-sensitive paper (the quality of the records deteriorated with age and exposure to light).

For each of the 11 seismic channels, a line balancing circuit was used to match the impedance of the amplifier to the high impedance of each active section of the streamer to enable optimum power transfer. A common mode rejection technique was used (Havill and Walton, 1975).

The analogue input to each channel was subject to an anti-aliasing filter. The alias filter was an active, low-pass filter with a 3 db point selected at a frequency of 62.5 Hz and a "roll-off" of 72 db/octave. The sampling frequency used for seismic acquisition was 256 Hz. Hence, the sampling interval was 4 ms and the Nyquist frequency was 125 Hz.

High- and low-pass analogue filters were optionally available on each seismic channel depending on the nature of the acoustic noise. The low-pass filter was active, with a 3 db point manually selectable from any of 3 values in the range 50 to 100 Hz and a "roll-off" of 24 db/octave. The high-pass filter was passive, with a 3 db point manually selectable from any of 3 values in the range of 5 to 35 Hz and a "roll-off" of 18 or 24 db/octave.

True amplitude recovery was made available by a binary gain ranging (BGR) amplifier with a dynamic range of 160 db. However, care was exercised in the selection of early gain control applied to the analogue signal in order to avoid saturation of the BGR amplifier by the first arrivals.

The Master Control Panel governed the operational sequence and the magnetic tape format. The length of recording time was set to 7 s for the multi-channel seismic data and to 12 s for sonobuoy data acquisition (channel 12). Adjustable elements of the digital gain control (DGC) were the rate of change of the amplifier gain applied to the time sequence representing late arrivals and the delay for which the analogue signal was to be held in order to prevent over amplification of early arrivals.

Each channel was sampled by an analogue multiplexer, subjected to automatic gain control and converted from analogue to digital form by a 16-bit word analogue-to-digital converter. The seismic data were then stored in multiplexed form on magnetic tape.

Thus, for each shotpoint, the sequence of events for the data acquisition process was as follows:

1. A timer pulse generated by an internal clock signals acquisition sequence initialisation.
2. Magnetic tape rewound until end-of-file (EOF) mark of previous data set located and any tape malfunction or malposition sensed. No errors indicated, then tape comes forward.
3. Preset early gains chosen for amplification of signal from each channel.
4. Format the magnetic tape and write header block data with early gains.
5. Fire airguns.
6. Seismic time sequence of each channel subject to pre-amplification and arrives at analogue multiplexer. Data multiplexed.
7. Analogue to digital conversion and seismic data stored in multiplexed format on magnetic tape.
8. "Read after write" facility and de-multiplexing of data for single channel display on shipborne monitor (EPC or Geospace display).

The shot interval was 21 s and the above sequence of events, 1 - 8, was repeated for every shotpoint.

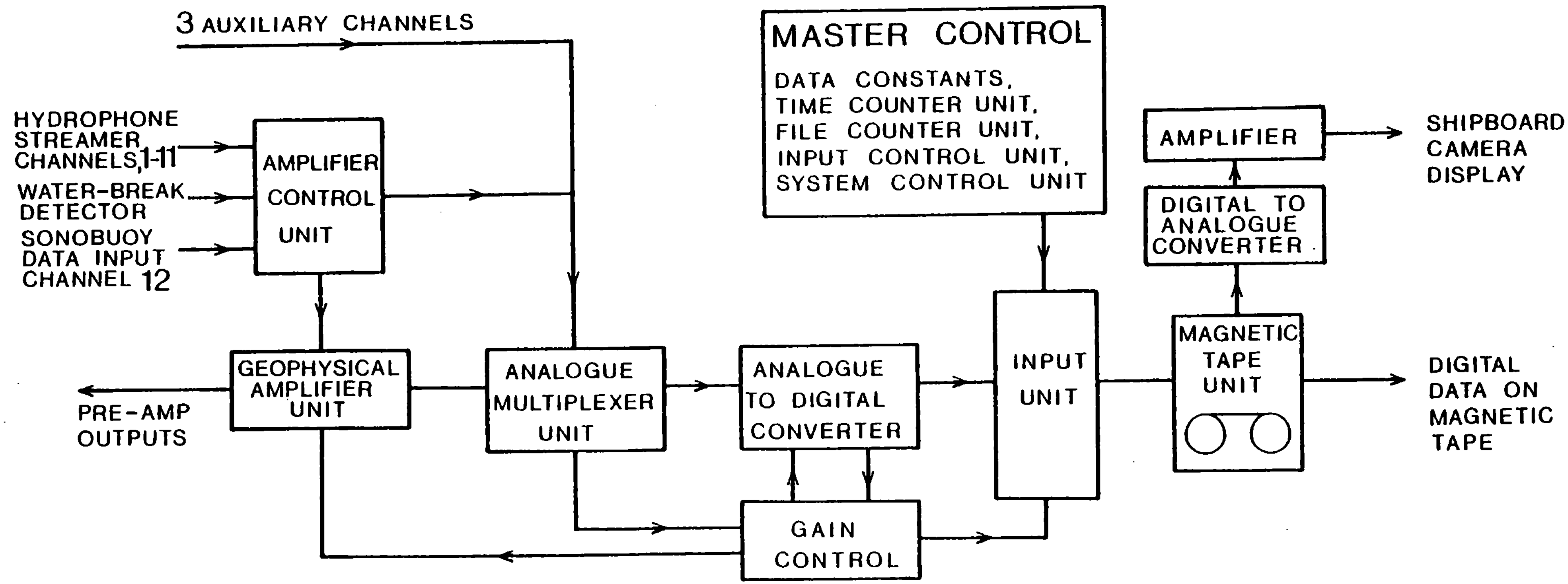

Figure 2.6 Schematic block diagram of the Series 1010 Geophysical Digital Recording System (SDS Data Systems, SDS 98 01 37A) used for multi-channel seismic reflection data acquisition on the East Greenland marine survey, 1977.

The A/D converter had facility for 30 input channels; 24 primary data channels, 3 auxiliary channels and 3 timing channels - "up-hole" geophone, water-break detector for the time origin and a time code for record delay since shot instant.

The "read after write" facility was basically the inverse of the recording sequence and parity checks were made to validate the most recently written data on the magnetic tape. Each 20-bit word consisted of 15 bits for the A/D conversion, 4 bits to store the binary gain factor and 1 bit to represent the "sign" of the signal. The reconstituted data was then displayed on the two EPC shipboard monitor display units in order to check the recorded data and to observe any subsurface geological features discernable on the single channel record. Channel 2 was chosen for display because it exhibited the highest signal to noise ratio. Record lengths of 1 and 4 s two-way travel time respectively were displayed.

The Geospace single-channel monitor recorder was used primarily to record the progress of disposable sonobuoy experiments.

The seismic acquisition system is summarised in Figure 2.6.

The seismic recording system was provided by Durham University and its operation was supervised by the senior scientist, Mr J.H. Peacock. The rest of the equipment and technical expertise was made available by the Natural Environment Research Council through the Research Vessels' Base, Barry.

2.3 Preliminary shipboard processing

Preliminary processing and reduction of gravity, magnetic, bathymetry and navigation data were carried out on a mobile IBM 1130 computer system (Stacey et al, 1972) installed in the ship's hold.

The geophysical data, sampled at 1 second intervals, were stored in multiplexed format in 10 second data blocks on magnetic tape by the modified Decca data logger. These data were transferred from magnetic tape on to disc, the data being de-multiplexed, checked and smoothed as required to provide a continuous function suitable for filtering.

The purpose of filtering the geophysical data recorded by the data logger was to remove the attenuation and phase distortion of the gravity data introduced by the heavy air damping of the gravimeter beam and to provide an accurate cut-off frequency for all the parameters related to the gravity measurements, including the recorded navigation data (Stacey et al, 1971). Frequency filtering was carried out in the discrete time domain by the convolution of the digital filter impulse response with the sampled data. Filtering was applied in two stages. A low-pass filter with cut-off frequency of 1/20 Hz was applied to all parameters and consisted of 141 coefficients. A second stage filter with cut-off frequency of 1/240 Hz, consisting of 191 coefficients, acted as a weighted low-pass filter for the gravity data and a flat low-pass filter for the other parameters.

Finally, the filtered navigational and geophysical data sampled at 1 s intervals were reduced to data sampled at 2 minute intervals, and also at 1/10 minute intervals for the bathymetric and magnetic data.

Having input selected satellite navigation data into the IBM 1130 computer, the ship's track calculated by dead reckoning was adjusted to fit the accurate satellite position fixes. In this way, position fixes at 2-minute intervals along ship's track were calculated. This completed the processing of navigation data.

The free air gravity anomaly was calculated using the International Gravity Formula (1967), having tied-in the relative readings of the ship-borne gravimeter to the absolute value of gravity at a temporary base station established in Reykjavik harbour. The details of the gravity tie-ins are given in Section 2.4.

The gravity readings taken at sea were corrected for the Eötvös effect caused by the motion of the ship relative to the rotating earth. The resulting centripetal acceleration was eliminated by applying the correction, E given by

$$E = 2\omega V \cos\phi \sin\alpha \qquad 2.9$$

where ω = the angular velocity of the earth

V = the absolute speed of the ship

ϕ = the latitude

α = the azimuth along which the ship is heading.

Equation 2.9 indicated that the navigation errors impose serious limitations on the accuracy of gravity measurements taken on a moving platform at sea. For example, for $\alpha = 90^{\circ}$ and $\phi = 66^{\circ}$, an error in ship's

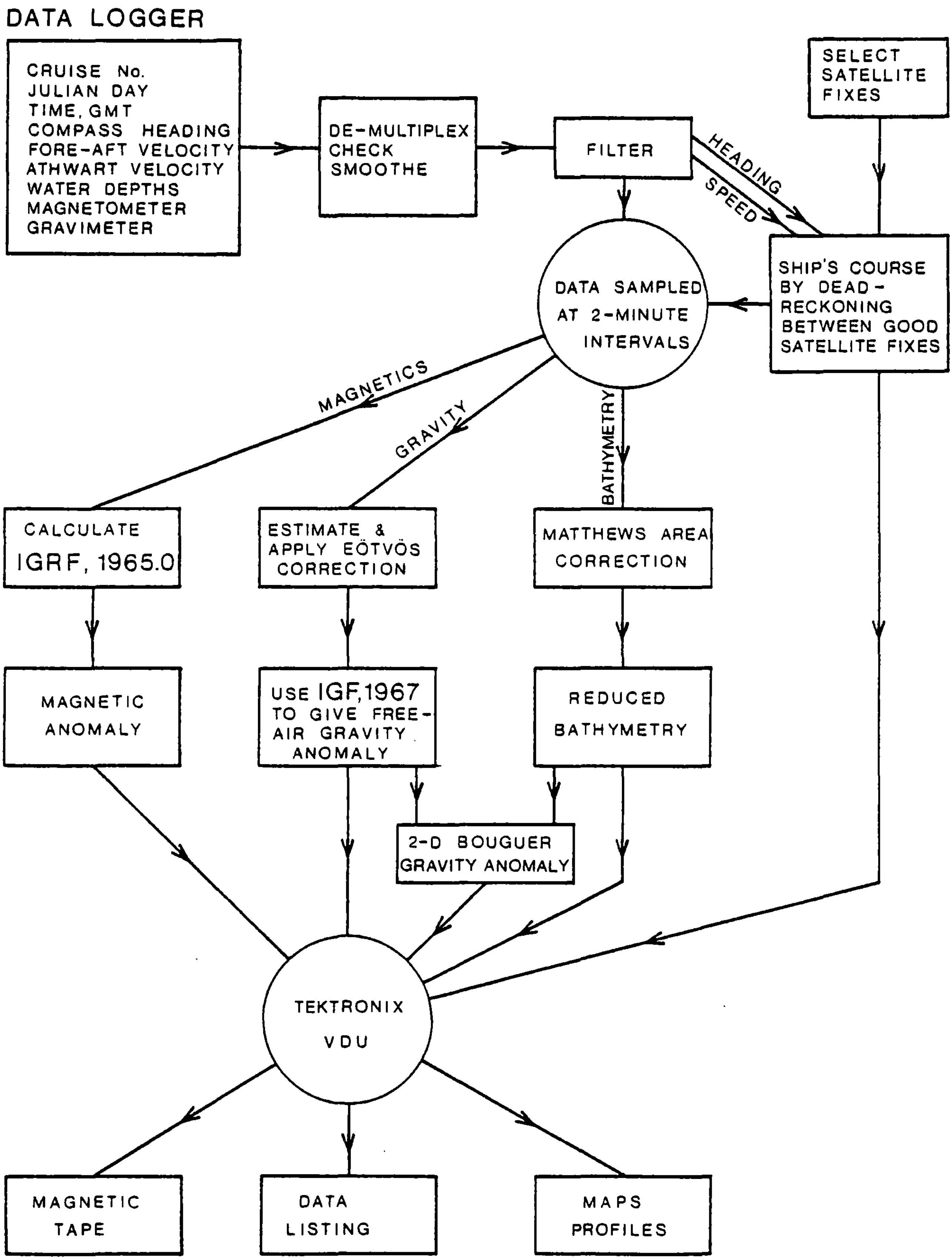

Figure 2.7 Programming sequence used for the reduction and preliminary processing of the marine geophysical data recorded on the data logger.

speed of 1 km hr^{-1} produces an effect of 1.7 mgal and an error in latitude of 100 m produces an effect of 0.7 mgal. For north-south motion, an error of 2^{o} in ship's heading results in an effect of 0.7 mgal.

Finally, the free air gravity anomaly was computed by subtracting the theoretical gravity value at the ship's geographical location from the corrected, observed gravity value at that point.

Instrument drift was investigated by a gravity tie-in to the gravity base station in Reykjavik during the mid-cruise port call on Julian Day 225. The observed instrument drift was + 0.38 mgal. Since the magnitude of the drift was small, no correction for instrument drift was applied to the gravity data. A further gravity tie-in was carried out in Manchester, England after completion of the total survey programme and the observed drift was + 0.29 mgal.

For the magnetic data, the magnetic anomaly was calculated as the difference between the observed total magnetic field and the theoretical value predicted by the International Geomagnetic Reference Field (IGRF), Epoch 1965.0. The spherical harmonic components of the IGRF were expressed in the Schmidt quasi-normalised form (Barraclough, 1978). No corrections were applied for diurnal variation.

Bathymetric data from the data logger magnetic tape were recorded in metres, a velocity of sound in water of 1463 m s^{-1} (800 fathom s^{-1}) having been assumed during the conversion of two-way transit times into depths by the precision depth recorder. Having located the relevant Matthews Area for the survey and input this information into the IBM 1130 computer, a correction for the variation in the velocity of sound in sea-water was applied so that corrected depths could be calculated. The Matthews Area correction takes the form of coefficients for a polynomial calculated to fit the corrections for a specified area and includes adjustments for salinity, temperature and location over the world's oceans (Matthews, 1939).

Throughout the processing sequence, the facility to display the data in the form of maps and profiles was used extensively. Obvious spikes in the data were edited manually. Finally, the processed geophysical data were displayed as profiles and as profiles along simplified ship's track on a map of scale 1 : 1,000,000 (Mercator projection). For completeness, the profile data are presented in Appendix A, and a chart with geophysical data plotted along simplified ship's track is stored in the pocket inside the backcover of this thesis (Enclosure 1).

The programming sequence used for the reduction and preliminary processing of the geophysical data is fully documented by Stacey and Allerton (1974). The logical procedure carried out is summarised in Figure 2.7.

2.4 Details of gravity tie-in

The La Coste and Romberg shipborne gravimeter only recorded relative changes in the value of gravity from one location to another. Therefore, it was necessary to tie-in the instrument readings to the known absolute value of gravity at a chosen base station before embarking on the survey programme.

A temporary gravity base station was established on the quay alongside the RRS Shackleton in Reykjavik harbour. This temporary station was tied-in to the gravity base station 0081 REYKJAVIK CH, located in the grounds of the Catholic Church in Reykjavik (Palmason et al, 1973), using a portable Worden gravimeter (model 115, meter no. 748, calibration constant = 0.0931 (3) mgals/division).

A check for instrument drift was made during the mid-cruise port call to Reykjavik using the same temporary base station established for the original tie-in at the beginning of the cruise.

After completion of the total survey programme, the ship returned to Manchester Dry Docks Ltd., where a temporary base station was established to which the shipborne gravimeter was tied-in. The quayside gravity station was then tied-in to the primary base station located at Daresbury (National Gravity Reference Net, 1973: F.B.M. no. 2900, grid reference SJ 5774 8235) using a portable La Coste and Romberg gravity meter (model G, instrument no. 453).

The various gravity tie-ins are summaried in Figure 2.8.

The Icelandic gravity values given by Palmason et al, (1973) were based on the old gravity reference system referred to a unique value of gravity at Potsdam, whereas the Daresbury gravity value was part of the NGRN'73 gravity network which was tied-in to IGSN'71 (Coron, 1972). The following extract was taken from Coron (1972), and translated thus:

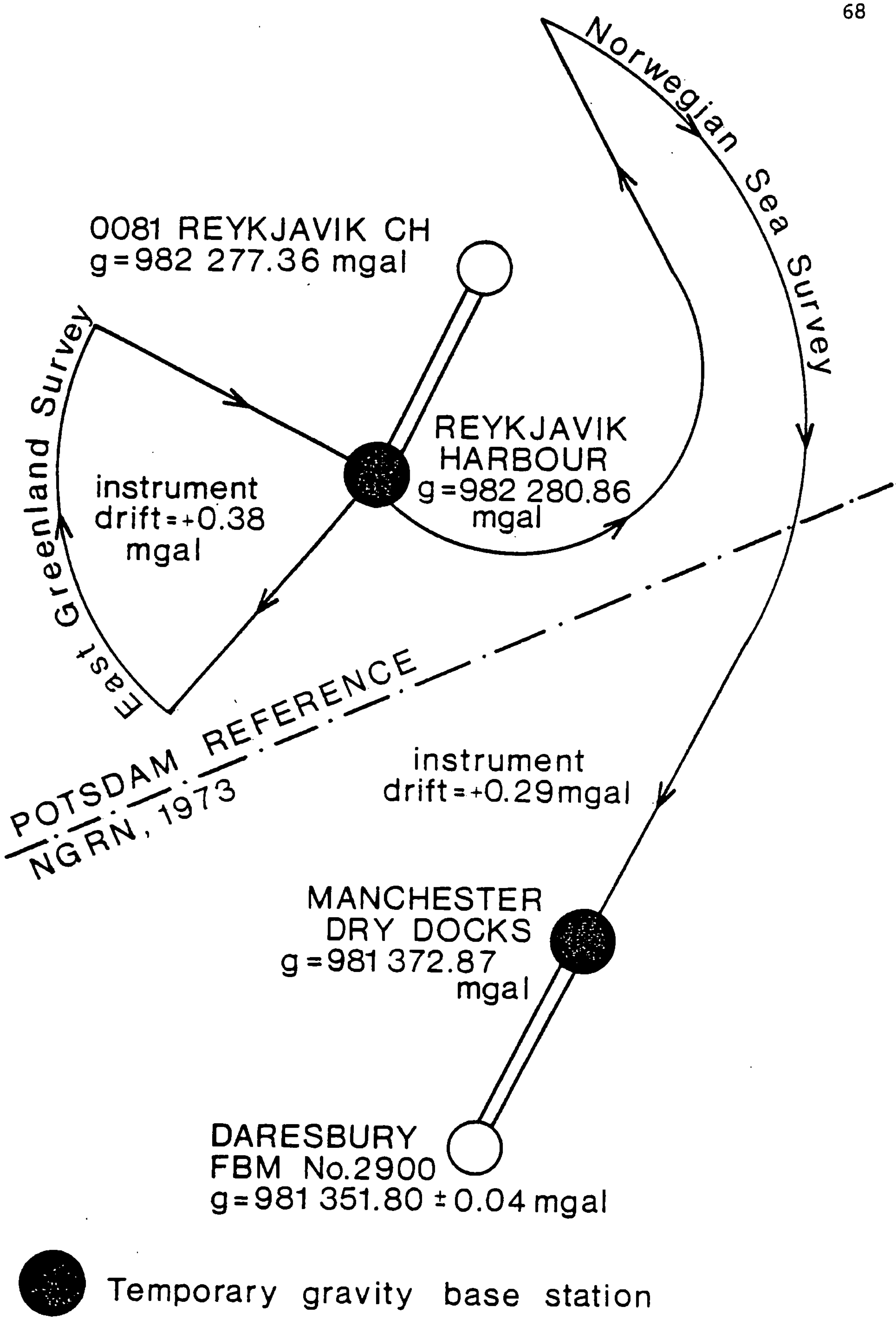

Figure 2.8 Diagram to summarise the details of gravity tie-ins made in Reykjavik and Manchester for the Durham marine geophysical survey, 1977.

"In the IGSN'71, the absolute value of g at Potsdam became 981260 mgal approximately, and all pre-existing gravity values based on the Potsdam reference value (981274 mgal) must be reduced by a factor of the order of 14 mgal in order to be converted into the Réseau Gravimétrique International Unifié 1971."

Thus, a factor of 14 mgal was subtracted from the apparent drift at Manchester Dry Docks Ltd. to obtain an instrument drift of + 0.29 mgal.

Since the observed values of instrument drift were small and any periodicity associated with the instrument characteristics was unknown, no drift correction was applied to the survey gravity data.

2.5 Magnetic Storms

A preliminary inspection of the magnetic anomaly along each profile of the East Greenland marine survey did not indicate the obvious presence of any strong magnetic disturbance due to magnetic storms.

Nevertheless, observatory magnetogram records were obtained from Eskdalemuir (Scotland), Leirvogur (Iceland) and Narssuarssuaq (South West Greenland) in order to confirm that the survey had been carried out during a magnetically quiet period. However, after detailed inspection of the observatory records, a radically different picture began to emerge.

The geographic latitude and longitude of each observatory were converted to geomagnetic latitude and longitude relative to the north magnetic pole using transformations proposed by Mead (1970). Mead gave the latitude, θ_o and longitude, λ_o of the north magnetic pole at Epoch 1965.0 as:

$$\theta_o = 78.565^\circ N \qquad \lambda_o = 69.761^\circ W$$

Assuming a westward precessional rotation of the geomagnetic dipole at a rate of 0.05° of longitude per year and a rotation of the dipole toward the geographic axis at a rate of 0.02° of latitude per year (Stacey, 1969), new geographic coordinates of the north magnetic pole for Epoch 1977.0 were calculated to be:

$$\theta_o = 78.805^\circ N \qquad \lambda_o = 70.361^\circ W$$

The geographic and geomagnetic dipole coordinates of the magnetic observatories are tabulated in Table 2.3.

Table 2.3 Geographic and geomagnetic coordinates of magnetic observatories at Epoch 1977.0

OBSERVATORY	GEOGRAPHIC COORDINATES degrees	GEOMAGNETIC COORDINATES degrees
Eskdalemuir	55.3 N 3.2 W	58.2 θ 83.8 λ
Lerwick	60.1 N 1.2 W	62.3 θ 90.0 λ
Leirvogur	64.2 N 21.7 W	69.9 θ 71.8 λ
Narssuarssuaq	61.2 N 45.4 W	70.8 θ 38.2 λ

Kraichman (1977) commented that the auroral zone is usually defined as the region between 65° and 75° geomagnetic latitude. Knecht (1972) was more specific and pointed out that at any given time, the auroral arcs are generally confined to a narrow, nearly oval belt encircling the geomagnetic pole. This belt is called the auroral oval and its extent is shown in Figure 2.9. Due to the earth's rotation, the auroral oval sweeps out a large geographic area. Additional to this diurnal variation, the extent of the oval is a function of magnetic activity, contracting towards the magnetic pole in quiet periods and expanding towards the geomagnetic equator during increased activity. The so-called auroral zone is a circular belt centred on 67° geomagnetic latitude (Knecht, 1972).

As shown in Figure 2.9, the auroral oval sweeps along the whole length of the East Greenland coastline and is therefore subject to the intense, impulsive and concentrated current flow of the auroral electrojet which represents a sharp focusing of current along the auroral oval. The magnetic disturbance is attributed to currents in the ionosphere and magnetosphere.

This indicates that the magnetogram records from the Lerwick and Eskdalemuir observatories, which lie outside the auroral zone as shown by their geomagnetic latitudes (Table 2.3) and the extent of the auroral oval (Figure 2.9), are quite unsuitable for predicting magnetic storm behaviour in the region of East Greenland. In the light of this, the

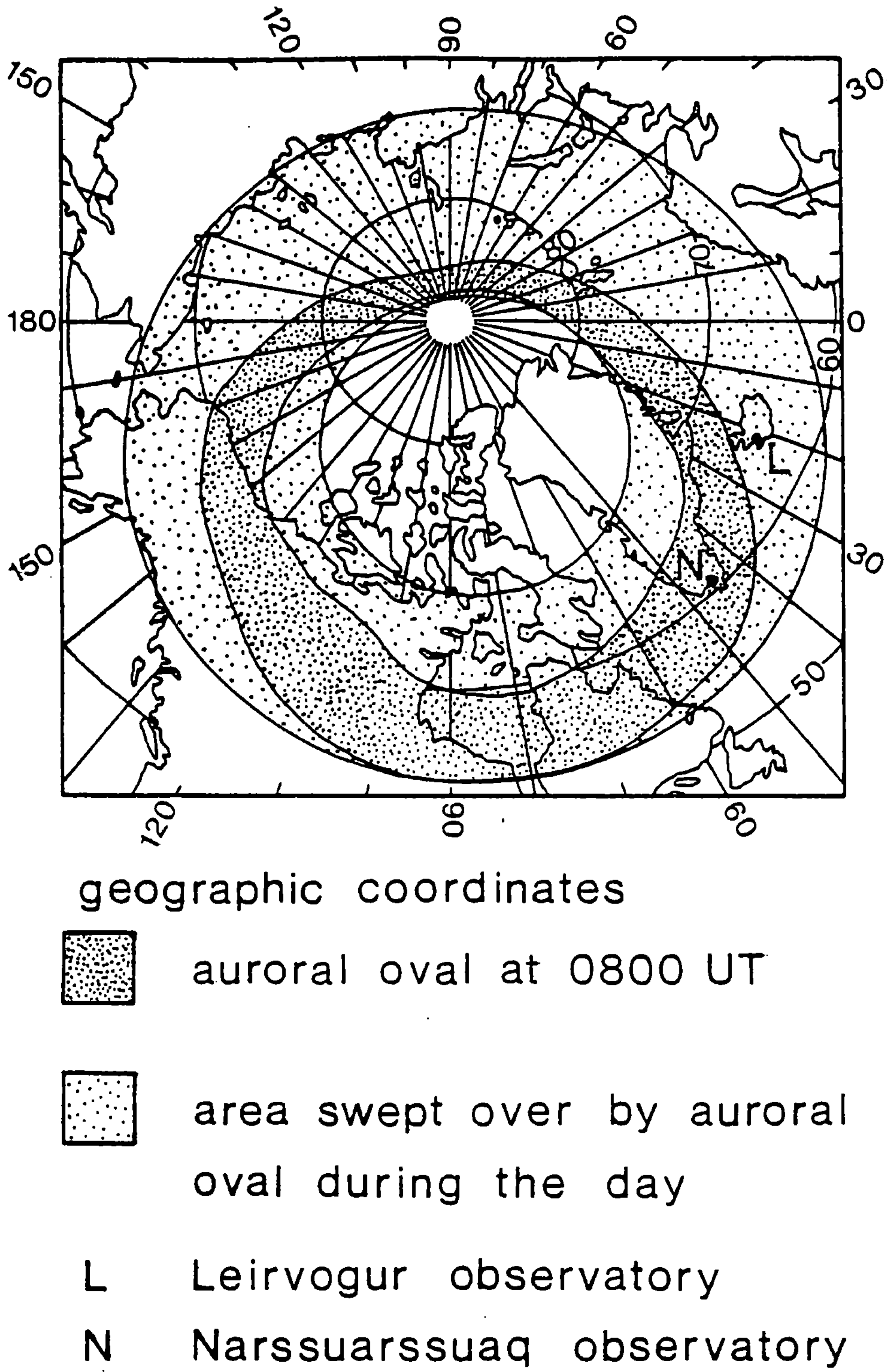

Figure 2.9 The location during moderate activity of the auroral oval and the extent of the area affected by its precession due to the earth's rotation. Redrawn from Knecht (1972).

magnetic data used by Featherstone (1976) and Featherstone, Bott and Peacock (1977) must be re-examined since these authors did not refer to observatory magnetograms recorded within the auroral zone.

The effect of the auroral magnetic storms was extensive. Storm activity was recorded every day and was usually of several hundred gammas amplitude for the horizontal component (typically the most disturbed component of the geomagnetic field). The auroral magnetic storms occurred predominantly in a time window between about midnight and 0800 hours the following morning, except when the storm continued throughout the day! By comparison, the maximum peak to peak magnetic storm value for the horizontal component recorded at Eskdalemuir over the period of the survey was 128 gamma.

The detailed effect of magnetic storms on individual magnetic "anomalies" is considered in relation to their interpretation (see Chapter 5). The accurate quantitative correction for magnetic storm effects was not attempted. Kraichman (1977) developed formulae for the prediction of magnetic and electric field fluctuations in the open ocean from magnetic field data recorded at land stations away from any coastlines. Both Leirvogur and Narssuarssuaq observatories are situated adjacent to coastlines and the whole survey was carried out along the coastline of East Greenland. Due to the discontinuity of conductivity at a coastline, perturbations occur in both electric and magnetic fields. The magnitude and spatial extent of the perturbation is a function of the conductivity contrast between land and sea, the pulsation period, the bottom configuration and the relative orientation of the coastline and ionospheric current (Kraichman, 1977). Due to these uncertainties, no corrections for magnetic storm fluctuations were applied to the magnetic anomalies.

CHAPTER 3

MAGNETIC AND GRAVITY INTERPRETATION METHODS

3.1 Introduction

The advent of the Fast Fourier Transform (FFT) algorithm of Cooley and Tukey (1965) has provided a valuable tool for the interpretation of gravity and magnetic anomalies in the spatial frequency domain. Anomalies of a complex nature in the spatial domain quite often reduce to a more simple, manageable form in the spatial frequency domain (Bhimasankaram, Nagendra and Rao, 1977) and the computational efficiency of the FFT algorithm facilitates transformation between the spatial and spatial frequency domains.

Before entering a detailed presentation of the interpretative techniques adopted, it is important to understand the nature of the geophysical data and the general problems involved in making a Fourier transformation from one domain to another.

The FFT algorithm and the general theory of frequency analysis assume that the function of interest has been sampled at equal intervals in time or space. The marine geophysical data were recorded digitally, processed and finally presented in digital form sampled at uniform intervals in time. Variations in ship's speed and heading reduced the data to an unevenly spaced digital sequence in the spatial domain distributed about a line of nominally constant heading.

In planning the survey, each profile was drawn along a line of constant heading perpendicular to the anticipated structural trend of the continental margin (a line of constant heading is called a rhumbline or loxodrome). However, due to the limitations of marine navigation, the actual geophysical data related to points which no longer accurately defined a line of constant azimuth. Since the ship sailed along profiles which were approximately lines of constant heading, the loxodrome was the natural choice for a baseline on to which recorded data were to be projected. The best fitting loxodrome through the navigational fixes was found by the method of least squares.

A useful property of the Mercator map projection is that a line of constant azimuth plots as a straight line. Recognising this property, the navigational fixes of each profile were first projected on to the major sphere enclosing the ellipsoid of revolution of the Earth by converting geodetic latitude to reduced latitude (Ewing and Mitchell, 1970; and Figure 3.1). This allowed the simple Mercator projection formulae for the case of a spherical Earth to be used to transform reduced latitude and longitude coordinate pairs on to the x-y plane. The projection formulae (Richardus and Adler, 1972) used were:

$$y = a \ln \{\tan (\frac{\pi}{4} + \frac{\phi}{2})\} \qquad 3.1$$

$$x = a\lambda$$

where ϕ = reduced latitude (see Figure 3.1)

λ = longitude

a = the equatorial radius of the earth.

The best fitting loxodrome was then fitted to the navigation data in the x-y plane by the method of least squares. Each navigation point was projected along a normal to the loxodrome and new coordinates calculated. The new x and y coordinates were transformed back into reduced latitude and longitude, and the reduced latitude was further converted into the equivalent geodetic latitude. The arc of a great circle was then fitted between each pair of points using spherical trigonometry. The radius of curvature at a given latitude was calculated using Euler's Theorem (Ewing and Mitchell, 1970) and the incremental distance between each pair of navigation points was found as the product of the radius of curvature in km and the angle of arc in radians. Therefore, the sampling interval calculated was the shortest distance along the Earth's surface between adjacent data points and the cumulative distance along ship's track was the sum of all such increments.

A listing of the computer program, MERCAT and running instructions appear in Appendix B.

Stansell (1978) quoted a root mean square radial error of 27 to 37 metres in satellite navigation positioning for a <u>stationary</u> receiver and recorded a maximum error of 77 metres (rms radial error = 32 m) for 69 fixes taken at a fixed location. The proposed method of calculating distance along ship's track was certainly within the limitations of precision of satellite navigation for a moving observer at sea.

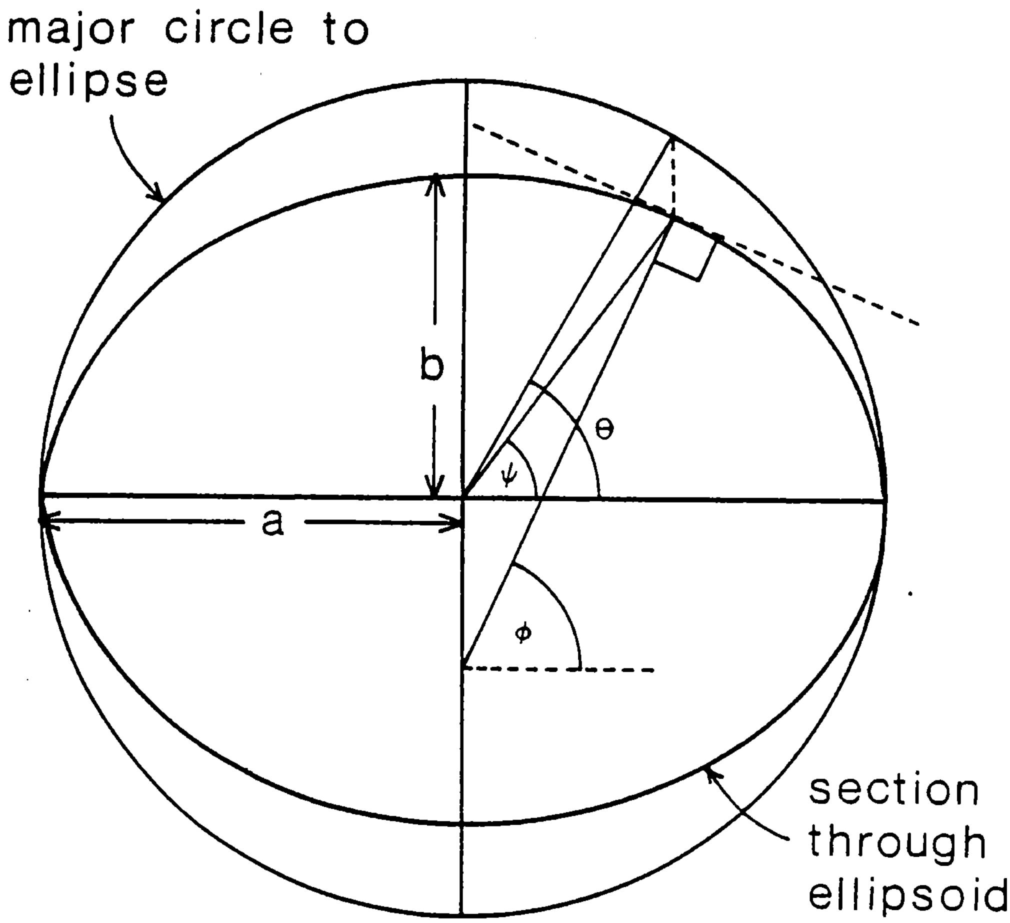

ϕ = geodetic latitude

ψ = geocentric latitude

θ = reduced latitude

$$f = \frac{a-b}{a} \qquad e^2 = 2f - f^2$$

$$\tan\theta = (1-e^2)^{\frac{1}{2}}\tan\phi$$

(after Ewing & Mitchell, 1970)

Figure 3.1 The relationship between geodetic, geocentric and reduced latitudes.

Before application of any frequency analysis methods, interpolation of the unevenly spaced magnetic data was carried out using the method of cubic spline interpolation (available as a standard subroutine on the NUMAC computer system). The final constant sample rate was chosen to be the mean spatial sampling interval of the data projected on to the loxodrome fitted by the method of least squares.

The spatial sampling interval, Δx determined the maximum spatial frequency or Nyquist frequency, f_N by the uniform sampling theorem (Hsu, 1967), to be:

$$f_N = \frac{1}{2\Delta x} \tag{3.2}$$

Suitable analogue and digital filters were applied during data acquisition and processing to prevent aliasing (see Section 2.3).

Difficulties arise in trying to estimate the frequency content of a "process" from a "sample" of finite length. This leads to the concept of a <u>data window</u>. If the "process" is sampled by a rectangular window, spurious high frequency components may be generated by the sharp cut-off at each end of the sample. Various data windows have been designed in order to taper data in the spatial domain prior to Fourier transformation. In power spectral analysis, a further problem concerns the statistical variance of the estimated power spectrum. The variance of the spectral estimate is reduced by its convolution with a suitable <u>spectral window</u> in the spatial frequency domain (Papoulis, 1977). The data window is applied to the sample in the spatial domain as a taper to eliminate spurious high-frequency components. The spectral window is applied as a convolution process in the spatial frequency domain in order to smooth the spectral estimate and thereby enhance its statistical reliability.

However, it is important to note that if a "sample" tends to taper itself, a more reliable spectral estimate is likely to be obtained if a rectangular data window is used. Further tapering will only distort the spectrum. This often applies to the transformation of horizontal or vertical derivatives and to isolated magnetic anomalies.

The magnetic and gravity interpretational techniques adopted in this work follow in the remaining sections of this chapter.

3.2 The interpretation of magnetic anomalies using spectral estimation techniques

The interpretation of isolated magnetic anomalies has conventionally taken the form of either the direct determination of characteristic parameters from the observed anomaly or the assumption that the body causing the anomaly is of a simple geometrical shape for which the analytical expression for its anomalous effect is known. The determination of characteristic parameters for magnetic anomalies is well established (Vacquier et al, 1951; Bruckshaw and Kunaratnam, 1963; Am, 1970) and estimates of depth, width and magnetisation can be found by plotting pairs of parameters on master curves drawn for ideal-shaped bodies, in particular, the arbitrarily magnetised dyke.

However, parameter determination is often subjective and is particularly sensitive to the accurate definition of the steeply dipping flanks of a magnetic anomaly. The removal of an appropriate regional anomaly may also be problematical (for example, in the method of Bruckshaw and Kunaratnam, 1963). In addition, an anomaly which is not completely isolated from other anomalous sources will be distorted by the superimposed effects of adjacent anomalies.

The power spectrum of magnetic anomalies, defined as the square of the amplitude of the frequency spectrum, has been used for the interpretation of aeromagnetic data (Horton et al, 1964; Naidu, 1969, 1970; Spector and Grant, 1970). The practical implementation of spectral estimation has special problems of its own. However, spectral analysis represents an attempt to introduce a relatively simple, semi-automatic approach to the interpretation of magnetic anomalies and it may be employed for data sets over which parameter techniques would be difficult to apply. In estimating the power spectrum (using FFT) all available field data are used, not just the field at certain characteristic points (Bhimasankaram et al, 1977) and averaging over a large number of values reduces the effect of small random errors on the interpretation of the results (Sharma and Geldart, 1968).

Spectral analysis has provided a method for the partial separation of effects due to near-surface high-amplitude components from those of deeper origin. Total separation of these effects is not possible because of spectral overlap between anomalies caused by "shallow" and "deep" sources (Bhattacharyya, 1966; Spector and Grant, 1970).

The underlying philosophy behind spectral analysis techniques for depth estimation to anomalous bodies is illustrated in the following section. Details of the practical estimation of power spectra are discussed with special reference to the maximum entropy method (MEM) and finally, an appraisal of the MEM spectral depth estimate technique is made.

3.2.1 Spectral analysis and the depth to buried magnetic sources

Treitel et al (1971) developed an interpretation model based on the assumption that the magnetic effect of the surface of magnetic basement rocks can be simulated by an uncorrelated distribution of magnetic line sources.

The following assumptions were made:

(1) The magnetic effect of a magnetic basement complex overlain by a sequence of sedimentary rocks can be approximated by a single uncorrelated distribution of infinitely long magnetic line sources* at a depth d below the profile of observation. Treitel et al (1971) conceded that magnetic bodies situated above this interface affect the validity of this assumption but appealed to field experience which vindicates their approach in many geological situations:

(2) the source strength is assumed to vary as an arbitrary, but bounded function, $m(x')$ per unit length of the spatial coordinate x' only;

(3) every elemental line source is assumed to be perpendicular to the (x',z) plane and extended to infinity in both normal directions;

(4) the Fourier transform, $M(K)$ of the magnetic source strength $m(x')$ is assumed to exist.

The geometry adopted for the derivation of the power spectrum due to a buried magnetic line source distribution is shown in Figure 3.2. However, the details of the derivation are omitted because it is the result of Treitel et al's work which is important here.

In terms of the total magnetic intensity vector, $\underline{T}(x)$ the power spectrum, $S_T(K)$ of $T(x)$ is given by

* poles

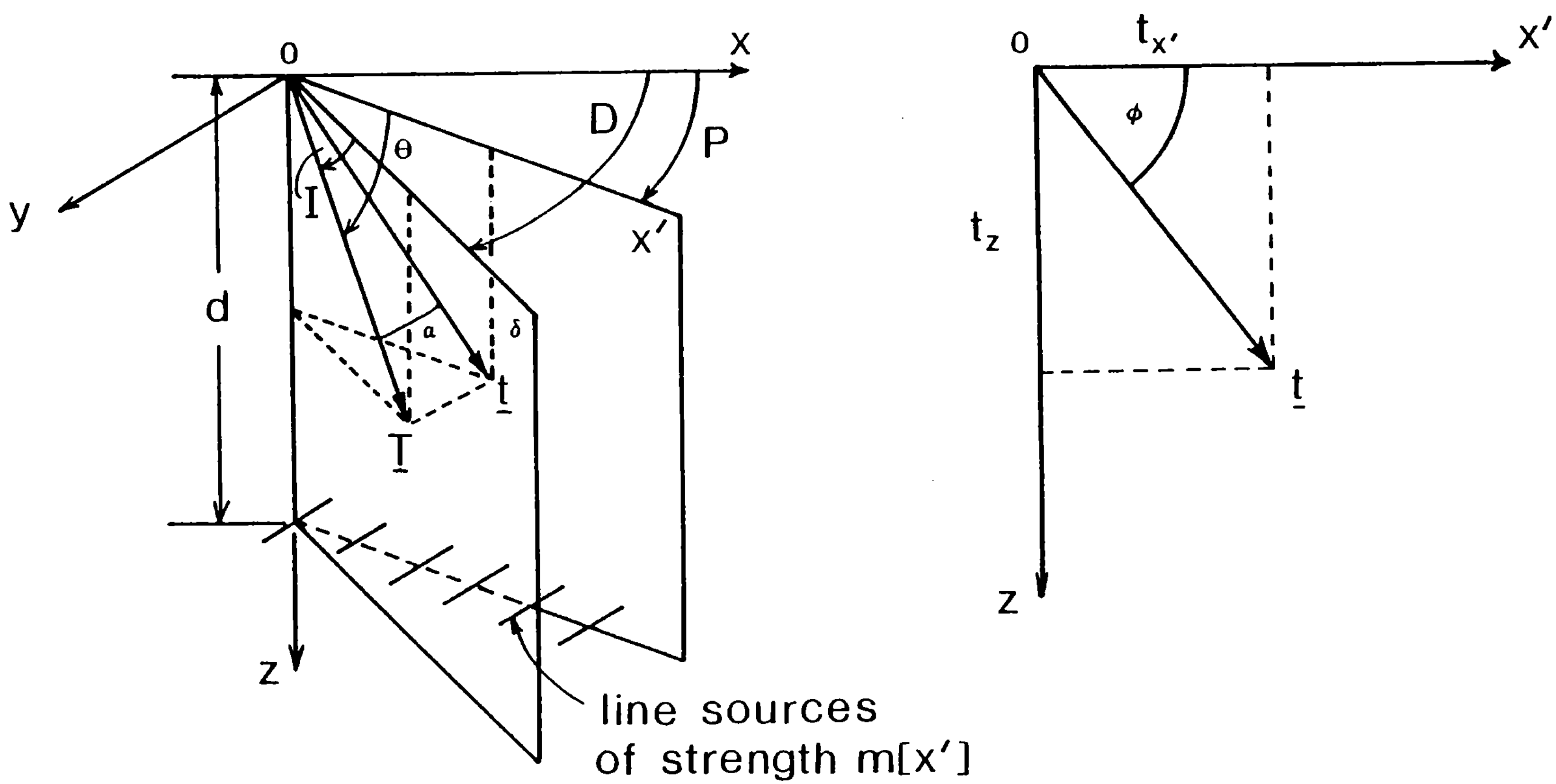

$$\cos a = +\left[\cos^2 I \cos^2(D-P) + \sin^2 I\right]^{1/2}$$

Figure 3.2 The geometry adopted for the derivation of the power spectrum due to a buried magnetic line source distribution (after Treitel et al., 1971).

$$S_T(K) = \left(\frac{2\pi A}{\cos\alpha}\right)^2 \exp\,(-2|K|d) \qquad 3.3$$

where α = the angle between $\underline{T}$ and $\underline{t}$, its projection in the plane of the profile (see Figure 3.2)

d = the depth to the magnetic basement surface

A^2 = the power spectrum of the uncorrelated line source strengths

K = the wavenumber.

The depth d enters the equation in the exponential term only. Treitel et al pointed out that the depth term is independent of the uncorrelated line source strengths, A^2 and the angle α between the vectors $\underline{T}$ and $\underline{t}$. From Equation 3.3, the power spectrum is independent of the inclination and declination of the Earth's magnetic field and the azimuth of the profile too.

Taking the natural logarithm of both sides of Equation 3.3 and normalising to the K = 0 term gives the reduced form

$$\ln S_T(K) = -2|K|d \qquad 3.4$$

This equation represents a straight line of slope, -2d, passing through the origin of a $\ln S_T(K)$ versus K plot. Therefore, the estimation of the depth of the magnetic source material, subject to the initial assumptions, reduces to the problem of measuring the slope of the log-power spectrum.

Green (1972) pointed out that in their derivation of the power spectrum of the total magnetic intensity caused by an uncorrelated distribution of magnetic line sources, Treitel et al (1971) had chosen their expression for the magnetic scalar potential (Grant and West, 1965; page 230) incorrectly. However, Green (1972) emphasised that this error does not alter the depth dependent term.

The power spectra of other simple bodies may be expressed in analytical form to yield additional interpretative models which may be applied in a variety of geological situations.

The case of a two-dimensional magnetised step is shown in Figure 3.3. The total field magnetic anomaly, ΔT due to a finite magnetised step (Nabighian, 1972) may be written in SI units as:

$$\Delta T(x,z) = \frac{\mu_o}{2\pi} kFc \sin \beta \left[(\theta_1 - \theta_2) \cos \phi + \ln\left(\frac{r_1}{r_2}\right) \sin \phi \right] \qquad 3.5$$

where μ_o = the magnetic permeability of free space
k = the susceptibility contrast of the step
F = the Earth's magnetic field
i = the inclination of the Earth's field
A = the angle between magnetic north and the positive x-axis
and $\tan I = \tan i / \cos A$.
The remaining parameters are defined in Figure 3.3.

The horizontal derivative is obtained by differentiating Equation 3.5 with respect to x and, allowing the thickness to approach infinity, this gives:

$$D_x(x,z) = 2kFc \sin \beta \frac{(d-z) \cos \phi + x \sin \phi}{(d-z)^2 + x^2} \qquad 3.6$$

where d = the depth to the upper surface of the infinite step.

This expression for $D_x(x,z)$ is also the magnetic anomaly due to an infinite thin sheet dipping at an angle β with respect to the horizontal and with its highest point at depth d. The Fourier transform of $D_x(x,z)$ at the Earth's surface, for which z = 0, is given by Nabighian (1972) as:

$$F(K) = \pi\alpha \exp(j\phi \,\mathrm{sgn}(K)) \,.\, \exp(-|K|d) \qquad 3.7$$

where $\alpha = 2kFc \sin \beta$
K = the wavenumber.

The power spectrum, S(K) is given by

$$S(K) = F(K) \, F^*(K)$$

where F(K) = the Fourier transform of F(K) and F*(K) represents its complex conjugate,

hence

$$S(K) = (\pi\alpha)^2 \exp(-2|K|d) \qquad 3.8$$

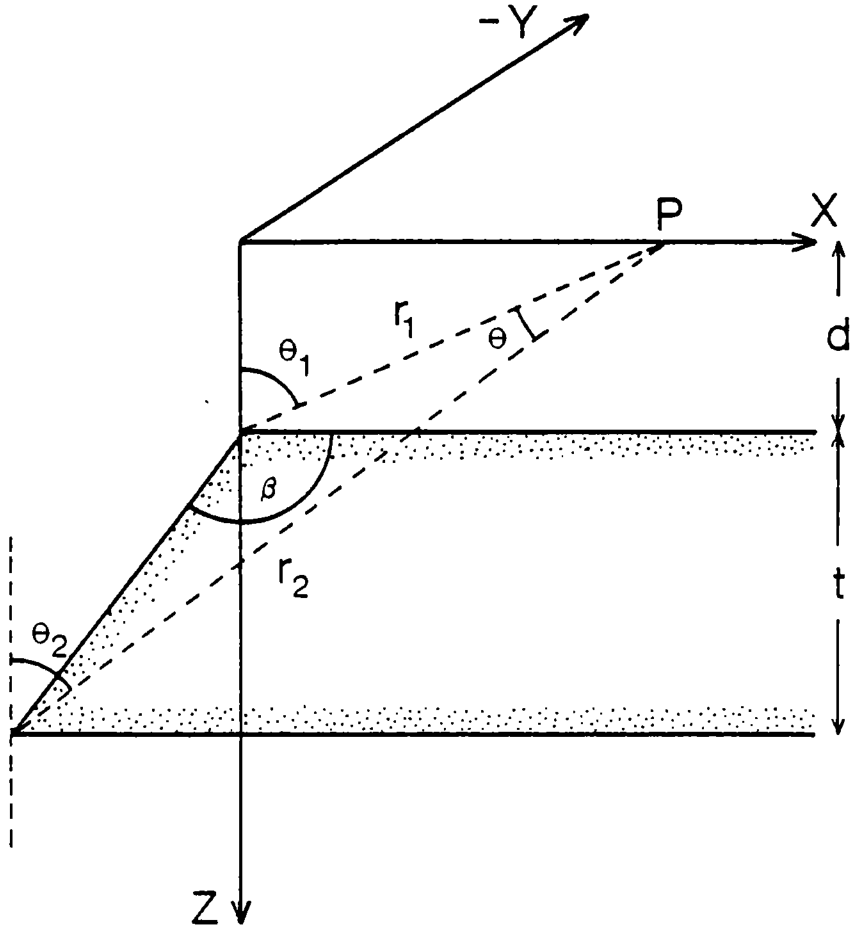

$$c = 1 - \cos^2 i.\sin^2 A$$

$$\phi = 2I - \beta - 90^\circ$$

Figure 3.3 The geometry for a two-dimensional magnetised step and the definition of related parameters (after Nabighian, 1972).

Taking the natural logarithm of both sides of Equation 3.8 and normalising to the K = 0 term, yields the result:

$$\ln S(K) = -2|K|d \tag{3.9}$$

Thus, the depth to the causative body may be estimated from the power spectrum obtained from the horizontal derivative of the anomaly in the case of an infinite magnetised step and directly from the power spectrum of the anomaly itself in the case of an infinite thin sheet. A thin sheet is defined as a body whose thickness is small relative to its depth of burial.

As previously observed, the exponential behaviour of the power spectrum, S(K) in Equation 3.9 is independent of the inclination and declination of the Earth's magnetic field and the profile azimuth. The profile must be oriented perpendicular to the strike of the body.

What about the effects of any resultant magnetisation present in the causative body? Following the format of Nabighian (1972) and the insight of Hood (1964), it is shown in Appendix C that the formula for the total field magnetic anomaly, ΔT due to a uniformly magnetised step, taking into account remanent magnetisation is given by

$$\Delta T = \frac{\mu o}{2\pi} Jbc \sin\beta \left[(\theta_1 - \theta_2) \cos\phi + \ln\left(\frac{r_1}{r_2}\right) \sin\phi \right] \tag{3.10}$$

where $\phi = \lambda + \psi - d - \frac{\pi}{2}$

J = the resultant magnetisation of the finite step.

The symbols are defined in Appendix C (Figures C.1 and C.2).

The form of this equation is identical to that given by Nabighian for the finite step, with induced magnetisation only, in Equation 3.5. Therefore, by Equation 3.8, it is concluded that the resultant magnetisation of the causative body has no effect on the depth dependent term for the power spectrum, S(K).

Gudmundsson (1966) gave the following equation for the Fourier transform of the magnetic anomaly due to a two-dimensional finite dyke:

$$F(K) = Ce^{-Kd_1} \left[\left(1 - e^{jK(d_2-d_1)\cos\beta}\right) . \; e^{-K(d_2-d_1)} \right] \frac{\sin K\Delta x}{K}$$

where d_1, d_2 = the depths to the upper and lower boundaries respectively

Δx = the half-width of the dyke

C = a constant

β = the angle of dip of the parallel-sided dyke.

For the infinite dyke case, $d_2 \to \infty$ and $d_2 >> d_1$, so that that power spectrum reduces to the form:

$$S(K) = C^2 e^{-2Kd_1} \cdot \frac{\sin^2 (K\Delta x)}{K^2}$$

If $K\Delta x \to 0$, that is, $K\Delta x << \frac{\pi}{2}$, then $\sin K\Delta x \simeq K\Delta x$ and so,

$$S(K) = C^2 \Delta x^2 \exp(-2Kd_1) \qquad 3.11$$

Under these circumstances, the interpretation is much simpler if the power spectrum of the actual magnetic anomaly is estimated rather than the spectrum of the gradient of the anomaly. The latter approach (Cassano and Rocca, 1975) leads to the evaluation of $S(K)/K^2$, an unnecessary complication.

Spector and Grant (1970) adopted a statistical approach in estimating the power spectrum caused by a number of independent ensembles of rectangular, vertical-sided parallelepipeds. According to Spector and Grant, the regional magnetic anomaly revealed on an aeromagnetic map is assumed to consist of the superposition of a large number of individual anomalies, many overlapping each other, which are the product of several ensembles of blocks of various dimensions and magnetisations. The power spectrum, reduced to the north magnetic pole, for such a statistical model in its one-dimensional profile form is:

$$\langle E(K) \rangle = 4\pi^2 \overline{M^2} \langle \exp(-2K\bar{d}) \rangle \langle 1 - \exp(-Kt) \rangle \langle S^2(K) \rangle \qquad 3.12$$

where $\langle E(K) \rangle$ = the expectation value of the energy density function

M = a magnetic moment per unit depth

d = the depth to an individual block

t = the thickness of an individual block

$\langle S^2(K) \rangle$ = a factor depending on the mean size of the blocks.

The term $\exp(-2K\bar{d})$, where $\bar{d}$ is the mean depth of the ensemble, is the dominant factor in the expression for the power spectrum. Spector and Grant (1970) extended their hypothesis to cover the presence of two distinct ensembles; the deeper source dominates at low wavenumbers but decays rapidly, and the shallower source dominates the high wavenumber range of the power spectrum. However, complete separation of the spectra of two sources is not possible due to spectral overlap of the anomalies (Bhattacharyya, 1966). Hahn et al (1976) emphasised that the presence of two straight line segments with different gradients in the power spectrum of the profile does not necessarily indicate magnetic sources at two different depths. The gentler sloping segment may represent a form of noise which is not completely random and these authors suggested that such noise may be introduced due to the inevitable smoothing procedure involved in acquisition of digital data. Beyond a certain wavenumber, the power spectrum is dominated by the contribution of measuring errors and in such cases, the spectrum shows a "white tail" (Hahn et al, 1976).

Green (1972) developed the statistical approach of Spector and Grant for the analysis of one-dimensional profiles. He proposed a method for correcting the power spectrum for the effect of the widths of the anomalous bodies. He suggested the use of the second vertical derivative, since the distance between the zeros of the second derivative is a reasonable estimator of the average width of the bodies within each ensemble. If the effect of body width was ignored, depth estimates were found to be overestimated by at least 30% (Green, 1972).

In developing Equation 3.12, Spector and Grant (1970) assumed that the statistical properties of the ensemble remained the same along the profile. This assumption is only valid provided that the profile lies within the same geological province (Gudmundsson, 1967; Naidu, 1970; Shuey et al, 1977). However, Green (1972) pointed out that thickness and depth estimates are independent of the inclination and declination of the geomagnetic field and any remnant magnetisation vectors respectively.

The statistics developed by Spector and Grant (1970) allow bodies within an ensemble to overlap. On the basis of geological observation and experience, the magnetic overprinting observed in aeromagnetic data was claimed to indicate the lack of sharp geological boundaries and the overlapping of magnetic units in many cases (Spector and Grant, 1974).

Hahn et al (1976) proposed a further innovation in spectral analysis of magnetic data whereby each straight line segment of the power spectrum is downward continued until its spectrum becomes "white". Each "white depth" is used in estimating the subsurface relief of the magnetic basement.

3.2.2 Estimation of power spectra

Three methods for the estimation of power spectra were investigated.

Lee (1972) developed a computer program for power spectral estimates for the determination of depth to magnetic basement based on the method of Treitel et al (1971). He adopted the Wiener-Khintchine theorem which states that the autocorrelation function of a time series and its energy spectral density constitute a Fourier transform pair. The simple result that the power spectrum of a real time series is given by the Fourier cosine transform of its autocorrelation function follows (Blackman and Tukey, 1958).

An alternative approach is the use of the Fast Fourier Transform (FFT) algorithm (for example, Claerbout, 1976). From the Fourier transform of the input waveform, the periodogram (Jones, 1965) power spectrum is calculated by multiplying the amplitude spectrum by its complex conjugate.

Finally, the maximum entropy method of spectral analysis was considered.

A major restriction imposed on all practical methods of power spectrum analysis is the finite length of the digitised input data series. The basic problem is to estimate the frequency content of an infinitely long "process" from an analysis of a "sample" of finite duration. The inevitable trade-off between resolution in the spatial and wavenumber domains respectively is expressed by a general statement of the uncertainty principle (Claerbout, 1976):

$$\Delta k \Delta T \gtrsim 2\pi \qquad 3.13$$

where Δk = the spectral bandwidth in the wavenumber domain

ΔT = the length of the input data series in the spatial domain.

For sharp resolution in the wavenumber domain, the input spatial data series must be long. The actual length of data series chosen is ideally governed by the maximum wavelength of interest and the rate at which the data is digitised governs the minimum wavelength which can be unambiguously sampled (the Nyquist sampling theorem, Equation 3.2).

The resolution problem is illustrated in Figure 3.4(a). The separation, s between two adjacent wavenumber components representing wavelengths λ and $\lambda + \Delta\lambda$ respectively is given by:

$$S = \frac{2\pi\Delta\lambda}{\lambda(\lambda+\Delta\lambda)} \qquad 3.14$$

where $\Delta\lambda$ = the separation between adjacent wavelength components.

In order to resolve these two wavelengths in the wavenumber domain, let us adopt the simple resolution criterion that

$$S \gtrsim \Delta k \qquad 3.15$$

By substitution for Δk and s from Equations 3.13 and 3.14, and re-arranging, then the wavelength separation, $\Delta\lambda$ may be expressed by:

$$\Delta\lambda \gtrsim \frac{\lambda^2}{\Delta T-\lambda} \qquad 3.16$$

This function is shown graphically in Figure 3.4(b). It is clear that wavelength resolution is not possible for wavelengths greater than or equal to the length of the input data set, since $\Delta\lambda \to \infty$. This places a severe restriction on the maximum wavelength which can be detected and resolved by a given data set of finite duration.

In the case of the Blackman and Tukey method, the autocorrelation function becomes less reliably defined for increasingly long lags due to the finite length of the data set. Indeed, Blackman and Tukey (1958) recommend maximum lag values no greater than about 5 or 10 per cent of the input data set length. Since the estimated power spectrum is represented at wavenumbers K_J given by:

$$K_J = \frac{\pi J}{M\Delta x} \qquad \text{for } J = 0, 1, 2, \ldots, M$$

where M = the maximum lag value

Δx = the sample spacing of the input data set,

this limitation on the maximum value of M imposes a serious drawback on the method in terms of its ability to resolve narrow-bandwidth frequency

(a)

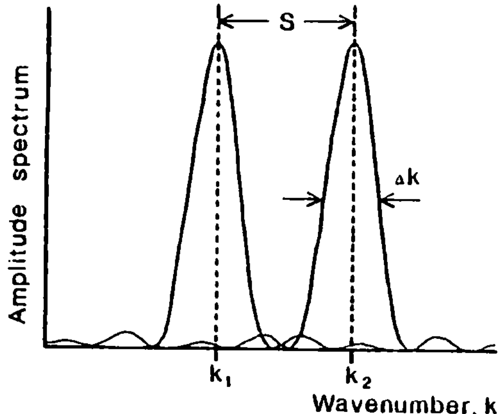

$$S = k_2 - k_1 = 2\pi\left(\frac{1}{\lambda_2} - \frac{1}{\lambda_1}\right)$$

$$= \frac{2\pi}{\lambda_2\lambda_1}\left(\lambda_1 - \lambda_2\right)$$

now $\lambda_1 > \lambda_2$ and $\Delta\lambda = \lambda_1 - \lambda_2$

hence, $S = \dfrac{2\pi\Delta\lambda}{\lambda_2\left(\lambda_2 + \Delta\lambda\right)}$

assume resolution criterion; $S \geq \Delta k$

since $\Delta k \approx 2\pi/\Delta T$, then $S \geq 2\pi/\Delta T$

by substitution for S and Δk, and re-arranging,

$$\boxed{\Delta\lambda \geq \frac{\lambda^2}{\Delta T - \lambda}}$$

(b)

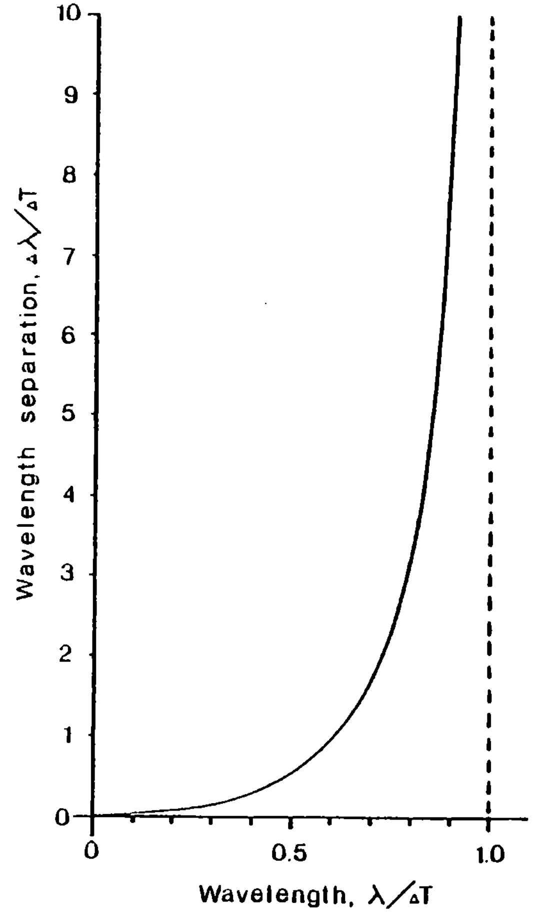

Figure 3.4(a) The problem of wavelength resolution in the wavenumber domain and the derivation of Equation 3.16. (b) A graph of wavelength separation, $\Delta\lambda$ against wavelength, λ with both parameters normalised to the length, ΔT of the input data series comprising the "sample".

components. This limit on the maximum lag value also means that long period variations taking place in the "process" may not be represented at all in the power spectrum estimated from the short duration "sample" (that is, the autocorrelation function formed from the "sample" may not even be defined out to its first zero crossing point).

Two problems common to the Blackman and Tukey approach and the FFT periodogram method are the introduction of spurious high-frequency components due to the sharp cut-off in data sampled by the data window and the reduction of variance in the wavenumber domain.

In order to minimise the effect of sampling the "process" and thereby generating high-frequency components at the discontinuities at each end of the "sample", a data window is chosen which will taper the discrete "sample" values to zero at each extremity of the window. An alternative approach to eliminating discontinuities introduced by sampling is the technique of reflecting the data contained within the data window as an inverted image of itself at both ends of the window. This creates an artificial periodicity not present in the actual "process" and thus introduces a spurious phase component. Black and Scollar (1969) propose a more elegant method of surrounding the data with "itself" by fitting a least squares polynomial surface (for 2-dimensional arrays) to the data and extrapolating it beyond the confines of the data window. These authors consider this technique to be superior to simply surrounding the data with zeros (and thereby padding-out the length of the data window to provide increased resolution in the wavenumber domain) because the repeated data contains noise with similar characteristics to the original data (see also Rao, Murthy and Rao, 1978 for end corrections).

These techniques make assumptions about the nature of the "process" outside the data window. The application of a taper to the "sample" assumes that the data values attributed to the "process" are zero outside the data window and data reflection techniques assume the continuation of data outside the sample to be periodic in an artificial way.

The statistical significance of the estimated power spectrum may be enhanced by the application of a spectral window in the frequency domain, which is equivalent to the multiplication of the original sample with the appropriate lag window. This smoothing process results in reduced resolution of frequency components in the power spectrum. Applying the uncertainty principle to the problem of frequency resolution, Ulrych and

Bishop (1975) point out that for an unsmoothed periodogram a data length of $1/(f_2-f_1)$ is necessary to resolve two peaks at frequencies f_1 and f_2. Furthermore, for non-rectangular data windows producing a smoothed periodogram, the length must be increased to $2/(f_2-f_1)$ to obtain the same separation.

However, the window functions associated with both conventional methods of spectral analysis are independent of the data and the statistical properties of the stationary process under scrutiny. Therefore, the estimated spectrum approaches the convolution of the window function and the true spectrum of the process in the frequency domain. The selection of appropriate window functions is not trivial and since the window does not depend on the properties of the true spectrum, erroneous results may occur. For example, negative values in the estimated power spectrum and peaks in the estimated spectrum which do not represent the true spectrum but are an artifact of leakage through a sidelobe of the window function.

The difficulties of tapering the "sample" with an appropriate data window, of statistical variance and resolution in the estimated power spectrum are most acute for data sets which are short relative to the wavelengths present in the process. It has already been established by Equation 3.16 that wavelengths greater than the length of the data set cannot be resolved. In such cases, the Blackman and Tukey method and the FFT algorithm are completely unsuitable for the reliable estimation of power spectra.

For a statistical analysis of aeromagnetic data, Horton, Hempkins and Hoffman (1964) emphasised that not only must the number of samples, N be large but also the length of the profile, $N\Delta x$ must be large relative to the features under study. From empirical studies, Regan and Hinze (1976) recommended that the data set length should be at least six times the maximum depth to the source of the magnetic anomaly. Cianciara and Marcak (1976) stated that profile lengths in excess of ten times the target depth yielded depth estimates of sufficient accuracy. In an attempt to relax these stringent requirements on profile length relative to target depth, the maximum entropy spectral analysis technique was investigated.

The maximum entropy method (MEM) of spectral estimation, a nonlinear technique proposed by Burg (1967), is not subject to the problems of choosing a suitable data window because it makes no explicit assumptions about the nature of the "process" outside the data "sample". Lacoss (1971)

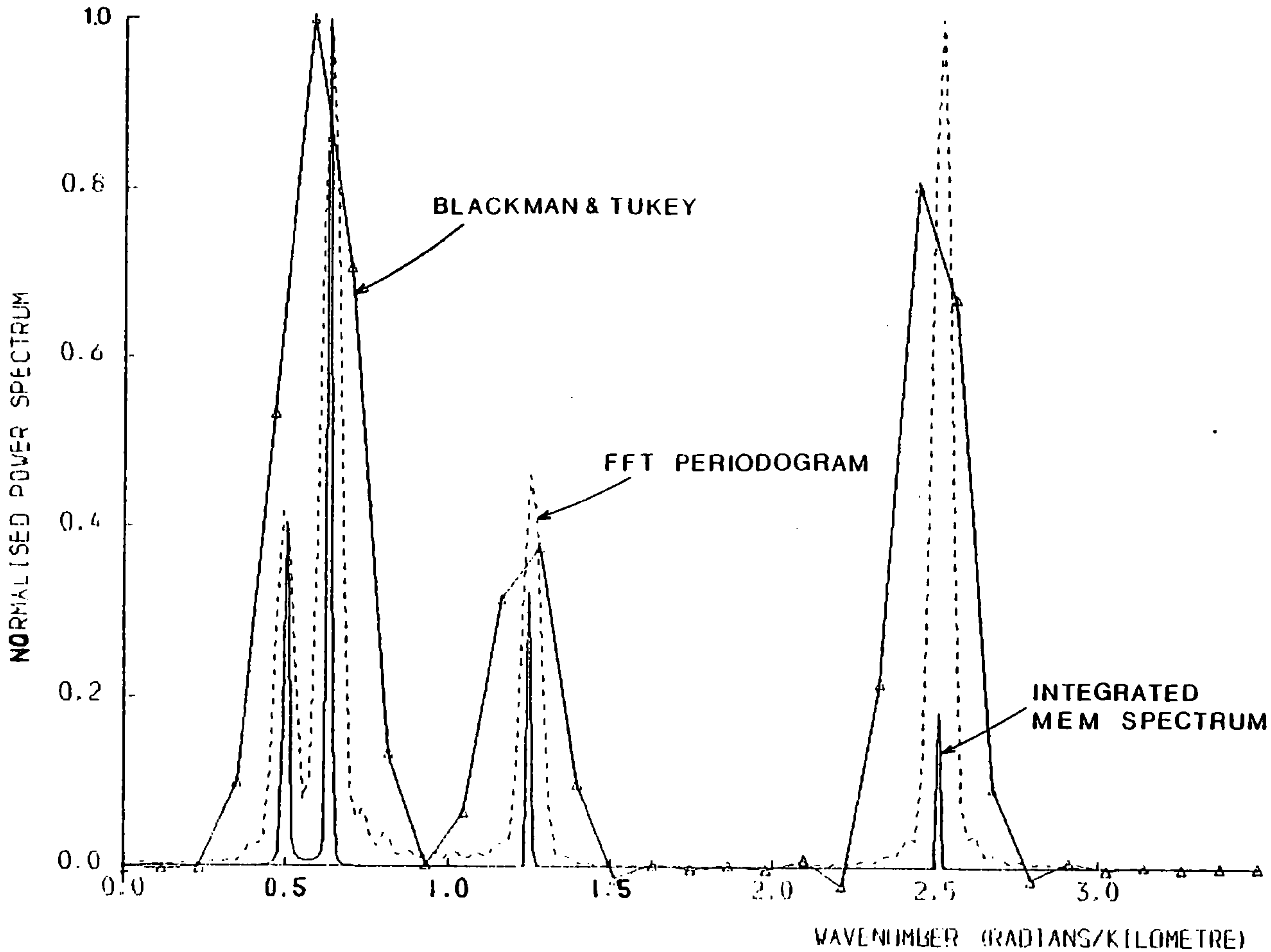

Figure 3.5 A comparison of the power spectra of a known signal computed by the Blackman and Tukey method, the FFT periodogram approach and the MEM technique (the Burg algorithm,) respectively. The signal consisted of 4 sinusoids of respective wavelengths 12.5, 10.0, 5.0 and 2.5km and respective amplitudes 1.0, 1.5, 1.0 and 1.5. The length of the data set was 90.0km. The spectra are normalised to the maximum amplitude of each spectrum.

points out that the method, when estimating power at one frequency, adjusts itself to be least disturbed by power at other frequencies such that the "window" adapts itself to the spectrum of the noise under analysis. Hence, MEM is classified as a data adaptive method. Ulrych and Bishop (1975) and Ulrych and Clayton (1976) emphasise that the MEM spectrum is an optimally smoothed one and the former authors conclude that the resolution is almost twice that of the periodogram spectrum. By the uncertainty principle, Equation 3.13, this implies that a data set of length, ΔT subjected to MEM spectral analysis exhibits a resolution equivalent to a data set of length, $2\Delta T$ subjected to conventional FFT periodogram analysis. For a segment of a stationary series which is short compared to the autocorrelation of the stationary series, the MEM spectral estimate is substantially superior to any truncated Fourier transform method (Claerbout, 1976). Its superiority over conventional spectral estimates is particularly demonstrated in its ability to resolve narrow spectral peaks and it always yields non-negative estimates of the power spectrum.

The Burg algorithm, adapted from Claerbout (1976), was used for spectral depth estimates over basement areas and isolated magnetic anomalies in an attempt to improve resolution and spectral definition for data sets of limited duration. The MEM spectral estimate for a known input signal is compared with conventional estimates made by the Blackman and Tukey method and the FFT periodogram in Figure 3.5. The enhanced resolving power of the MEM spectral estimate is clearly shown.

3.2.3 The maximum entropy method of spectral estimation

The maximum entropy method of spectral estimation is described on several levels by various authors (Lacoss, 1971; Burg, 1972; Ulrych and Bishop, 1975; Kanasewich, 1975; Claerbout, 1976). An outline of the principles involved is given here, together with important innovations on the statistical nature of the spectral estimate obtained and its relationship to the power contained in each frequency.

Communication theory is involved with transmitting information and a statistical definition of information, defining a quantity called <u>self information</u>, I is given by

$$I_i = k \log \frac{1}{p_i} = -k \log p_i \qquad 3.7$$

where k = a constant depending on the base chosen for the logarithm

p_i = the probability of occurrence of event, x_i.

This relationship indicates that an event with low probability of occurrence is thought to contain more significant information than an event with a high probability of occurrence.

The expectation value of the self information is defined as

$$\langle I_i \rangle = \sum_{i=1}^{M} p_i I_i \tag{3.18}$$

Following Shannon (1948), the <u>entropy</u>, H is defined as

$$H = -k \sum_{i=1}^{M} p_i \log p_i$$

Entropy is a measure of the disorder in a system. For a system where all p_i are zero except one, which is unity, the entropy is zero; the system is perfectly determined and no uncertainty exists. Entropy is positive for all other cases.

In his approach, Burg (1967) dispensed with conventional assumptions of spectral analysis which constrain the data to be periodic or zero outside the sample window. Instead, he used the statistical properties of the known sample as a constraint on prediction of the nature of the process beyond the data window. Burg demonstrated a method of obtaining the power spectrum by requiring the spectral estimate to be the most random (that is, to have the maximum entropy) of <u>any</u> power spectrum consistent with the statistical properties of the observed data. Essentially, the method uses available lags in the autocorrelation function without modification and proceeds to predict non-zero estimates of the autocorrelation function beyond those directly available from the data. Since the spectral estimate has maximum entropy, its resolution capability is very high (see Figure 3.5).

Applying Wiener optimum filter theory to the problem of prediction (Kanasewich, 1975), the impulse response, W of the prediction error filter required to operate on the data is given by:

$$AW = C \qquad 3.19$$

where A = the N x N autocorrelation matrix

C = the column vector representing the cross-correlation between the input signal and the desired output (the prediction error power)

W = a column vector containing the coefficients of the prediction error filter.

This embodies Burg's approach. Instead of estimating the autocorrelation function directly from data, he finds a minimum-phase prediction error filter directly from the data. If the input data is represented by s(x) and the spatial coefficients of the filter by w(x), the output, p(x) is given by:

$$s(x) * w(x) = p(x) \qquad 3.20$$

where * represents the operation of convolution. Transforming to the spatial frequency domain and using the spatial convolution theorem gives:

$$P(f) = S(f) \cdot W(f)$$

Rearranging this equation yields:

$$S(f) = \frac{P(f)}{W(f)} \qquad 3.21$$

Hence, the desired input spectrum may be estimated as the inverse of the spectrum of the prediction error filter. Since the output of a prediction error filter is a white spectrum, the effect of the filter operation on the input data is to whiten its spectrum.

The actual form of the maximum entropy power spectral estimate designated by Burg is derived by Chen and Stegen (1974). The derivation begins with the relationship between the entropy and the spectral density, $S_E(f)$ of a stationary random Gaussian process, given by Ulrych and Bishop (1975), as:

$$H = \frac{1}{4f_N} \int_{-f_N}^{f_N} \log S_E(f)\, df \qquad 3.22$$

where H = the entropy

f_N = the Nyquist frequency.

In order to maximise the entropy, H the stationary value is evaluated by using Lagrange's method of undetermined multipliers (Thomas, 1969) subject to the constraints that:

$$a_n = \int_{-f_N}^{f_N} S_E(f) e^{2\pi j f n \Delta t} \, df \qquad 3.23$$

where a_n = the autocorrelation coefficient for lag $n\Delta t$.

Equation 3.23 simply states that the autocorrelation function, a_n is the inverse Fourier transform of the power spectrum, $S_E(f)$. Since the autocorrelation function is only dependent on the lag $n\Delta t$, it is a constant under integration with respect of f, so that:

$$\int_{-f_N}^{f_N} a_n df = 2a_n f_N \qquad 3.24$$

and so, the constraints of Equation 3.23 may be rewritten as

$$\int_{-f_N}^{f_N} \left[S_E(f) e^{2\pi f j n \Delta t} - \frac{a_n}{2f_N} \right] df = 0 \qquad 3.25$$

Following Kanasewich (1975), the maximisation of entropy subject to the constraint of Equation 3.25 is carried out by introducing the undetermined Lagrange multipliers, λ_n, such that:

$$\delta \int_{-f_N}^{f_N} \left(\log S_E(f) - \sum_{n=-N}^{n=N} \lambda_n \left[S_E(f) e^{2\pi j f n \Delta t} - \frac{a_n}{2f_N} \right] \right) df = 0 \qquad 3.26$$

The maximum value of entropy must satisfy the Euler-Lagrange equation for an extremum (Kanasewich, 1975) which states:

$$\frac{\partial L}{\partial y} - \frac{d}{dx} \left(\frac{\partial L}{\partial y'} \right) = 0 \qquad 3.27$$

where L is identified as the integrand of Equation 3.26, Y as S_E and x as f.

Since $\frac{\partial L}{\partial y'} = 0$, it remains to determine $\frac{\partial L}{\partial S_E}$, which yields the expression:

$$S_E(f) = \frac{1}{\sum\limits_{n=-N}^{N} \lambda_n e^{2\pi j f n \Delta t}} \qquad 3.28$$

Introducing matrix notation whereby the column vectors Γ and E are defined by:

$$\Gamma = \begin{pmatrix} 1 \\ \Gamma_2 \\ \Gamma_3 \\ \vdots \\ \Gamma_{N+1} \end{pmatrix} \quad \text{and} \quad E = \begin{pmatrix} 1 \\ e^{\theta} \\ e^{2\theta} \\ \vdots \\ e^{N\theta} \end{pmatrix}$$

where $\theta = 2\pi j f \Delta t$ and since:

$$\Gamma^T E^* = 1 + \sum_{n=1}^{N} \Gamma_{n+1} e^{-n\theta}$$

and

$$E^T \Gamma^* = 1 + \sum_{n=1}^{N} \Gamma_{n+1} e^{n\theta}$$

then, because the power spectrum is real and positive or zero, Equation 3.28 may be rewritten in the form:

$$S_E(f) = \frac{P_{N+1} \Delta t}{E^T \Gamma^* \Gamma^T E^*} \qquad 3.29$$

or, as the equation derived by Burg, which gives:

$$S_E(f) = \frac{P_{N+1}}{2f_N \left| 1 + \sum\limits_{n=1}^{N} \Gamma_{n+1} e^{-2\pi j f n \Delta t} \right|^2} \qquad 3.30$$

This equation is analagous to Equation 3.21 with Γ_n representing the unknown prediction error filter coefficients giving a mean square error power P_{N+1}.

The detailed computation of the prediction error filter coefficients is expanded elsewhere (Andersen, 1974; Ulrych and Bishop, 1975; Kanasewich, 1975; Claerbout, 1976). It is sufficient to say that Burg recognised that the prediction error filter defined by Equation 3.19 depends on the autocorrelation of the data and not the data itself. This is because the autocorrelation function and spectral density estimate constitute a Fourier transform pair and are both phase independent. This means that the same filter is computed from both a spatial series and from a space-reversed (complex conjugate) spatial series. Burg therefore used a filter for forward and backward prediction and summed the prediction errors for each direction (Claerbout, 1976). In the Burg algorithm, the filter is constrained to be minimum phase by using a Levinson recursion technique to construct a filter of order (n+1) from one of order n (Kanasewich, 1975). If the filter is not minimum phase, the method yields an unsatisfactory spectral estimate (for further details, see Claerbout, 1976).

The maximum entropy method assumes that the input data represent a sample of a stationary random Gaussian process. Subject to this assumption, the input spectral estimate must be the inverse of the spectrum of the filter because the output of the prediction error filter is a constant (that is, a white spectrum).

The critical factor in the use of the Burg algorithm for MEM spectral estimation is the determination of the optimum length for the prediction error filter. An important contribution to this problem was made by Akaike (1969a, 1969b, 1970). Ulrych and Bishop (1975) emphasise the correspondence of MEM spectral analysis and the autoregressive representation of a random process and point out that the autoregressive representation of a stochastic process exhibits the maximum entropy of any representation. Treitel, Gutowski and Robinson (1977) define an autoregressive process, y_t by the relation:

$$y_t = x_t - b_1 y_{t-1} - b_2 y_{t-2} \dots - b_n y_{t-n} \qquad 3.31$$

where t = the discrete time variable

$b_1 \dots b_n$ = coefficients to be determined

x = the system input, in many cases taken to be uncorrelated random noise.

This equation shows that the value of y_t at time t is a linear combination of n previous values of the process y_t plus random noise.

Akaike worked on the estimation of the order of the autoregressive process in the representation of a stationary time series and he established a criterion for the determination of optimum filter length in terms of the final prediction error. The expression for the final prediction error of an M^{th} order process, in the form given by Ulrych and Bishop (1975), is:

$$(FPE)_M = \left[\frac{N + M + 1}{N - M - 1}\right] S_M^{\ 2} \qquad 3.32$$

where N = the number of terms in the input data set

M = the number of coefficients in the prediction error filter

$S_M^{\ 2}$ = the residual sum of squares for the M^{th} order autoregressive fit to the data.

This form of the FPE criterion assumes that the mean value of the input data has been removed prior to estimation of the prediction error filter coefficients. $S_M^{\ 2}$ actually represents the prediction error power and this may be calculated in the recursive scheme adopted by the Burg algorithm. The minimum value of the FPE gives an estimate of the optimum length for the prediction error filter and it represents the best mean square determination between the conflicting requirements of high resolution and low variance error. If the number of terms in the prediction error filter exceeds the Akaike criterion, frequency splittings and spurious peaks may give rise to an illusion of high resolution which is statistically unreliable. Fougere, Zawalick and Radoski (1976) found spontaneous line splitting whereby lines that should have been single split up into two or more components. These authors observed that splitting is a function of initial phase and signal length relative to wavelengths sampled. Ulrych and Bishop (1975) recommended a cut-off of M = N/2 for the maximum length of the prediction operator, especially in the presence of sharp spectral peaks. This recommendation arose from comparisons of the predicted order of a known autoregressive process using the Akaike FPE criterion and its actual order, which showed that a search for the first minimum in the FPE values often yielded more reliable results than the M^{th} order process indicated by the absolute minimum of $(FPE)_M$.

Berryman (1978) proposed a formula to calculate the operator length in MEM spectral analysis based on empirical studies of real seismic data. He proposed an operator length, M given by:

$$M = 2N/\ln 2N \qquad 3.33$$

where N = the number of elements in the input series.

The choice of this operator was not an attempt to estimate the order of any underlying autoregressive process. It was suggested on empirical grounds to obviate such difficulties as the lack of a clear minimum in the FPE of Akaike (1969a) and the observation by Treitel et al (1977) that unreliable spectra result from series which are not purely autoregressive in nature. Berryman pointed out that the operator length given by Equation 3.33 represents, in general, an upper bound on the operator lengths that would be obtained using the FPE criterion.

Chen and Stegen (1974) used Burg's algorithm and observed frequency shifts as a function of initial phase and length of sinusoid for data sets of short duration relative to the period of the sinusoidal component. Toman (1965) investigated the spectral shifts of truncated sinusoids and concluded that if the truncation length is less than or equal to 0.58 times the sinusoidal period, the peak of the spectral component is shifted to occur at dc.

It is important to note that the MEM spectral estimate is actually a spectral density estimate (Lacoss, 1971; Burg, 1972). The peak value of the MEM spectral estimate is proportional to the square of the power, whereas the area under the spectral line is proportional to the total power. Hence, to obtain a power spectrum for which the peak values are proportional to the power, the integrated MEM power spectrum must be adopted. Ulrych and Bishop (1975) point out that the variance of the integrated power spectrum is much smaller than the variance of the power spectrum density estimate. Johnsen and Andersen (1978) propose a new method of power estimation in MEM spectral analysis which avoids the problems associated with numerical integration of the area under each peak, especially difficult when the peaks are not well resolved. In this work, the power spectral density estimate was used for estimation of depth to magnetic sources.

3.2.4 Determination of depth to magnetic sources using the MEM spectral density estimate

The maximum entropy method of spectral density estimation is based on the relationship between the entropy and the spectral density of a stationary random Gaussian process (Equation 3.22). Furthermore, the equivalence of MEM spectral analysis to fitting an autoregressive model to the process under examination is emphasised by Ulrych and Bishop (1975) and Ulrych and Clayton (1976). In applying MEM spectral analysis to digital magnetic anomaly data, it is important to realise the nature of the underlying assumptions implicit in the technique.

Adopting a statistical approach, the magnetic anomaly is assumed to be a realisation of a stochastic (or random) process (Gudmundsson, 1967; Cianciara and Marcak, 1976; Hahn et al, 1976 ; Shuey et al, 1977). The further assumption of stationarity has been made by Gudmundsson (1967) and Shuey et al, (1977), although both authors pointed out that the assumption is only reasonable for profiles restricted to the same geological province. Statistical properties of the magnetic anomaly have been observed to differ from one geological province to another (Naidu, 1970). Cianciara and Marcak (1976) did not assume the process to be stationary. Instead, they evaluated the anticipated value of a nonstationary process by estimating the power spectra, $S_r(K)$ from several segments of the same profile and calculated the estimator of the anticipated spectrum, $S(K)$ in the following manner:

$$S(K) = \frac{1}{R} \sum_{r=1}^{R} S_r(K) \qquad 3.34$$

where K = the spatial wavenumber.

In estimating the power spectrum of a magnetic anomaly profile, it is assumed that the aperiodic function represented by the finite length anomaly may be synthesised by an infinite aggregate of sinusoids of all possible frequencies of differing amplitude and phase (Spector and Bhattacharyya, 1966). In practice, the frequency content of the sample is band-limited, the low frequency limit dictated by the length of the sample and the upper limit by the Nyquist frequency. Therefore, a real magnetic anomaly is assumed to represent a band-limited harmonic process with additive noise.

Ulrych and Clayton (1976) discuss the important aspect of model identification with particular reference to the representation of harmonic processes with noise in terms of autoregressive moving-average (ARMA) models. These authors develop their discussion in relation to the Wold decomposition theorem which states that any stationary stochastic process, y_t allows the decomposition:

$$y_t = u_t + v_t \qquad 3.35$$

where u_t and v_t are stationary, mutually uncorrelated, and have the following properties:

(1) v_t is deterministic

(2) u_t is non-deterministic with an absolutely continuous spectral distribution function and has the one-sided moving average (MA) representation:

$$u_t = \sum_{k=0}^{\infty} \psi_k e_{t-k} \qquad 3.36$$

where $\psi_o = 1$ and the variable, e_t has the properties:

$$E\{e_t\} = 0 , \qquad E\{e_t^2\} = \sigma_e^2$$

and

$$E\{e_t e_s\} = 0 \quad \text{for} \quad s \neq t .$$

The two models of interest may be represented by:

(a) the autoregressive (AR) model:

$$x_t = \sum_{k=1}^{P} b_k x_{t-k} + a_t \qquad 3.37$$

(b) the autoregressive moving-average (ARMA) model

$$y_t = \sum_{k=1}^{P} b_k y_{t-k} + n_t - \sum_{k=1}^{P} b_k n_{t-k} \qquad 3.38$$

where $y_t = x_t + n_t$
x_t = the harmonic process
n_t = the additive noise.

For the ARMA process of Equation 3.38, there are AR terms and MA terms. Ulrych and Clayton (1976) emphasise that the MEM spectrum for harmonic processes in additive noise is a smoothed version of the exact ARMA spectrum calculated by a method proposed by Pisarenko (1973). However, Ulrych and Clayton observed that the Pisarenko approach was particularly sensitive to the estimate of the autocovariance matrix and the frequencies were determined less accurately than with the MEM estimate when applied to short realisations of harmonic processes.

Treitel, Gutowski and Robinson (1977) stress the importance of the "correct" model identification to represent the underlying process subject to analysis and illustrate the distortion of the power spectrum which may result by incorrect choice of spectral analysis technique. Their results confirm Ulrych and Clayton's observation that the MEM estimate represents a smoothed version of the exact ARMA spectrum for a precisely generated ARMA process.

Although the magnetic data collected during the cruise were filtered and smoothed, the final magnetic anomaly is still subject to small random errors. Miller (1977) discusses the cause and likely magnitude of such random errors in detail.

Recent investigations carried out by Swingler (1979) indicate that the Burg method of MEM spectral estimation is not strictly applicable to all deterministic signals (including sinusoids) because of the bidirectional nature of the prediction operator. Swingler also shows that observed frequency shifts during processing of sinusoids with the Burg algorithm are caused by the implicit assumption that the autocovariance matrices are Toeplitz, in order to permit the adoption of the Levinson recursion scheme.

However, Swingler addressed the problem of resolving narrow spectral peaks from a harmonic signal containing multiple sinusoids. In estimating the power spectrum of magnetic anomalies, resolving narrow spectral peaks is not the problem. Instead, it is necessary to define the spectrum with sufficient accuracy, especially at low wavenumbers, since the power contribution from long wavelengths is generally substantially greater than the power at short wavelengths. Since Ulrych and Bishop (1975) pointed out that the resolution of the MEM spectral estimate was approximately twice that obtained from the periodogram spectrum, the equivalent length of the data set is almost twice its actual length (by the uncertainty principle, Equation 3.12). Therefore, the longest wavelength resolved by the data set should be almost doubled as a result of the predictive nature of the MEM technique.

Bearing these limitations in mind, the Burg algorithm for MEM spectral analysis was used to estimate the power spectrum for short segments of magnetic anomaly data. The applicability of the technique to magnetic profile data was tested on an empirical basis by assessing the accuracy of depth determinations made by analysis of magnetic anomalies generated from model bodies of known geometry.

A computer program entitled SPECTRAL was written in order to implement the MEM spectral estimation procedure using the Burg algorithm (Claerbout, 1976) on total field magnetic anomaly data. A listing of the computer program and operational instructions appear in Appendix B.

The computer program incorporated the facility for cubic spline interpolation of unevenly spaced input data. Prior to spectral analysis, the mean and any linear trend were removed from the data segment in order to comply with the assumption of a stationary random Gaussian process and to avoid distortion of the calculated spectrum. In estimating the input spectrum, the Fourier transform of the prediction error filter was calculated using the FFT algorithm. The power of the spectrum calculated by FFT is distributed over both negative and positive wavenumbers. For one dimensional profiles, this representation is meaningless since the power is considered to be restricted to positive wavenumbers (Horton et al, 1964; Cianciara and Marcak, 1976). Therefore, the values of power at all positive wavenumbers, except for the dc component, were doubled.

The following options for selecting appropriate prediction operator lengths were available in the program:

(1) the Akaike final prediction error criterion

(2) the empirical criterion proposed by Berryman

(3) calculation of all spectra for operator lengths between the values given by the Akaike and Berryman criteria respectively and finally, calculation of the average spectrum

(4) the selection of an arbitrary value for the operator length.

Option (3) was incorporated because Kane (1977) drew attention to a criterion mentioned by Currie (1973) whereby similar lines appearing in spectra for more than one operator length may be considered real and not an artifact of the MEM spectral estimate technique. The average spectrum was finally calculated to produce a more stable spectral estimate in which spectral peaks common to several individual spectra were reinforced and isolated peaks occurring on few individual spectra were relatively suppressed.

Kane (1977) suggested that in order to resolve long wavelength components, the length of the necessary prediction operator should be much longer than the arbitrary half data length cut-off proposed by Ulrych and Bishop (1975). In order to test this idea for magnetic profile data, option (4) was included to allow the input of a prediction operator of arbitrary length.

A further innovation, inspired by Cianciara and Marcak (1976), was made an integral part of the computer program. Any input profile was sub-divided into overlapping segments of chosen length. The MEM spectral density was calculated, using the appropriate operator length criterion, for each segment and finally, the average spectrum was estimated for the whole profile. This procedure is analagous to Equation 3.34 in which the expected value of a nonstationary process is evaluated from a number of different realisations of that process.

Running the computer program was designed as a two-pass, semi-automatic procedure:

1st pass: the MEM spectral density estimate is calculated using the selected operator length criterion and a graph of the natural logarithm of the normalised power spectrum versus wavenumber is plotted.

2nd pass: having chosen wavenumber limits between which straight line portions of the spectrum can be recognised, the program is re-run and a straight line is fitted through the data of each chosen segment of the spectrum by least squares regression. Depth estimates, with standard errors, are output for each straight line segment and for the average spectrum of each segment too.

This two-pass procedure is illustrated in Appendix B.

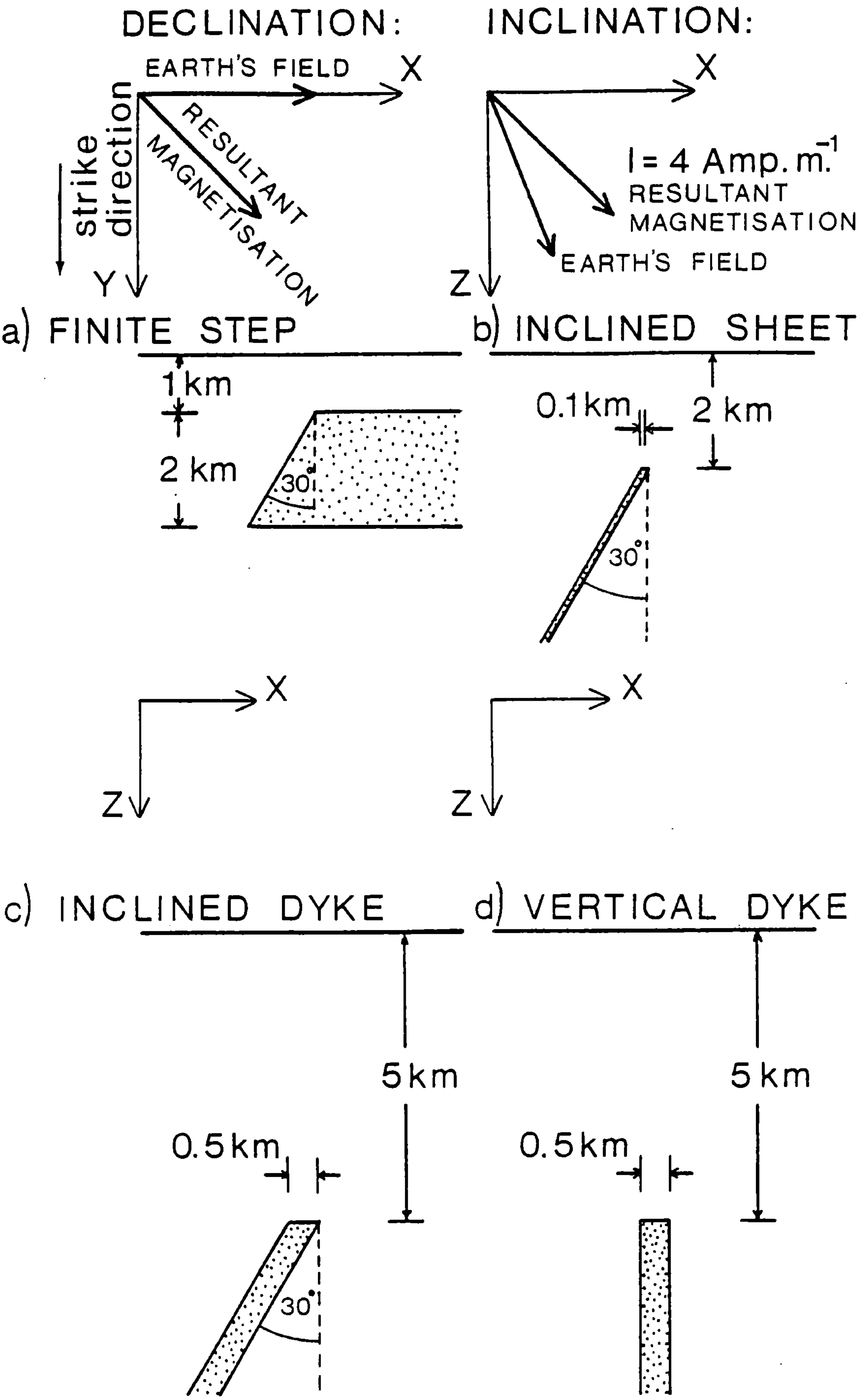

Figure 3.6 Model magnetic structures used to generate total field magnetic anomaly profiles for MEM spectral analysis and subsequent depth determination.

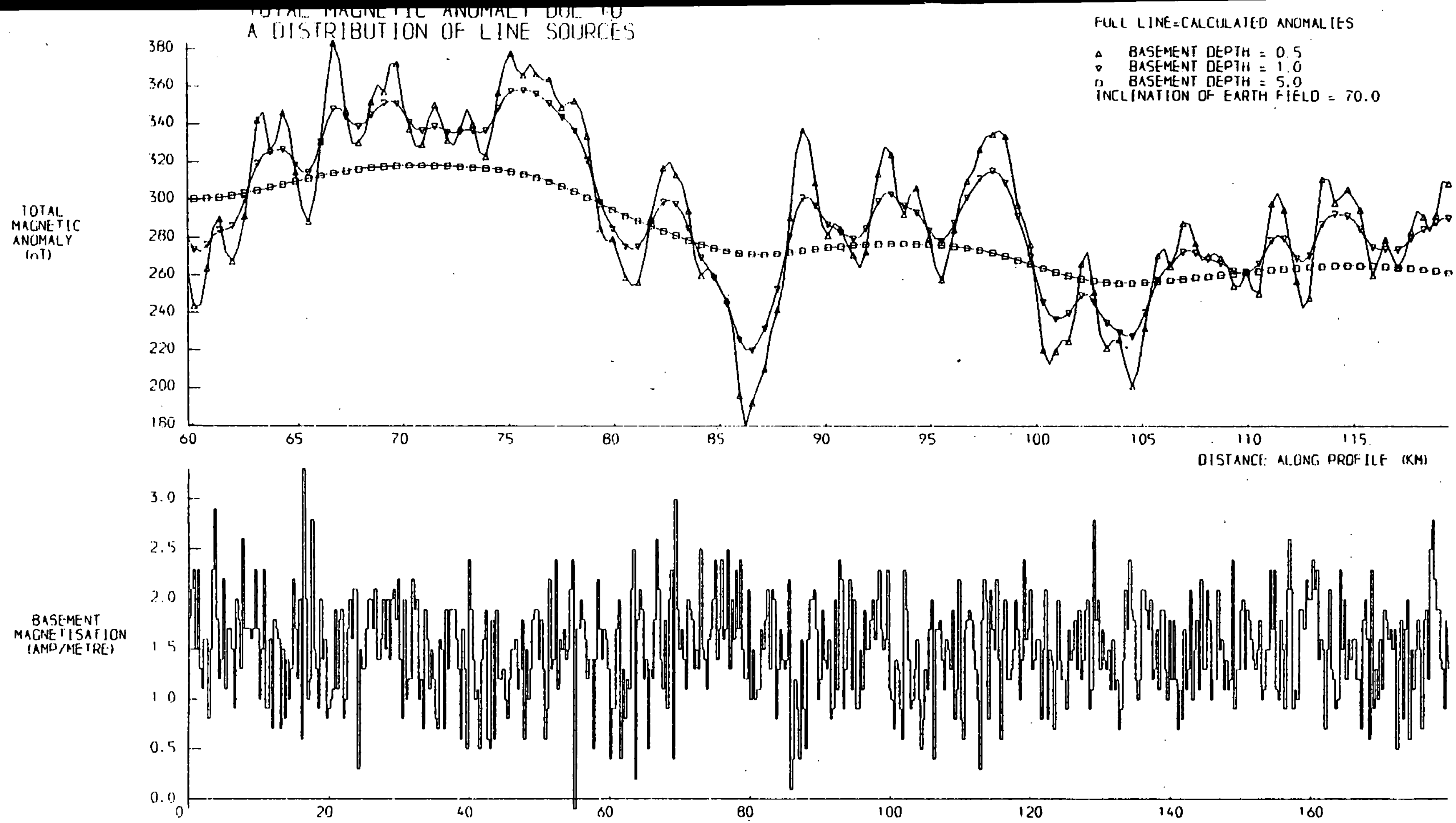

Figure 3.7 Model of randomly magnetised magnetic basement used for MEM spectral depth determination (generated by method of Treitel et al., 1971).

TABLE 3.1

Depth estimates to various model magnetised bodies using MEM spectral analysis on noise free anomalies. Constant sample interval, $\Delta x = 0.3$ km.

MAGNETIC BODY	ACTUAL DEPTH D, KM	PROFILE LENGTH T, KM	$\frac{\Delta T}{D}$	NO. OF SAMPLES N	ESTIMATED DEPTH BY LEAST SQUARES REGRESSION			NO. OF TERMS IN PREDICTION OPERATOR	
					AKAIKE	BERRYMAN	ALGEBRAIC SUM	AKAIKE	BERRYMAN
FINITE STEP	1.0	18.0	$(6)^{18}$	61	1.30±0.02	1.25±0.03	1.28±0.02	13	25
	(3.0)	9.0	$(3)^{9}$	31	1.43±0.04	1.25±0.07	1.32±0.09	9	15
INFINITE VERTICAL DYKE	5.0	30.0	6	101	5.29±0.21	4.82±0.08	4.86±0.05	14	38
		15.0	3	51	4.68±0.17	4.85±0.15	5.13±0.16	11	22
INFINITE INCLINED DYKE	5.0	30.0	6	101	5.34±0.25	5.62±0.24	5.65±0.16	20	38
		15.0	3	51	4.42±0.12	3.63±0.09	3.76±0.04	11	22
INFINITE THIN SHEET	2.0	10.2	5	35	1.47±0.11	1.70±0.11	1.77±0.29	13	16
		5.1	2.5	18	1.14±0.01	0.99±0.11	1.01±0.01	5	10
RANDOMLY MAGNETISED BASEMENT	5.0	30.0	6	100	4.16±0.10	5.14±0.37	4.55±0.28	11	37
		15.0	3	50	3.44±0.10*	3.32±0.07*	3.24±0.19	8	21
	1.0	6.0	6	20	-	0.97±0.04*	-	-	11

(*Depth estimated from average spectrum of several profiles within extent of anomaly)

TABLE 3.2

Depth estimates to various model magnetised bodies using MEM spectral analysis on anomalies plus additive random noise. Constant sample interval, $\Delta x = 0.3$ km.

MAGNETIC BODY	ACTUAL DEPTH D, KM	PROFILE LENGTH T, KM	$\frac{\Delta T}{D}$	NO. OF SAMPLES N	ESTIMATED DEPTH BY LEAST SQUARES REGRESSION			NO. OF TERMS IN PREDICTION OPERATOR	
					AKAIKE	BERRYMAN	ALGEBRAIC SUM	AKAIKE	BERRYMAN
FINITE STEP	1.0	18.0	$(6)^{18}$	61	1.21±0.01	1.22±0.03	1.21±0.01	9	25
	(3.0)	9.0	$(3)^{9}$	31	1.29±0.03	1.32±0.04	1.35±0.02	9	15
INFINITE VERTICAL DYKE	5.0	30.0	6	101	3.84±0.51	4.13±0.23	4.13±0.28	12	38
		15.0	3	51	2.74±0.28	5.00±0.42	4.18±0.54	8	22
INFINITE INCLINED DYKE	5.0	30.0	6	101	4.29±0.42	4.38±0.42	4.39±0.43	35	38
		15.0	3	51	3.15±0.28	3.93±0.36	3.34±0.38	8	22
INFINITE THIN SHEET	2.0	10.2	5	35	1.87±0.12	1.68±0.09	0.97±0.07	6	16
		5.1	2.5	18	0.22±0.00	2.27±0.21	1.34±0.11	2	10
RANDOMLY MAGNETISED BASEMENT	5.0	30.0	6	101	4.54±0.50	3.38±0.55	4.39±0.76	12	38
		15.0	3	50	1.26±0.04*	4.56±0.88*	3.72±0.41*	6	22
	1.0	6.0	6	20	1.29±0.12*	2.39±0.15*	1.83±0.10*	4	11

(*Depth estimated from average spectrum of several profiles within extent of anomaly)

The computer program SPECTRAL was applied to magnetic anomalies produced by the following model magnetic structures:

(1) finite magnetised step (horizontal derivative of anomaly)
(2) infinite vertical dyke
(3) infinite inclined dyke
(4) infinite thin sheet
(5) randomly magnetised basement.

Models (1) to (4) inclusive are illustrated in Figure 3.6 and model (5) is shown in Figure 3.7. The random numbers were generated by a standard subroutine available on the NUMAC computer (*NAG subroutine G05DDF). The random numbers represented a Gaussian process with an arithmetic mean of 1.5 and a standard deviation of 0.5.

Depth estimates for the noise-free anomalies are tabulated in Table 3.1. The same anomalies were then corrupted by the addition of random noise with zero mean and standard deviation of 2.0. The spectral depth estimates for the noisy data are tabulated in Table 3.2.

The magnetic anomalies for models (1) to (4) were calculated using the program MAGN, available in the Geophysics Department of the University of Durham. The magnetic anomaly due to a basement of random magnetic line sources was calculated by using the formulation of Treitel et al, (1971).

In order to test the predictive properties of the MEM spectral density estimate, various profile lengths relative to the depth of the particular magnetic body were investigated. In particular, Regan and Hinze (1976) recommended that the data set length from which the Fourier transform of a profile was to be estimated should be at least six times the maximum depth to the source of the anomaly. Therefore, profile lengths of 6 and 3 times the maximum depth respectively were used. For bodies whose depth extent tends to infinity for practical purposes, the depth estimate obtained relates to its upper surface only (see models (2) to (5) inclusive). For anomalies caused by bodies at different depths (see model (1)), their overlapping harmonic components produce spectral distortion. See Figure 3.8 and Figure 3.12.

A selection of MEM power spectral density estimates is displayed in Figures 3.8 to 3.15 inclusive. Each spectrum shows a pronounced peak at

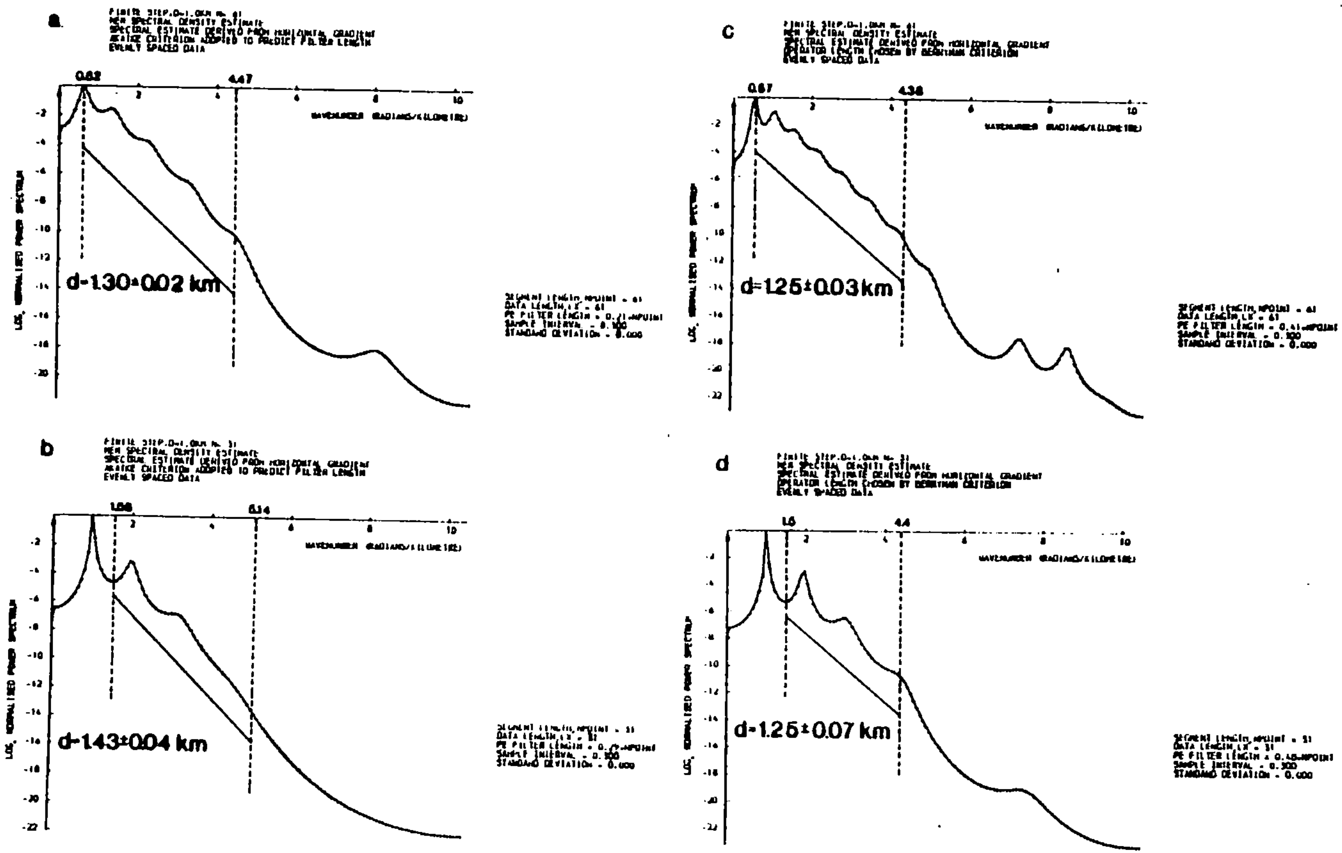

Figure 3.8 Natural logarithm, normalised MEM spectral density estimates for the finite step model (Figure 3.6a). (a) Profile length = 18km, Akaike criterion, (b) Profile length = 9km, Akaike criterion, (c) Profile length 18km, Berryman criterion, (d) Profile length = 9km, Berryman criterion. Line of regression and depth estimate indicated for each graph.

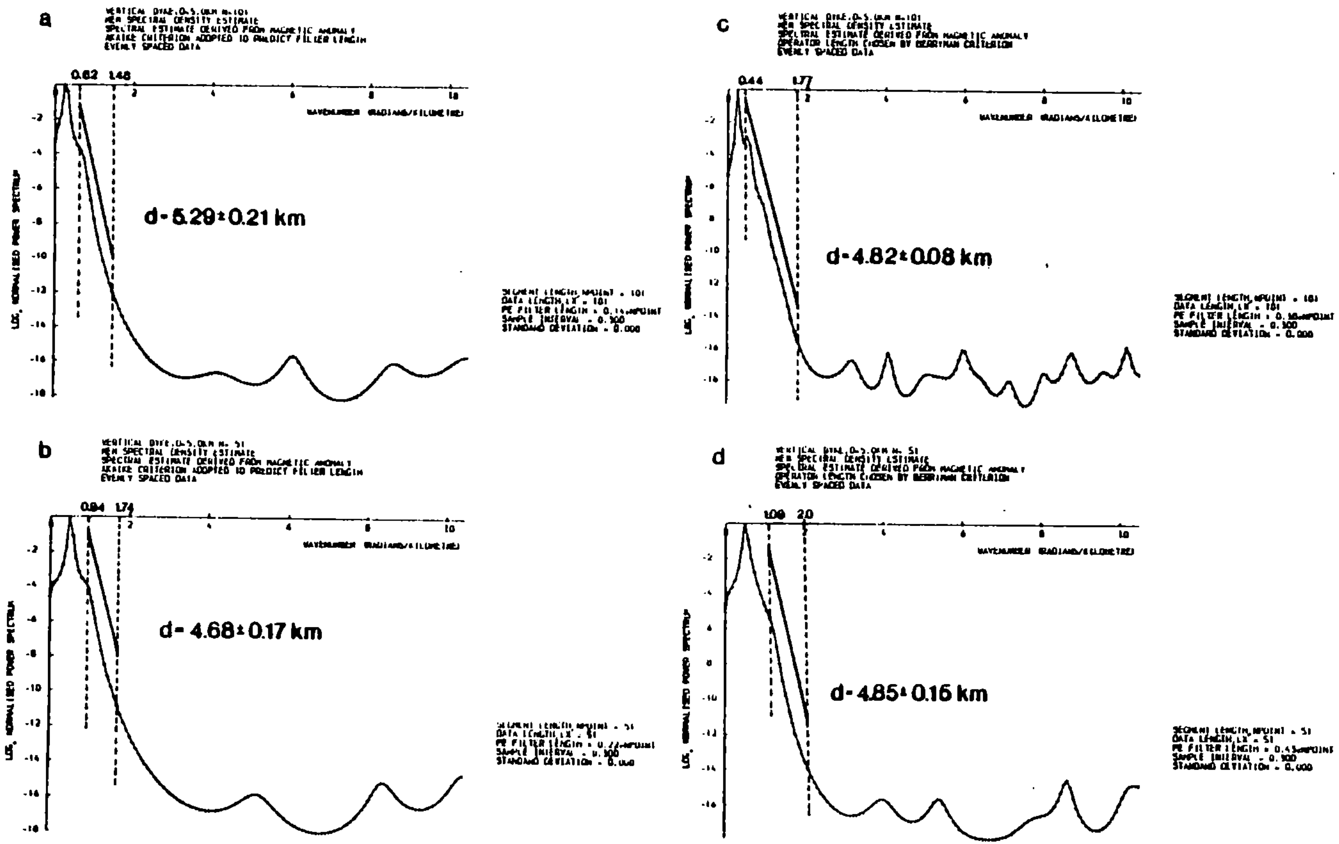

Figure 3.9 Natural logarithm, normalised MEM spectral density estimates for the vertical dyke model (Figure 3.6d). (a) Profile length = 15km, Akaike criterion, (b) Profile length = 15km, Akaike criterion, (c) Profile length = 30km, Berryman criterion, (d) Profile length = 15km, Berryman criterion. Line of regression and depth estimate indicated for each graph.

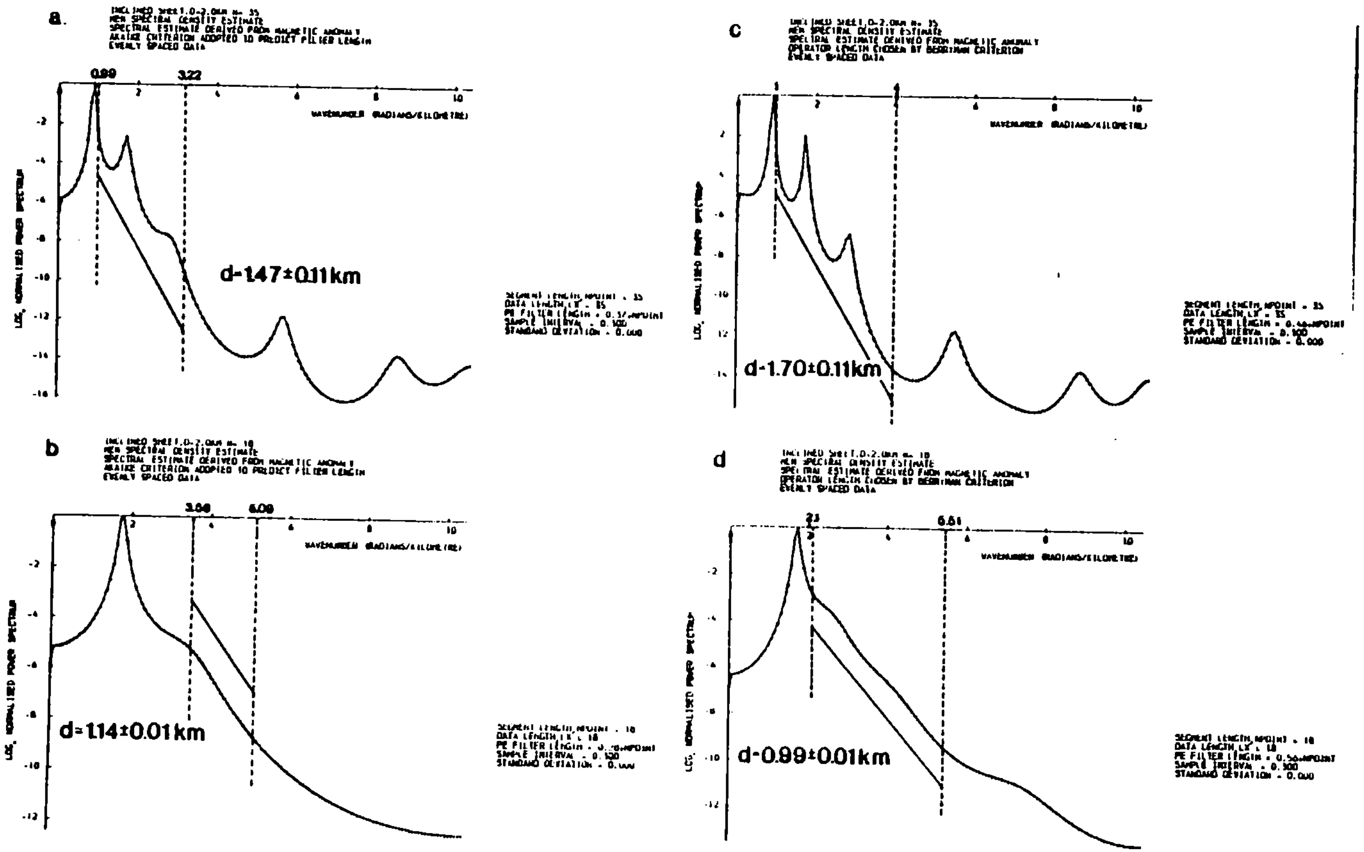

Figure 3.10 Natural logarithm, normalised MEM spectral density for the inclined sheet model (Figure 3.6b). (a) Profile length = 10.2km, Akaike criterion, (b) Profile length = 5.1km, Akaike criterion, (c) Profile length = 10.2km, Berryman criterion, (d) Profile length = 5.1km, Berryman criterion. Line of regression and depth estimate indicated for each graph.

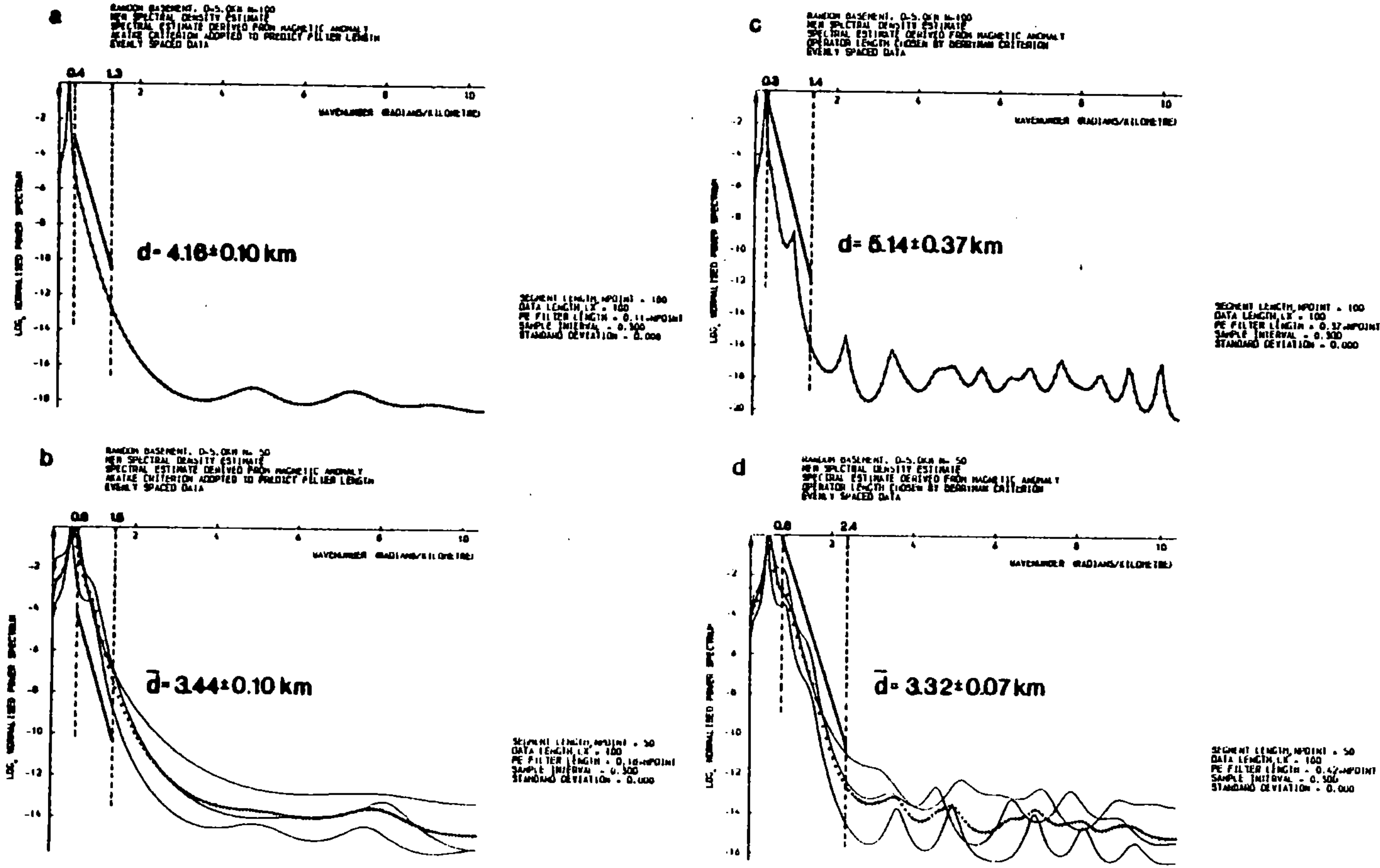

Figure 3.11 Natural logarithm, normalised MEM spectral density estimates for the randomly magnetised basement model (Figure 3.7). (a) Profile length = 29.7km, Akaike criterion, (b) Profile length = 14.7km, Akaike criterion, (c) Profile length = 29.7km, Berryman criterion, (d) Profile length = 14.7km, Berryman criterion. Line of regression and depth estimate indicated for each graph. Crosses indicate mean spectrum.

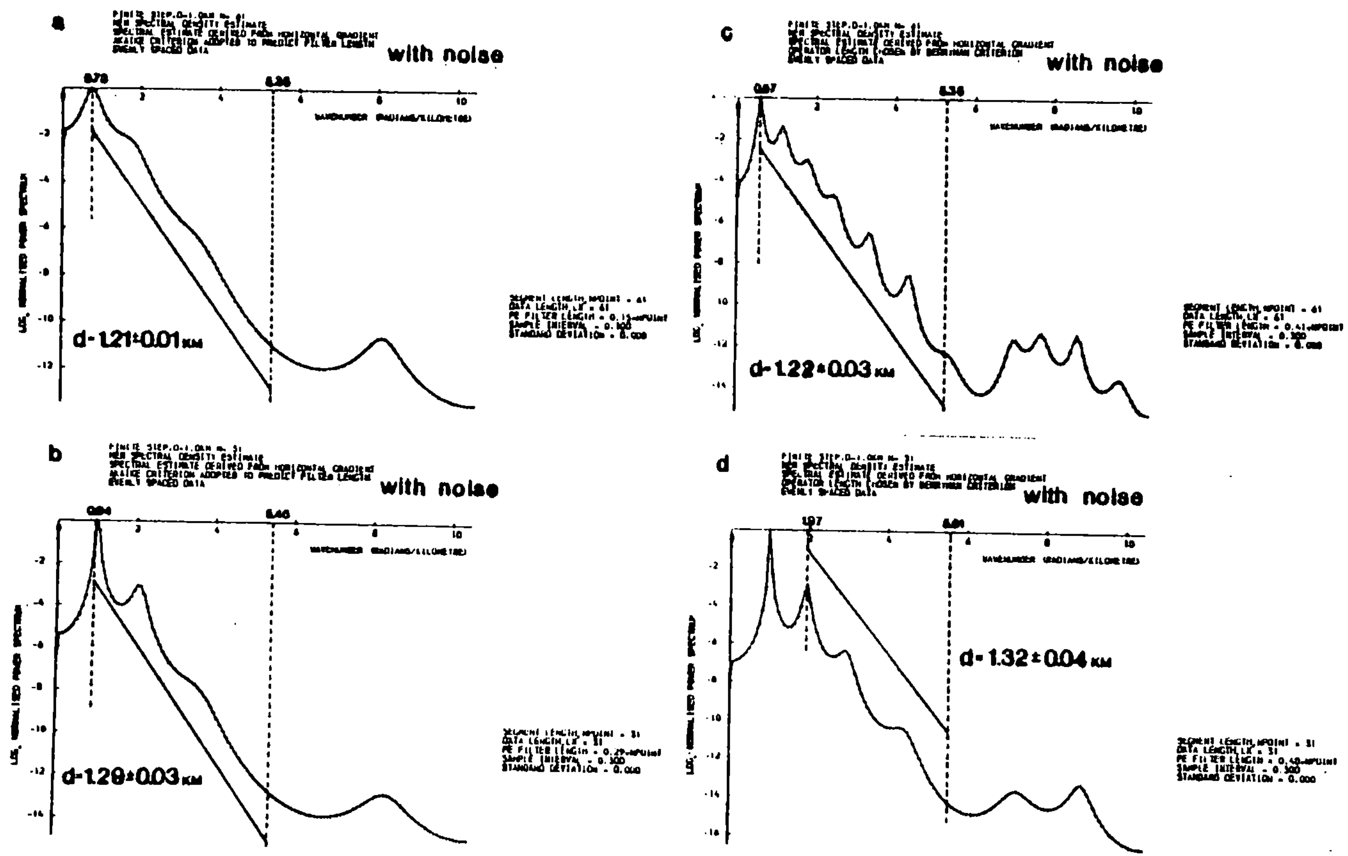

Figure 3.12 Natural logarithm, normalised MEM spectral density estimates for the finite step model (Figure 3.6a) with random noise. (a) Profile length = 18km, Akaike criterion, (b) Profile length = 9km, Akaike criterion, (c) Profile length = 18km, Berryman criterion, (d) Profile length = 9km, Berryman criterion. Line of regression and depth estimate indicated for each graph.

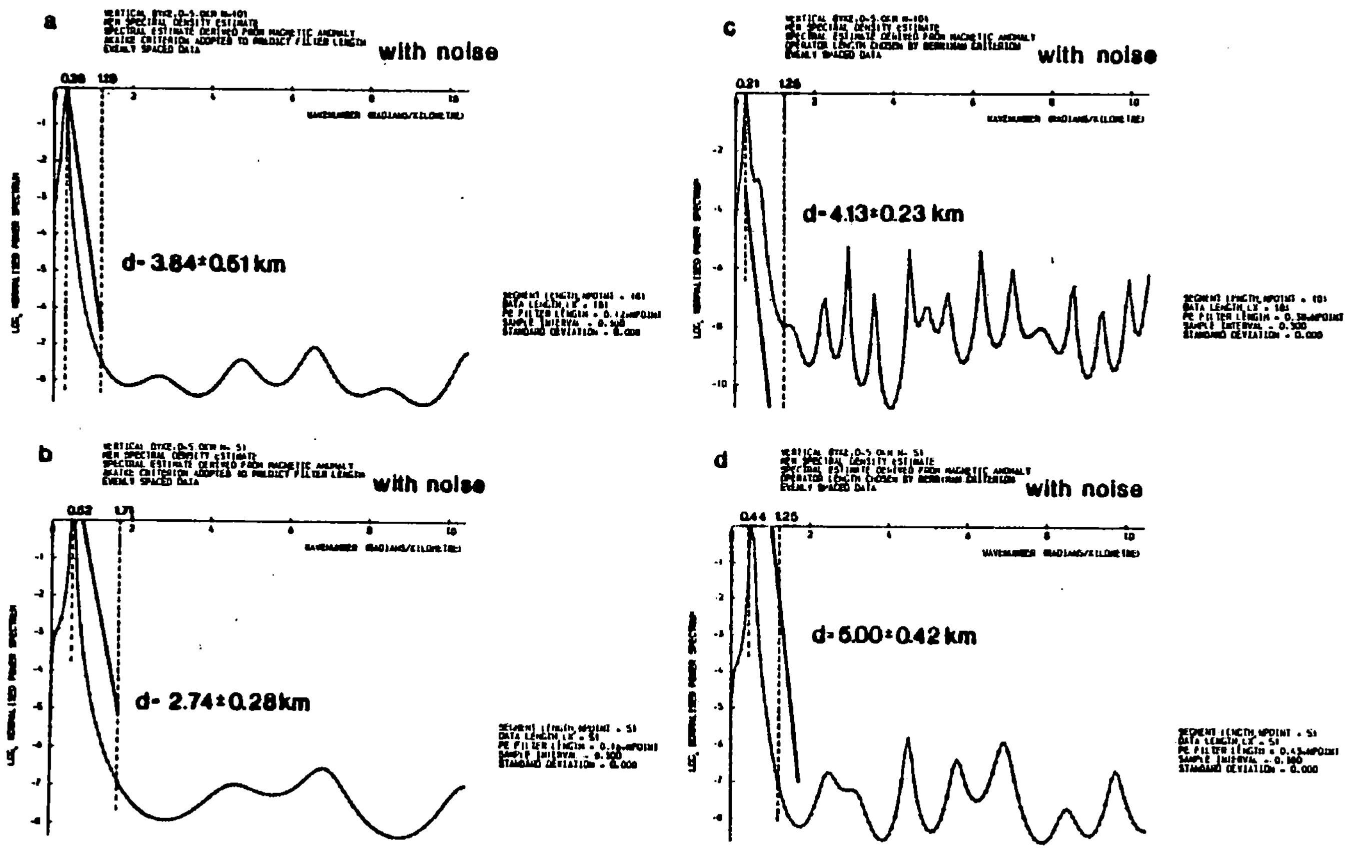

Figure 3.13 Natural logarithm, normalised MEM spectral density estimates for the vertical dyke model (Figure 3.6d) with random noise. (a) Profile length = 30km, Akaike criterion, (b) Profile length = 15km, Akaike criterion, (c) Profile length = 30km, Berryman criterion, (d) Profile length = 15km, Berryman criterion. Line of regression and depth estimate indicated for each graph.

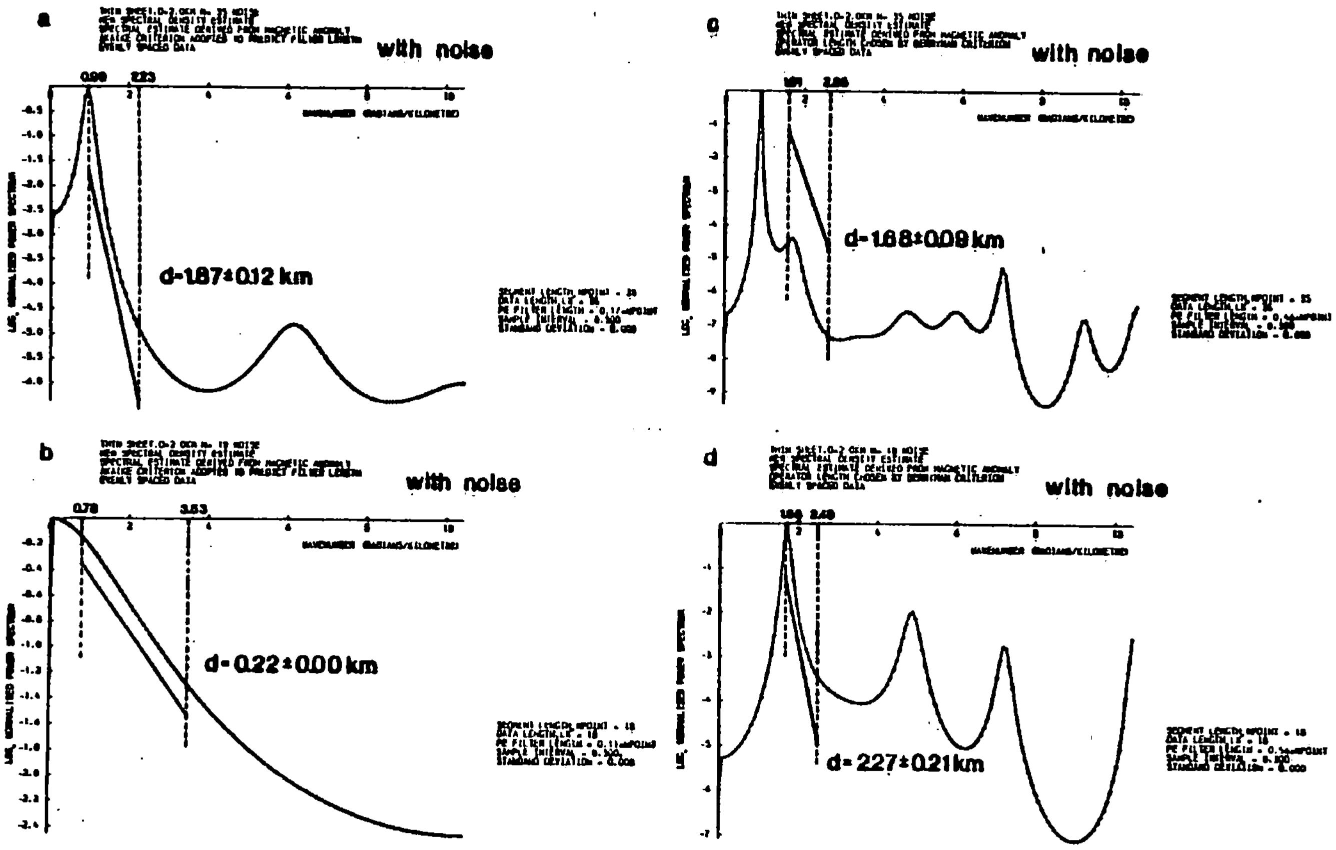

Figure 3.14 Natural logarithm, normalised MEM spectral density estimates for the thin sheet model (Figure 3.6b) with random noise. (a) Profile length = 10.2km, Akaike criterion, (b) Profile length = 5.1km, Akaike criterion, (c) Profile length = 10.2km, Berryman criterion, (d) Profile length = 5.1km, Berryman criterion. Line of regression and depth estimate indicated for each graph.

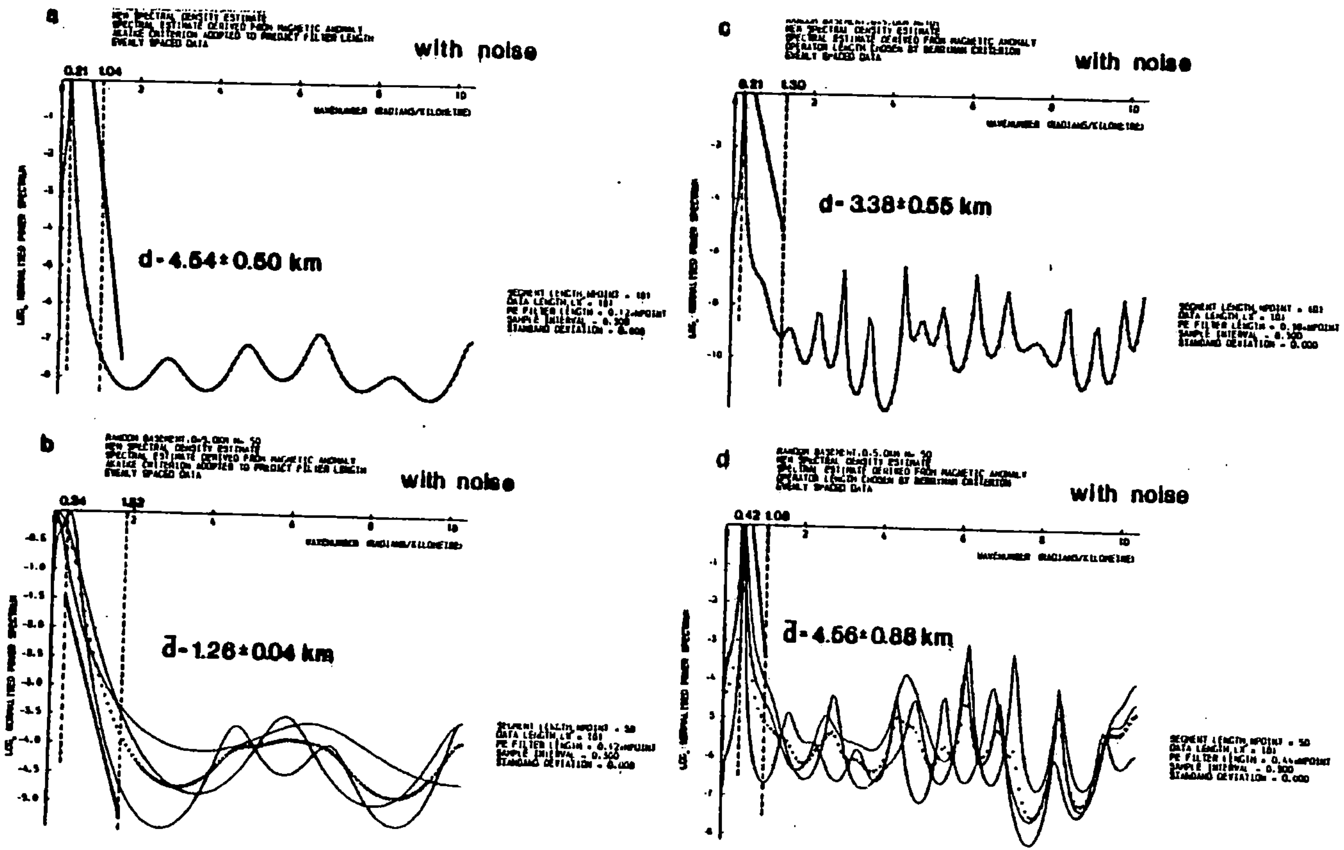

Figure 3.15 Natural logarithm, normalised MEM spectral density estimates for the randomly magnetised basement model (Figure 3.7) with random noise. (a) Profile length = 30km, Akaike criterion, (b) Profile length = 14.7km, Akaike criterion, (c) Profile length = 30km, Berryman criterion, (d) Profile length = 14.7km, Berryman criterion. Line of regression and depth estimate indicated for each graph. Crosses indicate mean spectrum.

low wavenumbers. The precise location of this peak appears to be a function of the initial phase of the input signal as shown for the multiple spectra of Figures 3.11 and 3.15. This dependence on initial phase may be an illusion since Swingler (1979) showed that observed frequency shifts are caused by assumptions implicit to the Burg algorithm itself. However, it was observed that the low wavenumber peak corresponded to a wavelength of the order of the length of the input data series. Taking this peak in the power spectrum to be a measure of the longest wavelength resolvable by the MEM technique before appreciable power loss at longer wavelengths, a graph was drawn to illustrate the dependence of the longest wavelength, λ_L to the length of the prediction error filter, LPEF. This graph is drawn in Figure 3.16.

If ΔT = the length of the input data series, all values of $\lambda_L/\Delta T$ lie between the limits 0.48 and 1.02 (except $\lambda_L/\Delta T$ for the thin sheet of Figure 3.14b). From Equation 3.16, it was deduced that the longest wavelength resolvable by a data set of finite length was less than the length of the data set itself. This was especially true since the assumed resolution criterion of Equation 3.15,

$$S \gtrsim \Delta k \tag{3.15}$$

was an optimistic one. As a result of the optimal smoothing property of the MEM spectral estimate (Ulrych and Bishop, 1975), it was supposed that the equivalent length of the data set would have been substantially increased due to the predictive nature of the MEM technique. However, the results of Figure 3.16 indicate that the predictive property of the Burg algorithm does not extend the maximum wavelength resolved beyond the length of the data set. The graph also indicates that the longest wavelength resolvable was sensibly independent of the length of the prediction error filter for the models analysed. This result is disappointing, although increased resolution at low wavenumbers is observed for long operator lengths (Figure 3.17) in agreement with Kane (1977). Improved resolution at low wavenumbers is accompanied by extremely peaky spectra at higher wavenumbers. This increased resolution at low wavenumbers is not a desirable feature for depth estimation from the slope of the log spectrum and implementation of long prediction operators was not pursued.

The uncertainty principle of Equation 3.13, that is,

$$\Delta k \; \Delta T \gtrsim 2\pi \tag{3.13}$$

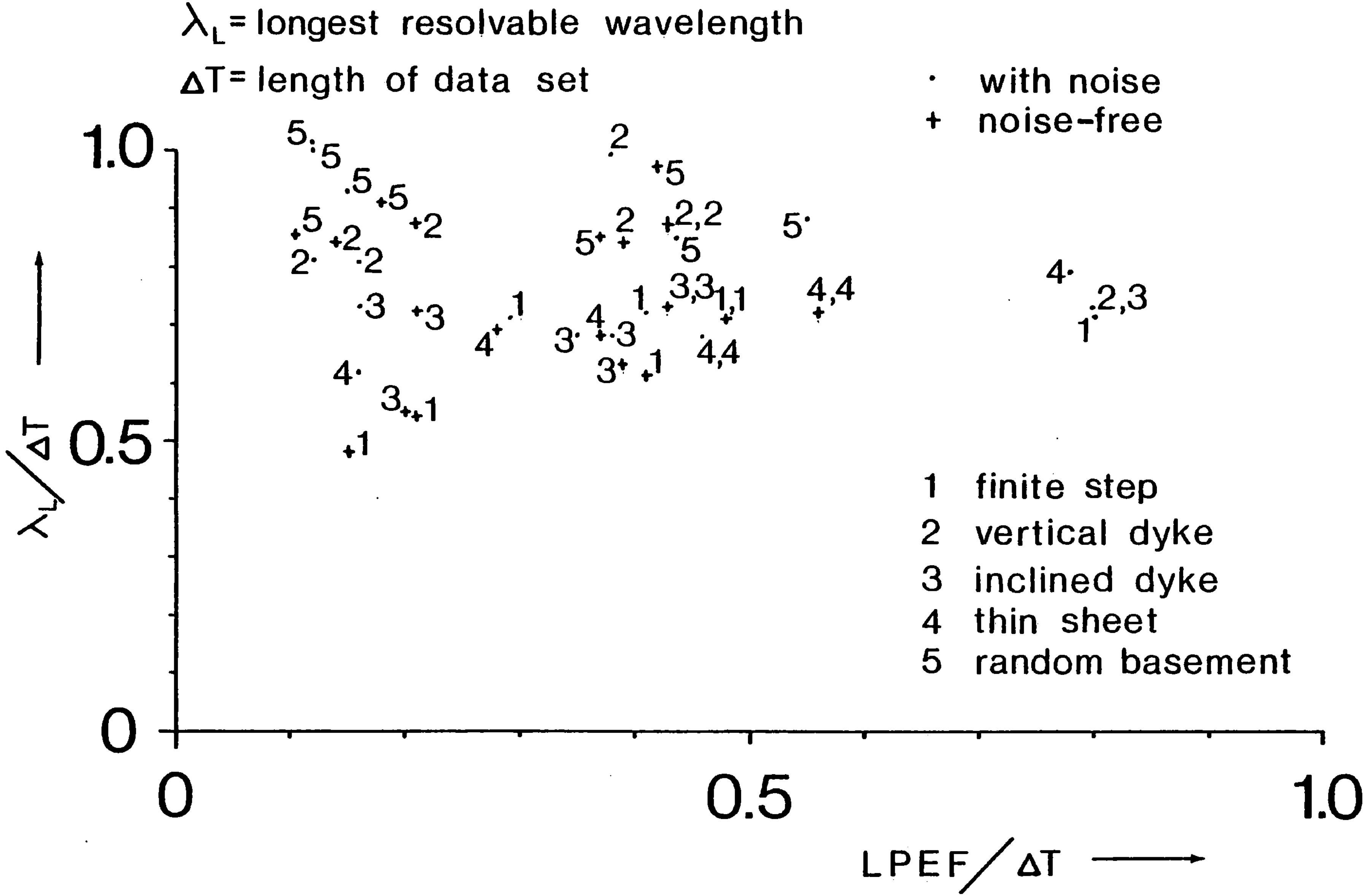

Figure 3.16 A graph indicating the relationship between an estimate of the longest resolvable wavelength, λ_L of a data series and the length of the prediction error filter, LPEF for that data series. Parameters λ_L and LPEF are normalised to the length of data set, ΔT.

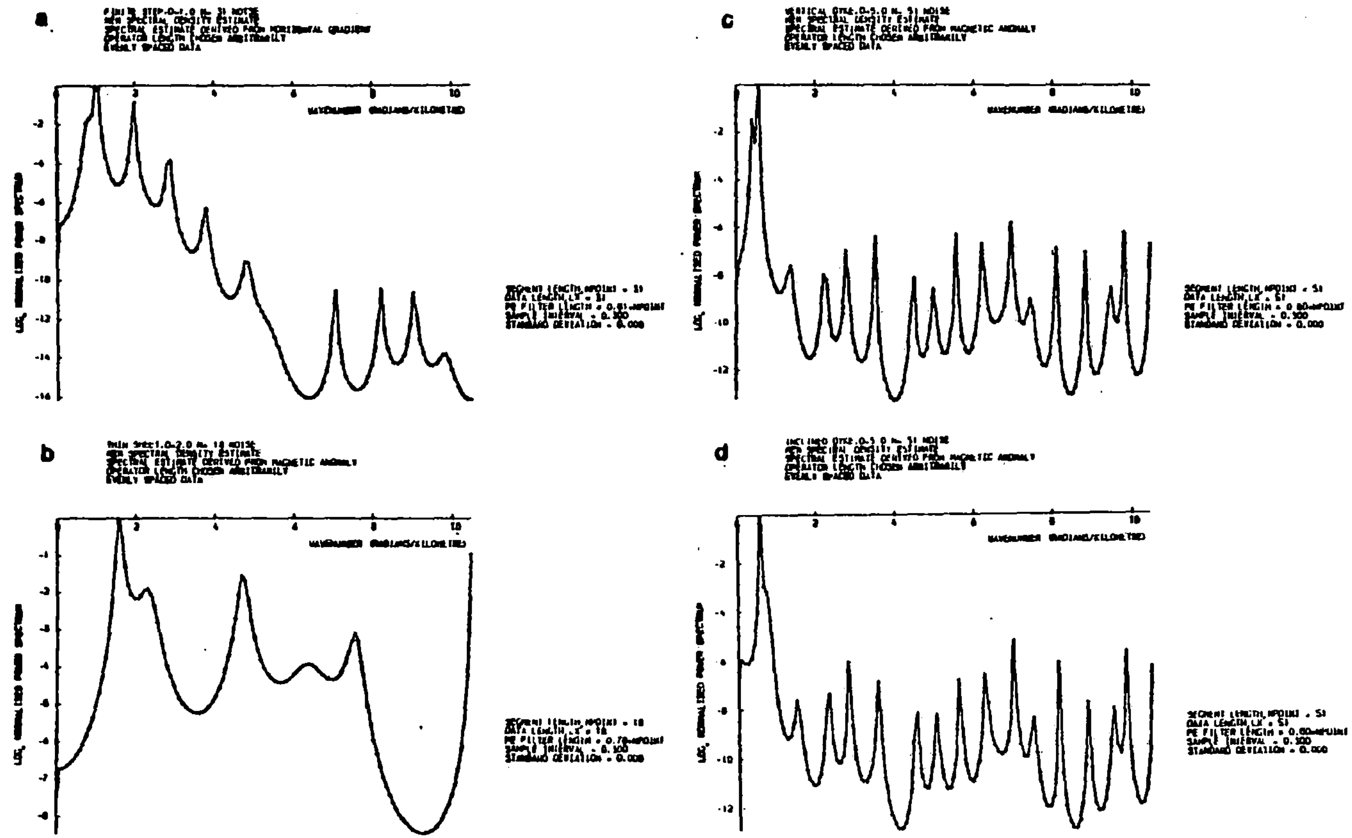

Figure 3.17 Natural logarithm, normalised MEM spectral density estimates for the magnetic models of Figure 3.6 with random noise. Each spectral estimate has been calculated using a prediction error filter of length, LPEF approximately equal to 0.8 of the data set length. (a) Finite step, profile length = 9km, (b) Thin sheet, profile length = 5.1km, (c) Vertical dyke, profile length = 15km, (d) Inclined dyke, profile length = 15km.

predicted that the equivalent length of the data set should have been $2\Delta T$. This apparent contradiction may be explained in terms of a trade-off between frequency resolution and statistical resolution. A more complete formulation of the uncertainty principle (Claerbout, 1976) states that:

$$\Delta k \ \Delta T \left(\frac{\Delta p}{p}\right)^2 > \pi \qquad 3.39$$

where Δk = the spectral bandwidth

ΔT = the length of the input data set

p = the variance of the spectral estimate

Δp = the error associated with the estimate of the variance.

Therefore, the improved resolution of the MEM spectral estimate is accommodated at the expense of statistical resolution in the estimated spectrum and not by increasing the equivalent length of the input data set.

Depth estimates obtained by fitting a least squares line of regression through the spectra between specified wavenumber limits are presented in Tables 3.1 and 3.2. Overall, the depth estimates confirm the recommendation of Regan and Hinze (1976) that the data set should be at least six times greater than the maximum depth to the causative body for reliable spectral determination. When the data set length was reduced to three times the maximum depth, the depth estimates were generally underestimated due to loss of power at low wavenumbers. Depth estimates for the finite step were consistently too large. This was probably due to a combination of spectral overlap between components generated by the upper and lower surfaces respectively and the fact that the sample spacing was 0.3 km. Such a large sample spacing meant that the shortest wavelength sampled was 0.6 km. Since there was likely to be appreciable power generated at shorter wavelengths by the upper surface at 1.0 km depth, the absence of this power in the high wavenumber components of the spectrum would tend to promote overestimates of depth to the upper surface of the step. An additional slope estimated from the first segment of curve in Figure 3.8a yields a depth of about 3 km i.e. the depth to the lower surface of the finite step.

The effect of additive noise is illustrated in Figures 3.12 to 3.15 inclusive. The power in high wavenumber components has been substantially increased and, in general, the depth estimates are less than those obtained from the noise-free anomalies.

The technique of calculating the mean spectrum from those generated over several segments of one profile was found to be unreliable. Its effectiveness was reduced due to the migration of the low wavenumber peak value as an apparent function of the initial phase. For more reliable estimates, care would have to be taken to ensure alignment of low wavenumber peaks prior to estimation of the mean spectrum. This procedure would only be valid for considerations of spectrum slope.

The choice between Akaike and Berryman criteria to determine the prediction operator length was not obvious due to the observed fluctuation in the tabulated depth estimates. However, the Berryman criterion seemed to produce marginally superior depth estimates for the data with additive random noise (Table 3.2).

The tentative application of MEM spectral analysis to magnetic anomalies produced reasonable depth estimates, even for very short data sets in some cases. However, the final accuracy of the procedure was disappointing and in general, the recommendation of Regan and Hinze (1976) for data sets at least six times greater than the maximum depth to the causative body remains valid. Therefore, these results demonstrate that MEM spectral analysis has little advantage over conventional techniques of spectral estimation for this particular application. However, it has allowed depth estimates to be made from very short data sets for which the Blackman and Tukey approach and the FFT periodogram method would have been less satisfactory.

3.3 Gravity modelling

A general purpose computer program, MGPLOT, was written for gravity modelling of profile gravity data and it incorporated the facility to plot observed magnetic and gravity data with calculated free-air or Bouguer gravity anomalies, calculated residuals, the 2-D isostatic gravity anomaly, bathymetry and the crustal model itself, including an isostatically compensated Moho discontinuity.

The standard approach to gravity interpretation was adopted whereby the near-surface structure was determined as accurately as possible from a combination of seismic reflection, sonobuoy and magnetic data. Isolated gravity anomalies were interpreted where possible to reveal subsurface structure. Having delineated near-surface structures, deep structure was inferred by inspection of the gravity residuals. Therefore, by "fixing" those structures determined with confidence by other methods, less well-known interfaces were adjusted in order to reduce the final residuals. This procedure was proposed as a comprehensive technique by Hammer (1963).

However, Hammer (1963) indicated a very real limitation of this approach. He emphasised the fundamental requirement of adequate definition of subsurface density contrasts and added a note of caution to the effect that deep structure inferred from gravity residuals is subject to all the uncertainties inherent in the near-surface structural interpretation. The accurate appraisal of subsurface density contrasts is absolutely crucial.

It was found to be easier and instructive to use the Bouguer anomaly during modelling of gravity anomalies. The Bouguer anomaly was calculated by replacing the seawater layer with material of the same density as the ocean floor sediments. This procedure effectively removed the sea-floor interface and obviated the effect of bathymetry on the calculated anomaly.

The two-dimensional isostatic gravity anomaly was calculated by equating pressures along the profile at a chosen depth of compensation, T to the pressure at the same depth beneath a crust of standard crustal density. The procedure and nomenclature are given in Figure 3.18 and the following equation was derived:

$$h_n = \frac{\rho_{n-1} \sum_{i=1}^{n-2} h_i - \sum_{i=1}^{n-2} \rho_i h_i}{\rho_n - \rho_{n-1}} \qquad 3.40$$

where ρ_i = the density of the ith layer

h_i = the thickness of the ith layer

and $\rho_c = \rho_{n-1}$, where ρ_c = the standard crustal density.

The depth, d to the isostatically compensated Moho is then given by:

$$d = T - h_n \qquad 4.41$$

These equations were used to calculate the two-dimensional isostatic Moho. The isostatic gravity anomaly was then calculated as the difference

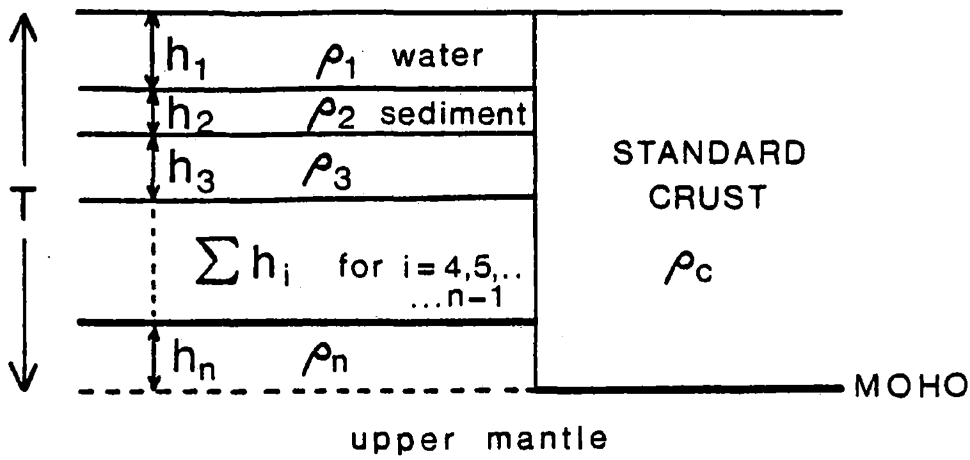

$$T = \sum_{i=1}^{n} h_i = \sum_{i=1}^{n-2} h_i + h_{n-1} + h_n \quad \ldots\ldots\ldots\ldots 1$$

Equate pressures at compensation depth, T;

$$T\rho_c = \sum_{i=1}^{n-2} \rho_i h_i + \rho_{n-1} h_{n-1} + \rho_n h_n \quad \ldots\ldots\ldots\ldots 2$$

Multiply equ.1 by ρ_{n-1} and subtract the resulting equation from equation 2 to give;

$$T(\rho_c - \rho_{n-1}) = \sum_{i=1}^{n-2} \rho_i h_i - \rho_{n-1} \sum_{i=1}^{n-2} h_i + h_n(\rho_n - \rho_{n-1})$$

If $\rho_c = \rho_{n-1}$, solving for h_n gives;

$$h_n = \frac{\rho_{n-1} \sum_{i=1}^{n-2} h_i - \sum_{i=1}^{n-2} \rho_i h_i}{(\rho_n - \rho_{n-1})}$$

$$\boxed{\therefore \text{Depth to isostatic moho} = T - h_n}$$

Figure 3.18 The derivation of Equations 3.40 and 3.41 respectively for the calculation of the depth to a 2-D isostatic Moho for the gravity profile models.

between the Bouguer anomaly and the computed anomaly of the anti-root (Bott, 1971). In calculating the isostatic anomaly, the Bouguer anomaly was evaluated by replacing all layers within the model crustal section with material of a single standard density. Therefore, the Bouguer anomaly referred to a crustal model of constant density between sea-level and Moho (Kearey, 1973).

The actual modelling of free-air gravity anomalies was carried out on a "trial and error" basis, those coordinates of a model which were confidently estimated being fixed and the other coordinates being allowed to move in a "sensible" way to provide a good fit with the observed gravity data.

CHAPTER 4

SEISMIC PROCESSING AND INTERPRETATION

4.1 Introduction

Despite the acquisition of multi-channel seismic reflection data during the geophysical cruise, no processing facilities were made available at the University of Durham. An offer made by The British Petroleum Company Limited to process some of the seismic data was therefore gratefully accepted.

The seismic data acquired along profile 11 were chosen for detailed processing (see Figure 1.1). This decision was made on the basis of gravity, magnetic and sonobuoy observations. A free-air gravity low of about 40 mgal, the subdued nature of the associated magnetic anomaly and the suite of velocities revealed by a sonobuoy refraction experiment to the north (depth to "basement" = 5.3 km) indicated the possible presence of a major sequence of Mesozoic sediments underlying the continental shelf. Spectral depth estimates using the maximum entropy method (Chapter 3) provided depths to magnetic basement of about 4.0 km. It was clear that an accurate interpretation of the seismic data collected along profile 11 was crucial to any proposal for the development of the continental margin.

Processing details are summarised in the following section. An interpretation of the processed section is then given and finally this is extended to encompass those reflection horizons identifiable on single-channel shipborne monitor records from contiguous profiles. For completeness, a discussion of available sonobuoy velocity values is also included and general conclusions are made about the nature of the continental margin of East Greenland.

4.2 Processing of multi-channel seismic reflection data

The processing sequence carried out by The British Petroleum Co. Ltd. was applied in 13 stages, after demultiplexing the seismic data:

(1) Amplitude recovery

The purpose of amplitude recovery is to compensate for the effects of spherical divergence, attenuation due to solid friction, energy loss due to reverberations and transmission losses due to propagation through many layer boundaries (Sheriff, 1975). In order to recover amplitude losses not relevant to subsurface geology and thereby re-establish relative amplitudes of reflected events, the following gain function was applied to the recorded reflection time series, point by point, along each trace:

$$\text{gain factor} = t\,e^{\alpha t} \qquad 4.1$$

where t = the two-way travel time

α = a constant = 0.2.

A static time correction was also applied at this stage in order to compensate for multiplexer delay (Waters, 1978).

(2) Trace editing

The 11 channels of recorded seismic data were displayed at selected shot points to enable assessment of recording fidelity and verification that each channel had been recorded correctly. It was found that no meaningful seismic data were recorded on channel 10 (see Enclosure 2). The precise reason for this is unknown but it was undoubtedly caused by malfunction of the acquisition system.

(3) Deconvolution

The final recorded seismic signal is the result of the convolution of the input signal consisting of the superposition of the airgun array pulse and the surface "ghost", and the filter coefficients (subsurface reflection coefficients) of the earth and subsequent recording system. The operation of deconvolution is an attempt to determine the coefficients of the recorded wavelet, including the input wavelet component, from an analysis of the recorded seismic traces themselves and then to design an inverse filter which when applied to the seismic trace will yield the primary reflection events encountered during the passage of the seismic signal through the earth filter. Convolution of the recorded seismic trace with this inverse filter produces pulse compression since its phase approaches zero and its amplitude spectrum is made flat (cf. the Dirac delta function). This procedure assumes that the filtered source impulse is minimum phase (Waters, 1978). The minimum phase condition provides a unique link between the phase and amplitude spectrum of the pulse.

Pulse compression is necessary due to selective absorption of high frequency components within the source signal during its passage through the earth filter which produces pulse broadening. Deconvolution attempts (a) to restore the sharp impulsive character of the recorded seismic signal and to enhance the definition of the onset of a reflection event, (b) to correct for non-whiteness in the spectra of the source and recording instrumentation impulse responses and (c) to reduce the reverberating tail of the pulse which obscures later events (G. Bowyer, pers. comm.).

Prewhitening was performed before the design of the deconvolution operator. This enhanced the power contained in high frequencies and is a technique used to reduce the dynamic range of the spectrum (Bloomfield, 1976).

(4) Normal moveout correction

The application of normal moveout corrections to the seismic time series is an essential prerequisite to common depth point (CDP) stacking.

In order to calculate the correct value of normal moveout (Dobrin, 1976; Waters, 1978), an appropriate stacking velocity must be assigned to each particular primary reflector. After removal of normal moveout from the seismic traces to be stacked together, primary reflection horizons should line-up from trace to trace within the CDP gather. Normal moveout corrections compensate for the effect of increasing offset between shot and receiver for waves which have a common subsurface reflection point (nominal, in practice) and reduce each seismic trace to one of normal incidence for primary reflection events.

A technique for estimation of appropriate stacking velocities for evaluation of normal moveout corrections was proposed by Taner and Koehler (1969).

Velocity functions were determined at an average interval of approximately 12 km on profile 11, except over a confused zone beneath the continental shelf where well-defined, identifiable reflection horizons were absent. Only one velocity function was evaluated here.

Application of normal moveout corrections to seismic traces has an undesirable effect on primary reflections called "NMO stretch" (Waters, 1978). Serious wave shape and spectrum distortion of the seismic pulse result.

(5) Dynamic offset dependent trace weighting

The degree to which the CDP stack is successful in long-wavelength multiple reflection elimination is a function of the differential moveout between primary and multiple reflections. Effective multiple cancellation is only possible for significantly large values of differential moveout obtained with long hydrophone streamers. The maximum offset available with the Flexotir streamer used for the 1977 Durham survey was 1253 m.

In order to enhance multiple attenuation within each CDP gather, dynamic offset dependent trace weighting was carried out before stacking so that seismic traces corresponding to long offsets were given greater weight than those traces recorded at short offsets.

However, pulse broadening due to attenuation of high frequencies is more pronounced at long offsets and the definition of primary reflection horizons is correspondingly less clear. Thus, a trade-off between enhanced multiple attenuation and sharp reflector definition must be recognised in this procedure.

This technique also reduces the signal to random noise ratio of the final stacked trace (G. Bowyer, pers. comm.).

(6) First break mutes

Muting consists of arbitrarily assigning zero values to seismic records in order to remove the direct water arrival and refraction events immediately following the water-break pulse. Direct and refracted arrivals are generally so strong that their removal is necessary in order to avoid significant degradation in the quality of near-surface reflection events (Telford et al, 1976).

(7) 11-fold common depth point (CDP) stack

After application of normal moveout corrections and muting, the traces within each gather were composited to form a nominal 11-fold CDP stack. Such traces summed are implicitly assumed to consist of seismic pulses reflected from a common subsurface point on a given horizon for each primary reflection event. The necessary shot spacing to give an 11-fold CDP stack was 50 m, that is, half the distance between centres of adjacent hydrophone groups along the streamer.

The average ship's velocity along profile 11 after projecting navigation data onto a line of constant heading was 11.32 km hr^{-1} and, given a constant shot interval of 21 s, the actual distance between shot points was approximately 66 m. The significance of this result is illustrated in Figure 4.1. Assuming the required geometry for optimum stacking has created a linear region of about 160 m over which nominally coincident reflection points have been evenly distributed for the case of a horizontal reflector. This phenomenon is exacerbated for a dipping horizon although the precise effect depends on its orientation relative to the shot-detector acquisition system. Distortion and smearing of primary signals is an inevitable consequence especially for horizons showing rapid topographic changes within the zone of reflection points.

The actual multiplicity of CDP stack was 10-fold because no useful primary reflection data appeared on channel 10.

Objectives of CDP stacking are (a) the improvement of primary signal to random noise ratio by a factor of $\sqrt{N}$, where N is the number of traces to be composited to form a stack, (b) the attenuation of long-wavelength multiple reflections, and (c) to maximise the ratio of primary P-wave reflections to all other reflections (multiples and mode-converted), refractions, diffractions and any externally generated noise, for example electrical pick-up, ship's tow noise, tailbuoy tugging, etc. (G. Bowyer, pers. comm.).

(8) F-K velocity filtering

The original "pie-slice" process of velocity filtering was proposed by Embree et al (1963). This method has now been superceded by a more general 2-D filter approach using the Fast Fourier Transform (FFT) algorithm (Waters, 1978).

The purpose of velocity filtering is to remove low velocity coherent noise from the CDP stacked seismic section. This was particularly necessary over the continental slope of profile 11 where differential moveout between primary and multiple events was not sufficient to give destructive interference of steeply dipping, long-wavelength multiples so that important geological detail remained obscured. Velocity filtering was also effective in removing steeply dipping diffractions and remnant noise due to ship noise and cable tugging not attenuated by the hydrophone array comprising the detector group of each channel (Figure 2.5).

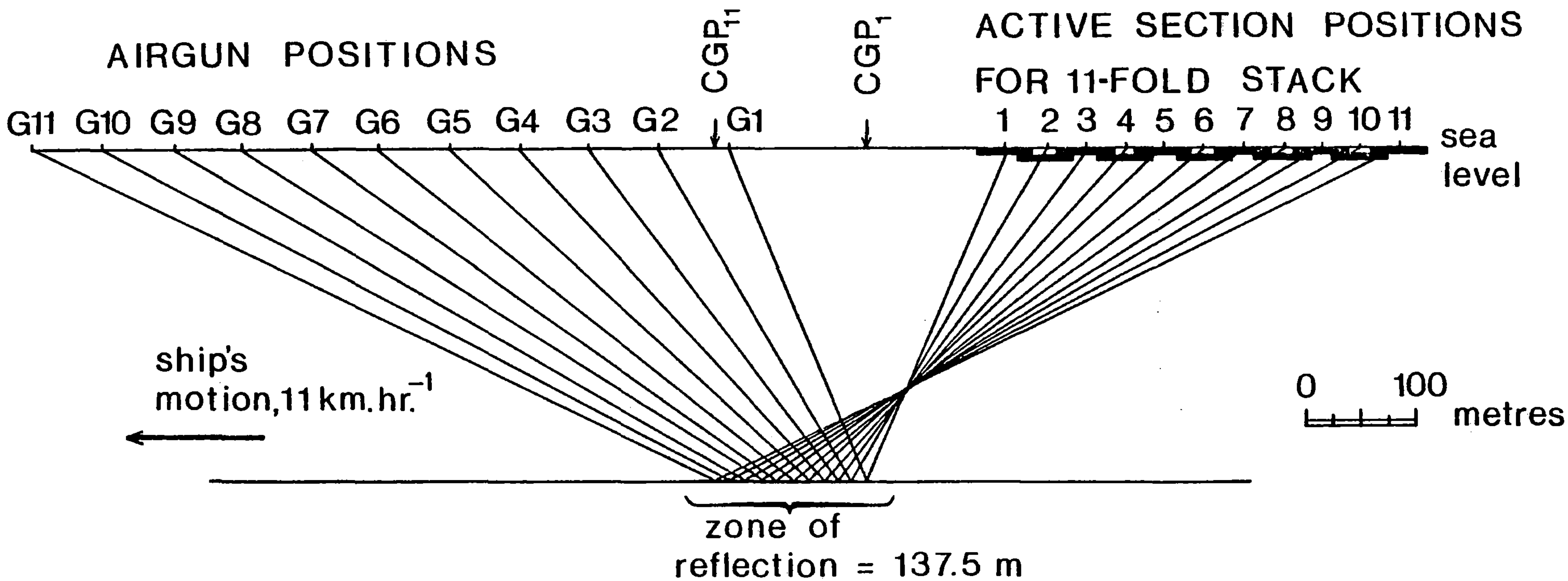

Figure 4.1 Diagram showing the actual configuration of sources and detectors for the CDP stack carried out by British Petroleum Co. Ltd. Note the region over which reflections are "smeared" in sharp contrast to the assumed common <u>point</u> of reflection for a flat, horizontal reflector.

The rejection zone specified by BP for F-K velocity filtering was for apparent velocities ≤ 10 ms/trace and this is equivalent to an apparent velocity of about 6.6 km s^{-1}.

(9) 3-fold weighted trace mix

The 3-fold weighted trace mix (in the ratio 1:2:1) was primarily a cosmetic, smoothing operation in order to improve reflector continuity and to facilitate geological interpretation of the final seismic section. The enhancement of laterally continuous events in this way was carried out because the signal to noise ratio on the stacked section was rather poor (G. Bowyer, pers. comm.).

(10) Static corrections

A static correction of 12 ms was added to each trace of the stacked seismic section in order to compensate for the depths of the airgun array (6.7 m) and the hydrophone streamer (12.2 m). This time correction was calculated assuming normal incidence reflection and a propagation velocity of 1500 m s^{-1} for seismic waves in water.

(11) Deconvolution

Application of normal moveout corrections introduces undesirable filtering effects by distorting the spectrum of primary pulse and by stretching the pulse width in the time domain. Deconvolution was applied as a spiking agent in an attempt to eliminate undesirable filtering effects, analogous to stage (3) above.

Pre-stack deconvolution is only partially effective because the high level of broad-band noise present on pre-stack traces tends to limit the amount of "whitening" achieved. The improved signal to noise ratio on post-stack CDP seismic data provides an opportunity to improve further pulse compression (G. Bowyer, pers. comm.).

Prewhitening was carried out in order to reduce the dynamic range of the spectrum.

(12) Time and space variant bandpass filter

Since the impulse from the airgun array has a finite bandwidth, pulses representing primary events on the seismic section are also band-limited. The function of bandpass filtering is to remove primarily recorded noise whilst retaining those frequencies within the bandwidth of the primary reflection events. A time-varying filter operation is used because the bandwidth of the seismic pulse changes with increasing time down each trace.

Each filter was zero phase so that the phase characteristics of the signal remained unaltered after filtering.

In filter design there exists a trade-off between noise cancellation enhanced by narrow-band filtering and improved resolution of primary events resulting from wide-band filtering.

(13) Dynamic equalisation

The final step in the processing sequence consisted of an amplitude normalisation procedure in order to suppress dominant, large-amplitude events and to enhance low amplitude primaries on the seismic display. The signal of each trace was scaled to a constant amplitude over a time-varying window down the trace (Waters, 1978).

This completed the data processing of multi-channel seismic data acquired along profile 11. The final CDP stacked section (Enclosure 2) is stored in the pocket on the inside cover of this thesis. The overall quality of the processed section is excellent, bearing in mind the crudely sub-optimal stack, and it is vastly superior to the single-channel ship-borne monitor records.

4.3 Geological interpretation of CDP stacked seismic section, profile 11

A line drawing of the geological interpretation of profile 11 is illustrated in Figure 4.2.

The resolution of reflecting horizons is limited by the wavelength of the incident seismic signal. Vertical resolution is of the order of 1/8 to 1/4 wavelength (Sheriff, 1977). For a dominant frequency of 50 Hz from shallow reflectors in a medium of velocity 1.8 to 2.5 km s^{-1}, the corresponding wavelength range is 36 to 50 m. Deeper reflections contain a lower dominant frequency, say 20 Hz and for rock velocities of 3.0 to 5.5 km s^{-1}, the signal wavelengths lie between 150 and 175 m. Therefore, bed thicknesses of about 12 m for shallow penetration and 68 m for deeper

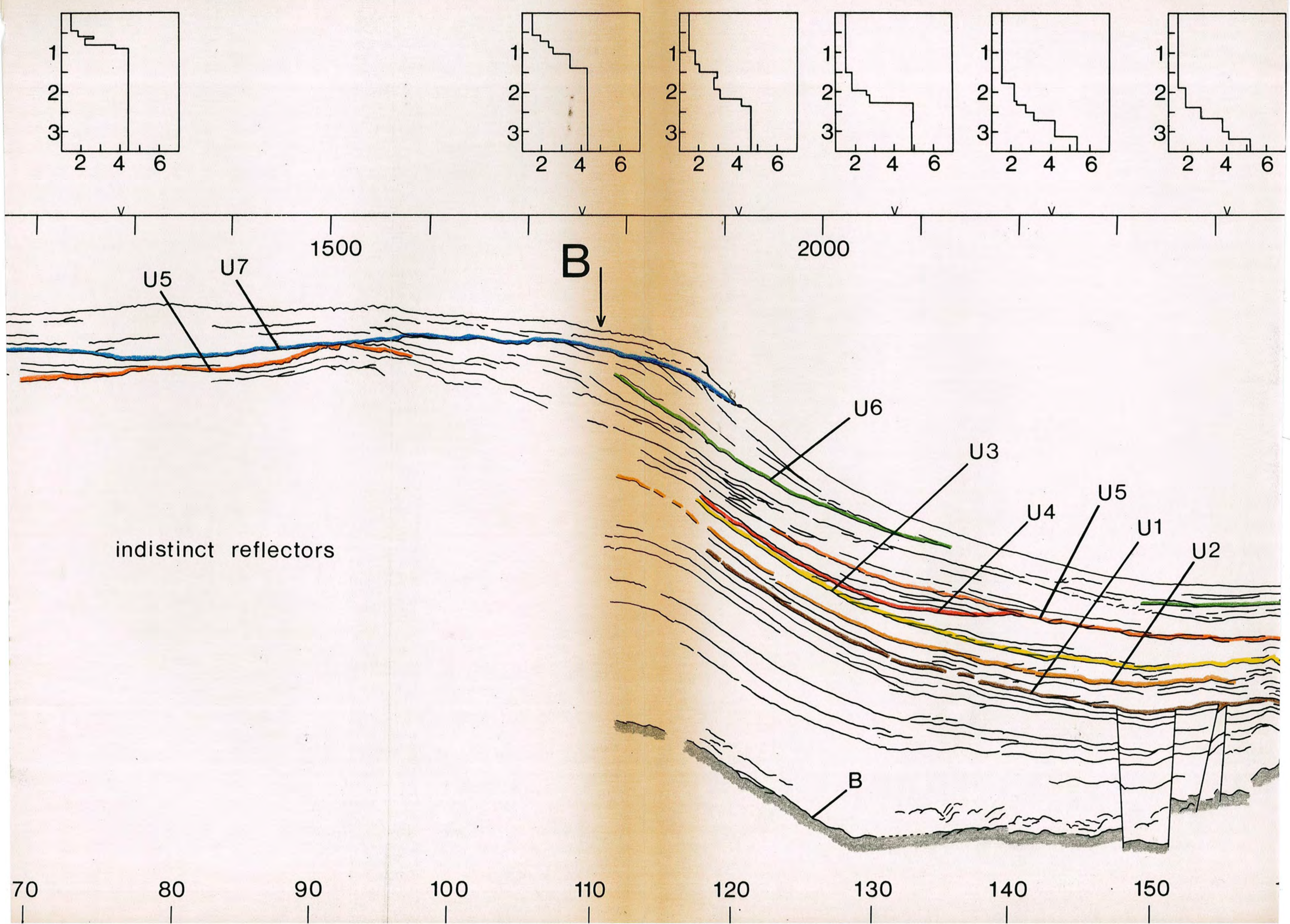

1500
2000
B
U5
U7
U6
U3
U4
U5
U1
U2
indistinct reflectors
B
70
80
90
100
110
120
130
140
150

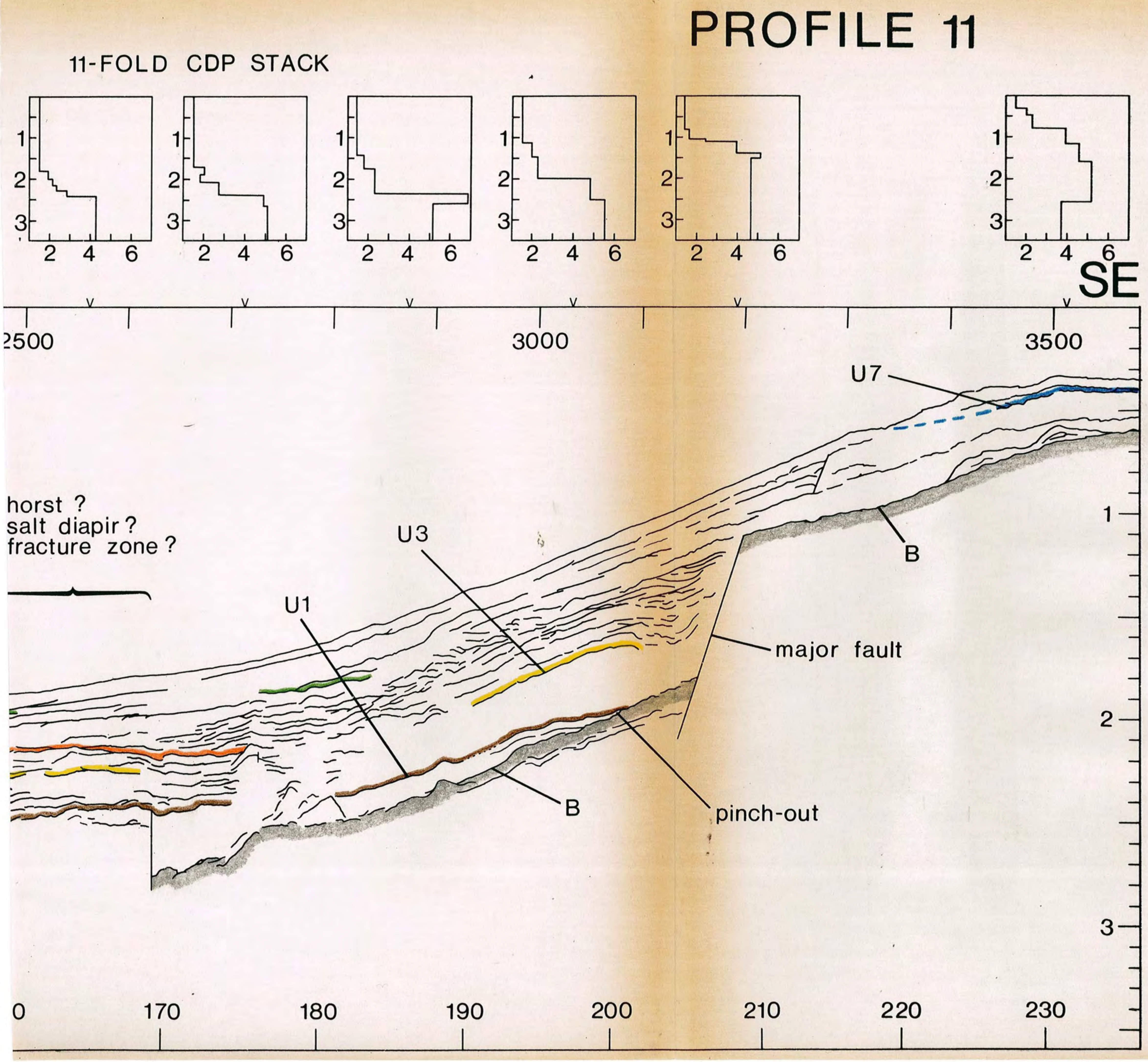
PROFILE 11
11-FOLD CDP STACK
SE
2500
3000
3500
U7
horst ?
salt diapir ?
fracture zone ?
U3
U1
B
major fault
pinch-out
B
170
180
190
200
210
220
230

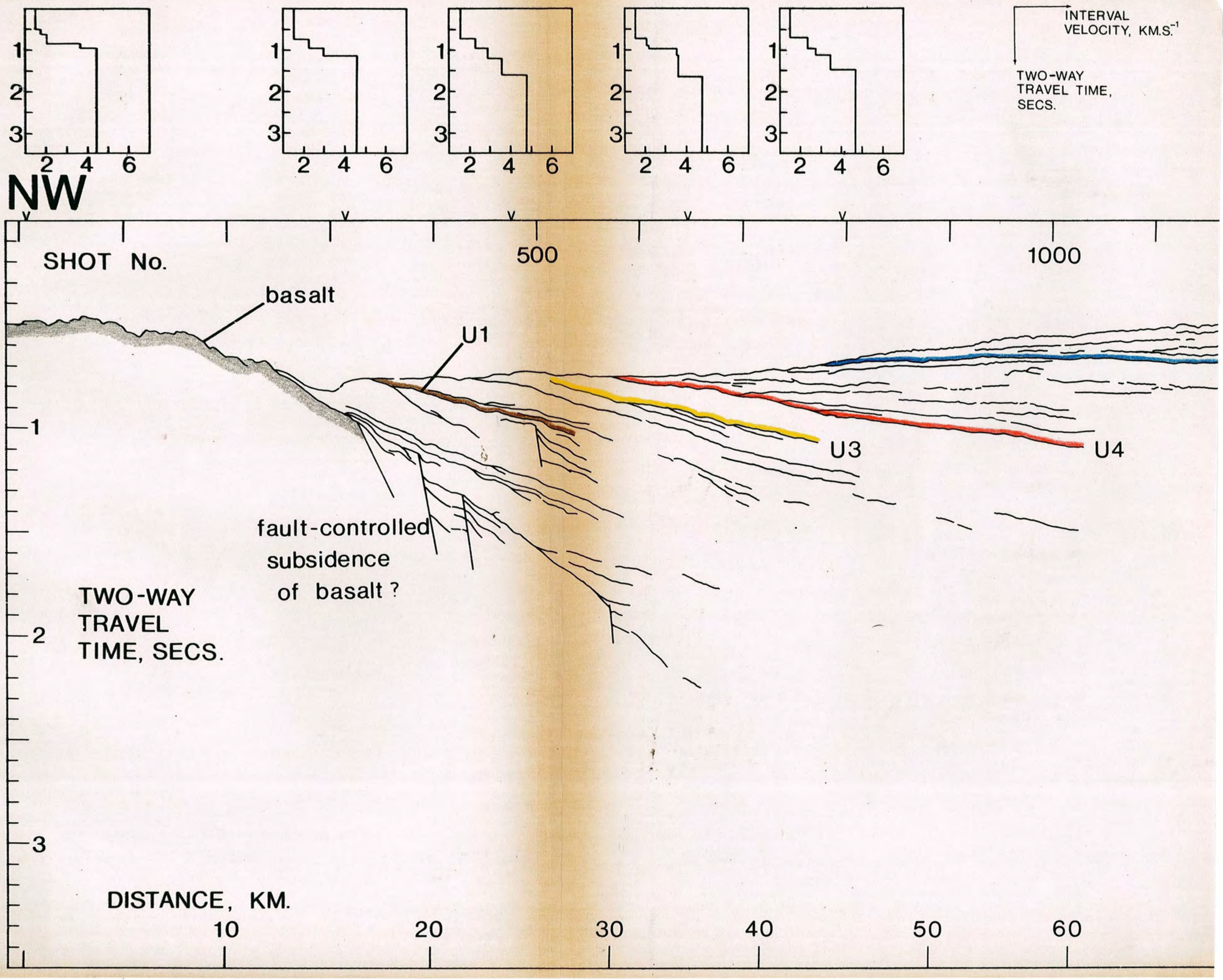
INTERVAL VELOCITY, KM.S.⁻¹
TWO-WAY TRAVEL TIME, SECS.
NW
SHOT No.
500
1000
basalt
U1
U3
U4
fault-controlled subsidence of basalt ?
TWO-WAY TRAVEL TIME, SECS.
DISTANCE, KM.
10
20
30
40
50
60

penetration represent the approximate limits of vertical seismic resolution. The two-way travel times corresponding to these bed thicknesses are about 10 and 25 ms respectively.

Sheriff (1976) emphasises that attributing stratigraphic significance to seismic details is a hazardous and incompletely understood procedure. Although no migrated seismic data or borehole information necessary for an accurate identification of reflecting horizons were available, an attempt was made to apply the principles of seismic stratigraphy (Payton, 1977) to the seismic section of profile 11.

Unconformity recognition was carried out by locating discordant relationships between reflectors characteristic of various depositional environments.

In discussing character and inter-relationships of seismic reflectors and inferring depositional history from them, three broad groups of sediments have been defined (Ewing et al, 1966; Eldholm and Windisch, 1974):

(1) pelagic sediments: usually thin, may show moderate stratification generally conformable with basement surface, acoustically very transparent due to isolation from sources of terrigenous detritus;

(2) homogeneous sediments: less specific origin, often weakly stratified, less transparent than pelagic deposits, may be quite thick;

(3) turbidites: smooth, highly stratified sequences of strong, reverberant reflections and penetration can be severely reduced due to their high reflectivity.

Seven unconformities were recognised on the seismic section. Correlation of sedimentary cycles with fluctuations in relative global sea level (Vail et al, 1977a) was attempted, subject to the constraints of known geological events onshore and the age of oceanic basement dated by recognition of oceanic magnetic anomalies offshore. In this way, a tentative stratigraphy has been developed.

Horizontal position on the seismic section is indicated by shot point (SP) number.

Horizon identification and the geological development of the continental margin along profile 11 are inferred as follows:

Horizon B

This horizon does not show a constant reflection signature and, with rare exception, represents the deepest recognisable reflector on the seismic section. Following Gairaud et al (1978), who distinguished three types of basalt marker horizon from good quality 24-fold coverage seismic reflection data by correlation with several DSDP boreholes (locations 337, 348 and 350) which reached basalt, horizon B has been interpreted as basalt. Between SP 2100 and SP 2480, and also SP 2660 to SP 2800, the general wavy, disturbed nature of the reflector is similar to that marker associated with basalt extrusions through tension cracks in the vicinity of the ocean-continent boundary south-east of the Jan Mayen Ridge (Gairaud et al, 1978). Its irregular surface may represent submarine pillow lavas, although well-defined diffraction hyperbolae characteristic of oceanic basement are absent. Interrupted reflectors are observed below this horizon at several locations (e.g. SP 2240).

Horizon B also appears as a relatively smooth, strong, laterally persistent reflector in the intervals SP 1800 to SP 1970, SP 2800 to SP 3150 and SP 3200 to SP 3580. Gairaud et al (1978) suggest that such a comparatively flat marker may be spread over a sedimentary unit and that it sometimes represents a tuff and volcanic breccia layer overlying basalt.

Irregular, hummocky sea floor topography to the north-west of SP 260 is interpreted as basalt. A high-amplitude, short-wavelength magnetic anomaly confirms this interpretation.

The position of the ocean-continent boundary, B along profile 11 is shown in Figure 4.2 and is inferred from Hinz and Schlüter (1980). The recognition of marine magnetic anomalies, the dating of oceanic crust, and the location of the ocean-continent boundary are discussed in Section 5.2.2. The important implication of the location of the continental margin on profile 11 is that horizon B is associated with continental crust to the NW of SP 1775 and with crust of oceanic affinity to the SE of SP 1775.

To the NW of SP 1775, horizon B, inferred to represent basalt on the basis of reflection character, is assumed to be related to the massive suite of plateau basalts along the Blosseville coast, situated about 30 km north-west of profile 11. The plateau basalts of East Greenland are known to be a Late Palaeocene-Early Eocene formation and probably span an age range of 52 - 55 Ma (Soper et al, 1976; modified to timescale of Hailwood et al, 1979; see Figure 1.4).

These basalts accumulated as a series of predominantly subaerial, laterally extensive, almost parallel flows in an approximately horizontal orientation (Deer, 1976). The individual flows are only rarely separated by erosional surfaces, coal seams and sediments and a continuous, uniform subsidence contemporaneous with lava effusion ensured that the upper surface of the lava succession was never far above sea level (Birkenmajer et al, 1976). A complete absence onshore of any intrusions representing likely feeders for the plateau basalts (eg Birkenmajer et al, 1976) has led to the proposal for an offshore lava source.

This major eruptive phase immediately preceded and probably continued throughout the initial stages of sea floor spreading between South East Greenland and the Rockall Plateau, and also the opening of the Norwegian Sea about the Aegir Ridge at anomaly 24 time (Soper et al, 1976). The plateau basalts were subsequently subjected to two important events.

Firstly, the formation of an anticlinal uplift centred on the Kangerdlugssuaq area, about 185 km WNW of SP 1 on profile 11. See Figure 1.1. The Kangerdlugssuaq dome (Brooks, 1973, 1979) is roughly elliptical with a NW-SE major axis and is some 200 km across. Brooks (1979) estimated a total uplift at the centre of the dome of the order of 6 km relative to present sea level but pointed out that this height was unlikely to have been actually attained due to isostatic rebound of the region as erosion stripped away successive rock layers. This domal uplift post-dated lava effusion, but convinced that dome and magmatism were related phenomena, Brooks (1979) proposed an age of formation similar to that of the alkaline magmas (e.g. the Kangerdlugssuaq syenite, 50.0 $\pm$ 0.4 Ma; Pankhurst et al, 1976). The erosion of the dome removed an estimated thickness of several kilometres of sediments and lavas at an early stage of its uplift in the Early Eocene and provided some 50,000 km^3 of sediment for deposition on the continental shelf (Brooks, 1979).

Secondly, the plateau basalts were subjected to a coastal flexure whereby both plateau and inland dome now plunge steeply below sea level in the coastal regions. Wager and Deer (1938) envisaged an enormous down-warp of the crust providing pronounced subsidence of the basalt lavas below sea level to form the submerged aseismic ridge in the Denmark Straits and corresponding uplift of the inland plateau to form the highest mountains in Greenland (up to 3700 m). Crustal flexure was associated with differential vertical movements of order 8 km (Haller, 1970). Nielsen (1975) proposed an alternative mechanism for coastal flexure in which a large scale pattern of marginal normal faults, dipping in both north and south directions caused rotation of fault blocks towards the coast and the variations of dip observed in the lavas. This interpretation is equivalent to the formation of a "half" graben structure parallel to the coast with fault-controlled subsidence towards the Denmark Straits. Coast-parallel Tertiary faulting has been recorded to the north in the region near Kap Dalton and Kap Brewster, south of Scoresby Sund (Birkenmajer, 1972) where individual faults downthrow by up to 2 km (Birkenmajer et al, 1976). The crustal flexure in the Kangerdlugssuaq region was associated with the intrusion of several generations of dyke swarms (Nielsen, 1978).

Brooks (1979) proposed an age of 50 - 55 Ma for the crustal flexure because it was observed to deform basalts and gabbroic intrusions (Skaergaard intrusion, 54.6 $\pm$ 1.7 Ma; Brooks and Gleadow, 1977) but not the later syenite intrusions (Kangerdlugssuaq syenite, 50.0 $\pm$ 0.4 Ma; Pankhurst et al, 1976). In Figure 1.4, an age of 50 - 52 Ma is given for the coastal flexure. The faulting observed in the Savoia Halvø district to the north (noted above) was a later event of possible Miocene age (Birkenmajer et al, 1976).

The formation of the Kangerdlugssuaq dome and the crustal flexure dominated subsequent patterns of sediment deposition on the continental margin.

The possibility of faulting affecting the basalt horizon between SP 300 and SP 600 is shown in Figure 4.2. A fault-controlled basalt contact is proposed in relation to its associated magnetic anomaly in Chapter 5. Continuation of the basalt horizon between SP 600 and SP 1800, a distance of some 80 km, is inferred but the exact nature of such a surface cannot be delineated from the seismic section due to poor data quality and absence of coherent reflectors in this zone for two-way travel times greater than 0.85 s. Spectral depth estimates based on an analysis of the magnetic anomaly along profile 11 were used in an attempt to trace the upper surface of the basalt over this interval (Chapter 5).

To the SE of SP 1775, horizon B is associated with oceanic crust. Vogt et al (1980) identified oceanic magnetic anomalies 13 to 22, related to spreading about the Reykjanes Ridge, in the Denmark Straits region and anomalies 6, 6A and 6B off the east coast of Greenland in the Norwegian

Sea associated with spreading about the Kolbeinsey Ridge. A fracture zone was inferred to separate these oceanic areas and in Chapter 5, it is speculated that the fracture zone intersects profile 11 at a shallow angle between SP 2480 and SP 2640 (Figure 5.7). The results of Chapter 5 will be quoted here without discussion.

Associated with crust of oceanic affinity formed by seafloor spreading, horizon B represents a diachronous surface and can only be assigned a unique age at a given location. Between SP 1775 and SP 2480, horizon B is associated with a wedge of oceanic crust to the north of the fracture zone and which probably contains subdued marine anomalies 7 through 18 (Nunns, 1980). Adjacent to the continental margin, the oceanic crust is likely to be about 41 Ma old, becoming younger to the SE but greater than 30 Ma old at SP 2480 (dates after Hailwood et al, 1979; Figure 1.4).

South-east of the proposed fracture zone, anomaly 13 has been projected onto profile 11 to intersect at about SP 2800 and this dates the oceanic crust at this point as 35 Ma old.

Before the recognition of the Denmark Straits fracture zone by Vogt et al (1980), the interpretation of the uplifted "horst" block between SP 2480 and SP 2640 was extremely puzzling. The absence of any obvious drape over this feature by contiguous pelagic sediments of Late Eocene to Late Oligocene (see horizon U1) suggested its fault-bounded uplift in Late Oligocene times. The reflection character on top of the horst is similar to the smooth, strong reflector of the basalt interface, B and the discontinuous, wavy appearance of weak reflections below it is like the interrupted reflectors observed below horizon B. However, the interpretation of the horst-like feature as uplifted basalt is not conclusively proved by the gravity or magnetic data (see Chapter 5). Also, the upthrown "horst" and associated faulting are not recognised on the neighbouring seismic profiles (see Section 4.4) and appear to be local features.

An alternative, if unlikely, explanation considered for the feature is salt or mud diapirism. Diapirs of Eocene siliceous oozes have been penetrated by drilling on the Voring Plateau (Talwani et al, 1976; Nilsen, 1978a). The undisturbed character of sediments above the "diapir" preclude its formation later than unconformity U1. This suggests its syn-depositional formation, sedimentation keeping pace with upward diapir growth (Stuart and Caughey, 1977). Flat-topped salt diapirs occur in the Campeche Fan area of the Gulf of Mexico (Ballard and Feden, 1970).

However, these proposals are dismissed in favour of the fracture zone hypothesis, put forward on the basis of the interpretation of marine magnetic anomalies by Vogt et al (1980), and this seems to be the simplest and most likely explanation for the structural feature between SP 2480 and SP 2640. Movement along the fracture zone associated with seafloor spreading and the creation of oceanic anomalies 7 through 18 in the wedge-shaped area of oceanic crust to the north of the fracture zone (Nunns, 1980) should have ceased about 27 Ma ago when the period of fan-shaped spreading about the Aegir Ridge in the Norwegian Basin stopped (Figure 1.4). The steep faulting defining the "horst" block and its associated normal faults only appear to affect unconformity U1 and older sediments (Figure 4.2). This observation is consistent with the proposed age of unconformity U1 and its correlation with a major lowstand in global sea level at 30 Ma indicated by Vail et al (1977b).

Horizon U1

Horizon U1 is a prominent reflector. It is tentatively identified as an unconformity on the basis of the onlap of weak, overlying reflectors between SP 2200 and SP 2400. Horizon U1 pinches out against horizon B at SP 3080 (cf. Nilsen, 1978a for the pattern of sedimentation during development of young ocean basins with special reference to the Norwegian-Greenland Seas).

The pinch-out of horizon U1 against horizon B occurs some 20 km south-east of the point of intersection along profile 11 of anomaly 13 and the line of the profile. Since anomaly 13 represents an age of about 35 Ma, it is argued in Chapter 5 that the oceanic crust beneath the pinch-out of horizon U1 is about 32 Ma old. Horizon U1 appears as a distinct marker on profile 11 and it is therefore tentatively correlated with the lowstand in global sea level proposed by Vail et al (1977b) in Late Oligocene times, 30 Ma ago (Figure 4.3).

The Greenland-Iceland-Faeroe aseismic ridge immediately to the south of profile 11 formed a land bridge between Greenland and Europe from Eocene to Middle Miocene times (Vogt, 1972; Talwani and Udintsev, 1976; Nilsen, 1978b; Grønlie, 1979) and therefore provided a major circulation barrier which prevented exchange of bottom water masses between the youthful ocean basin of the Norwegian Sea and open ocean of the Atlantic to the south. Circulation northwards was further restricted by the land bridge between Greenland and Svalbard (the De Geer route of Nilsen, 1978b) until opening of the Greenland Sea at about 36 Ma (Figure 1.4). Talwani and

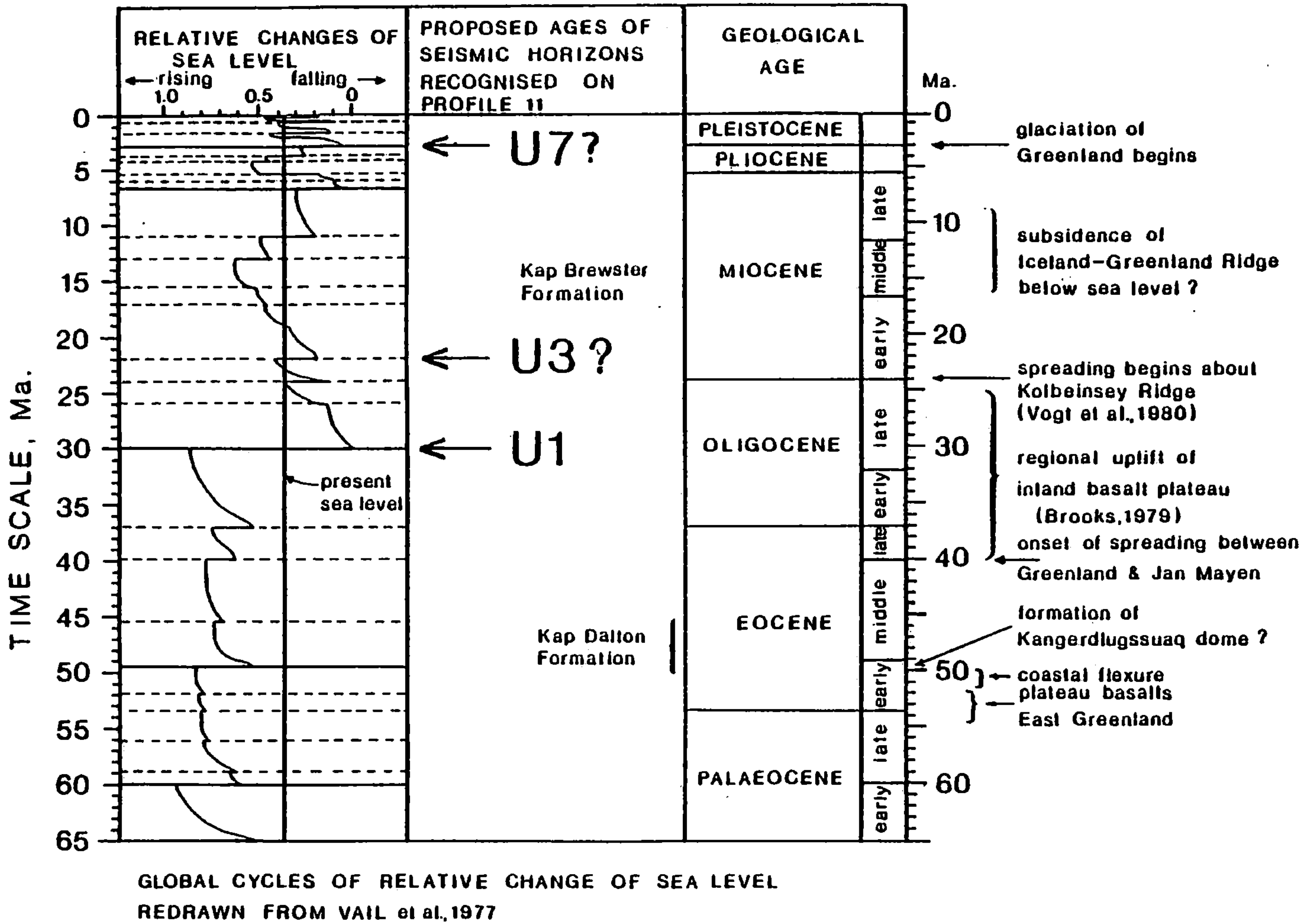

Figure 4.3 Correlation of geological events and unconformities with the global cycles of relative change of sea level during Tertiary time for the continental margin of East Greenland based on the seismic interpretation of profiles 11, 13 and 16.

Udintsev (1976) emphasise that the only circulation patterns existed with the North Sea and the basins of Northern Europe via a shallow sea extending over the Norwegian continental margin and Inner Vøring Plateau. This is substantiated by similarities in Eocene fauna from the Norwegian Sea and the North Sea and its environs.

Furthermore, parts of the Jan Mayen Ridge were at or above sea level from some time before the separation from East Greenland until Middle or Late Miocene times (Grønlie, 1979). Therefore, the wedge-shaped area of spreading, north of the Denmark Straits fracture zone and complementary to the fan-shaped spreading which took place in the Norwegian Basin about the Aegir Ridge between anomalies 7 and 20, represented a restricted basin. Such restricted depositional environments have been associated with formation of thick evaporite and black shale sequences in relatively deep water (Schmalz, 1969; Thiede, 1978).

The smoothness and lateral continuity of reflector B between SP 2850 and SP 3150 suggest subaerial basalt lava flow or tuff rather than the characteristically uneven surface of submarine pillow lavas with associated diffraction patterns. This interpretation is consistent with a land bridge between Greenland and Europe formed by the Greenland-Iceland-Faeroe Ridge. Profile 11 parallels the axis of the submerged Greenland-Iceland Ridge at a distance of about 130 km to the north-east.

Nilsen (1978b) points out that, for the Iceland-Faeroe Ridge, Eocene to Upper Oligocene marine sediments resting on basalts at DSDP Site 336 (Leg 38) situated on the north-east flank of the ridge clearly indicate that the ridge was subsiding before this time. A 30 m thick lateritic palaeosol overlying basalt at Site 336 and which was subsequently covered by microfossil-bearing marine mudstone, sandy mudstone and claystone of Middle Eocene to Late Oligocene age is described by Nilsen and Kerr (1978a, 1978b). Radiometric dates for the basalt horizon were determined as 40.4 $\pm$ 3.2 Ma and 43.4 $\pm$ 3.3 Ma (Talwani and Udintsev, 1976).

The disposition of reflectors in the sedimentary unit between horizon B and unconformity U1 is consistent with deposition in a gently subsiding basin. The structural "high" inferred by a series of dipping reflectors between SP 1800 and SP 2050 above horizon B is apparent structure associated with the rapid change in water depth over the continental shelf edge (Taner et al, 1970). The order of magnitude of this velocity "pull-up" phenomenon was estimated between SP 1840 and SP 2050 for a change in water depth of about 560 m over a horizontal distance of some 15 km. Assuming an average velocity of 2.5 km s^{-1} for the sediments beneath the shelf edge and a seismic velocity in water of 1.5 km s^{-1}, yields a velocity contrast of precisely 1.0 km s^{-1}. The difference, Δt in two-way travel time was estimated using the equation:

$$\Delta t = \frac{2d}{V_w V_s} (V_s - V_w) \qquad 4.2$$

where d = the differential water depth

V_s = the seismic velocity of the sediments

V_w = the seismic velocity of sea water.

Equation 4.2 gives an estimate of approximately 300 ms for the difference in two-way travel time for the parameters specified above. This effect and related lateral sediment velocity changes over the continental shelf edge due to greater compaction with increasing age and depth of burial westwards are probably wholly responsible for the apparent structure observed on the basalt interface (horizon B) and overlying sedimentary horizons prior to unconformity U3. Hence, the true dip of these horizons is probably to the west (cf. Grant, 1972).

The sediments beneath unconformity U1 are implied to be of Late Eocene to Late Oligocene age and therefore represent deposits possibly contemporaneous with the Kap Dalton Series, since the latter may range in age from Eocene to Oligocene (Henderson, 1976). The sediments of the Kap Dalton Series consist of sandstones, shales and tuffs with a marine fauna and at Kap Brewster, deposits of the same sequence are predominantly sandstones with some marls, and a basal conglomerate overlying a palaeosol horizon above Tertiary basalt (Henderson, 1976). The pre-unconformity U1 sediments are characterised by weak, wavy, relatively low amplitude reflectors and may indicate a more distal, pelagic sedimentation pattern in quiet marine conditions promoted by gentle subsidence. Jones et al (1970) associate a sequence of weakly stratified horizons with pelagic sedimentation in studies relating to sedimentary processes in the northern North Atlantic and Labrador Sea. Birkenmajer et al (1976) describe the Kap Dalton Formation as low-energy sediments emphasising the generally quiet depositional epoch prevalent at this time off the coast of East Greenland.

It is suggested that the earliest sequence of sediments deposited prior to unconformity U1 represents low-energy terrigenous sediment derived by erosion of the uplifted Kangerdlugssuaq dome since Early Tertiary relief along the Blosseville coast was subdued after cessation of basalt eruption (Brooks, 1979).

In the upper part of this sequence, several strong and continuous reflectors probably relate to phases of increased terrigenous input into the widening basin or to brief periods of non-deposition.

At about the same time as the onset of complementary seafloor spreading, north of the Denmark Straits fracture zone, associated with the anti-clockwise rotation of the Jan Mayen Ridge and the period of fan-shaped spreading in the Norwegian Basin, a large-scale regional uplift of the inland basalt plateau began and continued from Lower Oligocene until Miocene times (Brooks, 1979). The influx of relatively high-energy terrigenous sediments due to erosion of the uplifted basalts to the west may explain the more frequent occurrence of strong reflectors in the upper part of the pre-U1 sequence.

The identification of unconformity U1 between SP 340 and SP 540 is highly speculative. However, the increasing easterly dip with depth below this horizon is consistent with sediment accumulation along the boundary of a subsiding basin.

Roberts (1975) reported a similar sedimentary sequence in the Hatton-Rockall Basin beneath an unconformity, R4. Horizon R4 represents the top of Upper Eocene lithified oozes and was suggested to be of Upper Eocene - Late Oligocene age. Although the angular discordance of R4 increases towards the basin margins and the Late Eocene sediments may pinch out against basement, the Hatton-Rockall Basin is developed on continental crust of the Rockall Plateau (Roberts, 1975) and may not be strictly comparable to the conditions under which unconformity U1 was formed. R4 is also prominent in the Atlantic west of the Rockall Plateau where it has been observed to pinch out against oceanic crust dated from marine magnetic anomalies as 37 Ma old (Nilsen, 1978a).

Brooks (1979) emphasised the temporal separation between the coastal flexure and a subsequent episode of regional uplift during which the inland basalt plateau was elevated. These two separate events were originally considered contemporaneous by Wager (1947). The uplift occurred during the period from Lower Oligocene to Miocene, about 40 to 25 Ma ago (Brooks, 1979). According to the timescale of Hailwood <u>et al</u> (1979), a date of

40 Ma occurs in the Late Eocene (see Figure 1.4). Regional uplift was accompanied by severe, coast-parallel faulting along the northerly continuation of the crustal flexure, in the area south of Scoresby Sund (Birkenmajer et al, 1976; Brooks, 1979). This faulting episode probably relates to the onset of fan-shaped spreading in the Norwegian Basin resulting from the anti-clockwise rotation of the Jan Mayen Ridge. Rotation away from the East Greenland margin probably began about 41 Ma ago (Nunns, 1980).

Horizon U3

The regional uplift of the inland basalt plateau of East Greenland through Late Eocene to Miocene times caused the relatively quiet marine sedimentation with basin subsidence to be replaced by a prograding sequence of high-energy sediments.

The most well-developed marine onlap sequence between SP 1980 and SP 2240 is tentatively correlated with a surface of erosion truncating a succession of reflectors (between SP 580 and SP 750) interpreted as a coastal onlap series deposited during a relative highstand of sea level.

The thin Tertiary sequence between unconformities U1 and U3 west of SP 2500 is relatively stratified and represents a typical continental slope clastic facies deposited by turbidity currents. In contrast, the weakly stratified, almost transparent and homogeneous layer below unconformity U3 between SP 2940 and SP 3100 is interpreted as a sequence of distal sediments, deposited in relatively quiet marine conditions away from sources of terrigenous material.

The conspicuous escarpment at SP 3200 was originally interpreted as a normal fault, post-dating unconformity U3. The fault interpretation was made for the following reasons:

(1) the character of horizon B is similar on both sides of the fault;

(2) a thinned sequence of almost transparent material appears to the east of the fault, on the upthrown side. This was interpreted as possibly the same sedimentary facies as the distal deposits below U3 to the west of the fault plane;

(3) relatively well-bedded sediments overlying horizon U3 between SP 2900 and SP 3200 contain good reflectors attributed to terrigenous turbidites

with provenance to the east. This implies uplift of the landmass to the east and the likelihood of the subaerial erosion of the upthrown fault block.

However, this major basement step with a vertical magnitude of at least 800 m has been explained in terms of an abrupt increase in mantle-plume discharge and basalt magmatism about 25 Ma ago (Vogt, 1974). Talwani and Eldholm (1977) suggested that Iceland per se began to form in its present surface expression about 27 Ma ago, at the same time as seafloor spreading stopped about the Aegir Ridge. Vogt et al (1980) preferred to interpret the formation of the insular basement steps of Iceland as due to increased mantle-plume discharge rather than due to a westward jump in the spreading axis postulated by Talwani and Eldholm (1977).

Seafloor spreading about the Kolbeinsey Ridge began about anomaly 6C time (25 Ma ago) according to Vogt et al (1980) who dismissed the existence of the extinct Intermediate Iceland Plateau axis proposed by Johnson et al (1972) and Talwani and Eldholm (1977). Therefore, the most likely interpretation of the basement step at SP 3200 is as an escarpment formed about 25 Ma ago due to vigorous basalt magmatism in association with the onset of seafloor spreading about the Kolbeinsey Ridge. However, the basement escarpment is also observed on profiles 13 and 16 (Section 4.5) and the implied strike of this feature crosses oceanic anomalies 6B, 6A and 6 shown in Figure 5.7. The fault interpretation therefore cannot be ruled out but the sustained uplift of this basement feature is probably caused by proximity to Iceland and the formation of relatively thick Icelandic type crust by vigorous differentiation from anomalously low-density, hot upper mantle material beneath it (Bott, 1974).

Nunns (1980) suggested that the rate of spreading about the Aegir Ridge may have slowed down dramatically between anomalies 7 and 11. Vogt and Avery (1974) also indicate a marked decrease in spreading rate between 25 and 30 Ma ago for magnetic anomalies about the Reykjanes Ridge north of 56°N in the North East Atlantic. This provides an explanation for the close proximity of anomaly 13 (35 Ma) to the basement escarpment at SP 3200.

The observation of reflectors onlapping unconformities U1, U2 and U3 between SP 2000 and SP 2300 led to the idea that these horizons may represent surfaces upon which marine onlap has taken place. It is tentatively suggested that unconformity U3 correlates with the lowstand in global sea level at 22 Ma ago indicated in Figure 4.3 (Vail et al, 1977b). The proposed Early Miocene age for horizon U3 correlates well with the subsidence history of the Greenland-Iceland-Faeroe Ridge and its major impact on ocean circulation patterns in the North Atlantic ocean during Miocene times (Vogt, 1972).

Reflectors between SP 3100 and SP 3200, at about 1.6 s (Figure 4.2), outline a trough-like feature which interrupts horizon U3 and is interpreted as a marginal channel caused by the erosional action of strong bottom currents. In his reconstruction of topography along the Greenland-Iceland-Faeroe Ridge, Vogt (1972) indicated the location of a narrow, but relatively deep, submarine channel in the Denmark Straits to the west of Iceland about 10 Ma ago. The erosional channel incised into unconformity U3 alongside the basement escarpment on profile 11 is interpreted as being formed by the first strong currents flowing through the Denmark Straits in Early Miocene times, about 20 Ma ago, when the vigorous overflow of cold waters from the Norwegian Sea to the North Atlantic first began (Vogt, 1972). Bottom current velocities of Norwegian Sea overflow water of order 150 cm s^{-1} have been recorded in the Denmark Straits (Jones <u>et al</u>, 1970).

The date of onset of strong, bottom-scouring currents causing vigorous erosion at about 20 Ma ago correlates well with the proposed age of 22 Ma for unconformity U3.

<u>Sediments in the interval U3 - U7</u>

The Greenland-Iceland-Faeroe aseismic ridge continued to subside through Miocene times and probably sank below sea level in the Denmark Straits in Middle Miocene times (Vogt, 1972; Grønlie, 1979).

On the East Greenland margin, north-west of SP 2500, post-unconformity U3 sediments below horizon U7 appear to form a prograding sequence of sediments showing smooth, highly stratified layers of strong, reverberant reflections typical of continental slope turbidites (Ewing <u>et al</u>, 1966). Onlap and offlap relationships may be recognised and these formed the basis for unconformity recognition. No attempt has been made to correlate these horizons with the cycles of global sea level changes proposed by Vail <u>et al</u> (1977b) and illustrated in Figure 4.3.

Vogt <u>et al</u> (1980) note the locally extensive shelf prograding off the East Greenland margin and assign most of the deposition to have taken place during the last 3 Ma as a result of coalescing ice streams forming an "ice-delta". These ice streams are believed to have emanated from Kangerdlugssuaq Fjord south of the Denmark Straits and from Scoresby Sund to the north. The rôle of glaciation is discussed in connection with horizon U7. The contention of Vogt et al (1980) clearly conflicts with the interpretation of the present study and does seem to ignore major periods of uplift and erosion during the Tertiary emphasised by Brooks (1979). The truncation of seismic reflectors, especially horizons U1 and U3, against relatively well-dated basement features and oceanic magnetic anomalies lends support to the interpretation of this thesis.

This prograding sequence of sediments which accumulated over the likely range of between 3 and 22 Ma ago (Figure 4.3) is approximately contemporaneous with deposition of the Kap Brewster Formation. The basal conglomerate, sandstones and coarser clastics (Henderson, 1976) of this formation contain an abundant shallow-marine to littoral fauna and are of probable Miocene age (Birkenmajer, 1972).

South-east of SP 2700 along profile 11, the reflectors in the U3 - U7 interval are less well-stratified, although the sedimentary sequence overlying horizon U3 between SP 2950 and SP 3100 shows good bedding. There is evidence of post-depositional instability and slumping may have occurred between SP 2800 and SP 2980.

Some reflectors above horizon U3 between SP 2800 and SP 3000 show chaotic relationships and this sequence marginal to the basement escarpment at SP 3200 may have been deposited and/or reworked by strong bottom currents flowing southward and over the Greenland-Iceland Ridge into the Irminger Sea. These contour-following bottom currents and their action parallel to the coastline or submarine barrier contrast with the turbidity current deposits of a sedimentary sequence prograding in the direction normal to the continental slope. The increasing influence of contour currents formed by the southward overflow of cold Norwegian Sea waters as the subsidence of the Greenland-Iceland-Faeroe aseismic ridge continued in Miocene times is emphasised by Vogt (1972) and the erosional effect of such contour currents is illustrated by Featherstone (1976). It is possible that the post-U3 sedimentation south-east of SP 2800 on profile 11 has been dominated by the action of fast-flowing bottom currents or contour currents (from an original suggestion by Bott, pers. comm.). Progradation of the Iceland margin represented by the basement step at SP 3200 on profile 11 is not apparent, in contrast to sediment accumulation to the north and south-west of Iceland respectively (Vogt et al, 1980).

Horizon U7

Substantial erosion is inferred to have taken place in order to establish this unconformity since steeply-dipping reflectors associated with a prograding sequence of sediments are truncated and subcrop beneath it between SP 1500 and SP 1900 (Figure 4.2). Vigorous erosion may have been caused by the onset of fast-flowing contour currents as the Greenland-Iceland Ridge continued to subside below sea level in Middle Miocene times (Vogt, 1972; Grønlie, 1979).

However, it is probable that unconformity U7 was formed by glaciation. Greenland is considered to have become glaciated at the beginning of the Pleistocene (Brooks, 1979). The scouring action of glacial ice may have created erosional truncation of underlying beds between SP 800 and SP 1900. The overlying sediments may represent glacial seabed deposits transported to the continental shelf by glaciers or deposited offshore by melting icebergs. The sediments show horizontal stratification in contrast to the deposits below horizon U7.

The relatively deep water over the continental shelf of order 300 m is possibly a factor weighing against the formation of unconformity U7 by glacial ice. However, the present thickness of the Greenland Ice Sheet is about 2000 m and Gregersen (1971) gives a thickness of 2500 m for ice covering the inland Greenlandic Shield estimated from surface wave dispersion studies. Bearing in mind this thickness of ice and the extensive nature of glaciation during the Ice Ages of the Pleistocene, the formation of unconformity U7 by glacial scour and the subsequent deposition of stratified glacial marine sediments is not ruled out.

It is interesting to note the change in seabed character over the proposed glacial marine deposits. The smooth seafloor sedimentary horizon gives way to a small scale bottom roughness and this is typically associated with faster currents (Schneider et al, 1967).

Similar features appear above the basement escarpment of the Iceland Plateau between SP 3340 and SP 3580 and horizon U7 is speculatively indicated, overlain by presumed glacial seabed deposits.

The poor quality of the seismic record between SP 1000 and SP 1800 below 0.9 s has prevented reliable seismic interpretation in this zone of discontinuous, irregular reflectors. However, one feature is important.

At SP 1500, the sediments below unconformity U5 appear to form an anticlinal structure not seen in younger sediments above. This may be simply a topographic expression of the unconformity or it may indicate diapirism or intrusion from below.

4.4 The significance of interval velocities along profile 11

The results of velocity analysis carried out prior to CDP stacking appear above the seismic display of Enclosure 2 and interval velocities are shown graphically in Figure 4.2. Velocity functions were not evaluated between consistent pairs of reflectors and this devalued their usefulness in correlating lithological units on the basis of interval velocity.

However, by linear interpolation between stacking velocity values, the stacking velocities to horizons of interest were estimated for velocity functions 8 through 15 along profile 11 (Enclosure 2). Stacking velocities to the seafloor and horizons U3, U1 and B respectively were estimated. Assuming that the stacking velocities were approximately equivalent to root mean square (RMS) velocities, the Dix equation (Dix, 1955) was used to give a first order estimate of the interval velocities. The mean values of interval velocity for the 3 sequences of interest were calculated to be:

U3 → SEAFLOOR	2.07 ± 0.10 km s^{-1}
U1 → U3	2.63 ± 0.27 km s^{-1}
B → U1	3.98 ± 0.59 km s^{-1}

It was necessary to assess the effect on interval velocity values of the sub-optimal CDP stack (see Figure 4.1) whereby a shot interval of 50 m was assumed to provide nominal 11-fold coverage. In practice, a <u>minimum</u> value for the actual shot interval was 65 m. A likely speed of 6.5 knots along ship's track yields a maximum shot interval of some 70 m.

Stacking velocities estimated from seismic traces within a given CDP gather conform to a hyperbolic relationship of the form:

$$T^2 = T_o^2 + \frac{x^2}{V_{ST}^2} \qquad 4.3$$

where T_o = vertical incidence two-way travel time

V_{ST} = stacking velocity

and T = two-way travel time for shot-receiver offset, x.

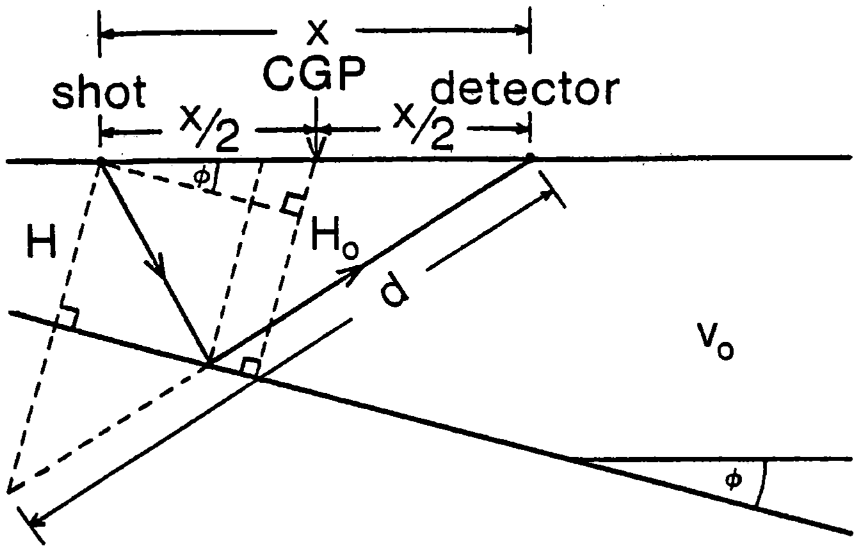

by the cosine rule,

$$d^2 = 4H^2 + x^2 + 4Hx.\cos(\phi + 90^\circ)$$

if T = two-way travel time,

$$T^2 = \frac{4H^2}{v_o^2} + \frac{x^2}{v_o^2} + \frac{4Hx.\sin\phi}{v_o^2}$$

however, $H = H(x)$

hence, $H = H_o - \frac{x}{2}\sin\phi$

by substitution and re-arranging, then

$$T^2 = \frac{4H_o^2}{v_o^2} + \frac{x^2\cos^2\phi}{v_o^2}$$

and if v_a = apparent velocity,

$$\boxed{v_a = \frac{v_o}{\cos\phi}}$$

Figure 4.4 Derivation of Equations 4.4 and 4.5 respectively, showing the effect of a single dipping reflector on the stacking velocity.

The stacking velocity is generally equated to RMS velocity and assuming horizontal, plane, parallel interfaces, the interval velocity of each seismically defined layer is calculated using the Dix equation (Dix, 1955). Sheriff (1976) points out that high quality RMS velocity values are required for reliable interval velocity estimates and he stresses that uncertainty in interval velocity calculations is always appreciably greater than for the RMS velocities used in the computation. Interval velocities calculated over intervals less than 200 ms are generally unreliable (op. cit.).

The effect of a single dipping reflector is illustrated in Figure 4.4, and for a horizon dipping at an angle, ϕ the Equation 4.3. becomes

$$T^2 = \frac{4\,H_o^{\,2}}{V_o^{\,2}} + \frac{x^2 \cos^2\phi}{V_o^{\,2}} \qquad 4.4$$

Symbols are defined in Figure 4.4. Hence, apparent velocity, V_A is given by

$$V_A = \frac{V_o}{\cos\phi} \qquad 4.5$$

For a conventional CDP gather in the presence of dipping reflectors, the "common depth point" becomes a function of offset and is replaced by the concept of a "common ground point" (CGP) (Taner and Koehler, 1969). The value of apparent velocity, V_A due to dip <u>always</u> increases for a CGP stack and is independent of updip or downdip shooting for a given value of H_o.

However, the nominal CGP stack carried out on the seismic data of profile 11 was subject to a systematic error in the position of the CGP due to an incorrect shot interval of 65 - 70 m. Using the symbols defined in Figure 4.5, the value of H_o in Equation 4.4 becomes a function of offset, x, dip of reflector, ϕ and direction of shooting relative to the dipping reflector. This is quantified as follows:

$$\begin{array}{ll} \text{DOWNDIP SHOOTING} & H_{on} = H_o - (n-1)\,\Delta h \\ \text{UPDIP SHOOTING} & H_{on} = H_o + (n-1)\,\Delta h \end{array} \qquad 4.6$$

where n = the streamer channel number which directly fixes offset, x for a marine survey.

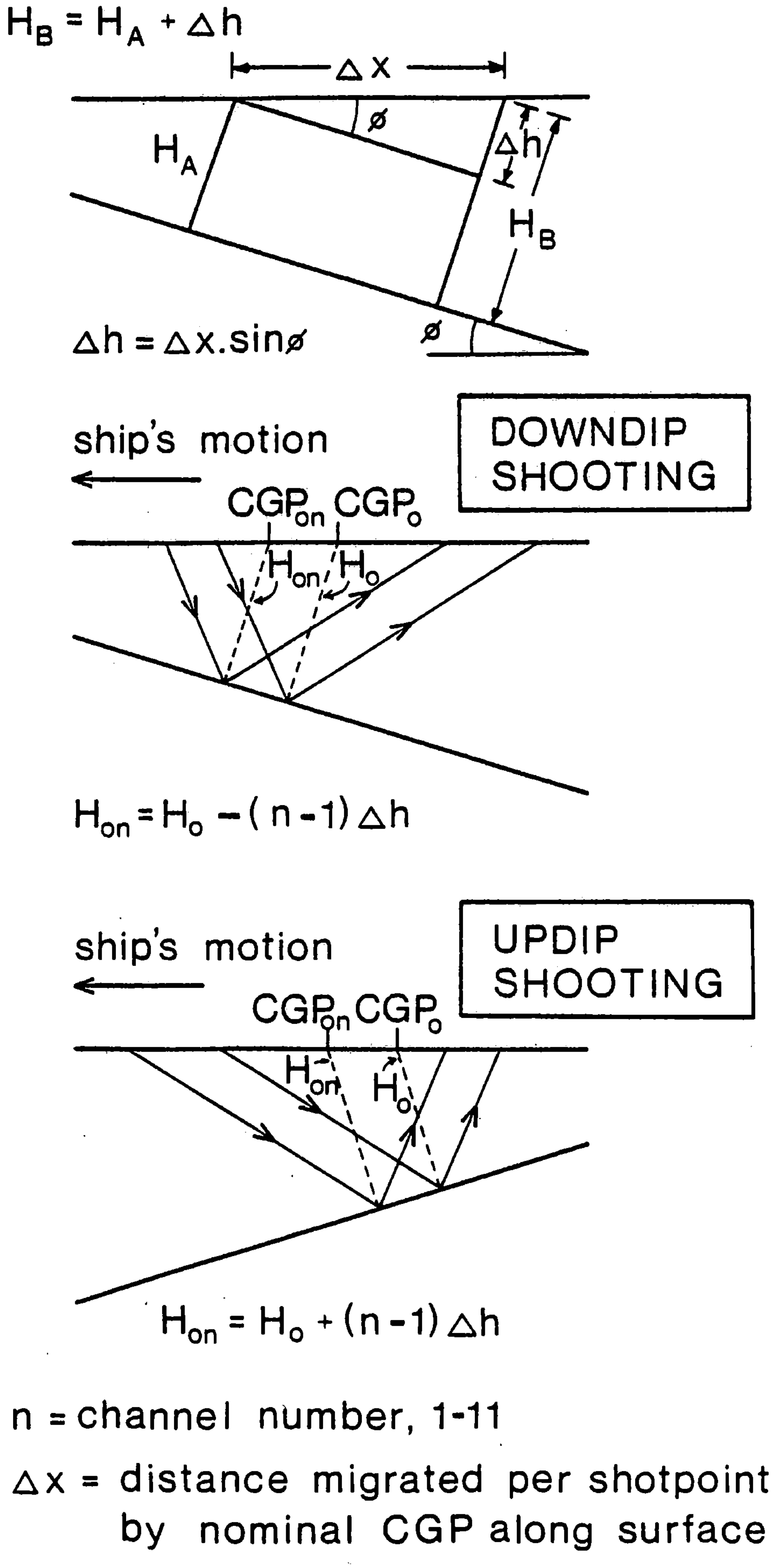

Figure 4.5 Definition of symbols used to assess the effect of incorrect shot interval on stacking velocity estimates.

The offset, x remained unchanged and correct due to the fixed geometry relating the airgun source and the hydrophone streamer.

The importance of the systematic migration of CGP along the surface is shown for a specific example in Figure 4.6.

An attempt was made to quantify further this effect by selecting a range of velocities, V_o and angles of dip, ϕ and calculating the appropriate apparent velocities, V_A for updip and downdip shooting assuming a fixed value of H_o = 2000 m. The results are shown in Figure 4.7a. Apparent velocity, V_A was estimated by making a $T^2 - X^2$ plot for each set of values of H_o, ϕ and V_o and a straight line of slope $1/V_{ST}^2$ was fitted through the data by the method of least squares. The ratio V_A/V_o was then calculated and was plotted against angle of dip, ϕ for updip and downdip shooting. The results are shown in Figure 4.7b. The variation of V_A/V_o for true CGP coverage is plotted for comparison. The factor of $1/\cos\phi$ from Equation 4.5 is swamped by the effects of CGP migration.

The important result emerges that the stacking velocities, and the interval velocities calculated from them via the Dix equation, are likely to be substantially in error for the processed data of profile 11 except where estimated over horizontal, plane, parallel reflecting horizons. The effects for a series of dipping reflectors will be more complex but the single inclined reflector serves to illustrate the effect of CGP migration.

As an illustrative example, Table 4.1 gives the effect of both downdip and updip shooting, as defined in Figure 4.5, on the interval velocities quoted above for the three intervals U3 → SEAFLOOR, U1 → U3 and B → U1 respectively. Constant values of H_o = 2000 m and Δx = 15 m are assumed for the case of parallel layers with constant dip.

The probable systematic errors in interval velocity values estimated from dipping horizons due to CGP migration are important when trying to infer lithology on the basis of interval velocity and also when correlating sedimentary units along profile 11 and with other sequences observed on adjacent profiles.

Furthermore, Grow et al (1979) emphasise the importance of target depth relative to the length of hydrophone streamer used to conduct the seismic survey. Interval velocities estimated for depths equal to 3 times the length of the streamer may be inaccurate by 15% or more. The high

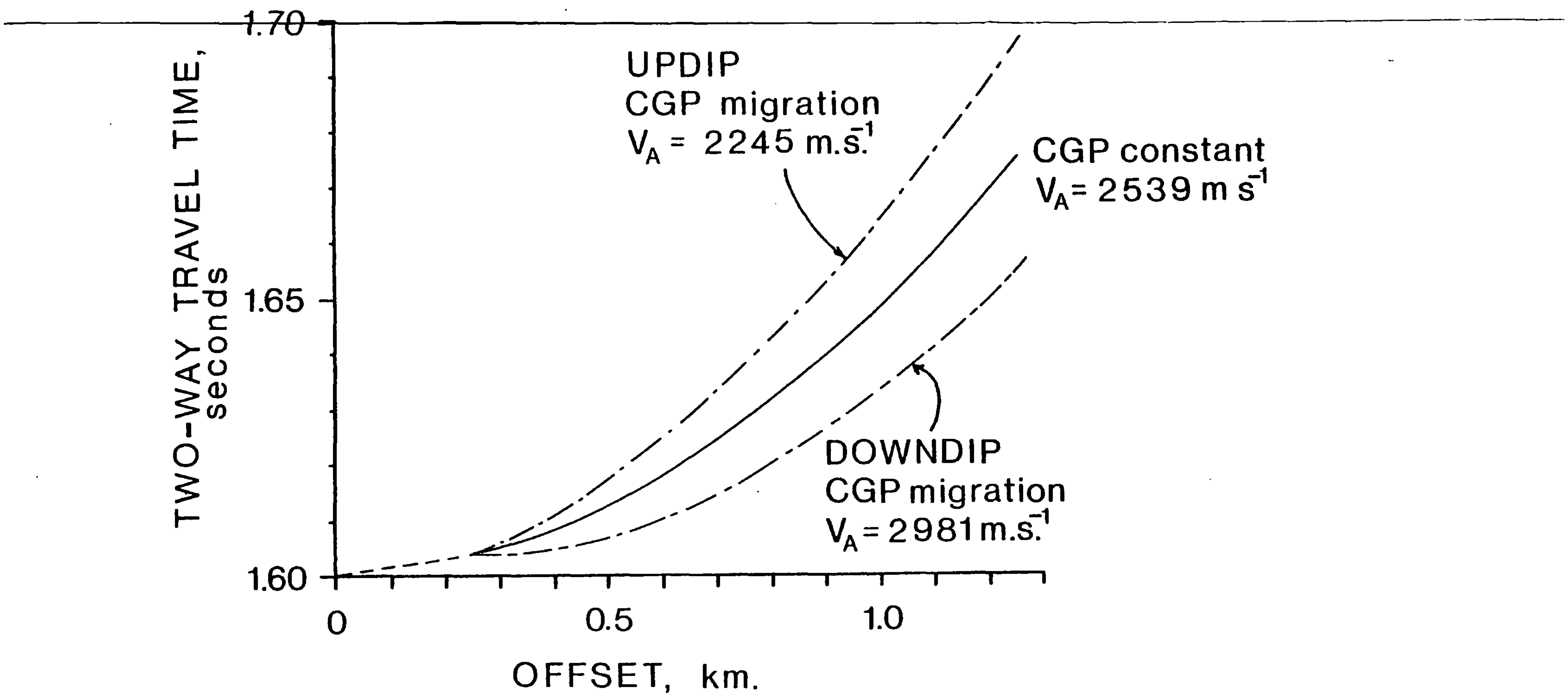

Figure 4.6 The effect upon stacking velocities of CGP migration along the surface of the profile. The curves are drawn for Ho = 2000m, Vo = 2500 m s^{-1}, Δx = 15m and angle of dip, ϕ = 10°.

H_o = initial value of H_{on} for n=1 in Equations 4.6.

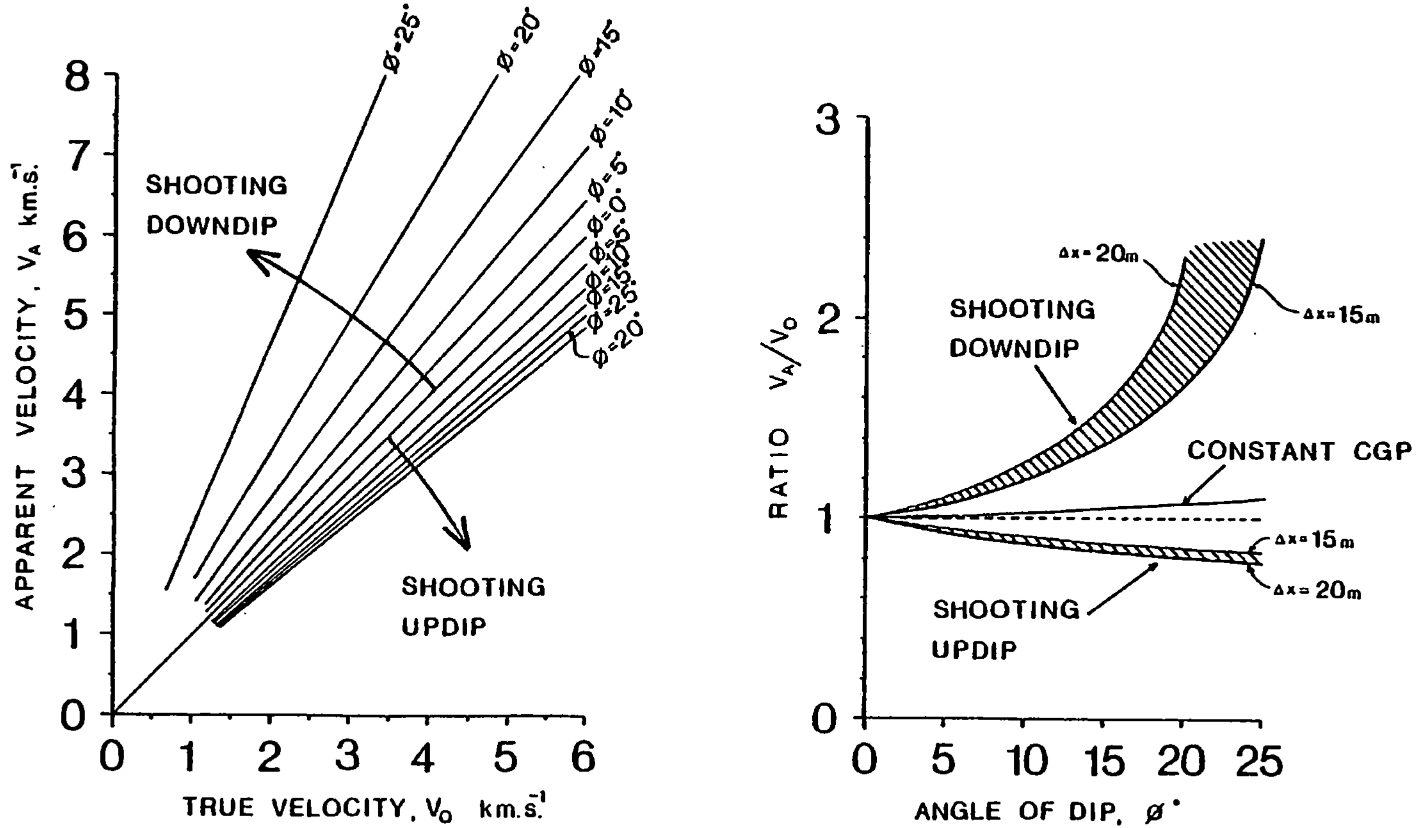

Figure 4.7 Effect of systematic CGP migration along the sea surface for Ho = 2000m,
(a) Relationship of V_A and Vo for various angles of dip, Ø for updip and downdip shooting.
(b) Variation of ratio V_A/Vo with angle of dip, Ø for a correct CGP gather and for updip and downdip shooting for the case of CGP migration.

TABLE 4.1

The Effect of CGP Migration on Interval Velocities Estimated from Stacking Velocities Along Profile 11 (for velocity functions 8 through 15).
H_o = 2000 m, Δx = 15 m

INTERVAL	SIMPLE DIX ESTIMATE OF INTERVAL VELOCITY km s^{-1}	CORRECTED VALUE FOR INTERVAL VELOCITY ASSUMING CONSTANT DIP, H = 2000 m, Δx = 15 m					
		DIP = 2^o		DIP = 5^o		DIP = 10^o	
		UPDIP SHOOTING	DOWNDIP SHOOTING	UPDIP SHOOTING	DOWNDIP SHOOTING	UPDIP SHOOTING	DOWNDIP SHOOTING
U3 → SEABED	2.07±0.10	2.11	2.01	2.20	1.94	2.30	1.74
U1 → U3	2.63±0.27	2.68	2.55	2.80	2.46	2.92	2.21
B → U1	3.98±0.59	4.06	3.86	4.23	3.72	4.42	3.35

velocity layers between SP 1900 and SP 2240 on profile 11 are at least 3 km below sea level, whilst the length of the streamer was 1100 m. This factor decreases the reliability of the interval velocities still further.

4.5 Interpretation of single-channel seismic monitor records

The single-channel seismic monitor records were not processed in any way. Therefore, the sea-bottom multiple event tended to obscure primary reflections, especially in relatively shallow water, and each primary signal consisted of several cycles due to the bubble pulse oscillation of the airguns. Without deconvolution, these strong arrivals overprint subsequent primary events and preclude a detailed analysis of the seismic record. Inter-bed multiples could easily masquerade as primary arrivals. These factors degrade the reliability of any interpretation and caution has been exercised in drawing intricate conclusions from these data.

The location of the profiles in the present survey is shown in Figure 1.1.

Line diagram interpretation of the two seismic profiles north of profile 11 is shown in Figure 4.8. Two horizons are tentatively identified and correlated with horizon B and unconformity U3 respectively on profile 11. Horizon B on profiles 13 and 16 represents the lowest identifiable reflector and therefore may not always correlate with a basaltic interface.

Identification of unconformity U3 is based on reflection character and velocity information. The general absence of coherent, strong reflectors in the transparent layer beneath U3 is similar to the Oligocene sediments beneath horizon U3 south-east of SP 2800 on profile 11. The velocity data from two sonobuoy stations, 13V28 and 14V28 (Figures 4.8 and 4.13) were projected on to profiles 13 and 16 as indicated in Figure 4.8. The correlation of interval and refraction velocities in ms^{-1} is proposed as follows:

	Profile 11	Profile 16 (13V28)	Profile 13 (14V28)
mostly MIOCENE and PLIOCENE sediments	2086	1800	1780
UNCONFORMITY, U3			
OLIGOCENE sediments	2590	2520	2550
HORIZON B?			
	?	4500	-

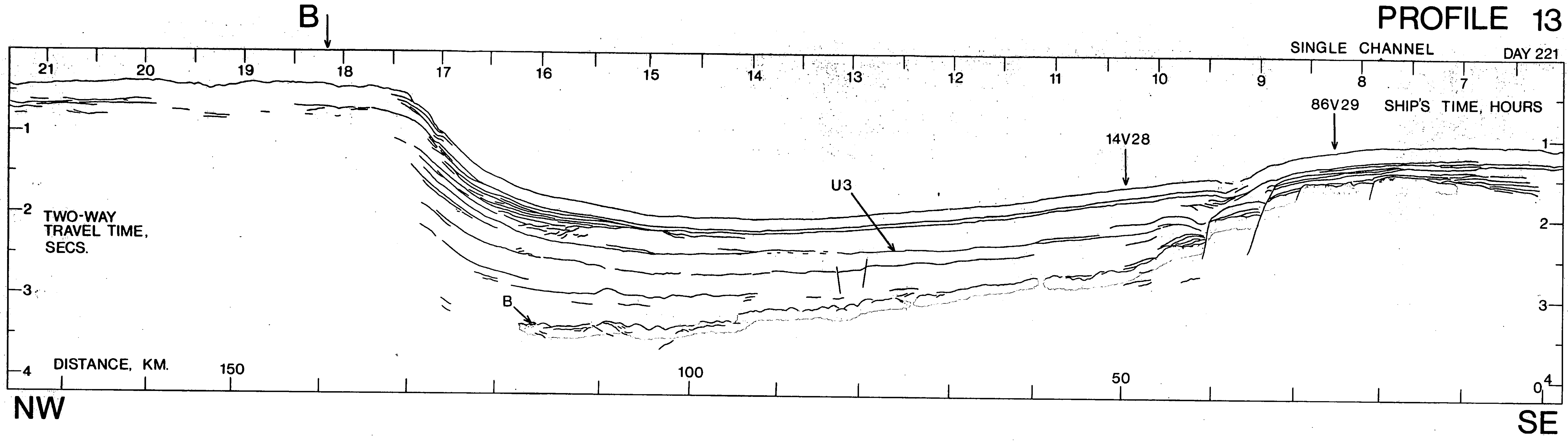
B
PROFILE 13
SINGLE CHANNEL
DAY 221
21
20
19
18
17
16
15
14
13
12
11
10
9
8
7
86V29
SHIP'S TIME, HOURS
14V28
U3
1
2
3
4
TWO-WAY
TRAVEL TIME,
SECS.
B
DISTANCE, KM.
150
100
50
0
NW
SE

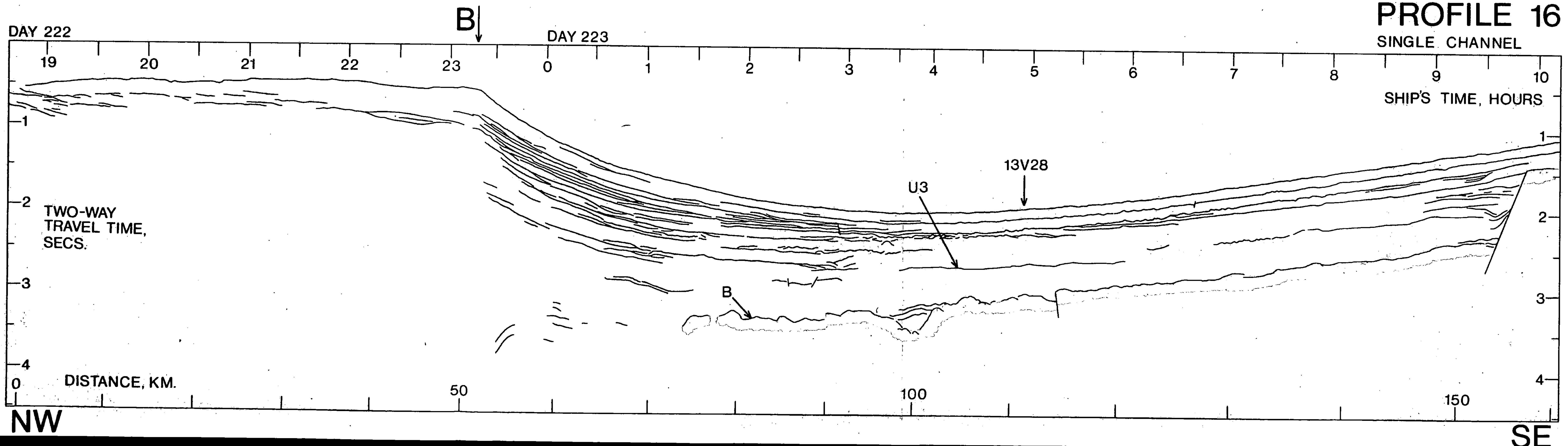
B
PROFILE 16
DAY 222
DAY 223
SINGLE CHANNEL
19
20
21
22
23
0
1
2
3
4
5
6
7
8
9
10
SHIP'S TIME, HOURS
13V28
U3
TWO-WAY
TRAVEL TIME,
SECS.
B
DISTANCE, KM.
0
50
100
150
NW
SE

Figure 4.8 Interpretation of single-channel seismic reflection data for profiles 13 and 16. The ocean-continent boundary, B is inferred from Hinz and Schluter (1980). The projected locations of sonobuoys 13V28, 14V28 and 86V29 are also shown (see Figure 1.2).

The interval velocity values for profile 11 were estimated from stacking velocity functions 13 through 15 (Enclosure 2) re-picked as described in Section 4.4 for the intervals U1 → U3 and U3 → SEAFLOOR respectively. The mean interval velocity, corrected for downdip shooting along parallel interfaces dipping at constant angle of 1° to the north-west (estimated from the dip of the seabed), for each interval is shown above.

Gairaud et al (1978) identified an unconformity, Horizon A, on the Jan Mayen Ridge which was dated as the contact between Upper Eocene and the Oligo-Miocene at the site of the DSDP 349 borehole. The interval velocities above Horizon A were 1.7 - 2.0 km s^{-1} and below the unconformity were 2.2 - 3.3 km s^{-1}. These authors state that the series underlying their Horizon A appeared to have undergone intense erosion in a subaerial environment.

Nunns (1980) has tentatively proposed an age of 30 Ma for Horizon A of Gairaud et al (1978), corresponding to its formation during the major fall in sea level in the Late Oligocene (Figure 4.3; Vail et al, 1977b). Since parts of the Jan Mayen Ridge were above sea level until the Miocene (Grønlie, 1979), only limited circulation was probably possible between the waters of the Norwegian Basin and the restricted basin formed by the complementary zone of seafloor spreading during the anti-clockwise rotation of the Jan Mayen Ridge away from Greenland between anomaly 18 and anomaly 7 time (discussed in Chapter 5, and after Nunns, 1980). The interpretation of unconformity U1 (Figure 4.3) implies that its time equivalent horizon to the east of the Jan Mayen Ridge is Horizon A of Gairaud et al (1978). The relatively high interval velocity of about 3.98 $\pm$ 0.59 km s^{-1} for sediments below unconformity U1 off the East Greenland margin probably reflects the greater influx of terrigenous detritus during the interval of deposition relative to contemporaneous deposits on the eastern flank of the Jan Mayen Ridge.

Two important structural observations were made on profiles 13 and 16:

(1) the fracture zone between SP 2480 and SP 2640 on profile 11, and its associated faulting to the west, were not identified;

(2) the basement escarpment at SP 3200 on profile 11 continues northwards and intersects profile 16 as a prominent scarp at about 156 km (Figure 4.8). However, between 20 and 45 km along profile 13 still

farther north, the major scarp degenerates into a series of apparently faulted blocks stepping down to the north-west. The absolute depth of the scarp-bounded basement plateau increases northwards from a two-way travel time of about 1.1 s on profile 11 to at least 1.5 s on profile 13. This possibly reflects the decreasing influence to the north of the thermal anomaly associated with Iceland. The major basement scarp has no topographic expression at the seafloor on profiles 11 and 16 but a shallow erosional channel has developed, associated with the westernmost, downfaulted (?) block on profile 13 between 33 and 40 km.

The pattern of sedimentation established in detail for profile 11 (Section 4.4) is also seen in its general aspects on profiles 13 and 16. The dominant influence of terrigenous detritus derived from the west is clearly seen in the form of prograding Tertiary sediments forming the continental slope of East Greenland and the general offlap of distal sediments on to horizon B, especially evident on profile 13 (Figure 4.8).

The recognition of marine magnetic anomalies 6B, 6A and 6 off the East Greenland coast north of the Denmark Straits by Vogt et al (1980) has inferred the age of oceanic crust along profiles 13 and 16. The oceanic anomalies are indicated in Figure 5.7. In particular, anomalies 6A and 6 impose very tight restrictions on the maximum age of unconformity U3. Extrapolating anomaly 6A on to profile 16 yields an age of about 23 Ma for the basement scarp at the SE extremity of the profile. The intersection of anomaly 6 on profile 13 coincides with the lowest basement step whose north-western edge occurs at 40 km along the profile and the age of material forming the step is therefore about 21 Ma (Figure 1.4). Horizon U3 has been tentatively correlated with a lowstand in sea level at 22 Ma (Figure 4.3) and is observed to offlap onto the basement scarp of profile 16 (with the development of an erosional channel similar to that on profile 11, Figure 4.2) and to offlap against the basement step of horizon B in profile 13. This tight control on the maximum age of horizon U3 seems to confirm the tentative correlation of Figure 4.3.

To the south of the submerged aseismic ridge, four seismic sections were interpreted and line diagrams are shown in Figures 4.9, 4.10, 4.11 and 4.12. Profile locations are indicated in Figure 1.1.

The Greenland-Iceland-Faeroe Ridge was a land bridge until its probable submergence in Middle Miocene times (Vogt, 1972; Grønlie, 1979)


NW
SE
DAY 217
SHIP'S TIME, HOURS
PROFILE 7
SINGLE CHANNEL
B
small-scale bottom roughness
119V30
12V28
B
TWO-WAY
TRAVEL TIME,
SECS.
DISTANCE, KM.
11
12
13
14
15
16
17
18
19
20
21
22
23
0
1
2
3
4
5
6
7
8
1
2
3
50
100
150
200
250

and presented an effective barrier to circulation between the Norwegian Sea and Atlantic Ocean. Therefore, correlation of sedimentary horizons north and south of the aseismic ridge was not anticipated although similarities in depositional style were apparent.

Immediately to the south of the aseismic ridge, profile 7 (Figure 4.9) shows a prograding wedge of Tertiary clastic sediments. Individual reflectors within the sequence dip eastwards with increasing steepness towards the shelf edge. The lateral extent of the prograding beds over a distance of some 180 km is emphasised by Brooks (1979) who attributes the exceptional width of the continental shelf here to erosion of the Kangerdlugssuaq dome throughout the Tertiary and predicts the occurrence of sediments as a prograding mantle on the continental slope. This is precisely what is observed on profile 7. Sediment transport would have been predominantly to the south and south-east. Subsequent Quaternary glaciation has eroded and scoured the shelf. The fast-flowing Norwegian Sea overflow currents have prevented further sedimentation on the shelf itself. The small-scale bottom roughness is probably caused by a combination of the erosional truncation of dipping beds and the action of bottom currents (Schneider et al, 1967).

Profile 5 shows the continental shelf and slope consisting of prograding sediments (Figure 4.10). A tentative location for the ocean-continent boundary, B is indicated at 110 km along the profile. This separates the irregular interface of the basaltic horizon of oceanic layer 2 to the east from the continental crustal material consisting of metamorphics and probably Mesozoic sediments to the west. This boundary is not clearly defined. Roberts (1975) notes that the transition from oceanic to continental basement is not marked by a major change in reflection character in the Rockall Trough. The "basement" (?) feature to the south-east of the proposed ocean-continent boundary, between 70 and 110 km, is implied to be a ridge of oceanic material. Similar topography on oceanic basement has been reported adjacent to the continental rise of eastern North America by Emery et al (1970).

Recognition of unconformities was tenuous. A tentative horizon separating an Early Tertiary sequence of transparent pelagic (?) sediments from an overlying sequence of stronger, more persistent reflectors is shown in Figure 4.10. This may correlate with horizon R4 of widespread occurrence in the North Atlantic region west of the Rockall Plateau (Nilsen, 1978a).


NW
SE
Day 215
17
16
15
14
13
12
11
10
9
8
7
6
5
4
3
2
SHIP'S TIME, HOURS
PROFILE 5
SINGLE CHANNEL
marine offlap
R4 ?
B?
marine onlap
pinch-out dated by marine anomaly 18 at 40-41 my.
R4 ?
D
B
?
TWO-WAY TRAVEL TIME, SECS.
1
2
3
4
DISTANCE, KM.
150
100
50

Figure 4.10 Interpretation of single-channel seismic reflection data for profile 5. The ocean-continent boundary, B is inferred from the recognition of marine magnetic anomalies in Chapter 5.

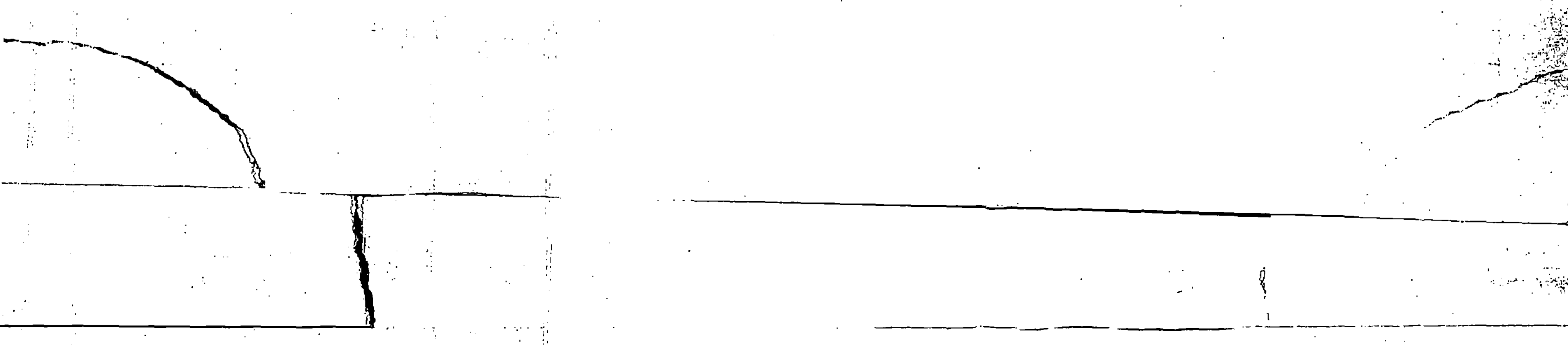

The angular discordance of the sedimentary horizon, D culminates in a pinch-out against oceanic "basement" dated as 40 - 41 Ma old from the marine magnetic anomaly 18 identified along the profile (Figure 5.7). This dates the underlying sediments to the north-west as Early to Middle Eocene.

The seabed exhibits several erosional channels along profile 5 at distances of 45, 50,70 and 98 km respectively.

The two profiles farther south, profile 3 (Figure 4.11) and profile 1 (Figure 4.12) show a distinctive wedge of prograded Tertiary sediments with a steeper continental slope (about 7^{o} compared to 2^{o} on profile 5 and 3^{o} on profile 7) carved back by the erosion caused by contour currents (Featherstone, 1976). These currents arise from the overflow of Norwegian Sea bottom water (1) through the Denmark Straits and (2) via the Faeroe-Shetland Channel, along the Gardar Ridge, then north-eastwards along the Reykjanes Ridge and finally turning south-westwards along the East Greenland margin in the Irminger Sea (for example, Nilsen, 1978a).

The position of the ocean-continent boundary, B has been marked on profiles 3 and 1 in Figures 4.11 and 4.12. The location was chosen as that point separating an irregular reflector to the east attributed to basalt of oceanic layer 2, and a smoother reflecting horizon to the west, possibly representing continental "basement" (magnetic anomalies were also used to identify the ocean-continent boundary - see Chapter 5). Eastward dipping seismic reflectors were indicated below the continental horizon on profile 3 between 156 and 165 km. These reflectors may indicate the presence of pre-Tertiary, probably Mesozoic, sediments deposited in a subsiding basin prior to seafloor spreading between Greenland and Rockall Plateau (cf. Featherstone, 1976). The steeply dipping reflectors between 0 and 30 km along profile 3 may also represent eroded Mesozoic sediments truncated at the seabed by glacial action.

The "basement" ridge-like feature located between 70 and 95 km on profile 1 may only be apparent. Its appearance, if it does exist, is certainly enhanced by a velocity "pull-down" effect immediately to the west due to the marginal channel observed above it at the seafloor (cf. Taner et al, 1970). Using Equation 4.2, a differential water depth of 375 m and a sediment velocity, V_S of 1.8 to 2.0 km s^{-1}, the difference in two-way travel time through sea water relative to the sediment would produce a "pull-down" of some 83 to 125 ms in reflectors beneath the erosional channel.


NW
SE
DAY 214
19
20
21
22
23
0
1
2
3
4
5
6
7
8
9
10
11
12
13
SHIP'S TIME, HOURS
PROFILE 3
SINGLE CHANNEL
coastal onlap
marine offlap
B
R4
B
TWO-WAY
TRAVEL TIME,
SECS.
1
2
3
4
DISTANCE, KM.
50
100
150
200

Figure 4.11 Interpretation of single-channel seismic reflection data for profile 3. The ocean-continent boundary, B is inferred from the recognition of marine magnetic anomalies in Chapter 5.

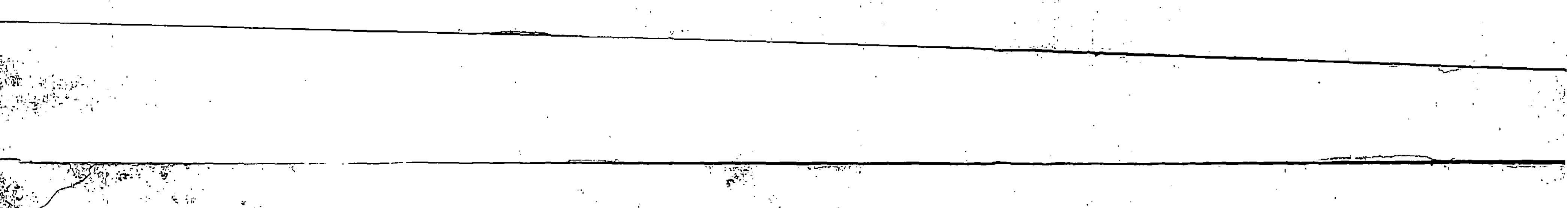

NW
SE
DAY 213
DAY 212
SHIP'S TIME, HOURS
PROFILE 1
SINGLE CHANNEL
TWO-WAY
TRAVEL TIME,
SECS.
DISTANCE, KM.
marine offlap
B
R4
B

Figure 4.12 Interpretation of single-channel seismic reflection data for profile 1. The ocean-continent boundary, B is inferred from the recognition of marine magnetic anomalies in Chapter 5.

The possible presence of reflector, R4 is shown on profiles 1 and 3, although the contrast between transparent, pelagic sediments overlain by well-stratified turbidites is not always convincing on the unprocessed shipborne monitor records.

The unconformity, U recognised to the east of the continental scarp along the East Greenland margin by Featherstone (1976) and Featherstone et al (1977) was not observed on the single-channel seismic records of profiles 1, 3, 5 and 7 to the south of the Denmark Straits. Unconformity U was considered to have been formed by the action of deep ocean contour currents originating as cold Norwegian Sea overflow water spilling over the Denmark Straits as the Greenland-Iceland-Faeroe Ridge subsided below sea level during Miocene times (Featherstone et al, 1977; Vogt, 1972). It was argued (op. cit.) that unconformity U separated marginal sediments below from a sequence of younger, oceanic sediments deposited as contourites to the east where the current velocity was reduced and active erosion was replaced by deposition. The presence of contour current sediment deposits away from the rapid current velocity regime of the continental slope is highly probable.

4.6 Refraction velocities along the continental margin of East Greenland

Seismic velocities derived from various disposable sonobuoy refraction and wide-angle reflection studies on the East Greenland continental margin and in the Norwegian Sea are shown schematically in Figure 4.13a and numerical values for selected locations are given in Figure 4.13b. The sonobuoy stations are identified in Figure 1.2.

The existence of major accumulations of Mesozoic, and possibly Palaeozoic, sediments has been predicted on the Vøring Plateau of the Norwegian margin (Talwani and Eldholm, 1972; Sellevoll, 1975), on the Jan Mayen Ridge (Talwani and Udintsev, 1976), on the Barents Shelf (Eldholm and Ewing, 1971) and southern Barents Sea area (Sundvor, 1975), on the Hebridean continental margin (Jones, 1978) and on the East Greenland continental margin (Johnson et al, 1975a). These predictions were made primarily from seismic velocities derived from disposable sonobuoy refraction experiments. A critical assumption was made that Tertiary sediments have velocities less than 2.5 km s^{-1}. This was based on evidence provided by Hornabrook (1967) and Wyrobeck (1969) that Tertiary sediments in the North Sea seldom exceed a velocity of 2.25 km s^{-1}, even when buried at great depths. Wyrobeck (1969) emphasised that the velocities found in the North Sea are only appropriate

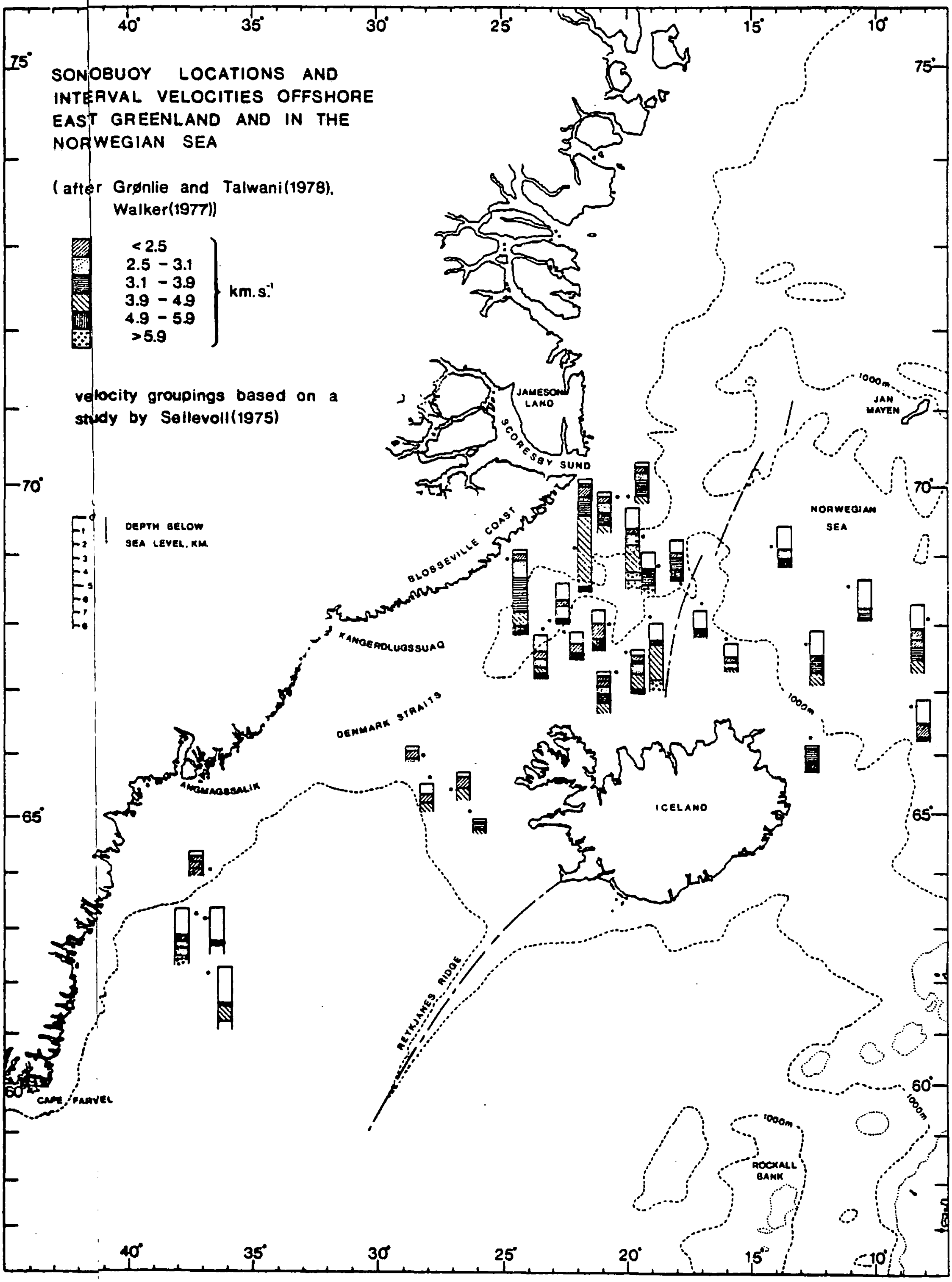

Figure 4.13(a) Interval velocities deduced from sonobuoy refraction studies on the East Greenland margin and in the Norwegian Sea.

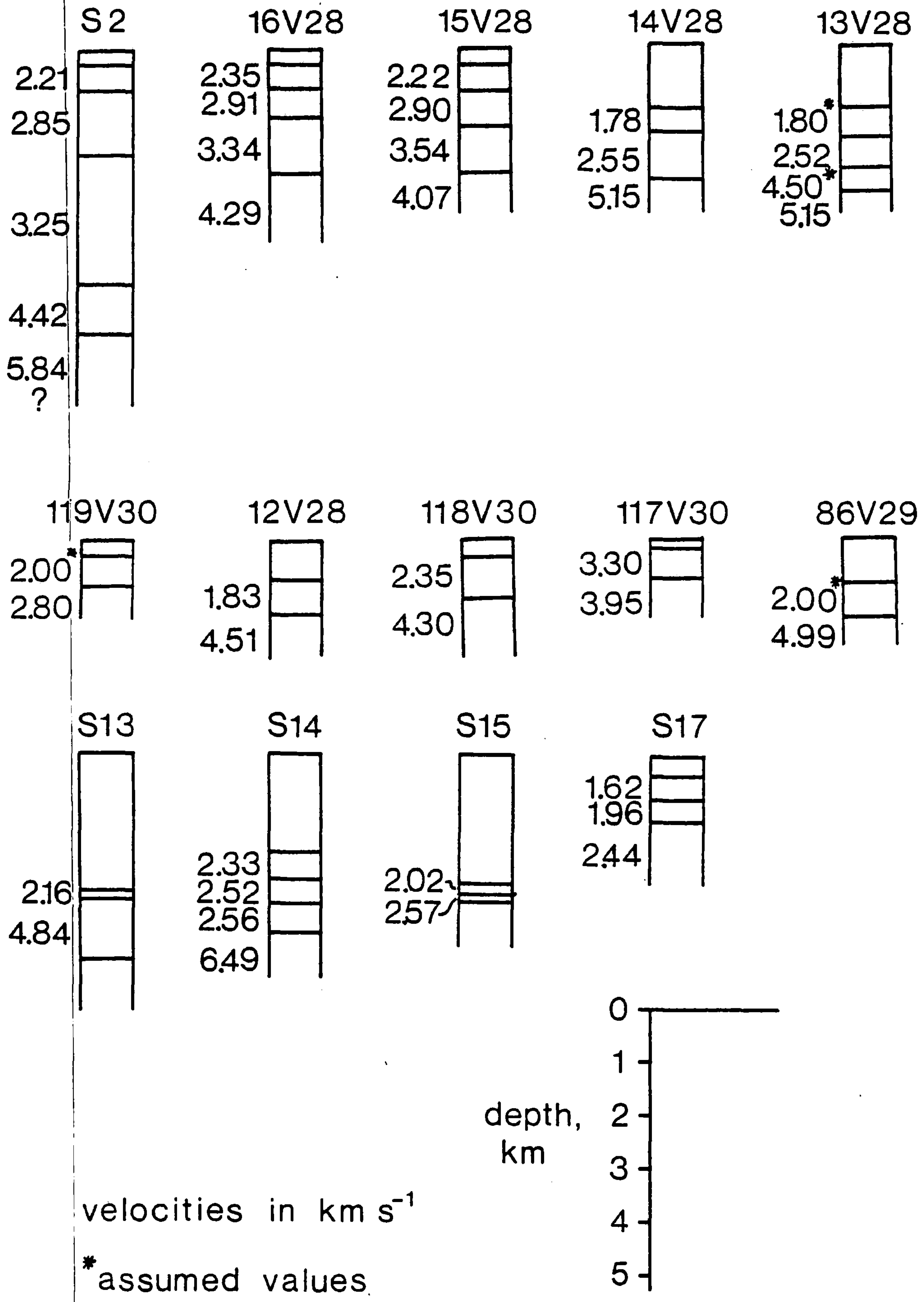

Figure 4.13(b) Sonobuoy refraction profiles for selected locations along the East Greenland continental margin (after Walker, 1977 and Gronlie and Talwani, 1978).

for comparison with surrounding areas which belong to the same northern European Permian Basin. Callomon et al (1972) indicated a narrow seaway between East Greenland and western Norway continuous with the Permian Basin of northern Europe in Permian times and which persisted more or less throughout the Mesozoic era. However, the extrapolation of North Sea sediment velocity-age relationships to the East Greenland continental margin must be considered highly tenuous. Lateral facies changes, differential rates of accumulation and burial, contrasting lithologies derived from different provenance and subsequent tectonic history impose major constraints on velocity-age interpretation extrapolated over even short distances.

In particular, Johnson et al (1975a) use two sonobuoy profiles, 15V28 and 16V28 (Eldholm and Windisch, 1974; Figures 1.2 and 4.13) to infer the presence of about 2.3 km of low velocity sediments (2.22 - 3.54 km s^{-1}) of presumed Tertiary and Mesozoic age overlying a "basement" of well-lithified Mesozoic or Palaeozoic strata of velocity 4.2 km s^{-1}.

However, the recognition of oceanic anomalies 6B, 6A and 6 to the west of sonobuoy locations 15V28 and 16V28 by Vogt et al (1980) implies that the sequence of refraction velocities must be associated with sediments and rocks of Tertiary age only.

The results of the sonobuoy experiment, S2 carried out during the 1977 Durham cruise are shown in Figure 4.13b. The original interpretation was made on the light-sensitive paper output from the shipborne Geospace digital seismic monitor recorder.

The refraction velocities 2.21, 2.85 and 3.25 km s^{-1} are interpreted as representing Tertiary sediments of cumulative thickness 4.1 km. Velocity-depth relationships for the Permian Basin of northern Europe and the North Sea, extrapolated from Wyrobeck (1969), are illustrated in Figure 4.14a. Typical velocity-depth curves for clastic and carbonate rocks and salt are shown in Figure 4.14b (after Sheriff, 1976).

Grow et al (1979) report seismic units of inferred Tertiary age with interval velocities from 1.7 to 2.7 km s^{-1}, increasing with age and depth of burial beneath the continental shelf and slope between Cape Hatteras and Cape Cod. Roberts (1975) gives an interval velocity of 2.8 km s^{-1} for an Oligocene chert sequence in the Hatton-Rockall Basin. Keen and Barrett (1972) used velocity data obtained by reversed refraction shooting and

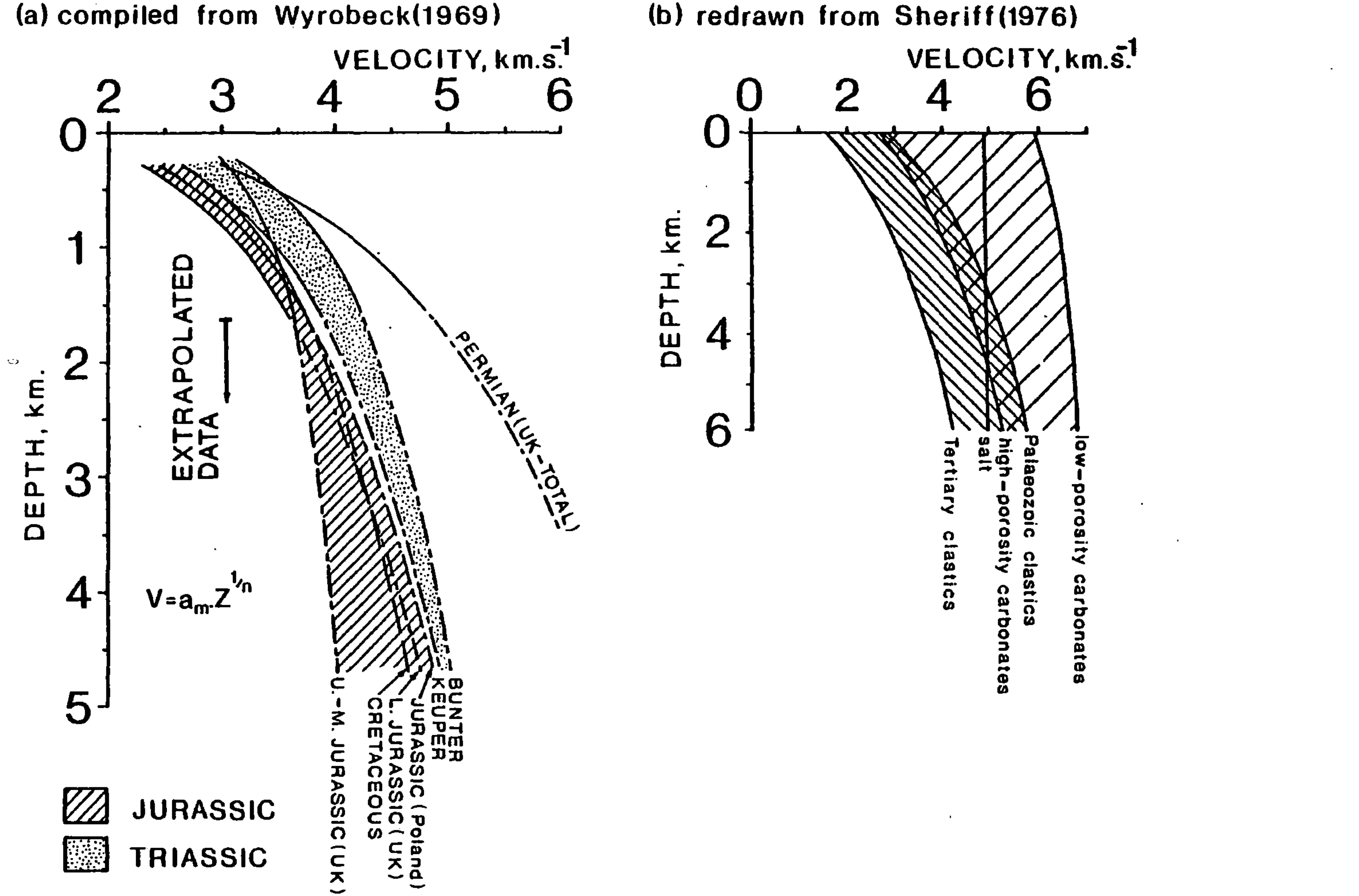

Figure 4.14(a) Velocity-depth relationships of the Permian basin of Northern Europe, including the North Sea and extrapolated beyond a depth of 1.5km using the regression curves of Wyrobeck (1969). (b) Diagram of typical velocity-depth relations redrawn from Sheriff (1976).

disposable sonobuoy techniques to identify two sedimentary units in Baffin Bay:

(1) unconsolidated and semi-consolidated sediment, 1.9 to 3.2 km s^{-1};

(2) consolidated sediment, 3.9 to 4.2 km s^{-1}.

Since seafloor spreading commenced in Baffin Bay at the same time as that in the Norwegian Sea at almost anomaly 24 time (Srivastava, 1978), these sediments must represent Tertiary units.

To illustrate further the wide fluctuations in interval velocities observed in Tertiary sediments, the following velocity relationships, based on well tie-ins, sonobuoy and two-ship refraction profiles, were assumed (Milliman, 1979) for the continental margin off Brazil:

1.7 - 2.1 km s^{-1}	post-Miocene
2.5 - 3.5	Miocene
3.8 - 4.4	Oligocene
4.6 - 5.2	Eocene

Gairaud et al (1978) obtained interval velocities in the range 1.7 to 3.3 km s^{-1} for Tertiary sediments on the Jan Mayen Ridge. These data illustrate the wide range of Tertiary sediment interval and refraction velocities observed at various localities and lend general support to the proposed interpretation.

The 4.42 km s^{-1} refractor of sonobuoy S2 (Figure 4.13b) is interpreted as the upper surface of Palaeocene-Eocene plateau basalt (about 1 km thick). A spectral depth estimate to magnetic sources below the line of the sonobuoy profile supports this conclusion (Section 5.2.1).

Palmason (1963, 1965) reports the results of seismic refraction experiments which gave average velocities of 4.16 and 5.06 km s^{-1} for Tertiary flood basalts in Iceland and 3.9 and 4.9 km s^{-1} for Tertiary basalts in the Faeroe Islands. Smythe et al (1978) have argued a similar case for the existence of Palaeocene-Eocene basalts on the Hebridean continental margin on the basis of a high velocity refractor of 4.4 ± 0.3 km s^{-1}.

The proximity of the onshore Tertiary plateau basalt province and the evidence for major downfaulting to the east (Birkenmajer, 1972; Birkenmajer et al, 1976) support this proposal. This contradicts the view of Johnson et al (1975a) who believed that the extrusive volcanic province south of Scoresby Sund did not extend offshore more than a few kilometres. The subdued magnetic signature offshore is explained in terms of basalt down-faulting and burial under a prograding sequence of Tertiary sediments. This interpretation is analagous to that proposed by Keen and Barrett (1972) for the continuity of basalts, downfaulted by several kilometres, from Cape Dyer across the Davis Strait sill in southern Baffin Bay, off West Greenland.

The probable continuation of the plateau basalts offshore is discussed in Chapter 5 in relation to the magnetic anomaly and the above interpretation is confirmed.

The refraction velocity of 5.84 km s^{-1} on sonobuoy S2 (Figure 4.13b) is tentatively interpreted as indicating continental metamorphic basement. A velocity of 5.8 km s^{-1} was measured by Keen and Barrett (1972) to the east of the Melville Bay graben (West Greenland) in an area of rough bottom topography without any sedimentary overburden. A possible correlation of this horizon with Precambrian basement rocks exposed on nearby islands was suggested. Refraction velocities from 5.62 to 6.54 km s^{-1} were attributed to Lower Palaeozoic or Precambrian metamorphic basement rocks on the continental margin off Labrador and eastern Newfoundland by Grant (1972). In particular, "basement" velocities of 5.80, 5.86 and 5.87 km s^{-1} were recorded, amongst others, in the above range.

The location of sonobuoy S2 is situated to the west of the ocean-continent boundary proposed by Larsen (1980), shown in Figure 5.7 and this lends further support to the proposed continental nature of the "basement" refractor.

The velocity profiles in the Norwegian Sea have largely been interpreted in terms of oceanic crustal models proposed and discussed by Ewing and Ewing (1959), Clague and Straley (1977) and Detrick and Watts (1979). Ewing and Ewing (1959) carried out refraction experiments in the Norwegian and Lofoten Basins and reported an oceanic layer 2 average velocity of 5.2 km s^{-1} (ranging from 4.96 km s^{-1} to 5.37 km s^{-1}) and of thickness between 2.5 and 3.0 km. This was underlain by a high velocity layer of average value 7.5 km s^{-1}.

The sonobuoy profiles associated with the Greenland-Iceland Ridge are interpreted in terms of a sequence of Tertiary sediments resting upon subaerially extruded flood basalts. In particular, the 4.51 km s^{-1} refractor of sonobuoy 12V28, the 4.30 km s^{-1} refractor of sonobuoy 118V30 and the 3.95 km s^{-1} refractor of sonobuoy 117V30 (Figure 4.13b) are inferred to represent the upper surface of Tertiary flood basalts on the basis of velocity correlation with the results of Palmason (1963, 1965) and Smythe et al (1978). This implies a sediment thickness of at least 600 m on this flank of the Greenland-Iceland Ridge.

Sonobuoy S14, situated almost precisely on the proposed ocean-continent boundary (Figure 5.7) on the South East Greenland margin provides a velocity of 6.49 km s^{-1}. The sonobuoy station is landward of the proposed ocean-continent boundary and this velocity is interpreted in terms of metamorphic continental basement, compatible with the standard continental crust velocity of 6.36 km s^{-1} proposed by Worzel (1974) (cf. Grant, 1972). Gregersen (1971) obtained an upper crustal P-wave velocity of 6.25 km s^{-1} from surface wave dispersion studies of the Greenlandic Shield.

The velocity of 4.84 km s^{-1} in profile S13 is interpreted as oceanic layer 2B (Clague and Straley, 1977). This velocity is consistent with a suite of refraction velocities ranging between 4.35 and 5.55 km s^{-1} for oceanic "basement" in the western North Atlantic (Houtz and Ewing, 1964).

It must always be remembered that seismic velocities alone lend themselves to ambiguous interpretation as indicated by the range of overlapping velocities in Figure 4.14. Alternative interpretations are always possible.

CHAPTER 5

MAGNETIC AND GRAVITY INTERPRETATION

5.1 Introduction

Methods developed for the interpretation of magnetic and gravity data were proposed and discussed in Chapter 3. In this chapter, the results of applying those techniques to the potential field data are presented and their geological significance relative to seismic reflection data discussed in Chapter 4 assessed.

5.2 Magnetic interpretation

In order to assess the extent of magnetic storms during the Durham cruises of 1973, 1974 and 1977, magnetogram records from two observatories located within the auroral zone were obtained.

Magnetic data collected on the continental margin of South East Greenland during 1973 and 1974 were visually correlated with observatory records from Narssuarssuaq (Figure 2.9). In addition to a large amplitude magnetic storm between Julian days 231 and 234 (1974) and a short-lived magnetic storm on day 202 (1973), reported by Featherstone (1976) having inspected magnetograms from Eskdalemuir and Lerwick, the Narssuarssuaq records revealed further disturbances caused by precession of the auroral oval and related ionospheric current phenomena. In particular, the magnetic low deduced as delineating the ocean-continent boundary (B-B', Figure 5.6) was affected by magnetic disturbances at the following times:

1973 Day 200 (2100 hrs) - Day 201 (0600 hrs)
Day 202 (0 - 0300 hrs)
Day 204 (0100 - 1200 hrs)
1974 Day 239 (2300 hrs) - Day 240 (0800 hrs).

However, these disturbing magnetic effects do not appear to invalidate the conclusions of Featherstone (1976) and Featherstone <u>et al</u> (1977).

Magnetogram records from Leirvogur and Narssuarssuaq observatories (Figure 2.9) were obtained to check the 1977 magnetic survey data. The extent of magnetic disturbances is indicated along the profile data of Appendix A. The extensive sunspot activity (Waldmeier, 1978) produced

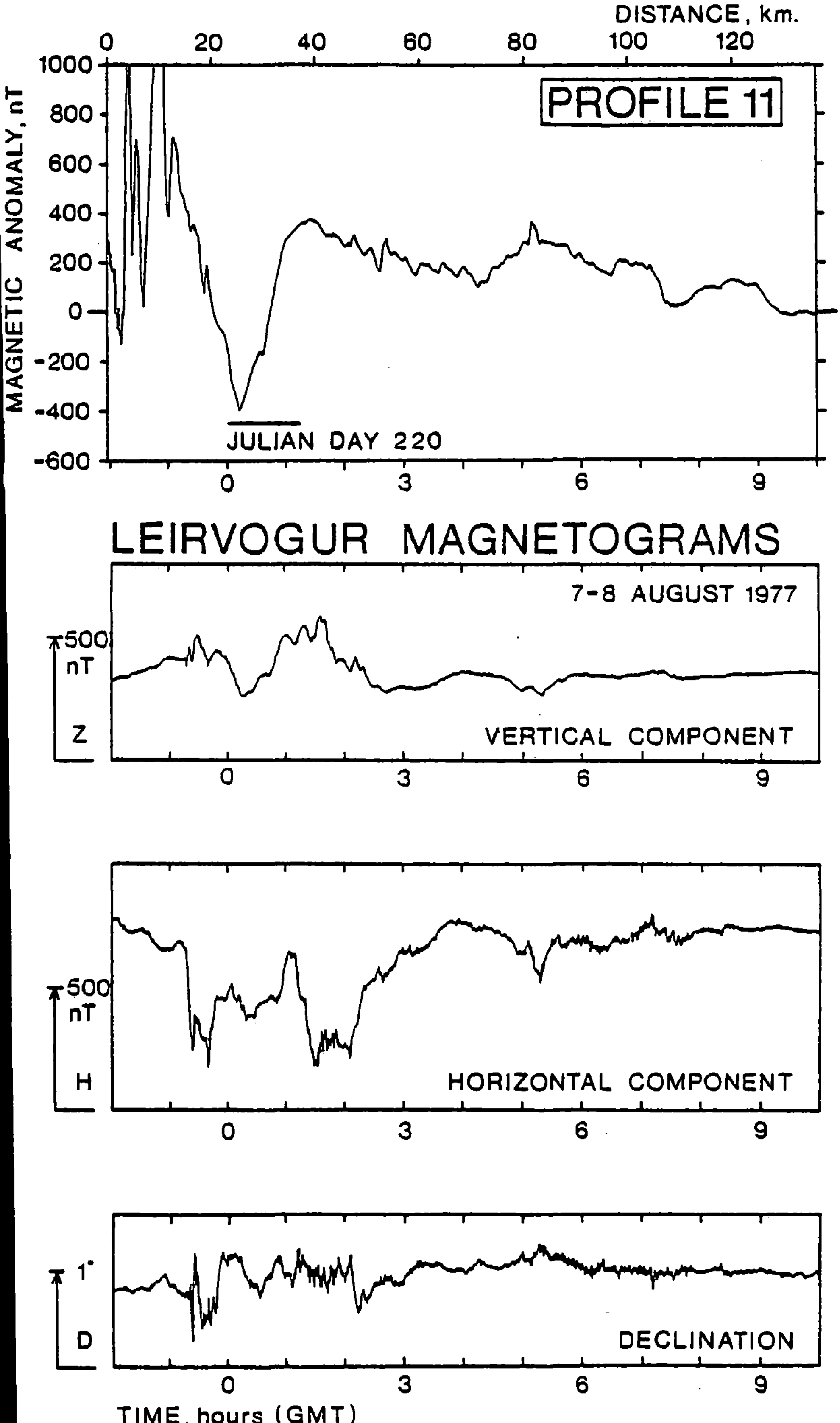

Figure 5.1 Magnetic anomaly from profile 11 with observatory magnetogram records from Leirvogur, drawn to show the impulsive effect of the precession of the auroral oval.

TABLE 5.1 MEM spectral depth estimates on real magnetic data.

PROFILE NUMBER	SEGMENT	SPATIAL LIMITS OF SPECTRAL ANALYSIS KM		DEPTH ESTIMATE WITH ERROR FROM SLOPE KM	CORRELATION COEFFICIENT	WAVENUMBER LIMITS OF LINEAR SEGMENT, RADS. KM^{-1}		NOS. OF PREDICTION ERROR FILTER COEFFICIENTS		TERMS IN SEGMENT
		XSTART	XEND			LOW-CUT	HIGH-CUT	AKAIKE	BERRYMAN	
11	1	48.01	78.83	1.30 ± 0.03	−0.9984	0.44	0.90	3	32	80
	2	63.62	94.44	2.14 ± 0.05	−0.9985	0.44	0.90	7	32	80
	3	79.22	110.05	4.02 ± 0.17	−0.9949	0.44	0.90	8	32	80
	4	94.83	125.66	3.65 ± 0.38	−0.9691	0.44	0.90	2	32	80
	5	110.44	141.27	2.49 ± 0.04	−0.9991	0.44	0.90	4	32	80
	6	119.27	158.43	2.34 ± 0.09	−0.9840	0.43	1.81*	8	38	100
	7	139.05	178.20	2.31 ± 0.28	−0.8705	0.43	1.81*	27	38	100
	8	158.82	197.98	2.54 ± 0.08	−0.9907	0.43	1.81*	5	38	100
	9	178.60	217.75	1.69 ± 0.14	−0.9338	0.43	1.81*	14	38	100
13	10	9.96	30.14	1.53 ± 0.03	−0.9977	0.84	1.89*	11	22	50
	11	9.96	30.14	6.40+0.77	−0.9723	0.49	0.84	11	22	50
	12	46.11	65.24	4.26 ± 0.38	−0.9626	0.48	1.22	3	22	50
	13	55.87	74.99	4.39 ± 0.07	−0.9986	0.48	1.22	10	22	50
1	14	33.11	50.77	2.18 ± 0.13	−0.9738	0.59	1.83*	4	22	50
	15	42.12	59.79	4.06 ± 0.26	−0.9682	0.59	1.83*	13	22	50

TABLE 5.1 (contd)

PROFILE NUMBER	SEGMENT	SPATIAL LIMITS OF SPECTRAL ANALYSIS KM		DEPTH ESTIMATE WITH ERROR FROM SLOPE, KM	CORRELATION COEFFICIENT	WAVENUMBER LIMITS OF LINEAR SEGMENT, RADS. KM^{-1}		NOS. OF PREDICTION ERROR FILTER COEFFICIENTS		TERMS IN SEGMENT
		XSTART	XEND			LOW-CUT	HIGH-CUT	AKAIKE	BERRYMAN	
1	16	51.13	68.80	2.65$\pm$0.13	-0.9827	0.59	1.83*	13	22	50
	17	60.15	77.81	2.27$\pm$0.11	-0.9810	0.59	1.83*	3	22	50
	18	69.16	86.82	2.67$\pm$0.23	-0.9450	0.59	1.83*	12	22	50
	19	112.52	129.46	2.59$\pm$0.17	-0.9719	0.48	1.55	5	22	50
	20	121.16	138.11	2.35$\pm$0.08	-0.9934	0.48	1.55	3	22	50
	21	129.81	146.75	2.40$\pm$0.11	-0.9877	0.48	1.55	6	22	50
	22	138.45	155.39	2.07$\pm$0.06	-0.9950	0.48	1.55	5	22	50
14	23	16.08	39.87	4.07$\pm$0.44	-0.9717	0.47	0.90	13	25	60

* depth estimates for which upper wavenumber cut-off limit exceeds the restriction of bandwidth proposed by Miller (1977) assuming that only data for wavelengths greater than 4 km are valid for geological interpretation.

prolonged magnetic storms during the period of the 1977 cruise, especially between day 217 (0030 hrs) and day 220 (0830 hrs). Strongly impulsive disturbances were also prominent in the vicinity of local midnight on most days. The magnitude of this impulsive behaviour due to the precession of the auroral oval is illustrated in Figure 5.1. An important magnetic anomaly along profile 11 affected by this magnetic activity is also shown, since an interpretation of the magnetic anomaly is proposed in the following sections.

5.2.1 Spectral depth estimates

Determination of depth to magnetic sources using the maximum entropy spectral density estimate was described in Section 3.2.4. The computer program SPECTRAL was used to analyse selected segments of real magnetic anomaly data in an attempt to define the depth of magnetic "basement" and, in particular, to map the buried surface of the subsided plateau basalts in the vicinity of the submerged aseismic ridge.

The spectral depth estimate technique was used on magnetic anomaly data from 4 profiles to delineate magnetic "basement" trends over areas where seismic data were poor or absent and to confirm the interpretation of selected horizons on the seismic sections. The results are tabulated in Table 5.1 and are summarised as follows:

<u>Profile 11</u>

MEM spectral depth estimates, and their associated standard deviations calculated by least squares regression, are indicated in Figure 5.2. The interface representing magnetic "basement" and defined by gravity modelling (Section 5.3.2) is also shown.

Despite the observation in Section 3.2.4 that the Berryman criterion for prediction operator length gave marginally superior depth estimates on model data with additive random noise, the Akaike criterion was adopted for analysis of real data. This was done to achieve smoother spectra and to avoid over-resolution at long wavelengths.

With reference to Figure 5.2, depth estimates over the range 50 to 110 km were attempted in order to define the upper surface of the postulated offshore continuation of the plateau basalts. Depth estimates over the range 110 to 220 km were carried out in order to test the interpretation

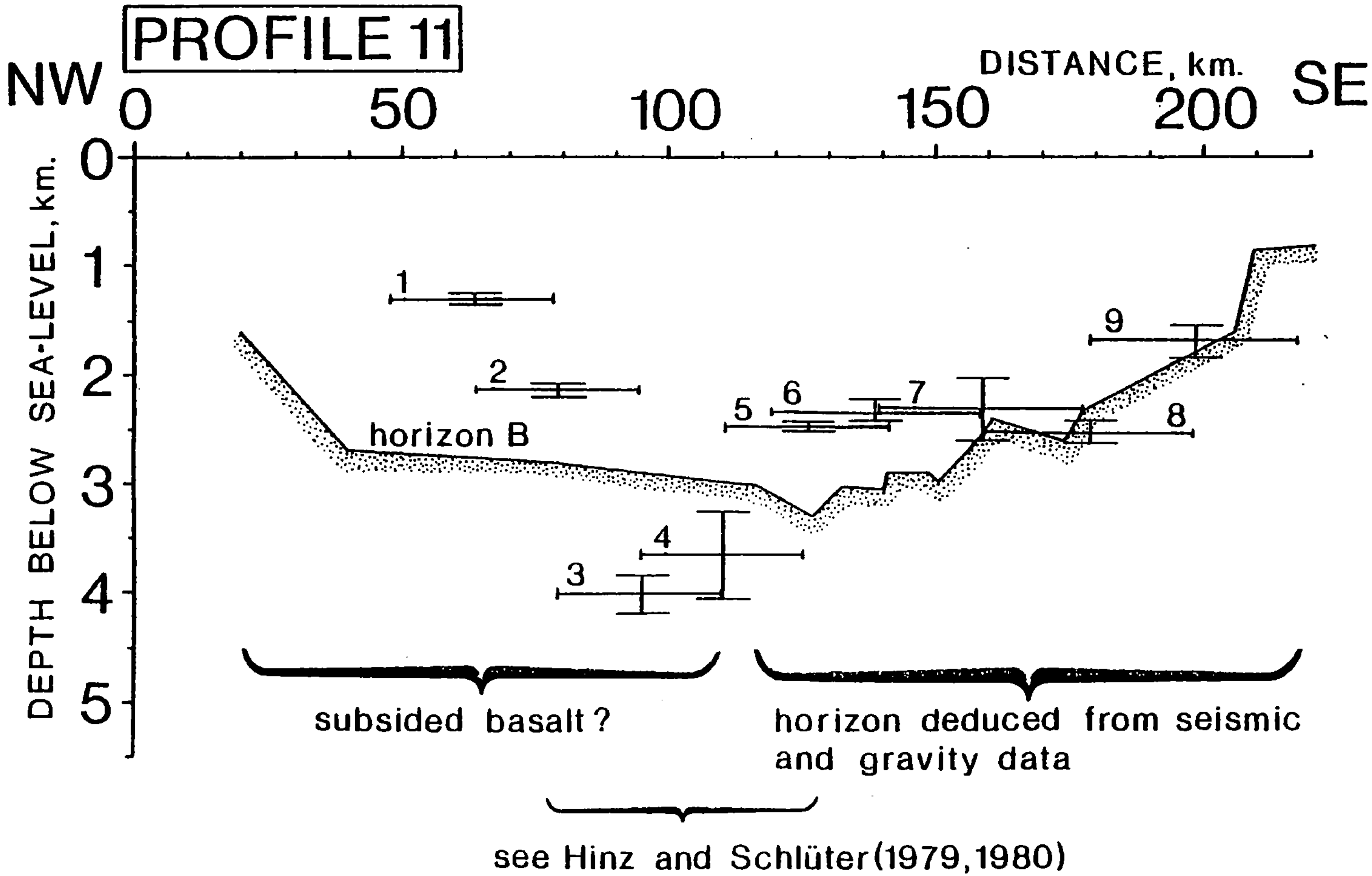

Figure 5.2 Spectral depth estimates using MEM spectral analysis along profile 11. Numbers adjacent to depth estimates represent data entries in Table 5.1.

of horizon B (Figure 4.2) from seismic reflection data as a basalt layer.

Bearing in mind the uncertainty involved in converting times picked along selected reflectors on unmigrated seismic reflection records, the spectral depth estimates agree surprisingly well with depths deduced for the basalt interface, horizon B, in subsequent gravity modelling. In general, estimated depths from the spectra were too shallow relative to the gravity model which was initially inferred from seismic reflection data and subject to relatively minor adjustment during the gravity modelling procedure.

Depth estimates nos. 1 through 4 (Figure 5.2) were puzzling. Reference to Figure 5.1 shows that the magnetic data were still subject to magnetic storm activity over the range 50 to 110 km along profile 11. This high-frequency noise would have increased the power represented in the spectra at high wavenumbers and this would result in shallow depth estimates (nos. 1 and 2 respectively).

The dilemma presented by the greater depth estimates of segments 3 (4.02 $\pm$ 0.17 km) and 4 (3.65 $\pm$ 0.38 km) respectively may be resolved in view of recent geophysical investigations by Hinz and Schlüter (1979, 1980). These authors reported the location of a graben zone based on the interpretation of multi-channel seismic reflection data. This graben zone intersects profile 11 as shown in Figure 5.7. Deep structure was not discernible on the seismic reflection record of profile 11 at this location (Figure 4.2, SP 1000 to SP 1800). The spectral depth estimates over segments 3 and 4 respectively are in good agreement with the depth models proposed by Hinz and Schlüter (1980), and also Larsen (1980).

The surface to which the spectral depth estimates refer is interpreted as the offshore continuation of the plateau basalts associated with a phase of faulting and rifting prior to the onset of seafloor spreading about 41 Ma ago (after Nunns, 1980; also Figure 4.3). The presence of pre-drift, Mesozoic sediments beneath the basalts cannot be ruled out but no direct evidence for their existence is apparent.

Miller (1977) analysed the relative importance of phenomena contributing to marine magnetic anomalies by comparison of magnetic data collected simultaneously at the sea surface and near the seafloor. His important conclusion was that magnetic data observed near the sea surface are contaminated by ionospheric noise and he deduced that, for his particular

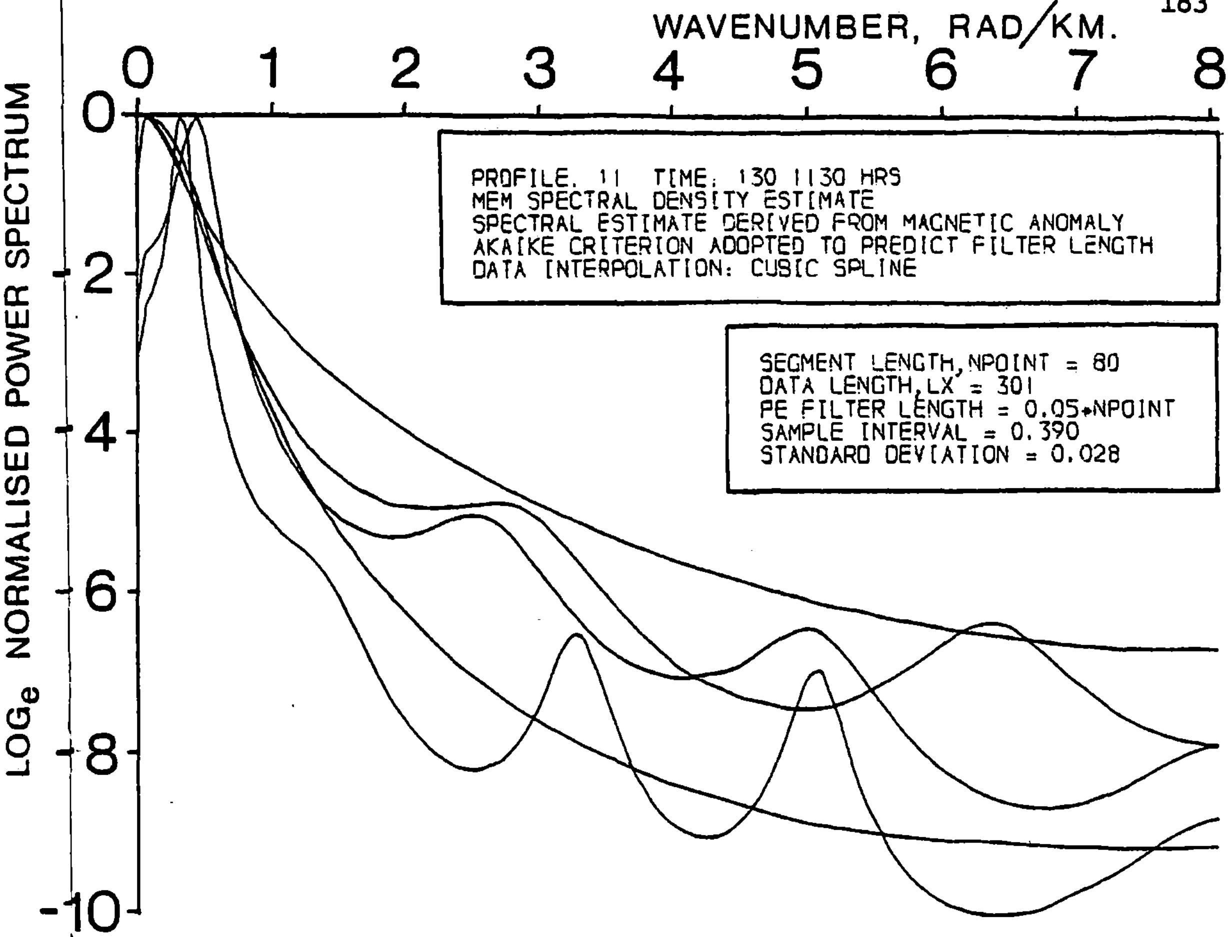

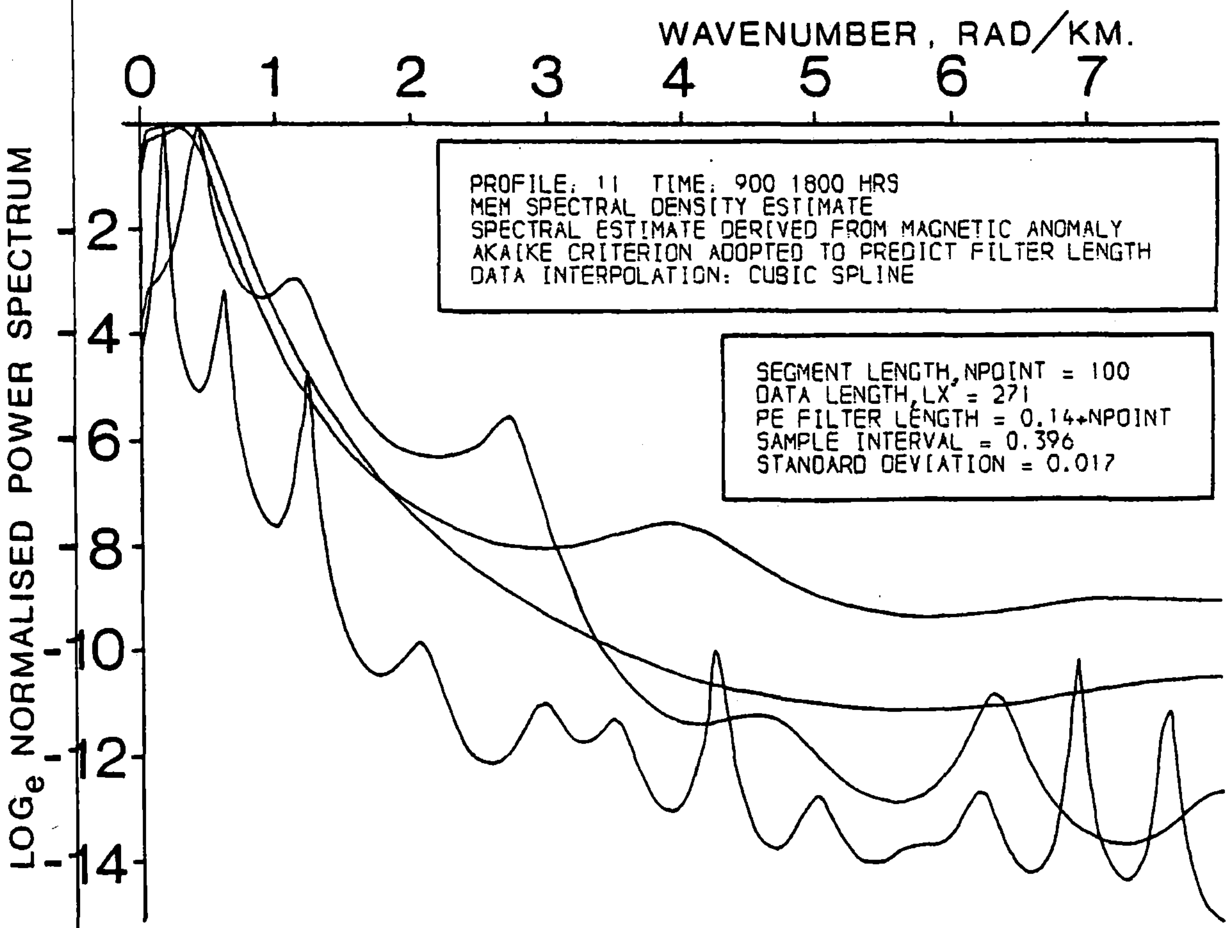

Figure 5.3 Natural logarithm of the MEM spectral density estimate curves for data analysed along profile 11.

survey, only data for wavelengths greater than 4 km were valid for geological interpretation. In principle, the faster survey speed (about 11 km hr^{-1} compared with 3.2 km hr^{-1} for Miller's survey) of the East Greenland project should have increased the bandwidth of geological validity to greater wavenumbers (at faster towing speeds, ionospheric variations are represented at lower wavenumbers where the geological power is stronger). However, the greater target depth to magnetic sources off the East Greenland coast would have tended to negate this effect (Miller, 1977). Therefore, Miller's result was adopted in general and portions of spectra defined beyond a wavenumber, K = 1.57 rad km^{-1} (equivalent to a wavelength of 4 km) were not used. Depth estimates for which this restriction of bandwidth was not applied are indicated by an asterisk (*) in Table 5.1.

The curves of the natural logarithm of the normalised MEM spectral density estimate for data analysed along profile 11 are shown in Figure 5.3.

Profile 13

Spectral depth estimates are compared with the magnetic "basement" deduced by gravity modelling in Figure 5.4. The depth estimates 10 and 11 were deduced from two different linear portions of the same log normalised spectral density estimate. The three depth estimates greater than 4 km were all evaluated from the steep slope associated with a highly resolved peak at long wavelengths in their respective log normalised spectra. This high resolution property at low wavenumbers appears to produce spurious results requiring interpretative discretion since the depths to magnetic sources indicated by estimates 11, 12 and 13 are difficult to justify geologically.

Profile 1

Depths to magnetic "basement" calculated by spectral analysis of segments from profile 1 are shown in Figure 5.5. The cluster of estimated depths to magnetic "basement" between 110 and 160 km agree very closely with the interface deduced by gravity modelling. The group of four depth values, located between 30 and 90 km, which represent underestimates of the depth to the horizon produced from gravity modelling, was calculated from MEM log normalised spectra generated from segments of magnetic data barely 6 times longer than the final estimated depths themselves (each data segment was only 18 km long). Regan and Hinze (1976) recommended the use of data sets at least 6 times longer than the maximum depth to the causative body

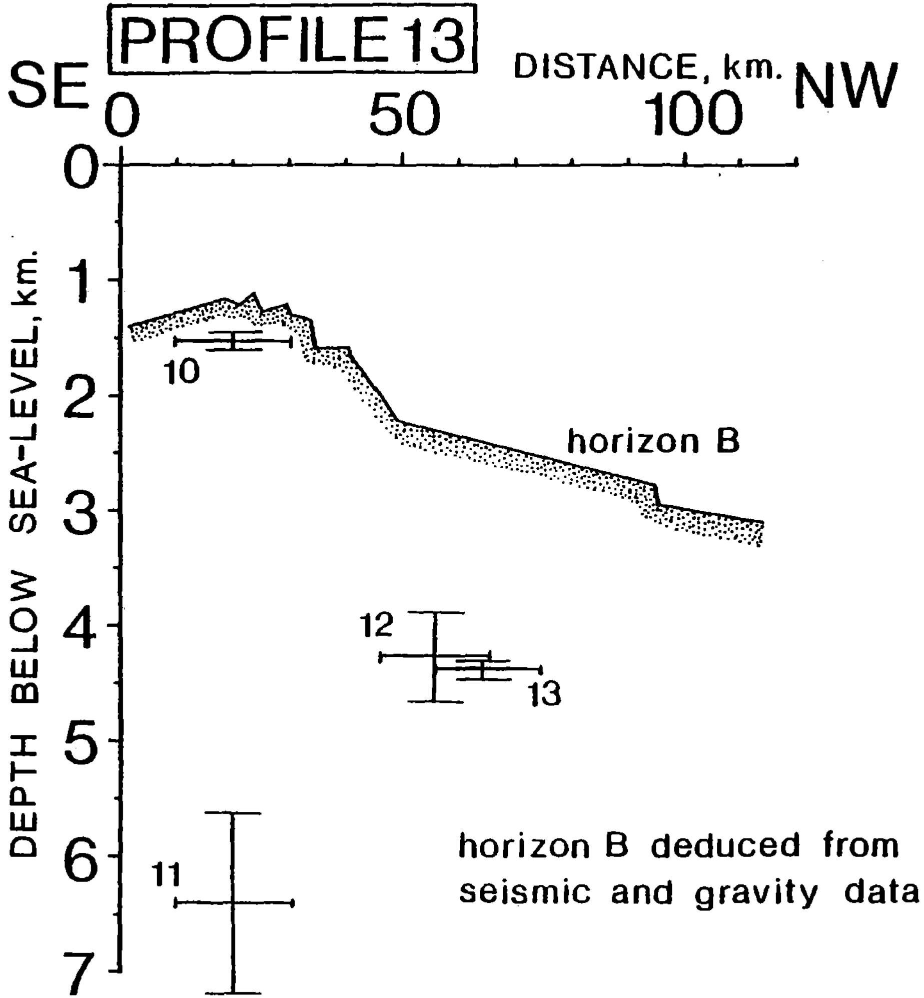

Figure 5.4 Spectral depth estimates using MEM spectral analysis along profile 13. Numbers adjacent to depth estimates represent data entries in Table 5.1.

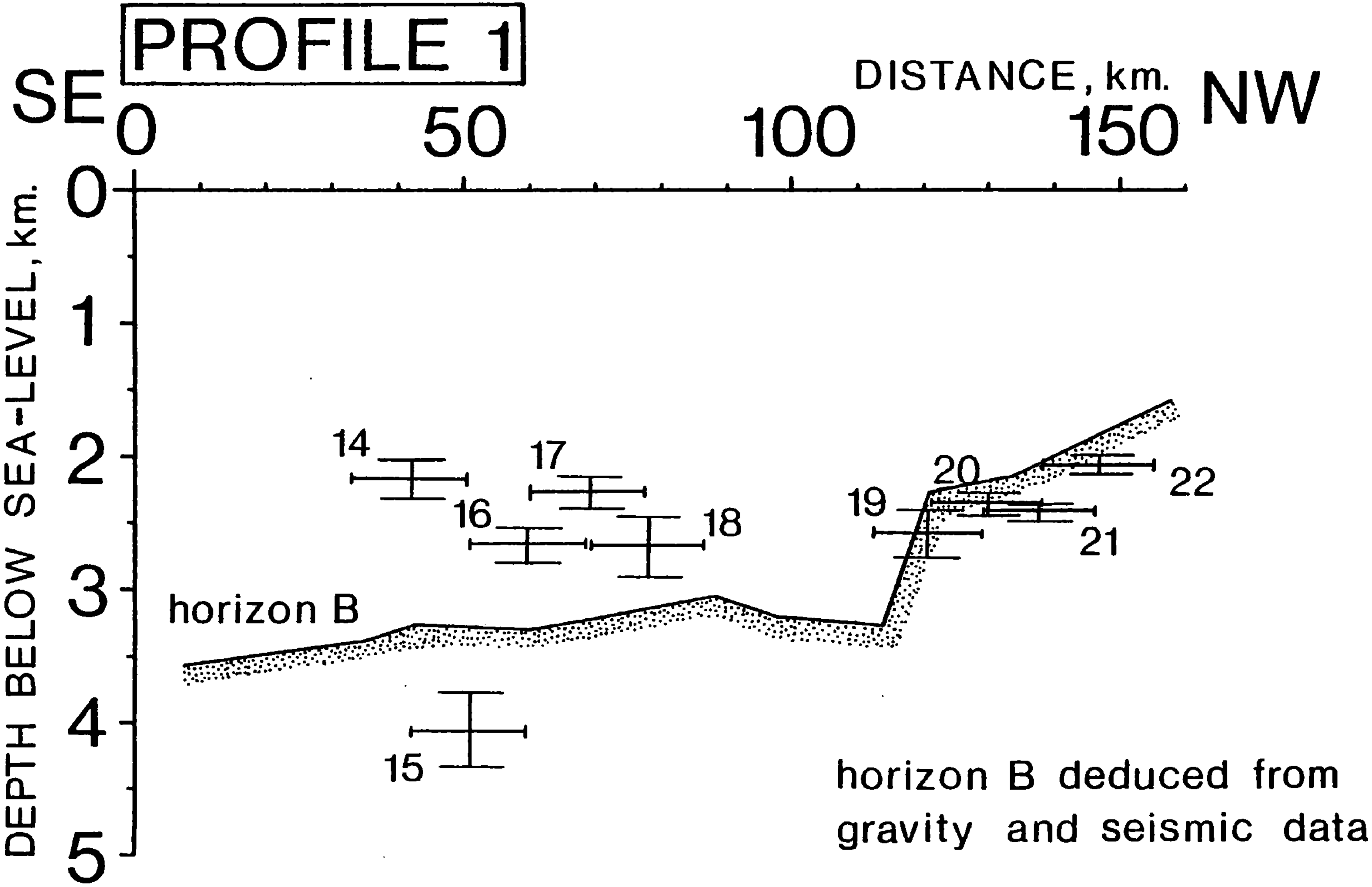

Figure 5.5 Spectral depth estimates using MEM spectral analysis along profile 1. Numbers adjacent to depth estimates represent data entries in Table 5.1.

(Section 3.2.4) and at the extreme of this criterion, unreliable depth estimates have apparently occurred.

Profile 14

In order to test the interpretation of seismic velocities associated with sonobuoy S2 shot along profile 14 (Figure 1.1), the segment of magnetic anomaly data acquired at the same time was subjected to spectral depth analysis. The estimated depth to magnetic "basement" was calculated to be 4.07 ± 0.44 km. This value corresponds to the depth of 4.36 km deduced from sonobuoy refraction arrivals for the depth to the 4.42 km s^{-1} refractor. This refractor velocity is believed to indicate the presence of a layer of Palaeocene-Eocene basalts and they are expected to form the local magnetic "basement". The spectral depth estimate of 4.07 km supports this interpretation (see Section 4.6).

However, it must be said that this is a fortunate result since the magnetic data of profile 14 were acquired during a magnetic storm. Such high-frequency noise would contribute to an under-estimated depth to buried magnetic sources.

5.2.2 Magnetic anomalies off the coast of East Greenland

A compilation of the magnetic anomaly data projected along simplified ship's track for the Durham geophysical research cruises of 1973, 1974 and 1977 is shown in Figure 5.6. The quantitative interpretation of individual magnetic anomalies was severely limited due to the extensive magnetic storm activity experienced especially during August 1977 (the extent of magnetic disturbances is indicated in Appendix A).

Although the magnetic profiles were widely spaced, an attempt was made to identify characteristic marine magnetic anomalies and to correlate anomalies northwards along the East Greenland continental margin from the Reykjanes Basin and into the Denmark Straits.

A straight line was fitted through the magnetic anomaly data of each profile by the method of least squares. This linear trend was subtracted from the anomaly data to remove a first order estimate of any regional field and to facilitate the recognition of characteristic oceanic magnetic anomalies. The reduced data are shown in Figure 5.7. The identification of individual oceanic anomalies in the Reykjanes Basin and along the east

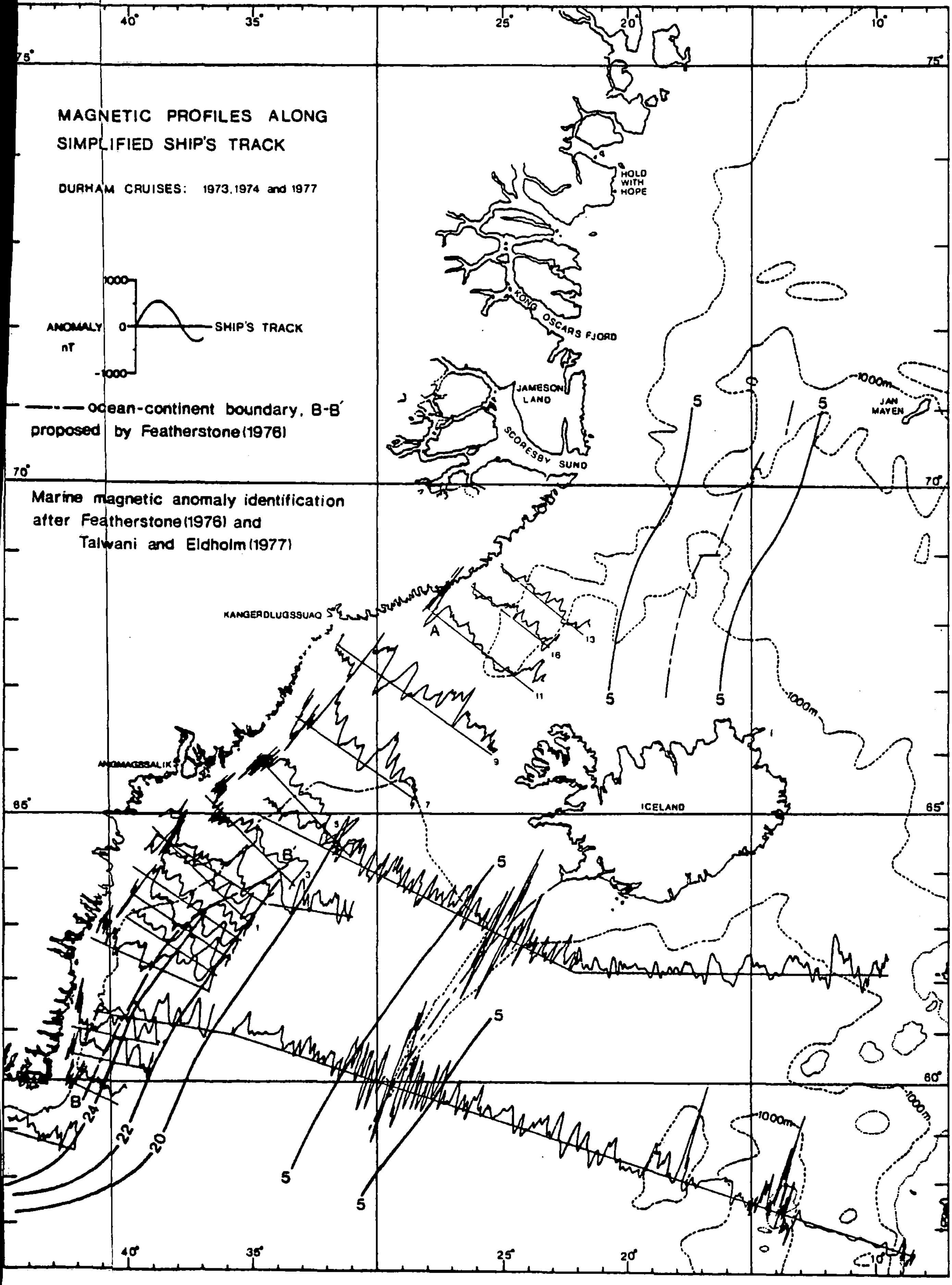

Figure 5.6 Magnetic anomaly profiles along simplified ship's track for Durham cruises 1973, 1974 and 1977. Numbers adjacent to profiles represent profile identification.

coast of Greenland was made with reference to Williams and McKenzie (1971), Vogt and Avery (1974), Featherstone (1976), Larsen (1980) and Vogt et al (1980). Anomaly identification and the tentative extrapolation of oceanic anomaly trends through the Denmark Straits are shown in Figure 5.7.

Recent work by Vogt et al (1980) suggests that the marine magnetic anomaly sequence 13 through 22 extends northwards into the Denmark Straits and that these lineations appear to terminate abruptly at a major fracture zone north of the submerged aseismic ridge. Prompted by this proposal, the magnetic anomalies 13, 18, 20 and 21 have been tentatively extrapolated through the Denmark Straits on the basis of visual correlation from profile to profile as shown in Figure 5.7. The location of the fracture zone proposed by Vogt et al (1980) was plotted from Larsen (1980).

The recognition of the Denmark Straits fracture zone and the truncation of linear marine magnetic anomalies against it provided crucial evidence for the interpretation of CDP stacked seismic data of profile 11 (Section 4.3). Having indicated the location of profile 11 and the inferred fracture zone respectively on the map of Figure 5.7, it became clear that an approximately linear extrapolation of the proposed fracture zone ESE intersected profile 11 at a shallow, acute angle between SP 2480 and SP 2640 (Figure 4.2). The puzzling structural feature and associated normal faulting observed on the CDP stacked seismic section, initially interpreted in terms of a faulted horst block or unlikely diapirism, became readily explicable as the expression of a fracture zone. This presents a more plausible explanation.

Vogt et al (1980) also identified magnetic anomalies 6, 6A and 6B off the margin of East Greenland north of Iceland as shown in Figure 5.7. Adopting the ocean-continent boundary north of the Greenland-Iceland Ridge proposed by Larsen (1980) implies the presence of a wedge of oceanic crust to the north of the supposed fracture zone. If this interpretation is correct, the "horst" between SP 2480 and SP 2640 on profile 11 separates oceanic crust of two contrasting ages. Nunns (1980) proposed the likely presence of a wedge of oceanic crust to the north of the Denmark Straits fracture zone, bounded eastwards by oceanic anomaly 6B (Vogt et al, 1980) and to the west by the band of very short wavelength magnetic anomalies adjacent to the Blosseville Coast of East Greenland. Nunns (1980) presents a convincing scheme for the formation of the fan-shaped anomaly pattern displayed by anomalies 20 through 7 in the Norwegian Basin, formed about the, now extinct, Aegir Ridge and caused by the anti-clockwise rotation of the Jan Mayen block as spreading continued. In order to accommodate fan-

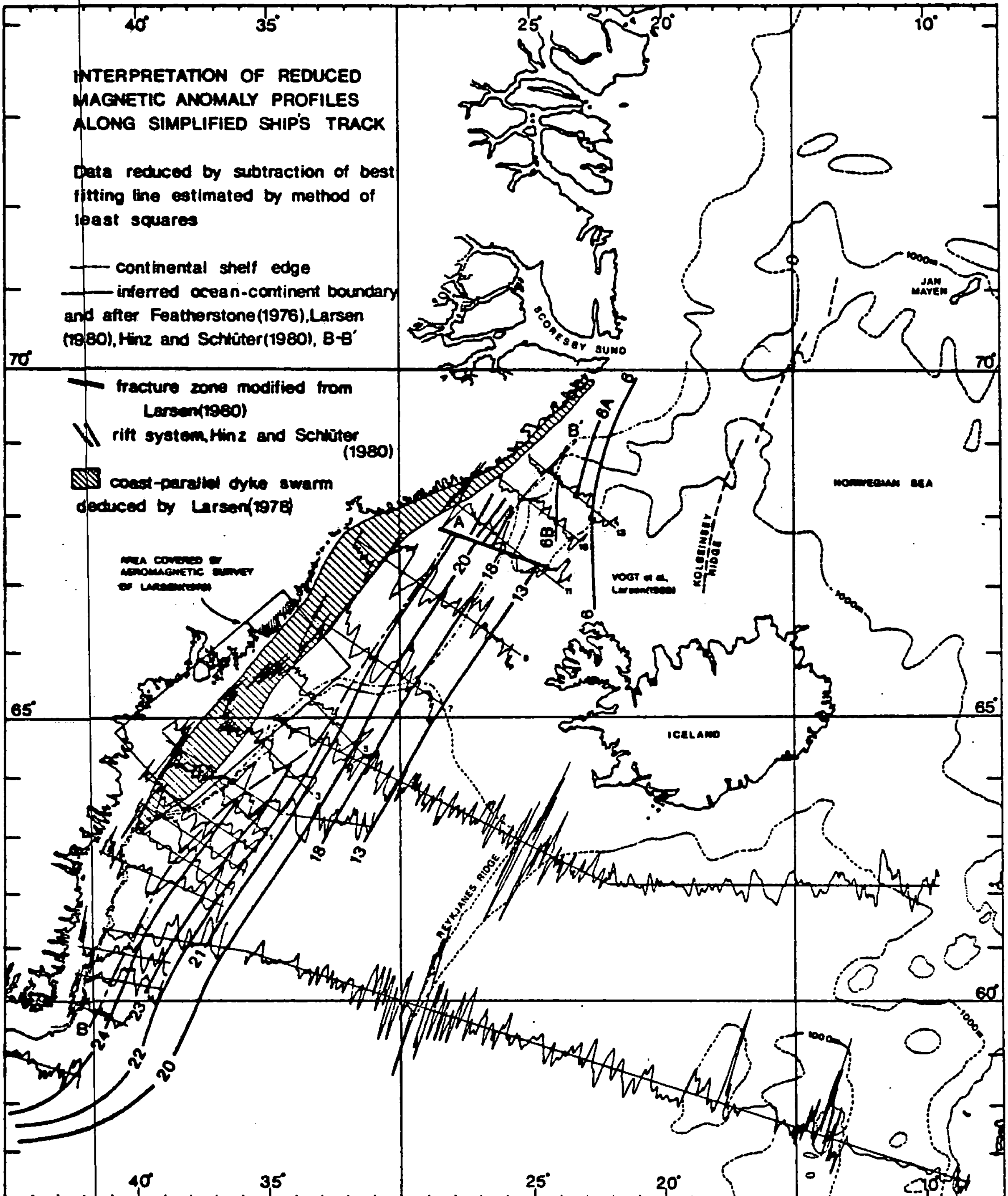

Figure 5.7 Proposed interpretation of marine magnetic anomalies along simplified ship's track for reduced magnetic anomaly data off the coast of East Greenland.

shaped spreading in the Norwegian Basin, complementary spreading was inferred to have taken place to the west of the Jan Mayen block forming a wedge-shaped zone of oceanic crust in which oceanic anomalies 7 through 18 may be present (Nunns, 1980).

Oceanic crust along profile 11 to the SE of the fracture zone (between SP 2480 and SP 2640) is dated at approximately 35 Ma by the location of anomaly 13 (Hailwood et al, 1979) and this implies a younger age for the basaltic horizon beneath the pinch-out of reflector U1 at SP 3080 (Figure 4.2). Assuming a half-spreading rate of order 0.8 cm yr^{-1} (Vogt and Avery, 1974), the distance of some 20 km between the projection of anomaly 13 on to profile 11 and the pinch-out of reflector U1 against horizon B represents about 3 Ma. Therefore, the age of horizon U1 must be younger than 32 Ma and since it represents a significant marker horizon on the seismic section, it is tentatively correlated with the major lowstand in global sea level in Late Oligocene times, about 30 Ma ago (Figure 4.3).

This interpretation is subject to the uncertainty associated with the recognition of oceanic anomalies and their tentative extrapolation via poor correlations through the Denmark Straits. However, the absence of a marked depth differential between oceanic crust of alleged contrasting ages across the fracture zone on profile 11 is inconclusive evidence since the age difference on either side of the fracture zone is not significantly large. The rate of subsidence of oceanic crust is a function of the age of the ocean basin (Parsons and Sclater, 1977; Royden et al, 1980).

Veevers (1977) made an important point relevant to this debate. He suggested that if basalt was emplaced subaerially, either above sea level or in an arid basin barred from the sea, initial oceanic crust would not contain typical seafloor spreading magnetic anomalies. Since the plateau basalts of the Blosseville Coast accumulated in predominantly subaerial conditions (Deer, 1976) and the Greenland-Iceland-Faeroe Ridge formed a land bridge between Greenland and Europe from Eocene to Middle Miocene times (Vogt, 1972; Talwani and Udintsev, 1976; Grønlie, 1979), the absence of well-defined and easily-correlated oceanic magnetic anomalies in the region of the Denmark Straits is not surprising.

The position of the ocean-continent boundary is inferred from the truncation of oceanic magnetic anomalies and by reference to recent work by Vogt et al (1980) and Larsen (1980). Nunns (1980) proposed a relatively simple scheme to explain the evolution of the Norwegian Sea and he independently developed a continental margin north of the Denmark Straits fracture zone similar to that indicated by Larsen (1980). The ocean-continent boundary proposed by Featherstone (1976) and located along a prominent trough in the magnetic anomaly has been adopted up to latitude 63°N. The continental margin is then considered to swing farther north and eastward to accommodate the truncation of anomalies 22 through 24 resulting from a westward jump of spreading axis in the Reykjanes Basin immediately prior to anomaly 21 time (Featherstone, 1976). This northward continuation of the ocean-continent boundary is supported by the evidence of the seismic reflection data discussed in Chapter 4. The proposed ocean-continent transition is shown in Figure 5.7 and this interpretation conflicts with that of Vogt et al (1980) and Larsen (1980) whose ocean-continent boundary south of the Denmark Straits fracture zone was located some kilometres westward and magnetic anomalies 22 and 23 persisted northwards up to the fracture zone itself.

The possibility that anomaly 22 continues north through the Denmark Straits and is truncated by the Denmark Straits fracture zone cannot be dismissed. Vogt et al (1980) recognised anomaly 22 at the western edge of the aeromagnetic survey south of the fracture zone and Featherstone et al (1977) suggested that the westward shift of axis in the Reykjanes Basin took place prior to anomaly 22. Nevertheless, the inferred location of the ocean-continent boundary from seismic data along profiles 3 and 5 respectively seems to preclude the northward continuation of anomaly 22 into the Denmark Straits and constrained by these data, the interpretation indicated in Figure 5.7 has been adopted in this study.

Voppel et al (1979) studied detailed magnetic measurements south of the Iceland-Faeroe Ridge and concluded that a westward jump of spreading axis must have taken place prior to anomaly 21 time. These authors stress the tenuous nature of their interpretation due to the difficulty of recognising oceanic anomalies older than anomaly 21. However, their proposal agrees with the conclusion of the present study that anomalies 22 through 24 are truncated by the ocean-continent boundary off East Greenland (Figure 5.7).

A careful study of oceanic anomalies 20 and 21 in Figure 5.7 shows a distinct bend in their generally linear disposition just north of 65°N. This observation agrees with the results of Johnson et al (1975b) who identified a left lateral offset of anomalies 20 and 21 at 65°N and they inferred the existence of a major fracture zone off the East Greenland continental margin at this latitude. The fracture zone is not shown explicitly in Figure 5.7 because its precise location cannot be specified from the widely spaced profile data of Johnson et al (1975b) and this study.

The accurate location of the ocean-continent boundary is a problem. The single-channel shipborne monitor records of profiles 5, 3 and 1 (Figures 4.10, 4.11 and 4.12 respectively) indicate a transition between relatively smooth continental-type acoustic basement and the irregular surface of the basaltic layer 2 associated with oceanic crust. However, even the seismic data provide only a rather subjective interpretation since the abrupt change anticipated at the continental margin is not always convincing. The seismic data to the north of profile 5 do not indicate the location of the ocean-continent boundary because the transition is obscured by sedimentary cover. Furthermore, the interpretation of gravity anomalies discussed in the following section does not uniquely define the zone of transition from oceanic to continental crust. The absence of well-defined oceanic magnetic anomalies precludes their use for an accurate definition of the ocean-continent boundary.

Larsen (1978) studied offshore aeromagnetic data in an area along the East Greenland coast shown in Figure 5.7 and although his correlation of magnetic anomalies from profile to profile is not definitive, he concludes that the coast-parallel dyke swarm of East Greenland continues on the continental shelf as a broad, coast-parallel belt. The massive intrusion of dykes along the East Greenland coast (Nielsen, 1975, 1978), their offshore continuation proposed by Larsen (1978) and the presence of high-amplitude, long-wavelength magnetic anomalies landward of the inferred ocean-continent boundary on profiles 3, 5 and 9 respectively support the idea that continental lithosphere may crack and allow the intrusion of dykes or diapirs from the mantle during the initial phases of rifting (Royden et al, 1980).

The possible offshore continuation of the Tertiary basalts along the Blosseville coastline between latitudes 68°N and 70°N was investigated by analysis of a prominent magnetic anomaly, marked A, along profile 11 (Figure 5.7). Irregular seafloor topography associated with a high-amplitude, short-wavelength magnetic anomaly to the north-west of SP 260 (profile 11, Figure 4.2) is interpreted as representing basalt (see Section 4.3). It is unfortunate that this crucial magnetic anomaly was subject to considerable interference by magnetic storm behaviour (Figure 5.1). However, it is considered that the general integrity of the anomaly is preserved despite the magnetic storm disturbance.

The magnetic interpretation is shown in Figure 5.8. The inclination and declination of the Earth's magnetic field were calculated from U.S. Naval Charts (U.S. Naval Oceanographic Office, 1966) and the inclination and declination of the basalt resultant magnetisation were estimated from data observed on the palaeomagnetic properties of some Tertiary lavas from East Greenland (Tarling, 1967).

Tertiary flood basalts are not necessarily highly magnetic and a mean value of natural remanent magnetisation (NRM) for East Greenland basalt flows of 0.24 A m^{-1} and a single measurement of 2.7 A m^{-1} of an individual basalt flow have been recorded by Faller (pers. comm.). However, a NRM value of 3.8 A m^{-1} for THOL 1 dykes (as defined by Nielsen, 1978) has also been reported (Faller, pers. comm.). For comparison, an arithmetic mean value for NRM of 5.0 A m^{-1} for the upper 230 m of Atlantic ocean crust was given by Faller et al (1978). The model shown in Figure 5.8 was developed with a resultant magnetisation of 4.0 A m^{-1}.

The model suggests that the plateau basalts are down-flexured and continue offshore beneath the proposed wedge of Tertiary sediments. This is a similar interpretation to that proposed by Larsen (1980). The basalt model assumes reverse magnetisation (Faller, 1975) and whilst not shown explicitly in Figure 5.8, the flexure of the basalts is assumed to be fault controlled (Nielsen, 1975).

This model is not unique. The total field magnetic anomaly due to a finite step model was calculated in order to illustrate the alternative proposal that the Tertiary plateau basalts actually terminate offshore. However, difficulty was found in matching the wavelength and amplitude of the observed anomaly with the finite step model, although the general anomaly shape calculated from the model was similar to the observed anomaly. Therefore, the finite step model was dismissed in favour of the geologically more acceptable structure presented in Figure 5.8.

The magnetic interpretation of Figure 5.8 indicates a greater thickness of Tertiary sediments, of order 6 km, overlying the basalt horizon than predicted by the spectral depth estimates (Figure 5.2) or subsequent gravity modelling (Figure 5.11), and also a steeper dip for the upper surface of the down-flexured basalts. Hence, the model shown in Figure 5.8 should be regarded as a qualitative indication only of the form of the

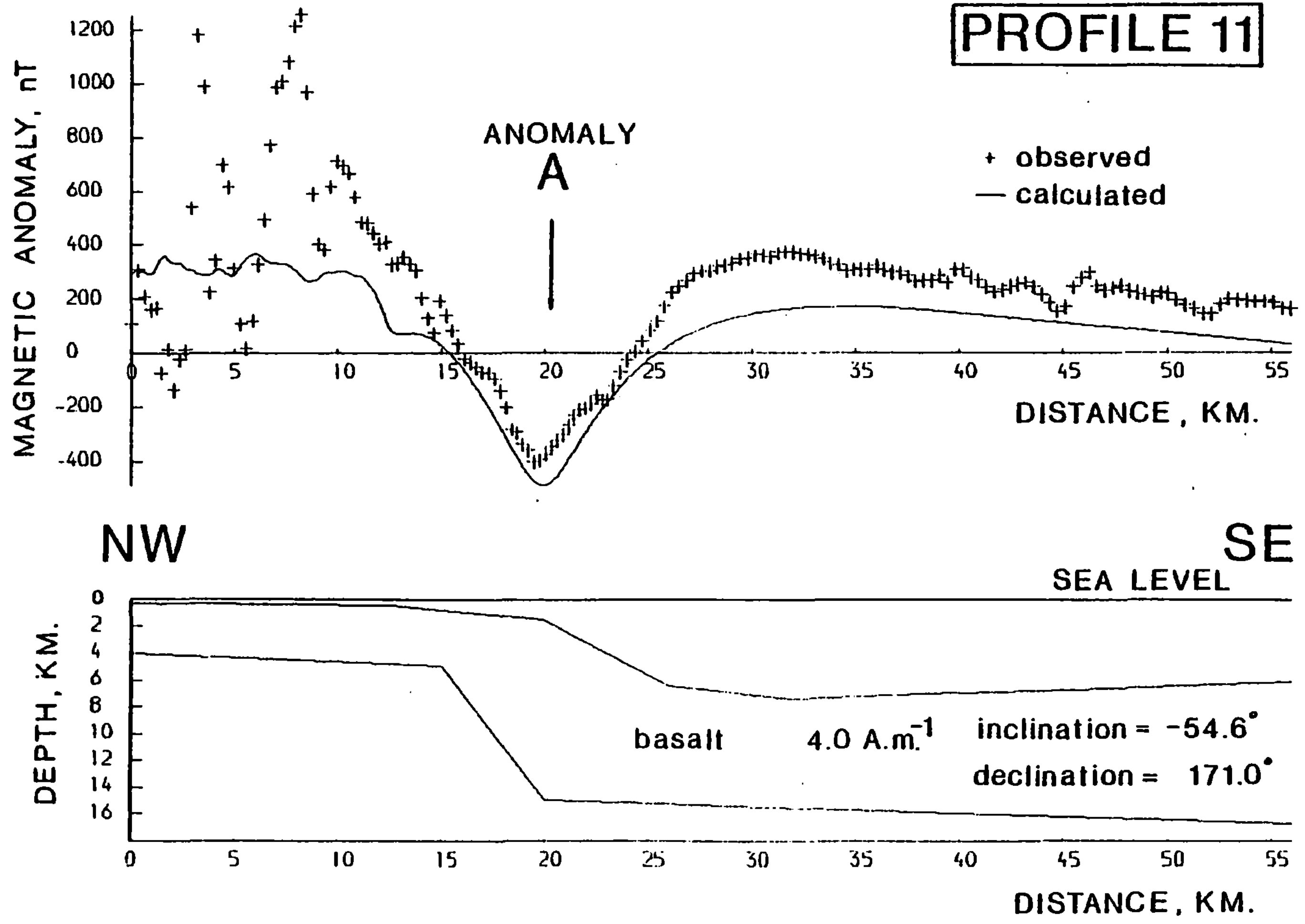

Figure 5.8 Interpretation of magnetic anomaly A along profile 11 as evidence for the offshore continuation of the plateau basalts.

plateau basalts offshore.

5.3 Gravity interpretation

The free air gravity anomaly values calculated from shipborne gravimeter measurements were tied-in to an absolute gravity value in Reykjavik, Iceland. This absolute gravity value was established with reference to the old gravity reference network referred to a unique value of gravity at Potsdam (Palmason et al, 1973). In order to reduce the gravity anomaly values to be compatible with the new IGSN '71 (Coron, 1972), the Potsdam datum correction of -14.0 mgal must be applied to the anomaly values (Woollard, 1979). Woollard emphasised that although the Potsdam correction appears to be a "poorly established, rounded-off value to an even milligal," it is essentially correct and the uncertainty is less than about 0.04 mgal.

This correction has not been applied to the gravity data presented in this thesis.

5.3.1 Assessment of subsurface densities

Estimation of densities for relatively shallow subsurface sedimentary units along selected profiles was carried out by projecting the results of contiguous sonobuoy refraction experiments on to the respective seismic sections and thereby identifying sedimentary units with an average refraction velocity. Each average velocity was then used in conjunction with the Nafe-Drake curve (Nafe and Drake, 1963; Grant and West, 1965) in order to establish a constant density for a given layer, assuming homogeneity and no lateral density variations within a given unit.

A constant density of 1.03 g cm^{-3} for seawater was adopted throughout the gravity modelling. Worzel (1974) proposed standard crustal structures for both oceanic and continental crust. He assigned an average density of 2.86 g cm^{-3} to standard oceanic crust and an average density of 2.84 g cm^{-3} to standard continental crust. Since the exact nature and location of the ocean-continent boundary along the East Greenland margin were unknown, a constant crustal density of 2.85 g cm^{-3} was assumed for both types of crust.

An estimate for the density of the metamorphic basement complex was investigated, although ultimately not incorporated into any of the gravity models. The following geological units comprising the metamorphic basement complex (Haller, 1970; Deer, 1976) were assigned average densities based on work by Smithson (1971):

(1) Granulitised acid gneisses in Kangerdlugssuaq region, 2.65 g cm^{-3}
(2) Amphibolite horizons forming approximately one tenth of metamorphic complex, 3.03 g cm^{-3}
(3) Small areas of sedimentary origin (garnet-sillimanite bearing gneisses), 2.80 g cm^{-3} (?)
(4) Migmatite gneiss group, 2.73 g cm^{-3}
(5) Microcline augen gneiss to microcline granite, 2.71 g cm^{-3}
(6) Amphibolite dykes, 3.03 g cm^{-3}.

The arithmetic mean (a gross simplification, since the figure has not been weighted in any way to compensate for the relative abundance of individual rock types) of the above six densities is 2.83 g cm^{-3}. Smithson (1971) reports mean densities of metamorphic terrains to be generally in the range 2.70 to 2.79 g cm^{-3}. In support, Ramberg (1976) reports Precambrian gneisses of Norway of density 2.74 g cm^{-3} and Smithson and Ramberg (1979) give gneisses of granulite facies in Norway a density of 2.70 g cm^{-3} and 2.75 g cm^{-3} for granitic rocks.

Due to its unknown extent laterally and at depth, the metamorphic basement complex was not modelled as a less dense unit within the continental crust. However, surface wave dispersion studies by Gregersen (1971) suggest a two-layer crustal model for the Greenlandic Shield, an upper "granitic" layer, 16.5 km thick and of density 2.80 g cm^{-3}, and a lower "basaltic" layer, 23.7 km thick and of density 2.85 g cm^{-3}. If the mean density value of 2.83 g cm^{-3} for the metamorphic units calculated above is at all representative, the absence of the metamorphic basement complex unit from the gravity models should not be a serious omission.

Average refraction velocities assigned to sedimentary units from nearby sonobuoy results were also used to convert two-way travel times extracted from unmigrated seismic sections (see Figures 4.2, 4.8, 4.9 and 4.12) into initial depth models for input into the gravity modelling procedure.

Gravity models were developed using a constant density of 3.30 g cm^{-3} for the upper mantle. In view of the uncertainties already existing in the delineation of near-surface structure and sedimentary units from limited seismic reflection data, it was considered unjustified to introduce the further refinement of trying to model lateral density changes in the upper mantle. However, it should be recognised that such heterogeneities exist and the importance of temperature gradients and their associated density variations in the lithosphere and asthenosphere in the North Atlantic Ocean has been illustrated by Haigh (1973).

Furthermore, a significant temperature gradient and associated thermal expansion within the oceanic lithosphere of a relatively young ocean basin (the Reykjanes Basin, for example) adjacent to the ocean-continent boundary will produce a lower value of density in the upper mantle beneath the oceanic crust. Featherstone (1976) estimated the value for the sub-oceanic upper mantle density to be 3.22 g cm^{-3} adjacent to the continental margin of East Greenland.

The choice of a suitable depth of compensation or level in the mantle below which lateral density variations do not occur was made somewhat arbitrarily. Values of the order of 30 km were used, similar to a depth of compensation of 32 km employed by Rabinowitz and LaBreque (1977). A more consistent lithospheric model with a depth of compensation of about 70 km and including lateral density variations would have been preferable (cf. Roots et al, 1979). Haigh (1973) estimated that the thickness of the oceanic lithosphere in the North Atlantic decreased northwards from 85 km to 64 km between 43°N and 61°N. The approach adopted in this study for the calculation of isostatic anomalies and isostatically compensated Moho discontinuities assumed an upper mantle structure of constant density without lateral inhomogeneities.

5.3.2 Gravity models

Gravity models for four selected profiles were developed.

<u>Profile 1</u>

The interpretation of the free air gravity anomaly, the isostatic anomaly and the magnetic anomaly of profile 1 is shown in Figure 5.9.

The range of sediment velocities, 1.62 to 2.57 km s^{-1} observed on sonobuoy results from locations S13, S14, S15 and S17 (Figures 1.2 and 4.13) were assessed and a mean sediment velocity of 2.3 km s^{-1} was assumed. The corresponding sediment density is 2.07 g cm^{-3} (Nafe and Drake, 1963).

Oceanic magnetic anomalies 22 through 24 have been identified in

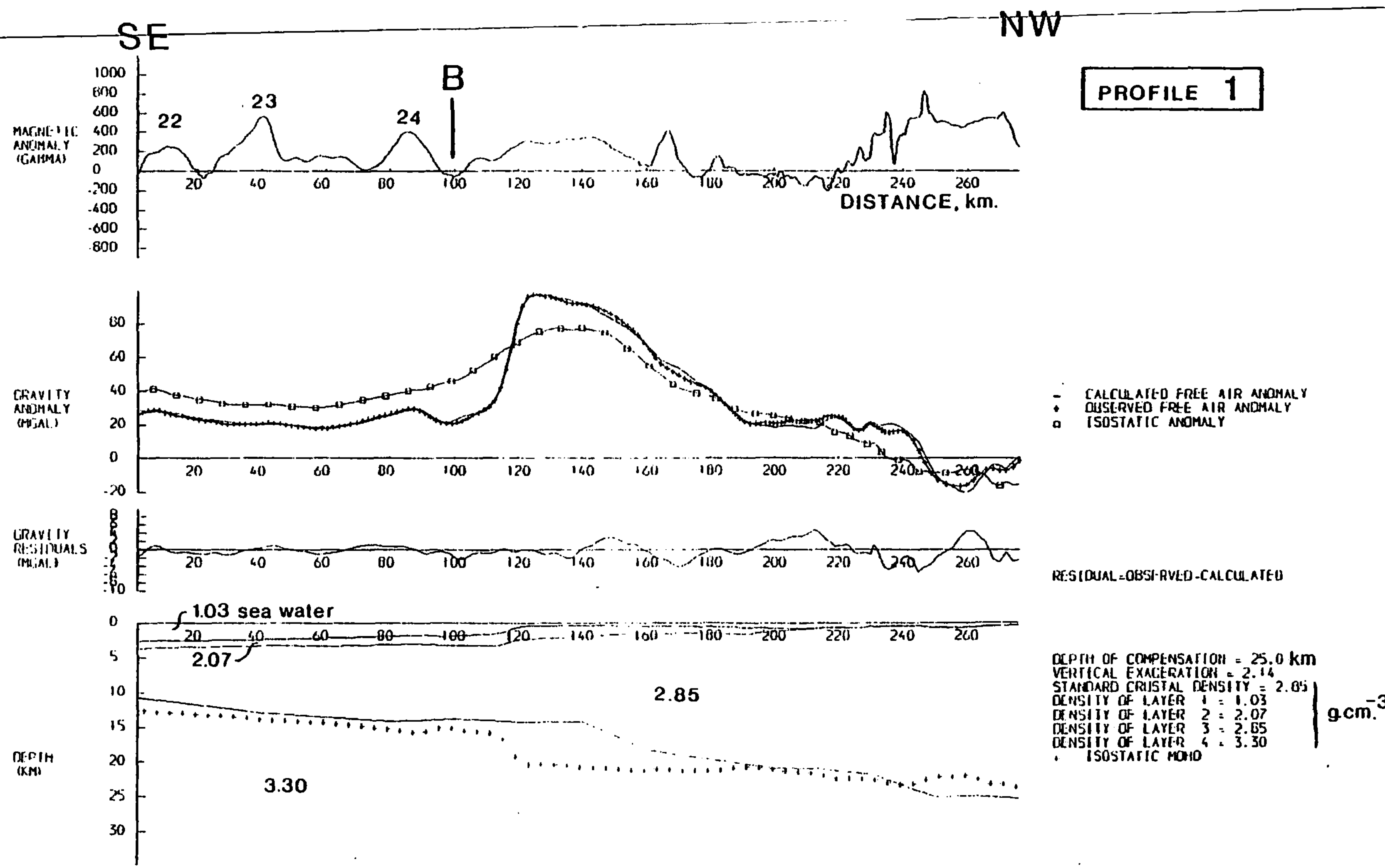

Figure 5.9 Gravity interpretation for profile 1. B represents the proposed ocean-continent boundary and marine magnetic anomalies 22 through 24 are also indicated.

Figure 5.9 and the inferred location of the ocean-continent boundary, B is shown some 20 km south-east of the continental slope. The location of the ocean-continent boundary is based on correlation of marine magnetic anomalies (Figure 5.7) and the single-channel seismic reflection record (Figure 4.12). This interpretation conflicts with that of Featherstone (1976) who located the ocean-continent boundary some 80 km seaward of the continental slope on a profile at an angle to and just south of profile 1. If the new interpretation is correct, representing a shift of some 25 km westward of the ocean-continent boundary, it casts doubt on the identification and interpretation of eastward dipping sub-Tertiary reflectors proposed by Featherstone (1976) at this latitude along the continental margin.

The gravity model indicates strongly attenuated, anomalously thin continental crust of 11 km thickness at the proposed ocean-continent boundary, thickening in a series of steps to 25 km at a distance westward of about 180 km. The thick oceanic crust adjacent to the continental crustal boundary is consistent with a mechanism for shallow spreading ridges in young oceans proposed by Roots et al (1979). However, these authors postulated a thickening of the oceanic crust at the continental margin of up to about 18 km thickness. This was not observed on profile 1 but the depth to the Moho was arbitrarily fixed at the eastern extremity of the profile to give a standard Moho depth of 11 km for oceanic crust. The continental crustal structure deduced by Gregersen (1971) for the Greenlandic Shield gave a crustal thickness of about 40 km and therefore the Moho is probably too shallow as shown in Figure 5.9. The shallow depth of the Moho beneath the continental crust is undoubtedly due to the assumption of a constant density upper mantle. Cooler lithosphere beneath the continental crust would result in a higher density in the upper mantle relative to that beneath oceanic crust. The increased density contrast between continental crust and upper mantle would yield a thicker crust in order to model a given free air gravity anomaly.

The computed Moho for complete isostatic compensation indicates that the continental margin and adjacent crust are more or less in isostatic equilibrium except that the prograded wedge of Tertiary sediments and the continental slope cut-back by contour current action remain uncompensated. Roots et al (1979) concluded that the ocean-continent boundary was essentially in isostatic equilibrium but their results were drawn from data gathered on a margin starved of sediments. The thick overburden of sediment encountered on the East Greenland margin has obscured this isostatic equilibrium, if indeed it does exist. The relative high in the computed two-dimensional isostatic anomaly also shows that the prograded wedge of Tertiary sediments is undercompensated. It is also possible that crustal flexure has partly accommodated sediment accumulation along the continental margin.

To the west of a point about 220 km along profile 1, the isostatic anomaly shows a deepening relative low and the computed Moho for complete isostatic equilibrium is shallower than for the Moho actually modelled. This over-compensation may be explained in terms of isostatic crustal rebound due to the removal of ice since the last glacial period (cf. the raised beaches of Fennoscandia, see Bott (1971), for example).

Profile 7

The interpretation of gravity and magnetic data along profile 7 is shown in Figure 5.10.

Taking into account the sonobuoy refraction velocities at sites 12V28 and 110V30 (Figures 1.2 and 4.13), an average seismic velocity of 2.3 km s^{-1} was assumed for the Tertiary sediments along the profile. The sediment density was estimated to be 2.07 g cm^{-3} (Nafe and Drake, 1963).

The tentative identification of oceanic anomalies 18 through 21 is also shown in Figure 5.10 and the location of the ocean-continent boundary has been inferred from the cessation of the marine magnetic anomaly sequence.

The two-dimensional isostatic anomaly indicates that isostatic equilibrium has been achieved except between approximately 140 and 230 km along the profile and this is interpreted as being caused by uncompensated Tertiary sediments.

The outstanding feature of this interpretation is the lack of variation in the depth to the Moho discontinuity across the inferred ocean-continent boundary. The thinning of continental crust is attributed to surface erosion during the initial stages of rifting and attenuation of the crust due to lower crustal mechanisms such as metamorphism and creep (Bott, 1979). The abnormally thick oceanic crust may be caused in part by the youth of the oceanic crustal material as proposed by Roots et al (1979). Lateral variations in upper mantle density would also provide a greater crustal thickness contrast across the ocean-continent boundary as discussed previously. However, it is more probable that the nearby submerged Greenland-Iceland aseismic ridge to the north is associated with thickened oceanic

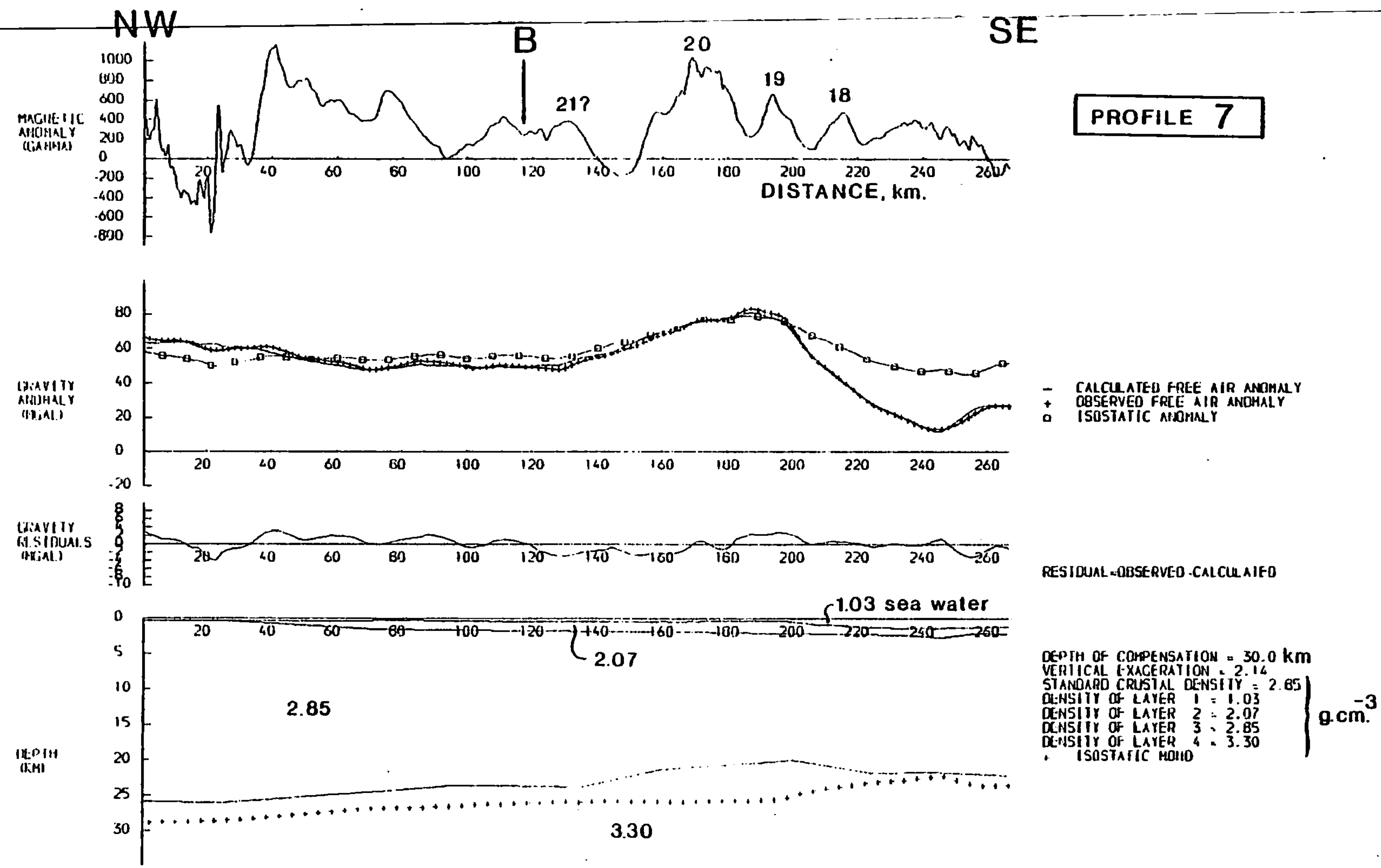

Figure 5.10 Gravity interpretation for profile 7. B represents the proposed ocean-continent boundary and marine magnetic anomalies 18 through 21 are also indicated.

crust of at least a thickness 20 - 25 km (Detrick and Watts, 1979 based on work by Bott et al, 1971) or even greater (cf. the crustal thickness beneath the Iceland-Faeroe Ridge, 30 - 35 km, after Bott and Gunnarsson, 1980). The thickness of oceanic crust beneath profile 7 has been influenced by proximity to the aseismic ridge.

This interpretation of thickened oceanic crust is supported by work carried out by Demenitskaya and Dibner (1966) who presented a sketch map of crustal thickness in the northern Atlantic regions which indicated a depth to the Moho of between 20 and 27.5 km in the vicinity of the Greenland-Iceland Ridge.

A detailed crustal model for the gravity data along profile 9, parallel to the crustal axis of the Greenland-Iceland Ridge is not presented. The shallow penetration of the single-channel shipborne monitor seismic display prevented any reliable estimate of upper crustal sediment structure due primarily to strong water-bottom multiple interference. A Bouguer anomaly calculated along the profile indicated a distinct low of some 16 mgal over an area of sediment cover suggested by the limited penetration of the seismic data. A density contrast of -0.75 g cm^{-3} indicates a sediment thickness of the order of 500 m in the deepest part of the section. However, the steep Bouguer anomaly gradients of 4.5 and 1.8 mgal km^{-1} observed by Bott et al (1971) over the continental margin between the Iceland-Faeroe Ridge and the Faeroe block were not observed along the western segment of profile 9 and the large magnitude variation in Bouguer anomaly of about 90 mgal was also absent. These results may indicate that the location of the ocean-continent boundary shown in Figure 5.7 is incorrect and that it should be displaced by a minimum of some 100 km to the west. This is unlikely, however, in view of the interpretation of oceanic magnetic anomalies in this study and by Voppel et al (1979).

Profile 11

The interpretation of gravity data along profile 11, to the north of the submerged aseismic ridge in the Denmark Straits, is shown in Figure 5.11.

The sediments along profile 11 were divided into two units. The proposed Early Miocene unconformity U3 was assumed to separate sediments of average velocities 2.1 and 3.0 km s^{-1} respectively (see Section 4.4). The corresponding densities are 2.00 and 2.22 g cm^{-3} (Nafe and Drake, 1963).

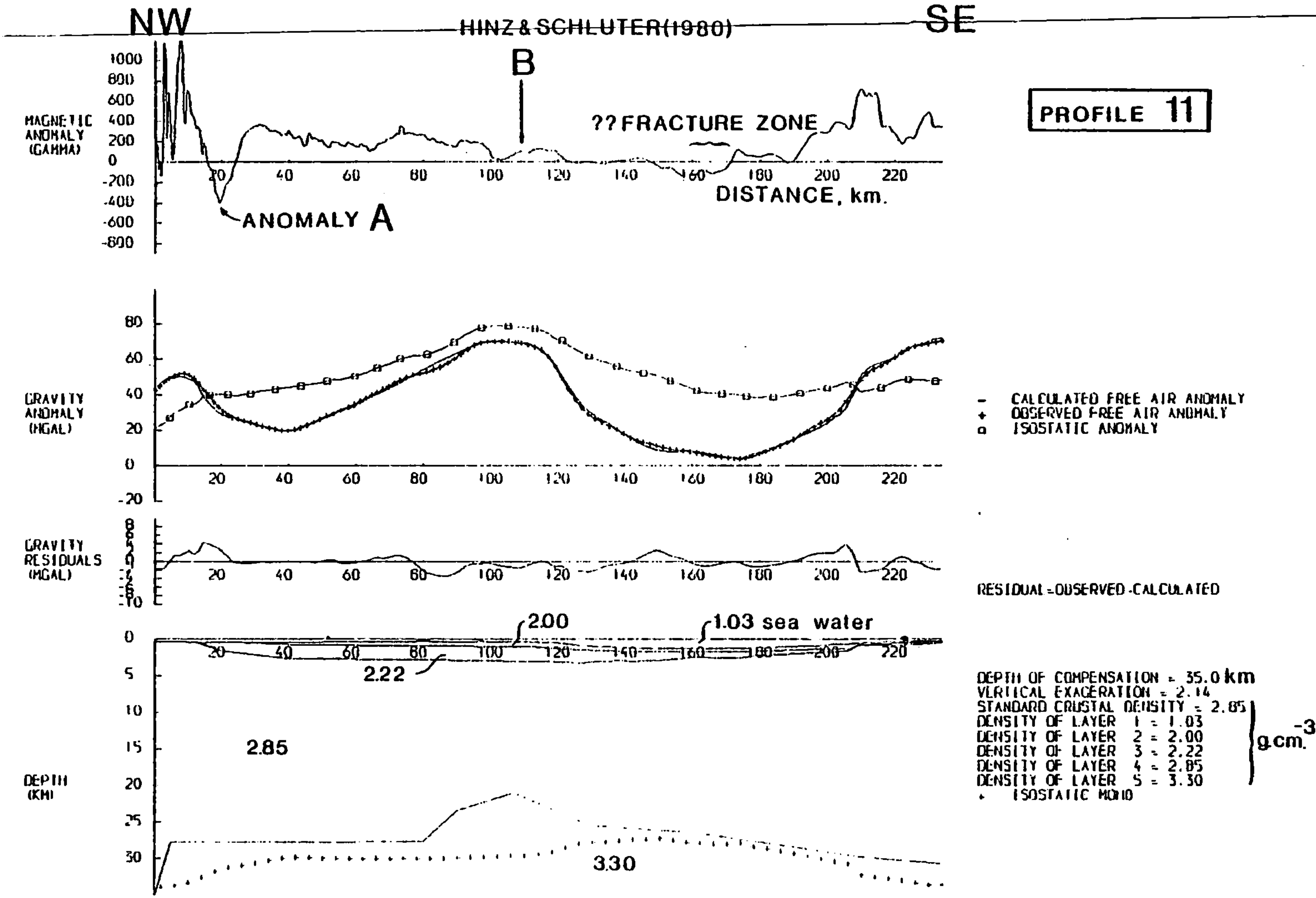

Figure 5.11 Gravity interpretation for profile 11. B represents the proposed ocean-continent boundary taken from Hinz and Schluter (1980).

The possible continuation of the plateau basalts of the Blosseville coast beneath the Tertiary prograded sediments (Section 5.2.2) was not included in detail in the gravity interpretation. A mean value of 2.86 g cm^{-3} for the bulk density of Tertiary basalts from the Faeroe Islands, under no confining pressure, was calculated from data presented by Kern and Richter (1979). This density was also found from the data of Saxov and Abrahamsen (1966). A density of 2.83 g cm^{-3} was quoted for Tertiary basalts of Iceland by Schleusner et al (1976). Kern and Richter (1979) further quoted a density range of 2.82 - 2.99 g cm^{-3} for Faeroese basalts at a confining pressure of 0.5 kbar (approximately equivalent to a depth of burial of 1300 m). A standard crustal density of 2.85 g cm^{-3} should ensure no major errors have been introduced into the gravity model solution due to the absence of the proposed basalt layer.

The striking aspect of the gravity interpretation in Figure 5.11 is the almost constant depth to the Moho. The two-dimensional isostatic anomaly and the isostatically compensated Moho indicate that the Tertiary sedimentary wedge between 80 and 130 km is undercompensated. The ocean-continent boundary was taken from Hinz and Schlüter (1980) and corresponds almost exactly with the location proposed by Larsen (1980). Nunns (1980) developed an ocean-continent boundary based on model reconstructions of the Norwegian-Greenland Seas and his continental margin was located about 27 km to the west of that indicated in Figure 5.11. Perhaps significantly, the ocean-continent boundary as shown coincides with the thinnest portion of crust predicted by the gravity model.

~~The very sharp increase in Moho depth inferred at the western extremity of profile 11 was necessary to accommodate the rapid fall in the free-air gravity anomaly to the west. This rapid crustal thickening is unlikely to be real, although it may indicate an area of overcompensation reflecting the effect of gravity loading during extensive glaciation due to thick surface ice cover.~~

The close proximity of the Greenland-Iceland aseismic ridge and its probable association with thickened crust of oceanic affinity explains the abnormal thickness of oceanic crust inferred by the gravity model. The formation of thick crust of oceanic type beneath the Greenland-Iceland-Faeroe Ridge has been explained in terms of an unusually vigorous differentiation of crustal material from an anomalously hot, low-density upper mantle (Bott et al, 1971; Bott, 1974). The subsequent subsidence of the aseismic ridge is attributed to the cooling and thermal contraction of the underlying lithosphere on which the ridge was built (Bott et al, 1971; Vogt, 1972). These authors explain the anomalously shallow depth of the Greenland-Iceland-Faeroe Ridge as a direct result of its remaining at or above sea level from the time of its formation in Eocene times until the Middle Miocene (Vogt, 1972; Nilsen, 1978b; Grønlie, 1979). The crustal thickness beneath the Iceland-Faeroe Ridge in its central and south-eastern parts has been estimated from crustal refraction seismology studies as between 30 and 35 km (Bott and Gunnarsson, 1980). It is the abnormal thickness of the crust along the aseismic ridge which maintains its unusually high elevation, although the upper mantle underlying it may be relatively less dense due to a residual thermal anomaly.

The location of the proposed fracture zone (Vogt et al, 1980) is shown in Figure 5.11. No gravity or magnetic anomaly is apparently associated with this feature. An estimate of the gravity anomaly due to such a structure was made using the formula:

$$A = 2G\rho\theta t$$

where A = the gravity anomaly
ρ = the density contrast
θ = the angle subtended by the causative body at the point of observation
t = the thickness of the causative body
and G = the gravitational constant.

Assuming $\rho = +0.71$ g cm^{-3} (sediment = 2.19 g cm^{-3} and basalt = 2.90 g cm^{-3} to give a maximum value for ρ) and calculating θ and t from Figure 4.2, the gravity anomaly computed was about +10 mgal. Since this was a maximum estimate assuming a two-dimensional structure, the gravity anomaly caused by the "horst" feature may not be reliably detected at the surface by marine gravity data. However, the age contrast between the oceanic crust on either side of the fracture zone is not markedly different and therefore, no significant change in elevation is apparent due to differential rates of thermal contraction in the underlying lithosphere.

Profile 13

The interpretation of gravity data along this profile proved to be rather difficult. A gravity model is shown in Figure 5.12 but the inferred Moho appears to be unrealistic.

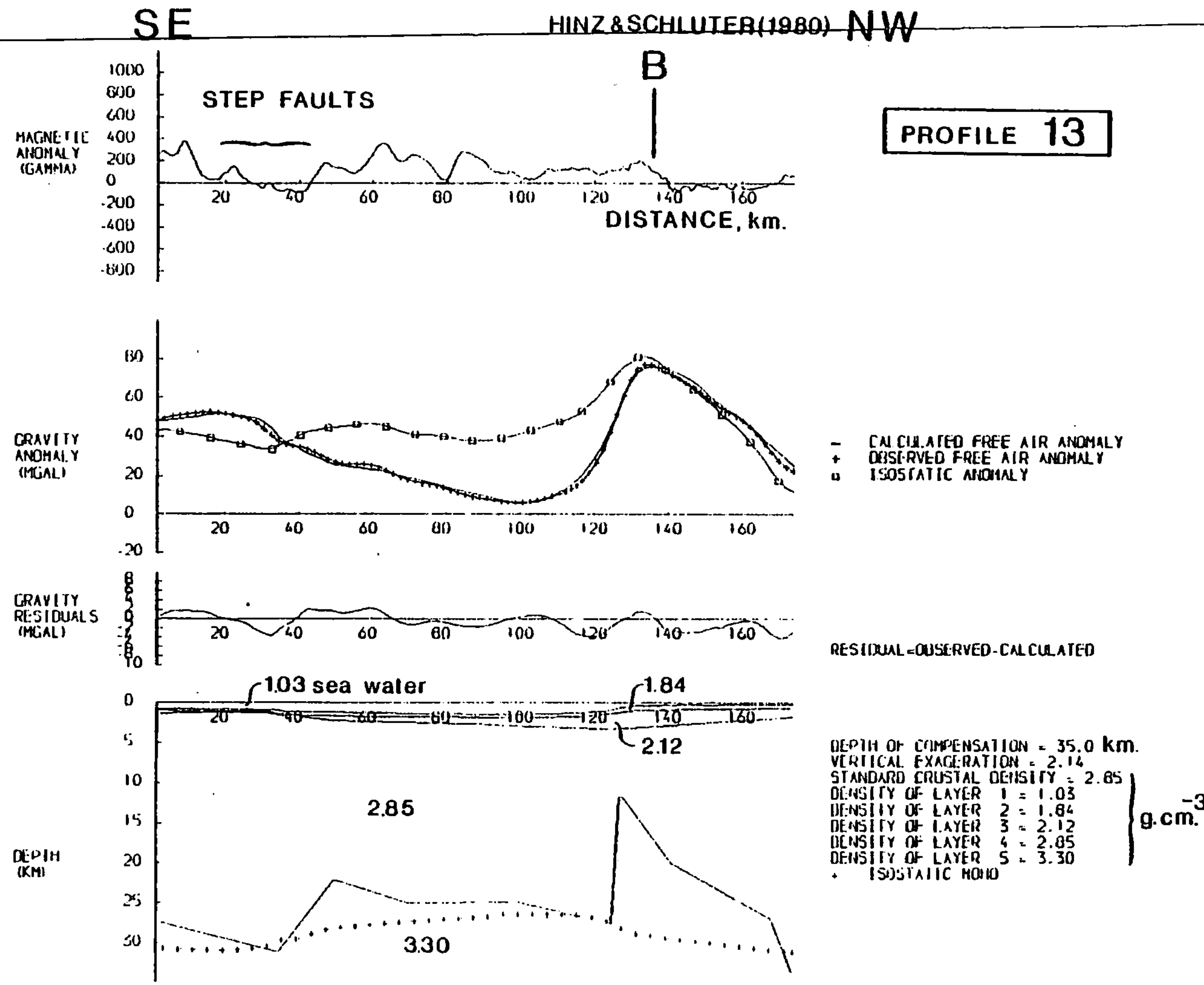

Figure 5.12 Gravity interpretation for profile 13. B represents the proposed ocean-continent boundary taken from Hinz and Schluter (1980).

The sediment velocities above and below the interpreted Early Miocene unconformity U3 were taken from the two sonobuoys, 14V28 and 86V29 (Figures 1.2 and 4.13). The velocities 1.78 and 2.55 km s^{-1} are equivalent to densities of 1.84 and 2.12 g cm^{-3} respectively (Nafe and Drake, 1963).

The ocean-continent boundary proposed by Hinz and Schlüter (1980) is also marked in Figure 5.12.

The major difficulty encountered in developing a crustal model consistent with the gravity data of profile 13 was fitting the observed free air gravity high situated to the west of 120 km along the profile. The inferred Moho seems to be nonsense. However, whilst apparently unrealistic, it does indicate the requirement for a high density causative body within the crust. Grow et al (1979) infer the presence of a large scale mafic intrusion on a marine seismic section off New Jersey on the east coast of North America. Their intrusion is associated with a magnetic anomaly of some 450 nT whereas there is no such anomaly recognisable on profile 13. Assuming a Curie point of 600^{o}C (Sheriff, 1980), the depth of 12 km to the modelled intrusion implies a geothermal gradient of 50^{o}C km^{-1} in order to ensure that such a mafic intrusion would have no magnetic signature. Such a geothermal gradient is unlikely.

The variation shown by the modelled Moho from the isostatically compensated Moho suggests that profile 13 is located in approximate isostatic equilibrium. The wedge of Tertiary sediments appears to be uncompensated, a feature characteristic of this continental margin to the south of the Denmark Straits also.

Since the oceanic crust is associated with spreading in the Norwegian Sea and, in particular, about the Kolbeinsey Ridge (Vogt et al, 1980), a relatively young ocean basin (24 Ma old, Figure 1.4), thick oceanic crust would be expected (Roots et al, 1979). However, the gravity model in Figure 5.12 is suspect and any further comments are superfluous.

For completeness, the free air gravity anomaly projected along simplified ship's track for the Durham cruises of 1973, 1974 and 1977 is shown in Figure 5.13.

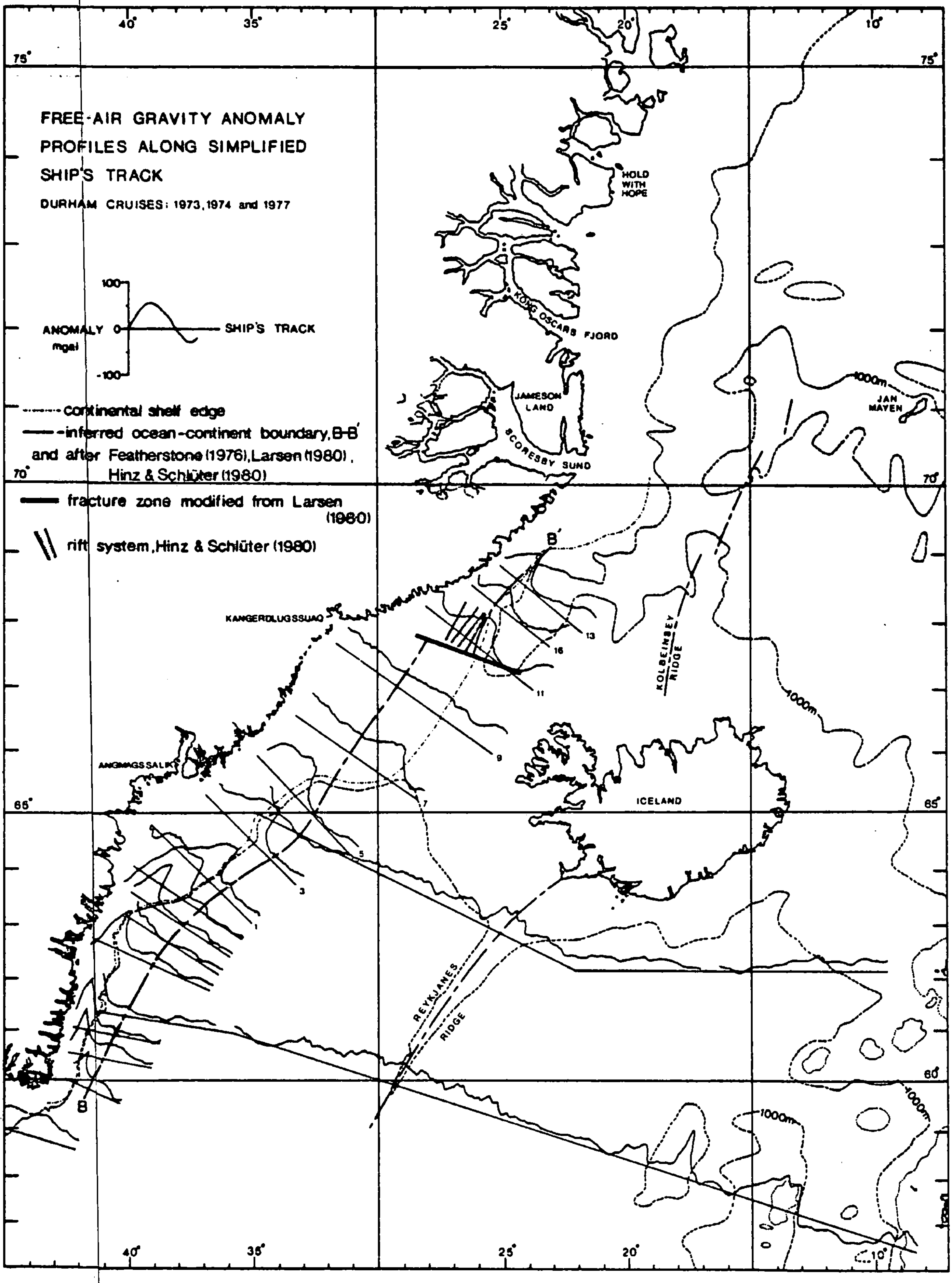

Figure 5.13 Interpretation of free air gravity anomaly profiles along simplified ship's track for Durham cruises 1973, 1974 and 1977.

CHAPTER 6

CONCLUSIONS

6.1 Introduction

The scientific goals of the 1977 Durham University marine geophysical survey of the continental margin of East Greenland were outlined in Chapter 1. This final chapter includes some remarks about the magnetic interpretation technique developed during the work and draws together the main conclusions of the thesis. Brief speculation on petroleum prospects draws the work to a close.

6.2 Magnetic interpretation techniques

The method of determining the depth to magnetic sources using the maximum entropy method (MEM) spectral density estimate was developed in Chapter 3 and applied to real data in Chapter 5. The results were disappointing when the method was applied to magnetic anomalies generated from model bodies of known geometry. Nevertheless, it has permitted spectral analysis to be performed on very short data sets for which more traditional methods would have been unsuitable. The recommendation that data sets be at least 6 times greater than the maximum depth to the causative body (Regan and Hinze, 1976) was confirmed.

When applied to real magnetic data, the accuracy of MEM spectral depth estimates was suspect, sometimes showing good agreement with structure inferred from seismic reflection data and gravity modelling, and at other times, demonstrating apparently unrealistic results.

6.3 Implications of the geophysical interpretation

Several scientific objectives were proposed at the beginning of this thesis. By extending previous geophysical work undertaken on the continental margin of East Greenland (Figure 1.1) from 63°N to 69°N, it has been possible to draw the following conclusions:

(1) The definition of the ocean-continent boundary depended on the interpretation of marine magnetic anomalies because the seismic character of oceanic and continental type "basement" was not significantly different (an observation also made by Roberts (1975) in the Rockall

Trough), except on profiles 5 (Figure 4.10) and 3 (Figure 4.11) respectively, and the variation in crustal thickness inferred by gravity modelling was not diagnostic of either oceanic or continental type crust. A lithospheric model with thick oceanic crust at the continental boundary was proposed by Roots et al (1979). Since the profiles along which magnetic data were available were widely separated and correlation of marine anomalies through the Denmark Straits was not definitive, the proposed ocean-continent boundary of Figure 5.7 must be considered tentative.

(2) The indication of the gravity interpretation of lines immediately adjacent to the submerged Greenland-Iceland Ridge (profiles 7 and 11 respectively) is that the aseismic ridge is isostatically compensated by local Airy-type thickening of oceanic crust beneath it (cf. the Iceland-Faeroe Ridge; Bott and Gunnarsson, 1980). This conclusion is supported by work carried out on the isostatic equilibrium of aseismic ridges by Detrick and Watts (1979).

(3) The interpretation of the geophysical data, in particular the magnetic anomaly, A along profile 11 (Figure 5.11), indicates that the plateau basalts of the Blosseville coast do not terminate offshore. Instead, the width of the magnetic anomaly, A, the implication of the seismic interpretation and the evidence supplied by seismic refraction velocities from sonobuoy, S2 (Figure 4.13) suggest that the plateau basalts were downflexured (under fault control, cf. Nielsen, 1975) and continue offshore beneath the prograding wedge of Tertiary sediments. This is an explicit statement of the nature of the offshore continuation of the plateau basalts, similar to that suggested by Larsen (1980).

(4) The detailed interpretation of processed multi-channel seismic reflection data along profile 11 and an assessment of sonobuoy refraction velocities off the East Greenland coast have raised doubts about the existence of a massive accumulation of pre-drift Mesozoic sediments in coast-parallel offshore basins as postulated by Surlyk (1977). Apart from southward extrapolation of the Mesozoic, south-plunging sedimentary basin of Jameson Land (north of Scoresby Sund, Figure 1.2), there is no geophysical evidence to the author's knowledge which supports the presence of an offshore continuation of the Mesozoic basin to the north in the vicinity of the Denmark Straits. Mesozoic sediments may be present offshore over continental crust but it is likely that they will be overlain by Tertiary plateau basalts in the region of, and to

the north of, the Denmark Straits.

(5) The wedge of prograded Tertiary sediments along the continental margin is not isostatically compensated. The location of the continental scarp, cut-back due to erosion by contour currents (Featherstone, 1976) bears no a priori relationship to the proposed ocean-continent boundary (Figure 5.7).

(6) The recognition of oceanic magnetic anomalies and the identification of the ocean-continent boundary, especially on profile 5 (Figure 4.10) and profile 3 (Figure 4.11), indicate the truncation of anomalies 22 through 24 against the continental margin of East Greenland. This conclusion is independently supported by Voppel et al (1979) from a study of detailed magnetic measurements south of the Iceland-Faeroe Ridge. Thus, the westward jump of the spreading axis in the Reykjanes Basin prior to anomaly 21 time proposed by Featherstone (1976) is confirmed.

(7) The seismic reflection data along profiles 13 and 16, and especially the processed multi-channel seismic reflection data of profile 11 (Chapter 4), have enabled the recognition of the offlap relationship between Tertiary sediments and the underlying oceanic crust as predicted by Nilsen (1978a). Two seismic horizons, U1 and U3 (Figure 4.2), have been tentatively dated and the possibility of a detailed seismic stratigraphic interpretation (Payton, 1977) of the Tertiary prograded sediments of the East Greenland margin to the north of the Denmark Straits has been suggested (Figure 4.2).

6.4 Ideas for future work

Further work on the East Greenland continental margin should include deep seismic refraction work to establish the actual depth to the Moho discontinuity, and hence provide crustal thicknesses. Reversed refraction lines parallel to and on each side of the proposed ocean-continent boundary should be undertaken in order to reduce any ambiguities of interpretation introduced by traversing the ocean-continent transition zone.

The acquisition of good quality multi-channel seismic reflection data over several profiles perpendicular to the continental slope (with strike-line cross-ties) should provide excellent records for the implementation of a seismic stratigraphic analysis of the East Greenland continental margin.

And of course, the luxury of deep drilling would provide definitive solutions concerning the age of oceanic crust north of the proposed fracture zone on profile 11, the confirmation of the offshore continuation of the Blosseville coast plateau basalts and the existence of deeply-buried Mesozoic sediments offshore, for example.

Further work should also be done to delineate the precise location of the fracture zone in the vicinity of profile 11. The apparent absence of any associated gravity or magnetic signature is rather puzzling (cf. the gravity anomalies associated with Jan Mayen and Greenland-Senja fracture zones respectively and described by Talwani and Eldholm, 1977). The delineation of the fracture zone affecting oceanic anomalies 20 and 21 at 65°N should also be carried out.

This thesis offers a few more insights into the structure of the continental margin of East Greenland. Further refinements may arise from continental motion studies and computer-oriented palaeogeographical reconstructions (for example, Nunns, 1980).

6.5 Petroleum prospects

Any development of offshore hydrocarbon accumulations will of necessity demand the application of deep-water drilling technology in water depths of 300 m or more on the continental shelf.

Onshore geology has been investigated for petroleum potential and the results tentatively extrapolated for their offshore implications (Stevens and Perch-Nielsen, 1972; Henderson, 1976). Attention has been focused on the Upper Permian - Lower Cretaceous rocks in which four samples were designated as potential source rocks (Henderson, 1976). However, since the existence of pre-Tertiary sediments offshore is not proven, these results may not necessarily apply. And if Mesozoic sediments are present east of the Blosseville coast, the wildcat driller may encounter the best cap rock in the world - plateau basalt of substantial thickness! The possibility of Tertiary source rocks cannot be ruled out (Hinz and Schlüter, 1980).

Reservoir rocks are likely to be present as porous sandstones within the thick prograded Tertiary sequence. The apparent absence of well-defined structures and salt (or mud) diapirism may indicate the requirement to look for subtle stratigraphic traps.

The search for hydrocarbons along the continental margin of East Greenland may provide the oil industry with a difficult proposition.

REFERENCES

Akaike, H., 1969a. Fitting autoregressive models for prediction. Ann. Inst. Statist. Math., 21, 243-247.

Akaike, H., 1969b. Power spectrum estimation through autoregressive model fitting. Ann. Inst. Statist. Math., 21, 407-419.

Akaike, H., 1970. Statistical predictor indentification. Ann. Inst. Statist. Math., 22, 203-217.

Am, K., 1972. The arbitrarily magnetised dyke: interpretation by charactersitics. Geoexploration, 10, 63-90.

Andersen, N., 1974. On the calculation of filter coefficients for maximum entropy spectral analysis. Geophysics, 39, 69-72.

Ballard, J.A. & Feden, R.H.,1970. Diapiric structures on the Campeche Shelf and Slope, Western Gulf of Mexico. Bull. Geol. Soc. Am., 81, 505-512.

Barraclough, D.R., 1978. Spherical harmonic models of the geomagnetic field. Geomagn. Bull. Inst. Geol. Sci., 8, 66 pages.

Bedenberger, J.W., Johnston, R.C. & Neitzel, E.B., 1970. Electroacoustic characterisitcs of marine seismic streamers. Geophysics, 35, 1054-1072.

Berggren, W.A., McKenna, M.C., Hardenbol, J. & Obradovich, J.D., 1978, Revised Palaeogene polarity time scale. J. Geology, 86, 67-81.

Berryman, J.G., 1978. Choice of operator length for maximum entropy spectral analysis. Geophysics, 43, 1384-1391.

Bhattacharyya, B.K., 1966. Continuous spectrum of the total magnetic field anomaly due to a rectangular prismatic body. Geophysics, 31, 97-121.

Bhimasankaram, V.L.S., Nagendra, R. & Seshagiri Rao, S.V., 1977. Interpretation of gravity anomalies due to finite inclined dykes using Fourier transformation. Geophysics, 42, 51-59.

Birkelund, T. & Perch-Nielsen, K., 1976. Late Palaeozoic - Mesozoic evolution of Central East Greenland. In: Escher, A. & Watt, W.S. (Editors), Geology of Greenland. Grønlands Geologiske Unders., The Geological Survey of Greenland, Copenhagen, 305-339.

Birkelund, T., Perch-Nielsen, K., Bridgwater, D., & Higgins, A.K., 1974. An outline of the geology of the Atlantic coast of Greenland. In: Nairn, A.E.M. & Stehli, F.G. (Editors), The Ocean basins and margins. Vol. 2: The North Atlantic. Plenum Press, New York-London, 125-159.

Birkenmajer, K.,1972. Report of investigations of Tertiary sediments of Kap Brester, Scoresby Sund, East Greenland. Rapp. Grønlands geol. Unders., 48, 85-91.

Birkenmajer, K., Emeleus, C.H. & Watt, W.S., 1976. Coast-parallel faulting of Tertiary lavas and sediments at Savoia Halvø, East Greenland. Unpublished manuscript, C.H. Emeleus, pers. comm.

Black, D.I. & Scollar, I., 1969. Spatial filtering in the wave-vector domain. Geophysics, 34, 916-923.

Blackman, R.B. & Tukey, J.W., 1958. The Measurement of Power Spectra from the point of view of communications engineering. Dover Publications, Inc., New York, 190 pages.

Bloomfield, P., 1976. Fourier Analysis of Time Series: An Introduction, 5th edition. John Wiley & Sons, Inc., New York, 258 pages.

Bott, M.H.P., 1971. The Interior of the Earth. Edward Arnold (Publishers) Ltd., London, 316 pages.

Bott, M.H.P., 1974. Deep structure, evolution and origin of the Icelandic transverse ridge. In: Kristjansson, L. (Editor), Geodynamics of Iceland and the North Atlantic Area. Proceedings of the NATO Advanced Study Institute, Reykjavik, Iceland, 1-7 July, 1974. D. Reidel Publ. Co., Dordrecht, Holland, 33-47.

Bott, M.H.P., 1979. Subsidence mechanisms at passive continental margins. In: Watkins, J.S., Montadert, L. & Dickerson, P.W. (Editors), Geological and Geophysical Investigations of Continental Margins. Am. Ass. Petrol. Geol., Memoir 29, Tulsa, Oklahoma, U.S.A., 3-9.

Bott, M.H.P., Browitt, C.W.A. & Stacey, A.P., 1971. The Deep Structure of the Iceland-Faeroe Ridge. Marine Geophys. Res., 1, 328-351.

Bott, M.H.P. & Gunnarsson, K., 1980. Crustal structure of the Iceland-Faeroe Ridge. J. Geophys., 47, 221-227.

Bott, M.H.P., Nielsen, P.H. & Sunderland, J., 1976. Converted P-waves originating at the continental margin between the Iceland-Faeroe Ridge and the Faeroe Block. Geophys. J. R. astr. Soc., 44, 229-238.

Bott, M.H.P., Sunderland, J., Smith, P.J., Casten, U. & Saxov, S., 1974. Evidence for continental crust beneath the Faeroe Islands. Nature, 248, 202-204.

Brandsaeter, H., Farestveit, A. & Ursin, B., 1979. A new high-resolution or deep penetration airgun array. Geophysics, 44, 865-879.

Brooks, C.K., 1973. Tertiary of Greenland - a volcanic and plutonic record of continental break-up. In: Pitcher, M.G. (Editor), Arctic Geology, Am. Ass. Petrol. Geol., Memoir 19, Tulsa, Oklahoma, U.S.A., 150-160.

Brooks, C.K., 1979. Geomorphological observations at Kangerdlugssuaq, East Greenland. Meddr. Grønland, Geoscience, 1, 1-21.

Brooks, C.K. & Gleadow, A.J.W., 1977. A fission-track age for the Skaergaard intrusion and the age of the East Greenland basalts. Geology, 5, 539-540.

Bruckshaw, J.M. & Kunaratnam, K., 1963. The interpretation of magnetic anomalies due to dykes. Geophys. Prospect., 11, 509-522.

Buchanan, D.J., 1977. Comment on 'The radiation of acoustic waves from an air-gun'. Geophys. Prospect., 25, 564-568.

Bullard, E.C. & Mason, R.G., 1963. The magnetic field over the oceans. In: Hill, M.N. (Editor), The Sea. Vol. 3: The Earth beneath the Sea, History. Interscience Publ., John Wiley & Sons, New York, 175-217.

Burg, J.P., 1967. Maximum entropy spectral analysis. Paper presented at the 37th Annual International SEG Meeting, Oklahoma City, Oklahoma, 31 October, 1967.

Burg, J.P., 1972. The relationship between maximum entropy spectra and maximum likelihood spectra. Geophysics, 37, 375-376.

Callomon, J.G., Donovan, D.T., & Trumpy, R., 1972. An annotated map of the Permian and Mesozoic formations of East Greenland. Meddr. Grønland, 168, 3, 35 pages.

Cande, S.C. & Kristoffersen, Y., 1977. Late Cretaceous magnetic anomalies in the North Atlantic. Earth Planet. Sci. Lett., 35, 215-224.

Carey, S.W., 1958. The tectonic approach to continental drift. In: Continental Drift Symposium, University of Tasmania, Hobart, 177-354 (not seen).

Cassano, E. & Rocca, F., 1975. Interpretation of magnetic anomalies using spectral estimation techniques. Geophys. Prospect., 23, 663-681.

Chen, W.Y. & Stegen, G.R., 1974. Experiments with maximum entropy power spectra of sinusoids. J. geophys. Res., 79, 3019-3022.

Cianciara, B. & Marcak, H., 1976. Interpretation of gravity anomalies by means of local power spectra. Geophys. Prospect., 24, 273-286.

Claerbout, J.F., 1976. Fundamentals of geophysical data processing. McGraw-Hill, New York, 274 pages.

Clague, D.A. & Straley, P.F., 1977. Petrologic nature of the oceanic Moho. Geology, 5, 133-136.

Cooley, J.W. & Tukey, J.W. 1965. An algorithm for the machine computation of complex Fourier series. Math. Comput., 19, 297-301.

Coron, S., 1972. Bureau Gravimetrique International, Information Bulletin, No. 29.

Currie, R.G., 1973. Fine structure of the sunspot spectrum - 2 to 70 years. Astrophys. Space Sci., 20, 509-518.

Deer, W.A., 1976. Tertiary igneous rocks between Scoresby Sund and Kap Gustav Holm, East Greenland. In: Escher, A. & Watt, W.S. (Editors), Geology of Greenland. Grønlands Geologiske Unders., The Geological Survey of Greenland, Copenhagen, 405-429.

Demenitskaya, R.M. & Dibner, V.D., 1966. Morphological structure and the earth's crust of the North Atlantic region. In: Poole, W.H. (Editor), Continental margins and island arcs, Geol. Surv. Canada, Paper 66-15, 63-79.

Detrick, R.S. & Watts, A.B., 1979. Analysis of isostacy in the World's oceans: 3. Aseismic Ridges. J. geophys. Res., 84, 3637-3653.

Dewey, J.F., Pitman, W.C., Ryan, W.B.F. & Bonin, J., 1973. Plate tectonics and the evolution of the Alpine System. Bull. Geol. Soc. Am., 84, 3137-3180.

Dix, C.H., 1955. Seismic velocities from surface measurements. Geophysics, 20, 68-86.

Dobrin, M.B., 1976. Introduction to geophysical prospecting, 3rd edition. McGraw-Hill, New York, 630 pages.

Eldholm, O. & Ewing, J., 1971. Marine geophysical survey in the south-western Barents Sea. J. geophys. Res., 76, 3832-3841.

Eldholm, O. & Windisch, C.C., 1974. The sediment distribution in the Norwegian-Greenland Sea. Bull. Geol. Soc. Am., 85, 1661-1676.

Embree, P., Burg, J.P. & Backus, M.M., 1963. Wide-band velocity filtering - the Pie-Slice process. Geophysics, 28, 948-974.

Emery, K.O., Uchupi, E., Phillips, J.D., Bowin, C.O., Bunce, E.T. & Knott, S.T., 1970. Continental rise of eastern North America. Bull. Am. Ass. Petrol. Geol., 54, 44-108.

Escher, A. & Watt, W.S. (Editors), 1976. Geology of Greenland. Grønlands Geologiske Unders., The Geological Survey of Greenland, Copenhagen, Denmark, 604 pages.

Ewing, C.E. & Mitchell, M.M., 1970. Introduction to Geodesy. American Elsevier Publ. Co., Inc., New York.

Ewing, J. & Ewing, M., 1959. Seismic refraction measurements in the Atlantic Ocean basins, in the Mediterranean Sea, on the Mid-Atlantic Ridge, and in the Norwegian Sea. Bull. Geol. Soc. Am., 70, 291-318.

Ewing, M., Le Pichon, X. & Ewing, J., 1966. Crustal structure of the mid-ocean ridges: 4. Sediment distribution in the Atlantic Ocean and the Cenozoic history of the Mid-Atlantic Ridge. J. geophys. Res., 71, 1611-1636.

Faller, A.M., 1975. Palaeomagnetism of the oldest Tertiary basalts in the Kangerdlugssuaq area of East Greenland. Bull. Geol. Soc. Denmark, 24, 173-178.

Faller, A.M., Steiner, M. & Kobayashi, K., 1978. Palaeomagnetism of basalts and interlayered sediments drilled during DSDP Leg 49 (N-S transect of the northern Mid-Atlantic Ridge). In: Luyendyk, B.P., Cann, J.R., et al., Initial Reports of the Deep Sea Drilling Project, 49: Washington, (U.S. Government Printing Office), 769-780.

Featherstone, P.S., 1976. A geophysical investigation of the south-east Greenland continental margin. Ph.D. thesis, University of Durham, 208 pages.

Featherstone, P.S., Bott, M.H.P. & Peacock, J.H., 1977. Structure of the continental margin of south-eastern Greenland. Geophys. J. R. astr. Soc., 48, 15-27.

Fleischer, U., 1971. Gravity surveys over the Reykjanes Ridge and between Iceland and the Faeroe Islands. Marine Geophys. Res., 1, 314-327.

Fleischer, U., Holzkamm, F., Vollbrecht, K. & Voppel, D., 1974. Die struktur des Island-Färöer-Rückens aus geophysikalischen Messungen. Deutsch. hydrogr. Zeit., 27, 97-113.

Forster, R., 1978. Evidence for an open seaway between northern and southern proto-Atlantic in Albian times. Nature, 272, 158-159.

Fougere, P.F., Zawalick, E.J. & Radoski, H.R., 1976. Spontaneous line splitting in maximum entropy power spectrum analysis. Phys. Earth Planet. Int., 12, 201-207.

Gairaud, H., Jacquart, G., Aubertin, F. & Beuzart, P., 1978. The Jan Mayen Ridge: synthesis of geological knowledge and new data. Ocean. Acta., 1, 335-358.

Giles, B.F., 1968. Pneumatic acoustic energy source. Geophys. Prospect., 16, 21-53.

Giles, B.F. & Johnston, R.C., 1973. System approach to air-gun array design. Geophys. Prospect., 21, 77-101.

Grant, A.C., 1972. The continental margin off Labrador and eastern Newfoundland - morphology and geology. Can. J. Earth Sci., 9, 1394-1430.

Grant, F.S. & West, G.F., 1965. Interpretation theory in applied geophysics. McGraw-Hill, New York, 584 pages.

Green, A.G., 1972. Magnetic profile analysis. Geophys. J. R. astr. Soc., 30, 393-403.

Gregersen, S., 1971. Surface wave dispersion and crust structure in Greenland. Geophys. J. R. astr. Soc., 22, 29-39.

Grønlie, G., 1979. Tertiary palaeogeography of the Norwegian-Greenland Sea. Norsk. Polarinstitutt, Skr., 170, 49-61.

Grønlie, G.& Talwani, M., 1978. Geophysical atlas of the Norwegian-Greenland Sea. VEMA Research Series 1V, Lamont-Doherty Geological Observatory, Palisades, New York.

Grow, J.A., Mattick, R.E. & Schlee, J.S., 1979. Multichannel seismic depth sections and interval velocities over outer continental shelf and upper continental slope between Cape Hatteras and Cape Cod. In: Watkins, J.S., Montadert, L. & Dickerson, P.W. (Editors), Geological and Geophysical Investigations of Continental Margins. Am. Ass. Petrol. Geol., Memoir 29, Tulsa, Oklahoma, U.S.A., 65-83.

Gudmundsson, G., 1966. Interpretation of one-dimensional magnetic anomalies by use of the Fourier transform. Geophys. J. R. astr. Soc., 12, 87-97.

Gudmundsson, G., 1967. Spectral analysis of magnetic surveys. Ge[illegible] J. R. astr. Soc., 13, 325-337.

Hahn, A., Kind, E.G. & Mishra, D.C., 1976. Depth estimation of magn[illegible] sources by means of Fourier amplitude spectra. Geophys. Prospec[illegible] 24, 287-308.

Haigh, B.I.R., 1973. North Atlantic oceanic topography and lateral variations in the upper mantle. Geophys. J. R. astr. Soc., 33, 405-420.

Hailwood, E.A., Bock. W., Costa, L., Dupeuble, P.A., Müller, C. & Schnitker, D., 1979. Chronology and biostratigraphy of north-east Atlantic sediments, DSDP Leg 48. In: Montadert, L., Roberts, D.G., et al., Initial Reports of the Deep Sea Drilling Project, 48: Washington (U.S. Government Printing Office), 377-414.

Haller, J., 1970. Tectonic map of East Greenland. Meddr. Grønland, 171, 286 pages.

Haller, J., 1971. Geology of the East Greenland Caledonides. Interscience, John Wiley & Sons, London, 413 pages.

Hammer, S., 1963. Deep gravity interpretation by stripping. Geophysics, 28, 369-378.

Harrison, C.G.A., McDougall, I. & Watkins, N.D., 1979. A geomagnetic field reversal time scale back to 13.0 million years before present. Earth Planet. Sci. Lett., 42, 143-152.

Hassan, M.Y., 1953. Tertiary faunas from Kap Brewster, East Greenland. Meddr. Grønland, 3, 5, 42 pages.

Havill, R.L. & Walton, A.K., 1975. Elements of Electronics for Physical Scientists. MacMillan Press Ltd., London, 321 pages.

Heiland, C.A., 1940. Geophysical Exploration. 4th printing, Prentice-Hall, Inc., New York, 1951, 1013 pages.

Heirtzler, J.R., Dickson, G.O., Herron, E.M., Pitman III, W.C., & Le Pichon, X., 1968. Marine magnetic anomalies, geomagnetic field reversals and motions of the ocean floor and continents. J. geophys. Res., 73, 2119-2136.

Henderson, G., 1976. Petroleum geology. In: Escher, A. & Watt, W.S. (Editors), Geology of Greenland. Grønland Geologiske Unders., The Geological Survey of Greenland, Copenhagen, 489-505.

Henriksen, N. & Higgins, A.K., 1976. East Greenland Caledonian fold belt. In: Escher, A. & Watt, W.S. (Editors), Geology of Greenland. Grønland Geologiske Unders., The Geological Survey of Greenland, Copenhagen, 182-246.

Hinz, K. & Schlüter, H. -U., 1979. The North Atlantic - Results of geophysical investigations by the Federal Institute for Geosciences and Natural Resources on North Atlantic continental margins. Oil Gas - European Mag., 3, 31-38.

Hinz, K. & Schlüter, H. -U., 1980. Continental margin off East Greenland. In: Proceedings of the 10th World Petroleum Congress, Bucharest, Vol. 2, Exploration Supply and Demand, Special Paper No. 7, Heyden & Son Ltd., London, 405-418.

Hood, P.J., 1964. The Königsberger ratio and the dipping-dyke equation. Geophys. Prospect., 12, 440-456.

Hornabrook, J.T., 1967. Seismic interpretation problems in the North Sea with special reference to the discovery well, 48 /6-1. Proceedings of the 7th World Petroleum Congress, Mexico, Vol. 2, 837-856.

Horton, C.W., Hempkins, H.B. & Hoffman, A.A.J., 1964. A statistical analysis of some aeromagnetic maps for the northwestern Canadian Shield. Geophysics, 29, 582-601.

Houtz, R.E. & Ewing, J.I., 1964. Sedimentary velocities of the western North Atlantic margin. Bull. Seis. Soc. Am., 54, 867-895.

Hsu, H.P., 1970. Fourier Analysis. Revised Edition, Simon & Schuster, New York, 274 pages.

Ingles, A.D., 1971. The interpretation of magnetic anomalies between Iceland and Scotland. Ph.D. thesis, University of Durham, 152 pages.

Johnsen, S.J. & Andersen, N., 1978. On power estimation in maximum entropy spectral analysis. Geophysics, 43, 681-690.

Johnson, G.L. & Heezen, B.C., 1967. Morphology and evolution of the Norwegian-Greenland Sea. Deep-Sea Res., 14, 755-771.

Johnson, G.L., McMillan, N.J. & Egloff, J., 1975a. East Greenland continental margin. In: Yorath, C.J., Parker, E.R. & Glass, D.J. (Editors), Canada's Continental Margins and Offshore Petroleum Exploration, Can. Soc. Petrol. Geol., Memoir 4, 205-224.

Johnson, G.L., Sommerhoff, G. & Egloff, J., 1975b. Structure and morphology of the west Reykjanes Basin and the southeast Greenland continental margin. Marine Geol., 18, 175-196.

Johnson, G.L., Southall, I.R., Young, D.W. & Vogt, P.R., 1972. The origin and structure of the Iceland Plateau and Kolbeinsey Ridge. J. geophys. Res., 77, 5688-5696.

Johnson, G.L. & Tanner, B., 1972. Geophysical observations on the Iceland - Faeroe Ridge. Jökull, 21, 45-52.

Jones, E.J.W., 1978. Seismic evidence for sedimentary troughs of Mesozoic age on the Hebridean continental margin. Nature, 272, 789-792.

Jones, E.J.W., Ewing, M., Ewing, J.I. & Eittreim, S.L., 1970. Influences of Norwegian Sea overflow water on sedimentation in the northern North Atlantic and Labrador Sea. J. geophys. Res., 75, 1655-1680.

Jones, R.H., 1965. A reappraisal of the periodogram in spectral analysis. Technometrics, 7, 531-542.

Kanasewich, E.R., 1975. Time sequence analysis in geophysics. 2nd revised edition, The University of Alberta Press, Edmonton, Alberta, Canada, 364 pages.

Kane, R.P., 1977. Power spectrum analysis of solar and geophysical parameters. J. Geomag. Geoelect., 29, 471-495.

Kearey, P., 1973. Crustal structure of the eastern Caribbean in the region of the Lesser Antilles and Aves Ridge. Ph.D. thesis, University of Durham.

Keen, C.E. & Barret, D.L., 1972. Seismic refraction studies in Baffin Bay: an example of a developing ocean basin. Geophys. J. R. astr. Soc., 30, 253-271.

Kern, H. & Richter, A., 1979. Compressional and shear wave velocities at high temperature and confining pressure in basalts from the Faeroe Islands. Tectonophysics, 54, 231-252.

Knecht, D.J., 1972. The Geomagnetic Field (a revision of Chapter 11, Handbook of Geophysics and Space Environments). AFCRL -72-0570, Air Force Surveys in Geophysics, No. 246, Project 7601, Air Force Cambridge Research Laboratories, Mass., U.S.A.

Kraichman, M.B., 1977. Electromagnetic background noise in the ocean due to geomagnetic activity in the period range 0.5 to 1000 seconds. US Naval Surface Weapons Centre, White Oak Lab., Silver Spring, Md., Technical Report, NSWC/WOL/TR-77-41, 1977, 35 pages.

Kristoffersen, Y., 1978. Sea-floor spreading and the early opening of the North Atlantic. Earth Planet. Sci. Lett., 38, 273-290.

Kristoffersen, Y. & Talwani, M., 1977. Extinct triple junction south of Greenland and the Tertiary motion of Greenland relative to North America. Bull. Geol. Soc. Am., 88, 1037-1049.

Kruczyk, J., Kadzialko-Hofmokl, M., Jelenska, M., Birkenmajer, K. & Arakelyants, M.M., 1977. Tertiary polarity events in Lower Silesian basalts and their K-Ar age. Acta Geophysica Poloinca, 25, 183-191 (reference to abstract only).

LaBrecque, J.L., Kent, D.V. & Cande, S.C., 1977. Revised magnetic polarity time scale for late Cretaceous and Cenozoic time. Geology, 5, 330-335.

Lacoss, R.T., 1971. Data adaptive spectral analysis methods. Geophysics, 36, 661-675.

LaCoste, L.J.B., 1967. Measurement of gravity at sea and in the air. Rev. Geophys. Space Phys., 5, 477-526.

LaCoste, L., Clarkson, N. & Hamilton, G., 1967. LaCoste and Romberg stabilised platform shipboard gravity meter. Geophysics, 32, 99-109.

Larsen, H.C., 1978. Offshore continuation of East Greenland dyke swarm and North Atlantic formation. Nature, 274, 220-223.

Larsen, H.C., 1980. Geological perspectives of the East Greenland continental margin. Bull. Geol. Soc. Denmark, 29, 77-101.

Larson, R.L. & Hilde, T.W.C., 1975. A revised time scale of magnetic reversals for the early Cretaceous and late Jurassic. J. geophys. Res., 80, 2586-2594.

Larson, R.L. & Ladd, J.W., 1973. Evidence for the opening of the South Atlantic in the early Cretaceous. Nature, 246, 209-212.

Laughton, A.S., 1975. Tectonic evolution of the northeast Atlantic ocean - a review. Norges geol. Unders., 316, 169-193.

Lee, M.K., 1972. Use of the one-dimensional power spectrum for depth determination to magnetic structures. M.Sc. thesis, University of Durham.

Le Pichon, X., Francheteau, J. & Bonin, J., 1976. Plate Tectonics, 2nd edition. Developments in Geotectonics - 6, Elsevier Scientific Publ. Co., Amsterdam, 311 pages.

Le Pichon, X. & Sibuet, J.C., 1971a. Western extension of the boundary between European and Iberian plates during the Pyrenean orogeny. Earth Planet. Sci. Lett., 12, 83-88.

Le Pichon, X. & Sibuet, J.C., 1971b. Comments on the evolution of the northeast Atlantic. Nature, 233, 257-258.

Le Pichon, X., Sibuet, J.C. & Francheteau, J., 1977. The fit of the continents around the North Atlantic Ocean. Tectonophysics, 38, 169-209.

Matthews, D.J., 1939. Tables of the velocity of sound in pure water and sea water for use in echo sounding and echo ranging. Admiralty Hydrographic Dept., London, 52 pages.

Mayne, W.H. & Quay, R.G., 1971. Seismic signatures of large air guns. Geophysics, 36, 1162-1173.

Mead, G.D., 1970. International Geomagnetic Reference Field 1965.0 in dipole coordinates. J. geophys. Res., 75, 4372-4374.

Miller, S.P., 1977. The validity of the geological interpretations of marine magnetic anomalies. Geophys. J. R. astr. Soc., 50, 1-21.

Milliman, J.D., 1979. Morphology and structure of Amazon upper continental margin. Bull. Am. Ass. Petrol. Geol., 63, 934-950.

Nabighian, M.N., 1972. The analytic signal of two-dimensional magnetic bodies with polygonal cross-section: its properties and use for automated anomaly interpretation. Geophysics, 37, 507-517.

Nafe, J.E. & Drake, C.L., 1963. Physical properties of marine sediments. In: Hill, M.N. (Editor), The Sea. Vol. 3: The Earth beneath the Sea, History, Interscience Publ., John Wiley & Sons, New York, 794-815.

Naidu, P.S., 1969. Estimation of spectrum and cross-spectrum of aeromagnetic field using fast digital Fourier transform (FDFT) techniques. Geophys. Prospect., 17, 344-361.

Naidu, P.S., 1970. Statistical structure of aeromagnetic field. Geophysics, 35, 279-292.

Nielsen, T.F.D., 1975. Possible mechanism of continental break-up in the North Atlantic. Nature, 253, 182-184.

Nielsen, T.F.D, 1978. The Tertiary dyke swarms of the Kangerdlugssuaq area, East Greenland. An example of magmatic development during continental break-up. Contrib. Mineral Petrol., 67, 63-78.

Nilsen, T.H., 1978a. Sedimentation in the Northeast Atlantic Ocean and Norwegian Sea. In: Bowes, D.R. & Leake, B.E. (Editors), Crustal Evolution in Northwestern Britain and Adjacent Regions, Geol. J. Spec. Issue No. 10, Seel House Press, Liverpool, England, 433-454.

Nilsen, T.H., 1978b. Lower Tertiary laterite on the Iceland-Faeroe Ridge and the Thulean land bridge. Nature, 274, 786-788.

Nilsen, T.H. & Kerr, D.R., 1978a. Turbidites, redbeds, sedimentary structures, and trace fossils observed in DSDP Leg 38 cores and the sedimentary history of the Norwegian-Greenland Sea. In: Talwani, M., Udintsev, G., et al., Initial Reports of the Deep Sea Drilling Project, Supplement 38: Washington, (U.S. Government Printing Office), 259-288.

Nilsen, T.H. & Kerr, D.R., 1978b. Palaeoclimatic and palaeogeographic implications of a lower Tertiary laterite (latosol) on the Iceland-Faeroe Ridge, North Atlantic region. Geol. Mag., 115, 153-182.

Nooteboom, J.J., 1978. Signature and amplitude of linear airgun arrays. Geophys. Prospect., 26 , 194-201.

Nunns, A.G., 1980. Marine geophysical investigations in the Norwegian-Greenland Sea between the latitudes of 62° N and 74° N. Ph.D. thesis, University of Durham. 185 pages plus appendices.

Odin, G.S., Curry, D., & Hunziker, J.C., 1978. Radiometric dates from NW European glauconites and the Palaeogene time-scale. J. geol. Soc. London, 135, 481-497.

Oxford Isotope Geology Laboratory & McGregor, V.R., 1971. Isotopic dating of very early Precambrian amphibolite facies gneisses from the Godthaab district, West Greenland. Earth Planet. Sci. Lett., 12, 245-259.

Palmason, G., 1963. Seismic refraction investigation of the basalt lavas in northern and eastern Iceland. Jökull, 3, 40-60.

Palmason, G., 1965. Seismic refraction measurements of the basalt lavas of the Faeroe Islands. Tectonophysics, 2, 475-482.

Palmason, G., 1974. The insular margin of Iceland. In: Burk, C.A. & Drake, C.L. (Editors), The Geology of Continental Margins, Springer-Verlag, New York, 375-379.

Palmason, G., Nilsen, T.H. & Thorbergsson, G., 1973. Gravity base station network in Iceland 1968-1970. Jökull, 23, 70-124.

Pankhurst, R.J., Beckinsale, R.D. & Brooks, C.K., 1976. Strontium and oxygen isotope evidence relating to the petrogenesis of the Kangerdlugssuaq alkaline intrusion, East Greenland. Contrib. Mineral. Petrol., 54, 17-42.

Papoulis, A., 1977. Signal analysis. McGraw-Hill, New York, 431 pages.

Parsons, B. & Sclater, J.G., 1977. An analysis of the variation of ocean floor bathymetry and heat flow with age. J. geophys. Res., 82, 803-827.

Payton, C.E. (Editor), 1977. Seismic Stratigraphy-applications to hydrocarbon exploration. Am. Ass. Petrol. Geol., Memoir 26, Tulsa, Oklahoma, U.S.A. 516 pages.

Pisarenko, V.F., 1973. The retrieval of harmonics from a covariance function. Geophys. J. R. astr. Soc., 33, 347-366.

Pitman III, W.C. & Talwani, M., 1972. Sea-floor spreading in the North Atlantic. Bull. Geol. Soc. Am., 83, 619-646.

Rabinowitz, P.D. & LaBrecque, J.L., 1977. The isostatic gravity anomaly: key to the evolution of the ocean-continent boundary at passive continental margins. Earth Planet. Sci. Lett., 35, 145-150.

Ramberg, I.B., 1976. Gravity interpretation of the Oslo Graben and associated igneous rocks. Norges geol. Unders., 325, 194 pages (with reference to abstract only).

Rao, B.S.R., Murthy, I.V.R. & Rao, D.B., 1978. Interpretation of magnetic anomalies with Fourier transforms, employing end corrections. J. Geophys. Zeit. Geophysik, 44, 257-272.

Regan, R.D. & Hinze, W.J., 1976. The effect of finite data length in the spectral analysis of ideal gravity anomalies. Geophysics, 41, 44-55.

Renick, Jr., H., 1974. Some implications of simple geometric analysis of marine cable feathering in seismic exploration. Geophys. Prospect., 22, 54-67.

Reyment, R.A., 1969. Ammonite biostratigraphy, continental drift and oscillatory transgressions. Nature, 224, 137-140.

Richardus, P. & Adler, R.K., 1972. Map projections for Geodesists, Cartographers and Geographers. North-Holland Publ. Co., Amsterdam-London.

Ries, A.C., 1978. The opening of the Bay of Biscay: a review. Earth Sci. Rev., 14, 35-63.

Roberts, D.G., 1975. Marine geology of the Rockall Plateau and Trough. Phil. Trans. Roy. Soc., London, A278, 447-509.

Robinson, J., 1980. A geophysical study of the continental margin west of Norway. Ph.D. thesis, University of Durham.

Roots, W.D., Veevers, J.J. & Clowes, D.F., 1979. Lithospheric model with thick oceanic crust at the continental boundary: a mechanism for shallow spreading ridges in young oceans. Earth Planet. Sci. Lett., 43, 417-433.

Royden, L., Sclater, J.G. & von Herzen, R.P., 1980. Continental margin subsidence and heat flow: important parameters in formation of petroleum hydrocarbons. Bull. Am. Ass. Petrol. Geol., 64, 173-187.

Russell, M.J., 1976. A possible Lower Permian age for the onset of ocean floor spreading in the northern North Atlantic. Scott. J. Geol., 12, 315-323.

Russell, M.J. & Smythe, D.K., 1978. Evidence for an early Permian oceanic rift in the northern North Atlantic. In: Neumann, E.R. & Ramberg, I.B. (Editors), Petrology and Geochemistry of Continental Rifts, Vol. 1. D. Reidel Publ. Co., Holland, 173-179.

Saemundsson, K., 1974. Evolution of the axial rifting zone in northern Iceland and the Tjørnes fracture zone. Bull. Geol. Soc. Am., 85, 495-504.

Safar, M.H., 1976a. Calibration of marine seismic sources using a hydrophone of unknown sensitivity. Geophys. Prospect., 24, 328-333.

Safar, M.H., 1976b. The radiation of acoustic waves from an air-gun. Geophys. Prospect., 24 765-772.

Safar, M.H., 1978. Reply to comments on 'The radiation of acoustic waves from an air-gun'. Geophys. Prospect., 26, 464-476.

Savit, C.H., Brustad, J.T. & Sider, J., 1958. The moveout filter. Geophysics, 23, 1-25.

Saxov, S. & Abrahamsen, N., 1966. Some geophysical investigations in the Faeroe Islands: a preliminary report. Zeit.Geophysik, 32, 455-471.

Schleusener, A., Torge, W. & Drewes, H., 1976. The gravity field of northeastern Iceland. J. Geophys. Zeit. Geophysik, 42, 27-45.

Schmalz, R.F., 1969. Deep water evaporite deposition: a genetic model. Bull. Am. Ass. Petrol.Geol., 53, 798-823.

Schneider, E.D., Fox, P.J., Hollister, C.D., Needham, H.D. & Heezen, B.C., 1967. Further evidence of contour currents in the western North Atlantic. Earth Planet. Sci. Lett., 2, 351-359.

Schoenberger, M. & Mifsud, J.F., 1974. Hydrophone streamer noise. Geophysics, 39, 781-793.

Schult, A. & Guerreiro, S.D.C., 1979. Palaeomagnetism of Mesozoic igneous rocks from the Maranhao Basin, Brazil, and the time of opening of the South Atlantic. Earth Planet. Sci. Lett., 42, 427-436.

Scrutton, R.A. & Roberts, D.G., 1971. Structure of Rockall Plateau and Trough, north-east Atlantic. In: Delaney, F.M. (Editor), ICSU/SCOR Working Party 31 Symposium, Cambridge, 1970: The Geology of the East Atlantic Continental Margin, 2. Europe, Inst. Geol. Sci., Report No. 70/14, 170 pages, 77-87.

Sellevoll, M.A., 1975. Seismic refraction measurements and continuous seismic profiling on the continental margin off Norway between 60° N and 69° N. Norges geol. Unders., 316, 219-235.

Shannon, C.E., 1948. A mathematical theory of communication. Bell System Tech. J., 27, 379-423.

Sharma, B. & Geldart, L.P., 1968. Analysis of gravity anomalies of two-dimensional faults using Fourier transforms. Geophys. Prospect., 16, 77-93.

Sheriff, R.E., 1973. Encyclopaedic Dictionary of Exploration Geophysics, Society of Exploration Geophysicists, Tulsa, Oklahoma, U.S.A. Reprinted 1980. 266 pages.

Sheriff, R.E., 1975. Factors affecting seismic amplitudes. Geophys. Prospect., 23, 125-138.

Sheriff, R.E., 1976. Inferring stratigraphy from seismic data. Bull. Am. Ass. Petrol. Geol., 60, 528-542.

Sheriff, R.E., 1977. Limitations on resolution of seismic reflections and geologic detail derivable from them. In: Payton, C.E. (Editor), Seismic Stratigraphy - applications to hydrocarbon exploration. Am. Ass. Petrol. Geol., Memoir 26, Tulsa, Oklahoma, U.S.A., 3-14.

Shuey, R.T., Schellinger, D.K., Tripp, A.C. & Alley, L.B., 1977. Curie depth determination from aeromagnetic spectra. Geophys. J. R. astr. Soc., 50, 75-101.

Smith, S.G., 1975. Measurement of air gun waveforms. Geophys. J. R. astr. Soc., 42, 273-280.

Smithson, S.B., 1971. Densities of metamorphic rocks. Geophysics, 36, 690-694.

Smithson, S.B. & Ramberg, I.B., 1979. Gravity interpretation of the Egersund anorthosite complex, Norway: its petrological and geothermal significance. Bull. Geol. Soc. Am., 90, 199-204.

Smythe, D.K., Kenolty, N. & Russell, M.J., 1978. Comments on 'Seismic evidence for Mesozoic sedimentary troughs on the Hebridean continental margin' by E.J.W. Jones. Nature, 276, 420.

Soper, N.J., Downie, C., Higgins, A.C. & Costa, L.I., 1976. Biostratigraphic ages of Tertiary basalts on the East Greenland continental margin and their relationship to plate separation in the north east Atlantic. Earth Planet. Sci. Lett., 32, 149-157.

Spector, A. & Bhattacharyya, B.K., 1966. Energy density spectrum and autocorrelation function of anomalies due to simple magnetic models. Geophys. Prospect., 14, 242-272.

Spector, A. & Grant, F.S., 1970. Statistical models for interpreting aeromagnetic data. Geophysics, 35, 293-302.

Spector, A. & Grant, F.S., 1974. Reply by authors to the discussion by G. Gudmundsson. Geophysics, 39, 112-113.

Srivastava, S.P., 1978. Evolution of the Labrador Sea and its bearing on the early evolution of the North Atlantic. Geophys. J. R. astr. Soc., 52, 313-357.

Stacey, A.P. & Allerton, H.A., 1974. Computer System for reduction, display and storage of navigation, gravity, magnetic and depth data recorded in continental shelf or deep-ocean areas. Manuals: 1-12. Institute of Oceanographic Sciences, Research Vessel Base, Barry, South Wales. October, 1974.

Stacey, A.P., Fasham, M.J.R., Black, D.I. & Scrutton, R.A., 1971. Design and application of digital filters for the Graf-Askania Gss2, NO. 11 Sea Gravity Meter. Marine Geophys. Res., 1, 220-232.

Stacey, A.P., Gray, F., Allerton, H.A. & Sewart, D.I., 1972. A logger and mobile computer system for marine data acquisition and reduction. Ocean. Int., 72, 350-352.

Stacey, F.D., 1969. Physics of the Earth. 3rd edition. John Wiley & Sons, Inc., New York, 324 pages.

Stansell, T.A., 1978. The TRANSIT Navigation Satellite System: status, theory, performance, applications. Magnavox Government and Industrial Electronics Co., Advanced Products Division, 2829, Maricopa Street, Torrance, Calif. 90503, U.S.A., 83 pages.

Stevens, N.B.H. & Perch-Nielsen, K., 1972. Sampling for oil source rock analysis, Scoresby Sund region, Central East Greenland. Rapp. Grønlands geol. Unders., 55, 47-48.

Stuart, C.J. & Caughey, C.A., 1977. Seismic facies and sedimentology of terrigerous Pleistocene deposits in northwest and central Gulf of Mexico. In: Payton, C.E. (Editor), Seismic Stratigraphy - applications to hydrocarbon exploration. Am. Ass. Petrol. Geol., Memoir 26, Tulsa, Oklahoma, U.S.A., 249-275.

Sundvor, E., 1975. Thickness and distribution of sedimentary rocks in the southern Barents SEa. Norges geol. Unders., 316, 237-240.

Surlyk, F., 1977. Mesozoic faulting in East Greenland. In: Frost, R.T.C. & Dikkers, A.J. (Editors), Fault Tectonics in NW Europe, Geol.Mijnbouw, 56, 311-327.

Surlyk, F., 1978. Jurassic basin evolution of East Greenland. Nature, 274, 130-133.

Swingler, D.N., 1979. A comparison between Burg's Maximum Entropy Method and a nonrecursive technique for the spectral analysis of deterministic signals. J. geophys. Res., 84, 679-685.

Talwani, M. & Eldholm, O., 1972. Continental margin off Norway: a geophysical study. Bull. Geol. Soc. Am., 83, 3575-3606.

Talwani, M. & Eldholm, O., 1977. Evolution of the Norwegian-Greenland Sea. Bull. Geol. Soc. Am., 88, 969-999.

Talwani, M., Grim, P., Holcombe, T., Luyendyk, B., Meyers, H. & Smith, S., 1972. Formats for Marine Geophysical Data Exchange. U.S. Department of Commerce, NOAA, Environmental Data Service, 19 pages.

Talwani, M. & Udintsev, G., 1976. Tectonic synthesis. In: Talwani, M., Udintsev, G., et al., Initial Reports of the Deep Sea Drilling Project, 38: Washington, (U.S. Government Printing Office), 1213-1242.

Talwani, M., Udintsev, G., et al., 1976. Initial Reports of the Deep Sea Drilling Project, 38: Washington (U.S. Government Printing Office), 1256 pages.

Taner, M.T., Cook, E.E. & Neidell, N.S., 1970. Limitations of the reflection seismic method; lessons from computer simulations. Geophysics, 35, 551-573.

Taner, M.T. & Koehler, F., 1969 Velocity Spectra-digital computer derivation and applications of velocity functions. Geophysics, 34, 859-881.

Tarling, D.H., 1967. The palaeomagnetic properties of some Tertiary lavas from East Greenland. Earth Planet. Sci. Lett., 3, 81-88.

Tarling, D.H. & Mitchell, J.G., 1976. Revised Cenozoic polarity time scale. Geology, 4, 133-136.

Telford, W.M., Geldart, L.P., Sheriff, R.E. & Keys, D.A., 1976. Applied Geophysics. Cambridge University Press, Cambridge, England. 860 pages.

Thiede, J., 1978. Pelagic sedimentation in immature ocean basins. In: Ramberg, I.B. & Neumann, E.R. (Editors), Tectonics and Geophysics of Continental Rifts, Reidel Publ. Co. Ltd., Holland, 237-248.

Thomas, J.B., 1969. An Introduction to Statistical Communication Theory. 6th edition. John Wiley & Sons, New York, 670 pages.

Toman, K., 1965. The spectral shifts of truncated sinusoids. J. geophys. Res., 70, 1749-1750.

Treitel, S., Clement, W.G., & Kaul, R.K., 1971. The spectral determination of depths to buried magnetic basement rocks. Geophys. J. R. astr. Soc., 24, 415-428.

Treitel, S., Gutowski, P.R. & Robinson, E.A., 1977. Empirical spectral analysis revisited. In: Miller, J.H. (Editor), Topics in Numerical Analysis, Vol. 3. Academic Press, New York, 429-446.

Ulrych, T.J. & Bishop, T.N., 1975. Maximum entropy spectral analysis and autoregressive decomposition. Rev. Geophys. Space Phys., 13, 183-200.

Ulrych, T.J. & Clayton, R.W., 1976. Time series modelling and maximum entropy. Phys. Earth Planet. Int., 12, 188-200.

U.S. Naval Oceanographic Office, 1966. Charts of the Earth's Magnetic Field, Epoch 1965.0:

Chart 1700 Magnetic inclination or dip

Chart 1703 Total intensity of Earth's magnetic force

Chart 1706 Magnetic variation

3rd edition, January, 1966.

Vacquier, V., Steenland, N.C., Henderson, R.G. & Zietz, I., 1951. Interpretation of Aeromagnetic Maps. Geol. Soc. America, Memoir 47, 151 pages.

Vail, P.R., Mitchum, R.M., Jr. & Thompson, S., III, 1977a. Seismic stratigraphy and global changes of sea level, part 3: relative changes of sea level from coastal onlap. In: Payton, C.E. (Editor), Seismic Stratigraphy - applications to hydrocarbon exploration. Am. Ass. Petrol. Geol., Memoir 26, Tulsa, Oklahoma, U.S.A., 63-81.

Vail, P.R., Mitchum, R.M., Jr. & Thompson, S.,III, 1977b. Seismic stratigraphy and global changes of sea level, part 4: global cycles of relative changes of sea level. In: Payton, C.E. (Editor), Seismic Stratigraphy - applications to hydrocarbon exploration. Am. Ass. Petrol. Geol., Memoir 26, Tulsa, Oklahoma, U.S.A., 83-97.

Valliant, H.D., Halpenny, J., Beach, R. & Cooper, R.V., 1976. Sea-gravimeter trials on the Halifax Test Range aboard CSS Hudson, 1972. Geophysics, 41, 700-711.

Vann, I.R., 1974. A modified predrift fit of Greenland and western Europe. Nature, 251, 209-211.

Veevers, J.J., 1977. Palaeobathymetry of the crest of spreading ridges related to the age of ocean basins. Earth Planet. Sci. Lett., 34, 100-106.

Vine, F.J. & Matthews, D.H., 1963. Magnetic anomalies over oceanic ridges. Nature, 199, 947-949.

Vogt, P.R., 1972. The Faeroe-Iceland-Greenland aseismic ridge and the western boundary undercurrent. Nature, 239, 79-81.

Vogt, P.R., 1974. The Iceland phenomenon: imprints of a hot spot on the ocean crust, and implications for flow below the plates. In: Kristjansson, L. (Editor), Geodynamics of Iceland and the North Atlantic Area. Proceedings of the NATO Advanced Study Institute, Reykjavik, Iceland, 1-7 July, 1974. D. Reidel Publ. Co., Dordrecht, Holland, 49-62.

Vogt, P.R. & Avery, O.E., 1974. Detailed magnetic surveys in the northeast Atlantic and Labrador Sea. J. geophys. Res., 79, 363-389.

Vogt, P.R., Johnson, G.L. & Kristjansson, L., 1980. Morphology and Magnetic anomalies north of Iceland. In: Jacoby, W., Björnsson, A. & Moller, D. (Editors), Iceland-Evolution, Active Tectonics and Structure. J. Geophys., 47, 67-80.

Voppel, D., Srivastava, S.P. & Fleischer, U., 1979. Detailed magnetic measurements south of the Iceland-Faeroe Ridge. Deutsch. hydrogr. Zeit., 32, 154-172.

Wager, L.R., 1935. Geological investigations in East Greenland: Part 2, Geology of Kap Dalton. Meddr. Grønland, 105, 3, 1-32.

Wager, L.R., 1947. Geological investigations in East Greenland: Part 4, The stratigraphy and tectonics of Knud Rasmussens Land and the Kangerdlugssuaq region. Meddr. Grønland, 134, 5, 64 pages.

Wager, L.R. & Deer, W.A., 1938. A dyke swarm and crustal flexure in East Greenland. Geol. Mag., 75, 39-46.

Waldmeier, , M., 1978. Solar activity in 1978. In: Frost, J.M. (Editor), World Radio TV Handbook, Vol. 32. Billboard Publications, London 44-45.

Walker, C.D.T., 1977. Wide-angle reflection studies at sea. Ph.D. thesis, University of Durham.

Waters, K.H., 1978. Reflection Seismology: a tool for energy resource exploration. John Wiley & Sons, Inc., New York, 377 pages.

Williams, C.A., 1975. Sea floor spreading in the Bay of Biscay and its relationship to the North Atlantic. Earth Planet. Sci. Lett., 24, 440-456.

Williams, C.A. & McKenzie, D., 1971. The evolution of the North-East Atlantic. Nature, 232, 168-173.

Woollard, G.P., 1979. The new gravity system - changes in international gravity base values and anomaly values. Geophysics, 44, 1352-1366.

Worzel, J.L., 1974.Standard oceanic and continental structure. In: Burk, C.A. & Drake, C.L. (Editors), The Geology of Continental Margins. Springer-Verlag, Berlin, Heidelberg and New York, 59-66.

Worzel, J.L. & Harrison, J.C., 1963. Gravity at sea. In: Hill, M.N. (Edtior), The Sea. Vol. 3: The Earth beneath the Sea,History. Interscience Publ., John Wiley & Sons, New York, 134-174.

Wyrobeck, S.M., 1969. General appraisal of velocities of the Permian Basin of northern Europe, including the North Sea. J. Inst. Petrol., London, 55, 1-13.

Ziolkowski, A., 1970. A method for calculating the output pressure waveform from an air-gun. Geophys, J. R. astr. Soc., 21, 137-161.

Ziolkowski, A., 1971. Design of marine seismic reflection profiling system using air-guns as a sound source. Geophys. J. R. astr. Soc., 23, 499-530.

Ziolkowski, A., 1977. Comments on 'The radiation of acoustic waves from an air-gun'. Geophys. Prospect., 25, 560-563.

Zverev, S.M., Kosminskaya, I.P., Krasil'shchikova, G.A., et al., 1977. Deep structure of Iceland and the Iceland-Faeroe-Shetland region based on seismic studies (NASP-72). Int. Geol. Rev., 19, 11-24.

APPENDIX A

GEOPHYSICAL DATA FROM THE 1977 EAST GREENLAND CRUISE

Gravity, magnetic, bathymetric and navigational data are stored on a magnetic tape located at the NUMAC System tape library, Newcastle-Upon-Tyne. The tape name is GPO4Ø1. The data are recorded in Merged-Merged Format 3 (Talwani et al, 1972) on ½ inch, 9 track, 800 BPI, NRZ, IBM compatible magnetic tape and each logical record represents a card image of 80 characters length. Individual logical records are separated by an inter-block gap. The recorded data represent processed 2-minute data values (see Figure 2.7).

The format of each card image on magnetic tape is indicated in Table A.1.

The computer commands for data retrieval from magnetic tape and their subsequent storage in a temporary file are as follows:

```
ØEMPTY  -filename
ØMOUNT GPO4Ø1 *T* NV
ØCOPY *T*  -filename
```

In order to facilitate rapid access to specific profile data on magnetic tape, a modified data file was established in which the cruise identification information in columns 1 through 8 was deleted and profile start and end markers were edited into the new file (consistent with Nunns, 1980). In particular, the first line of each profile was designated with the profile number (format: I5) and the second line of each profile contained the number of lines of 2-minute data values stored for that profile (format: I5). The end-of-profile marker was denoted by the negative value of the profile number in the last line of data for that profile (format: I5). Furthermore, seismic tape identifiers were edited into the profile data (format: I10) and the duration of the seismic tape was indicated in the following line by the appropriate integer number of 2-minute data values (format: I10).

Distance calculated along simplified ship's track (km) was entered into the modified data file in format F7.2 in columns 46 through 52.

These modified data and various uncompiled computer programs are stored on magnetic tape, QGK2Ø2 located in the NUMAC tape library. The

Table A.1 The format for geophysical data stored in each logical record as one card image on the magnetic tape, GPO4Ø1.

A8	Cruise designation Ship/Cruise No./Year
3X	
I1	Time zone
1X	
3I2	Year/Month/Day
1X	
I5	Time (hours/tenths of minutes)
F8.4	Latitude (decimal degrees: + north, - south)
F9.4	Longitude (decimal degrees: + east, - west)
10X	
I5	Uncorrected depth (metres)
I5	Corrected depth (metres)
I2	Matthews area
1X	
I5	Total magnetic field (gamma)
I5	Magnetic anomaly; IGRF 1967 (gamma)
I5	Free air gravity anomaly (tenths of mgals)

files were stored on tape using the MTS file save program *FS. The command for mounting this magnetic tape (1600 BPI, DSL, volume label = VTLADAT) is:

$MOUNT QGK2Ø2 *T* VTLADAT

Various versions of working data files exist on this tape. In particular, the following files (version number in parentheses) are important:

GREENLD (4): listing of edited cruise data with start and end profile markers and seismic tape markers, distance along ship's track (km) estimated by projection on to great circle through data points (method later abandoned).

LSHEAD (1): listing of edited cruise data with start of profile markers, distance along ship's track (km) and geocentric coordinates calculated by projection of data on to best fitting rhumbline (in least squares sense, program MERCAT). Each profile is terminated by a data summary including the heading (degrees) and average velocity (km hr^{-1}) along the projected profile, the average sample spacing (km) and the RMS error in the sample spacing (km).

LSHEAD (2): the same as LSHEAD (1) except that projected coordinates are geodetic coordinates.

The computer programs, MERCAT and SPECTRAL, are also stored on this magnetic tape (uncompiled source programs).

The geophysical data recorded along profiles 1 through 16 are reproduced on the following pages and consist of:

total field magnetic anomaly (gamma)
free air gravity anomaly (mgal)
Eötvös correction (mgal)
corrected bathymetry (metres)
ship's speed (km hr^{-1})
ship's course (degrees)
distance along ship's track (km)
time (Julian day/hours, GMT).

Information relating to the start and end of each profile in terms of time and geographical coordinates is presented in Table A.2.

TABLE A.2

Temporal and geographical coordinates of the start and end of each data profile for the East Greenland Cruise, 1977.

PROFILE NUMBER	START OF PROFILE					END OF PROFILE				
	DATE 1977	JULIAN DAY	TIME GMT	LATITUDE °N	LONGITUDE °W	DATE 1977	JULIAN DAY	TIME GMT	LATITUDE °N	LONGITUDE °W
1	31 JULY	212	0322	63.0119	35.0912	1 AUGUST	213	0710	64.7634	39.0736
2	1 AUGUST	213	0800	64.8286	38.9547	1 AUGUST	213	1718	65.3085	37.0450
3	1 AUGUST	213	1800	65.2757	36.9156	2 AUGUST	214	1332	63.6989	33.3180
4	2 AUGUST	214	1350	63.6898	33.2555	3 AUGUST	215	0040	64.1901	31.2627
5	3 AUGUST	215	0100	64.2619	31.1362	3 AUGUST	215	2200	65.9126	34.8640
6	3 AUGUST	215	2304	65.9925	34.9730	4 AUGUST	216	1026	66.5491	33.3895
7	4 AUGUST	216	1046	66.5528	33.3240	5 AUGUST	217	0856	65.2004	28.4616
8	5 AUGUST	217	0910	65.2064	28.4063	5 AUGUST	217	2258	65.9135	25.4407
9	5 AUGUST	217	2316	65.9380	25.4380	7 AUGUST	219	0430	67.6721	31.6761
10	7 AUGUST	219	0516	67.7127	31.7436	7 AUGUST	219	2130	68.2476	28.1982
11	7 AUGUST	219	2158	68.2403	28.1010	8 AUGUST	220	1842	66.9495	23.7420
12	8 AUGUST	220	2000	67.0094	23.5950	9 AUGUST	221	0554	67.8273	21.7113
13	9 AUGUST	221	0612	67.8536	21.7416	9 AUGUST	221	2112	68.8179	25.0750
14	9 AUGUST	221	2140	68.8513	25.0478	10 AUGUST	222	0220	69.1104	23.8963
15	10 AUGUST	222	0720	68.9385	23.1956	10 AUGUST	222	1824	68.5603	26.2221
16	10 AUGUST	222	1844	68.5361	26.2074	11 AUGUST	223	1044	67.6541	23.0733

The reader's attention is drawn to the remarks made in Sections 2.4 and 5.3 respectively regarding the absolute values of the free air gravity anomaly stored on magnetic tape and presented in the following diagrams.

The extent of magnetic storms indicated by magnetogram records from Leirvogur and Narssuarssuaq (Figure 2.9) is shown schematically along each of the following data profiles by a thick black, horizontal line.

The seismic reflection data are stored in multiplexed form (SEG A format) on magnetic tapes (numbers 1 through 148) stored in the Department of Geological Sciences, University of Durham.

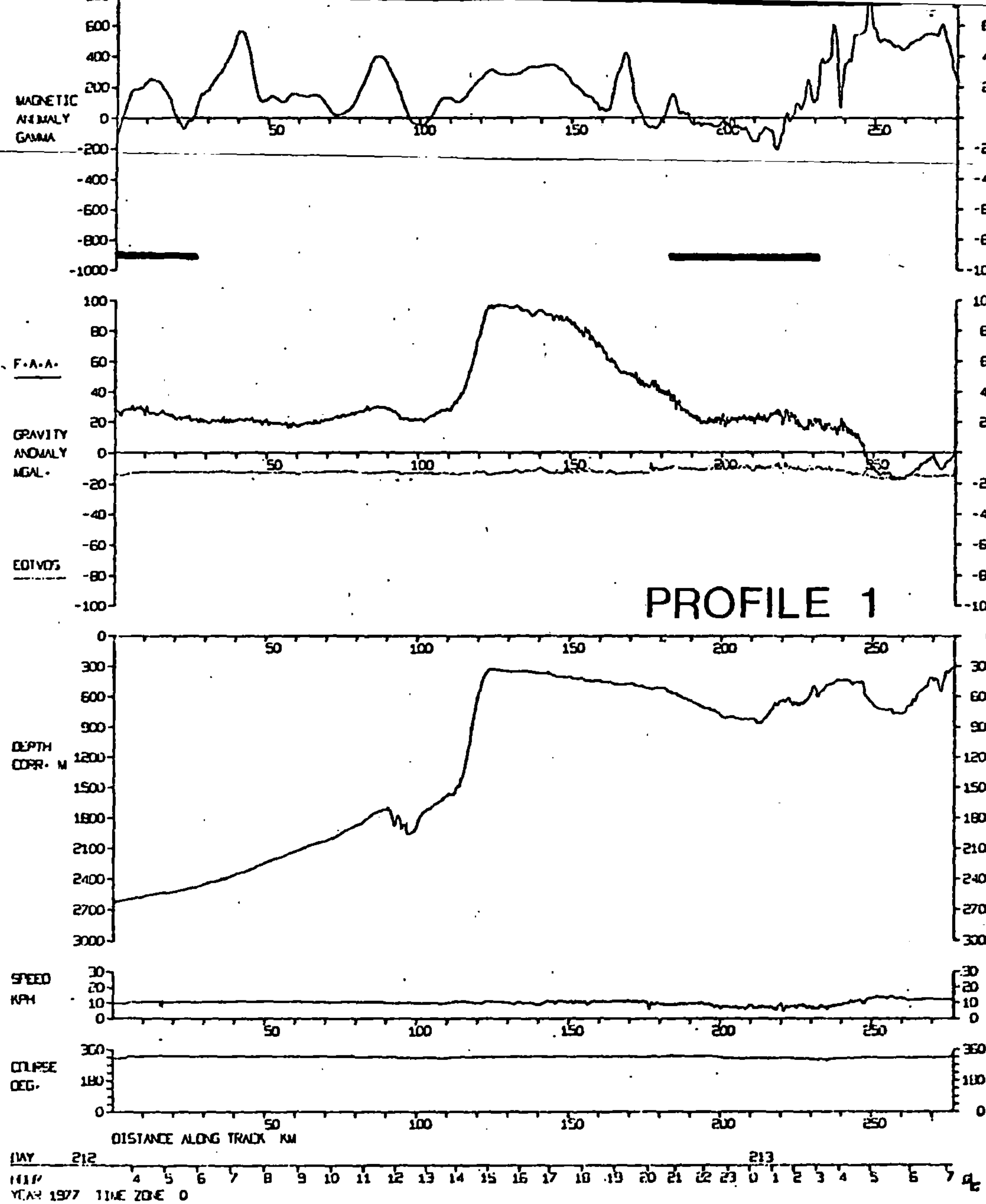
MAGNETIC ANOMALY GAMMA
F.A.A.
GRAVITY ANOMALY MGAL.
EOTVOS
PROFILE 1
DEPTH CORR. M
SPEED KPH
COURSE DEG.
DISTANCE ALONG TRACK KM
DAY 212 213
HOUR
YEAR 1977 TIME ZONE 0

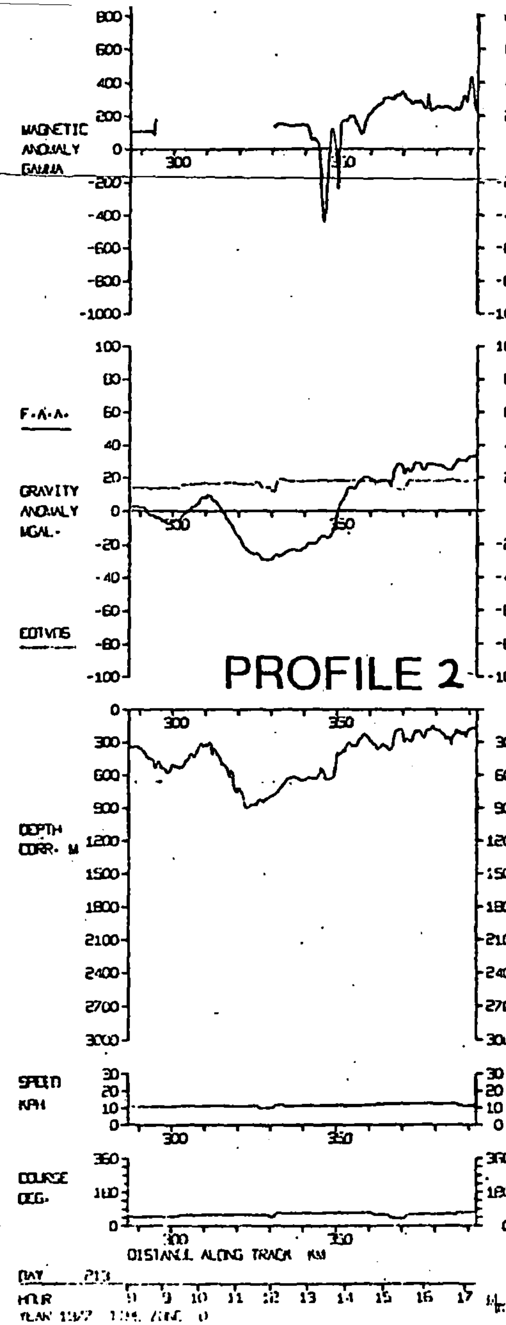
MAGNETIC ANOMALY GAMMA
F.A.A.
GRAVITY ANOMALY MGAL.
EOTVOS
PROFILE 2
DEPTH CORR. M
SPEED KPH
COURSE DEG.
DISTANCE ALONG TRACK KM

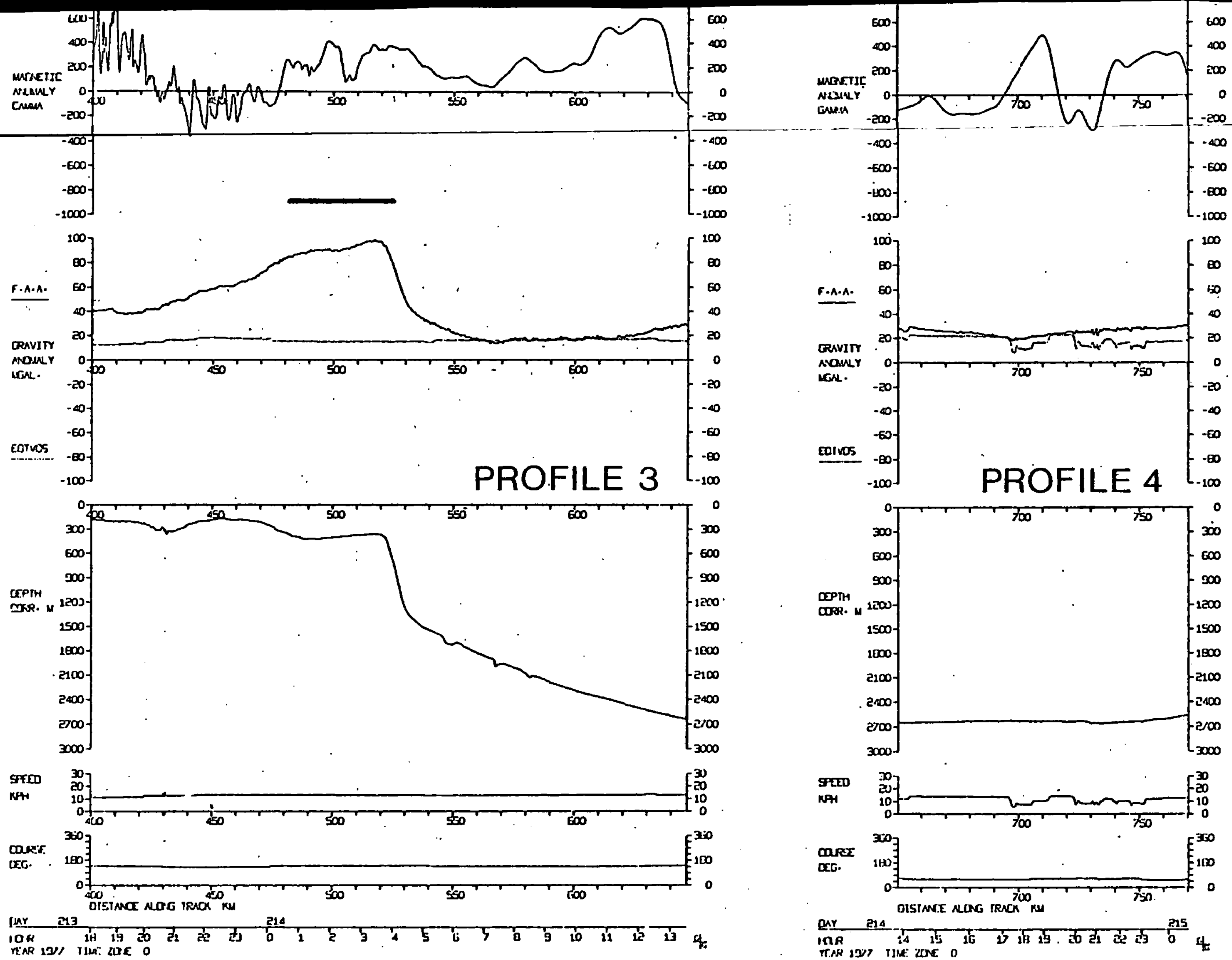

PROFILE 3
PROFILE 4
MAGNETIC ANOMALY GAMMA
F.A.A.
GRAVITY ANOMALY MGAL.
EOTVOS
DEPTH CORR. M
SPEED KPH
COURSE DEG.
DISTANCE ALONG TRACK KM
DAY
HOUR
YEAR 1977 TIME ZONE 0

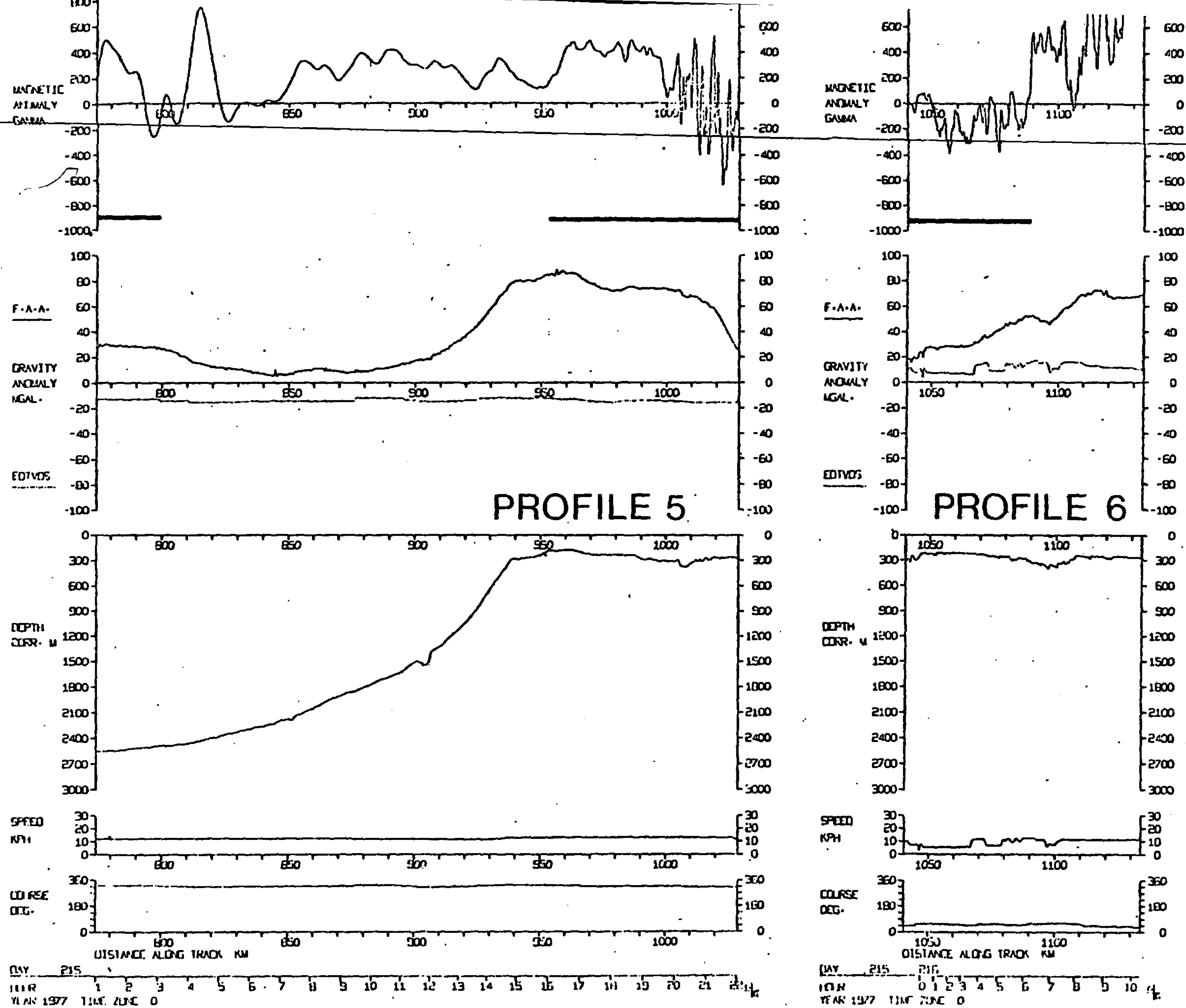
MAGNETIC ANOMALY GAMMA
F.A.A.
GRAVITY ANOMALY MGAL.
EOTVOS
PROFILE 5
PROFILE 6
DEPTH CORR. M
SPEED KPH
COURSE DEG.
DISTANCE ALONG TRACK KM
DAY 215
DAY 215 216
HOUR
YEAR 1977 TIME ZONE 0

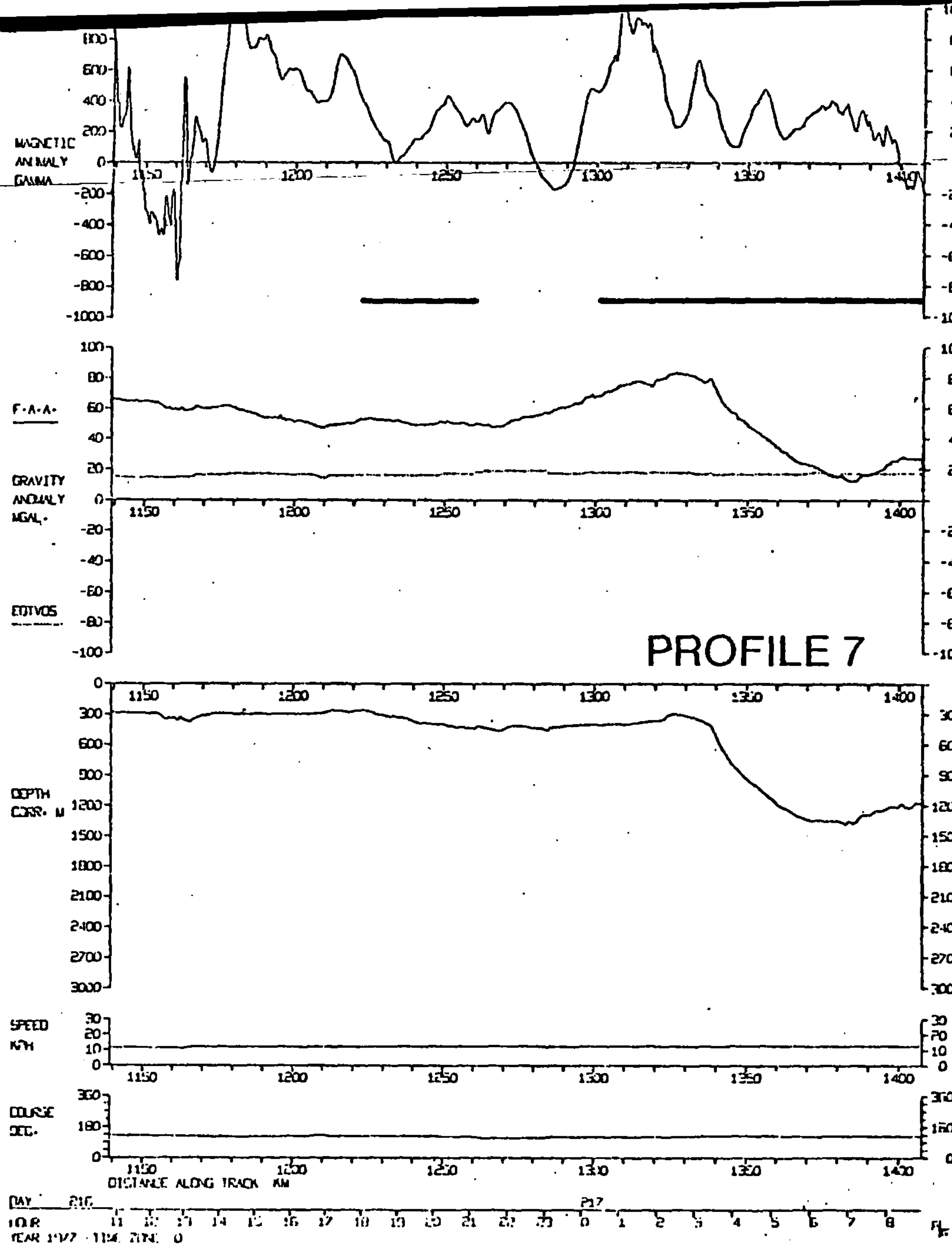
PROFILE 7
MAGNETIC ANOMALY GAMMA
F.A.A.
GRAVITY ANOMALY MGAL.
EOTVOS
DEPTH CORR. M
SPEED KPH
COURSE DEG.
DISTANCE ALONG TRACK KM
DAY 216 217
HOUR
YEAR 1977 TIME ZONE 0

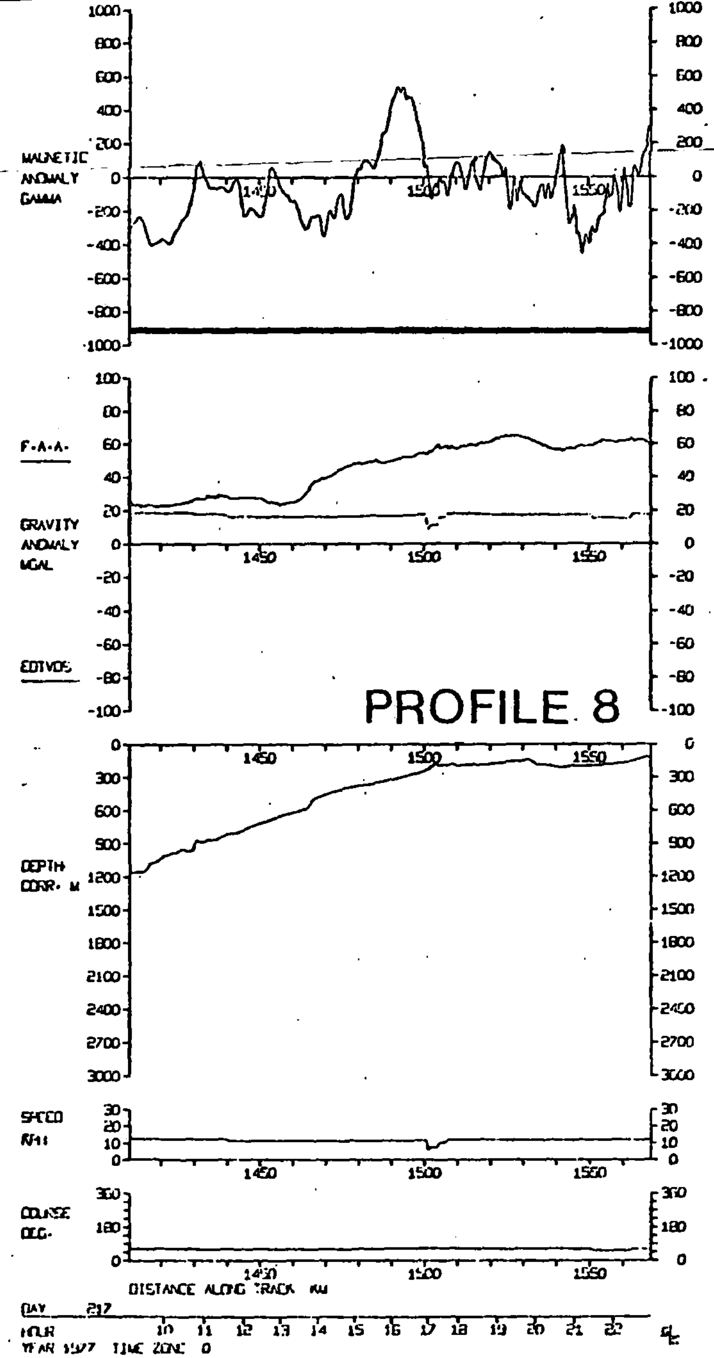
PROFILE 8
MAGNETIC ANOMALY GAMMA
F.A.A.
GRAVITY ANOMALY MGAL
EOTVOS
DEPTH CORR. M
SPEED KPH
COURSE DEG.
DISTANCE ALONG TRACK KM
DAY 217
HOUR
YEAR 1977 TIME ZONE 0

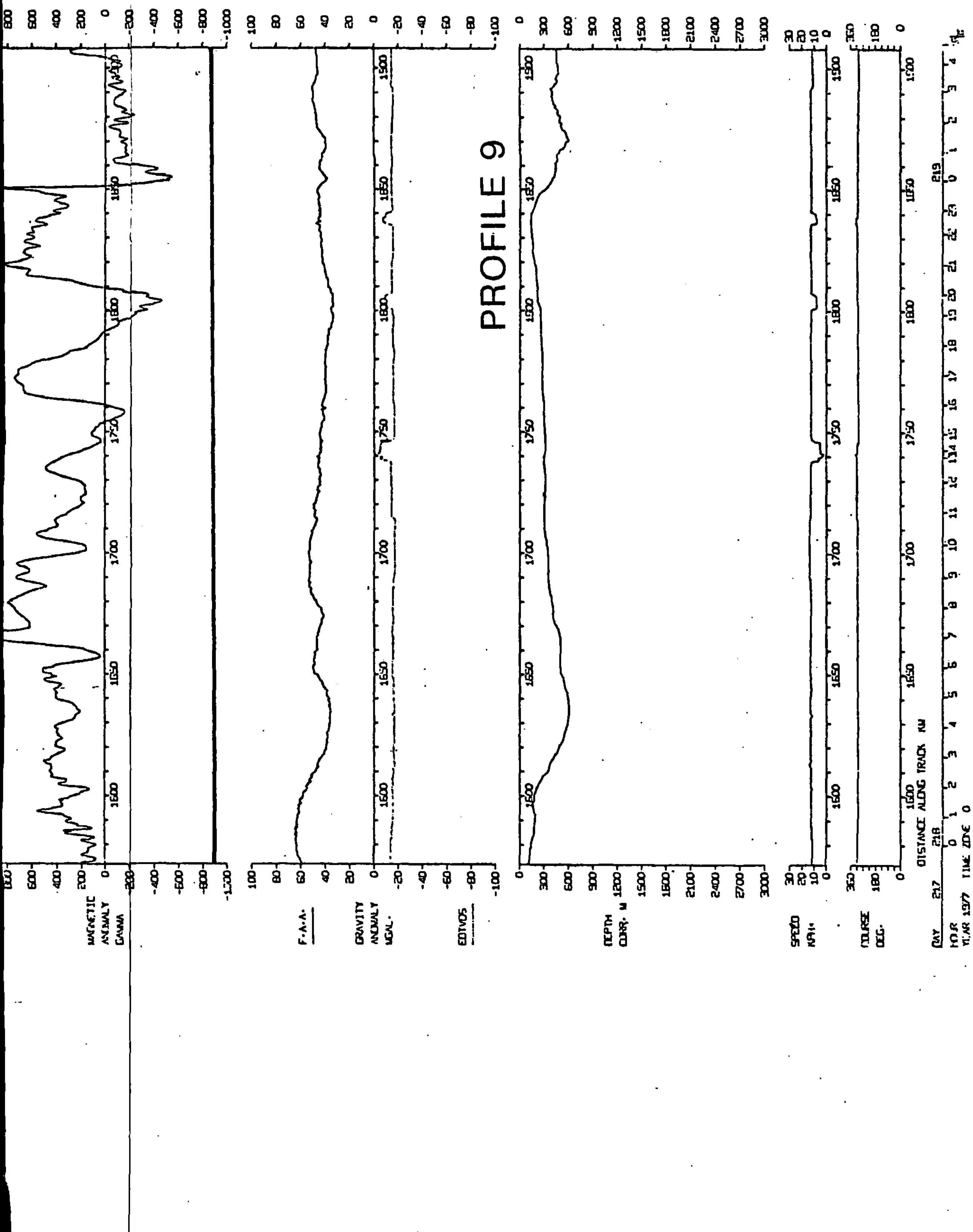
PROFILE 9
MAGNETIC ANOMALY GAMMA
F.A.A.
GRAVITY ANOMALY MGAL.
EOTVOS
DEPTH CORR. M
SPEED KPH
COURSE DEG.
DISTANCE ALONG TRACK KM
DAY
HOUR
YEAR 1977 TIME ZONE 0

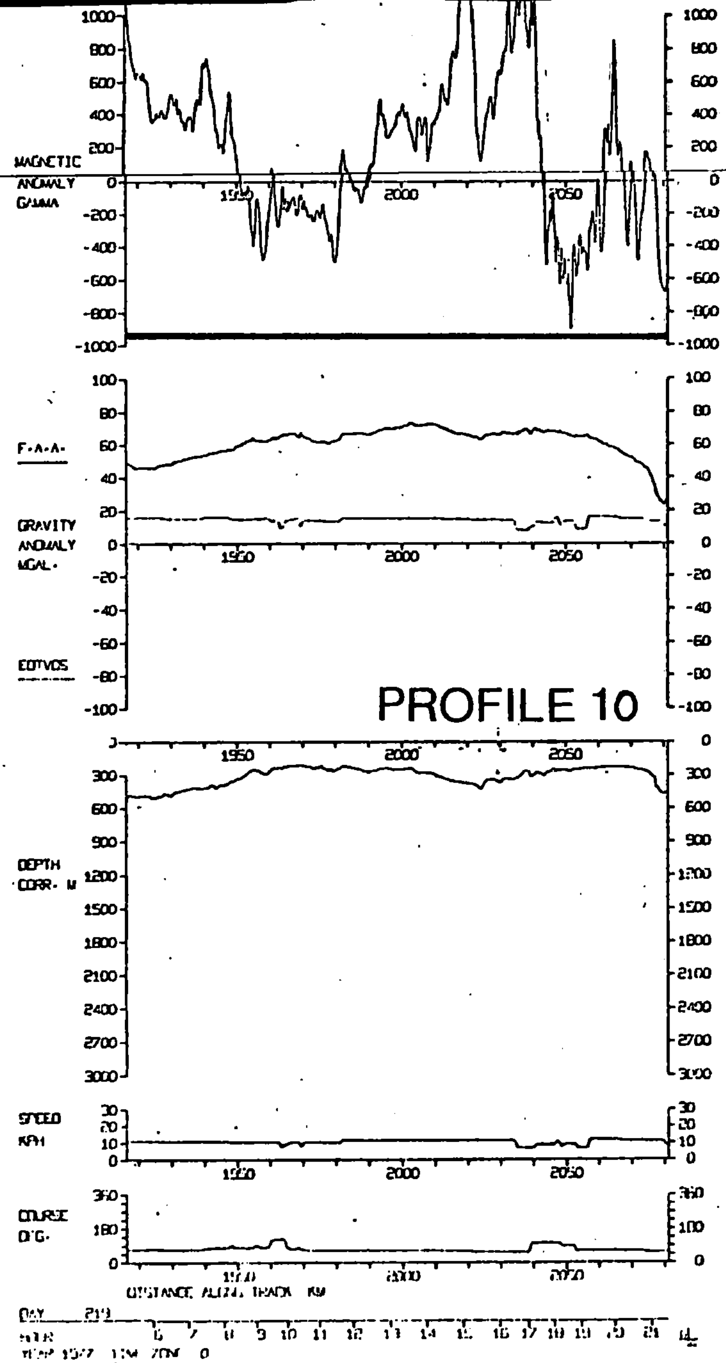
MAGNETIC
ANOMALY
GAMMA
F.A.A.
GRAVITY
ANOMALY
MGAL.
EOTVOS
PROFILE 10
DEPTH
CORR. M
SPEED
KPH
COURSE
DEG.
DISTANCE ALONG TRACK KM
DAY 219
HOUR
YEAR 1977 TIME ZONE 0

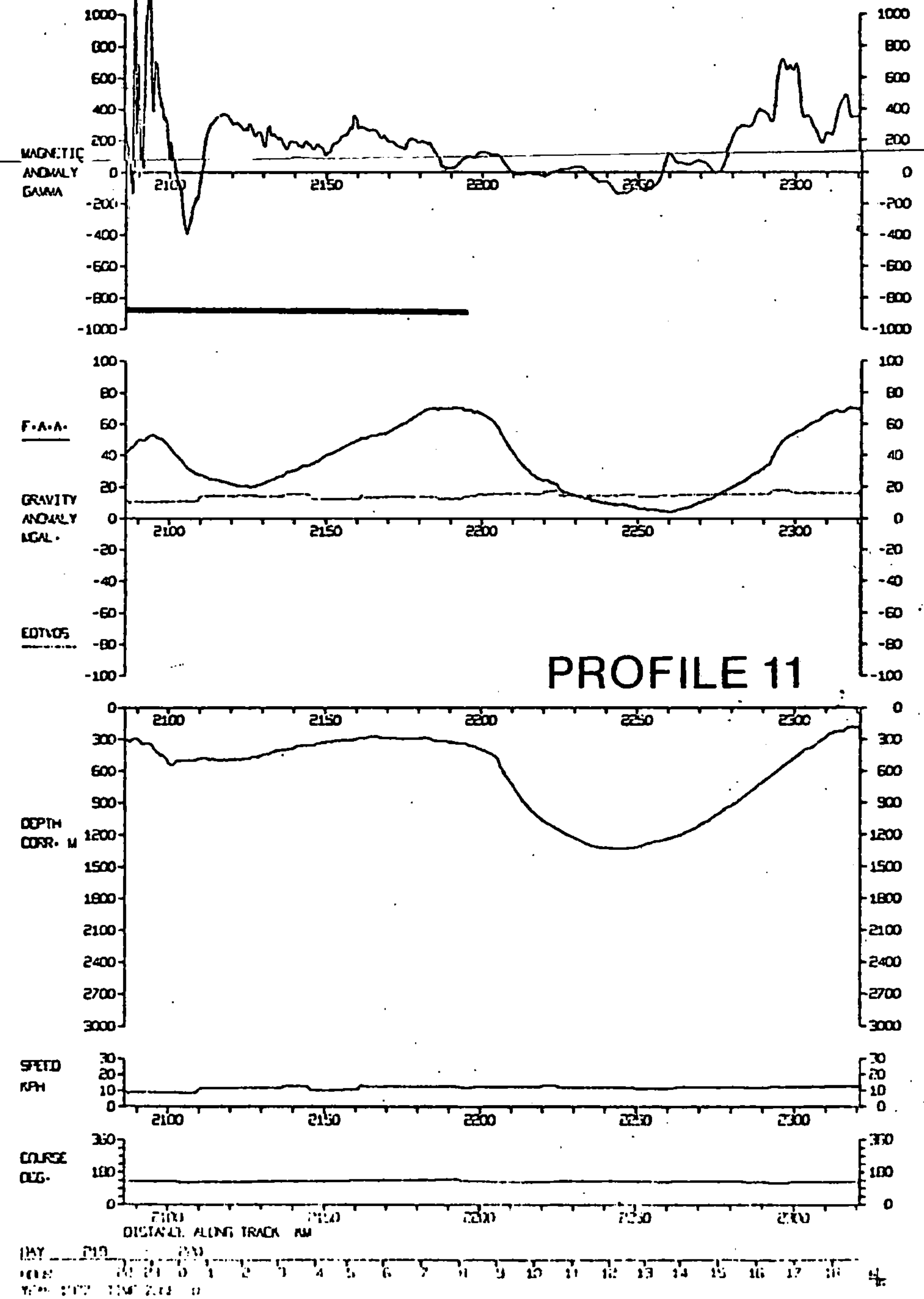
MAGNETIC
ANOMALY
GAMMA
F.A.A.
GRAVITY
ANOMALY
MGAL.
EOTVOS
PROFILE 11
DEPTH
CORR. M
SPEED
KPH
COURSE
DEG.
DISTANCE ALONG TRACK KM
DAY 219
HOUR

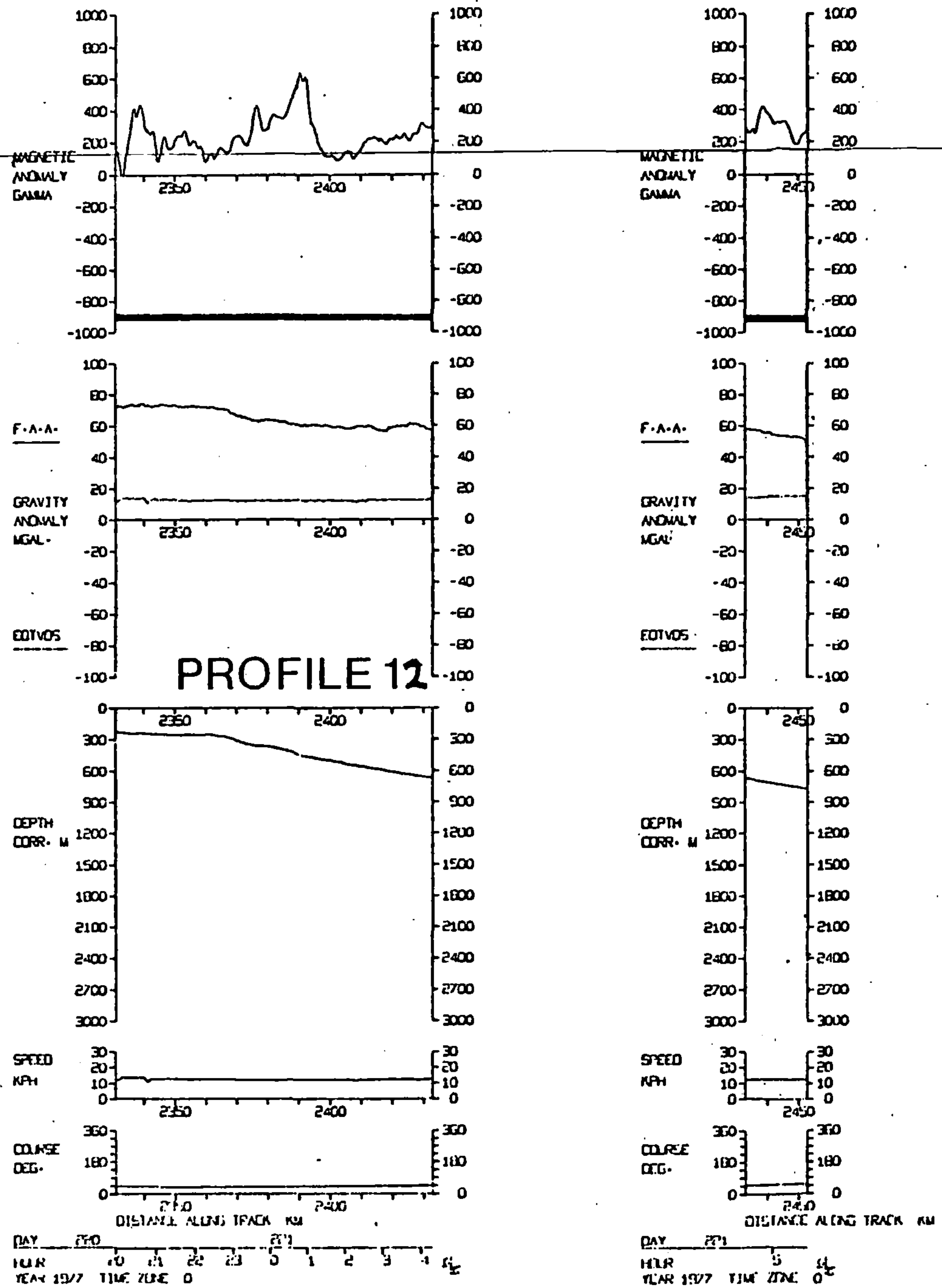
MAGNETIC ANOMALY GAMMA
F.A.A.
GRAVITY ANOMALY MGAL.
EOTVOS
DEPTH CORR. M
SPEED KPH
COURSE DEG.
DISTANCE ALONG TRACK KM
DAY
HOUR
YEAR 1977 TIME ZONE 0

PROFILE 12

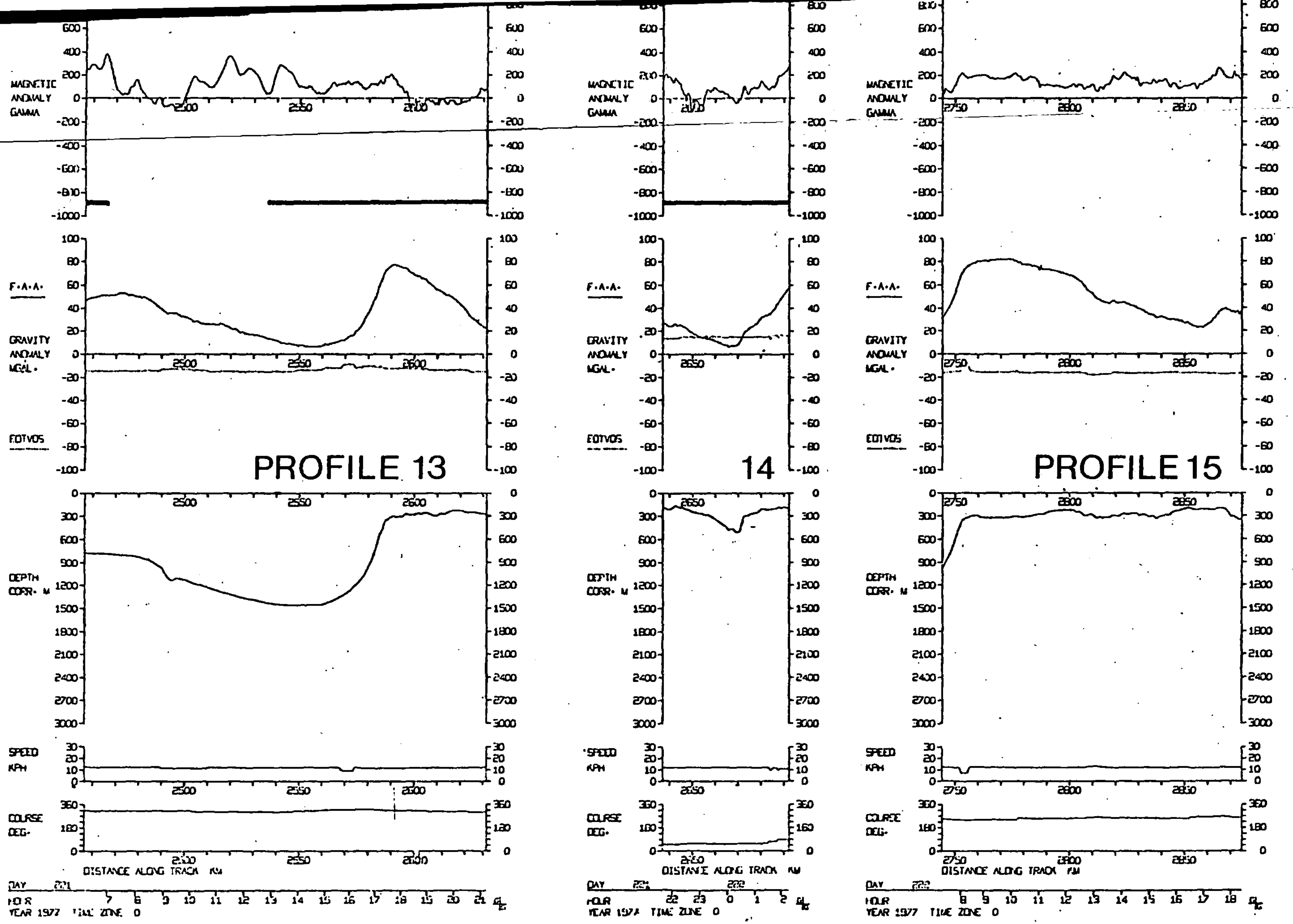
PROFILE 13
14
PROFILE 15
MAGNETIC ANOMALY GAMMA
F.A.A.
GRAVITY ANOMALY MGAL.
EOTVOS
DEPTH CORR. M
SPEED KPH
COURSE DEG.
DISTANCE ALONG TRACK KM
DAY
HOUR
YEAR 1977 TIME ZONE 0

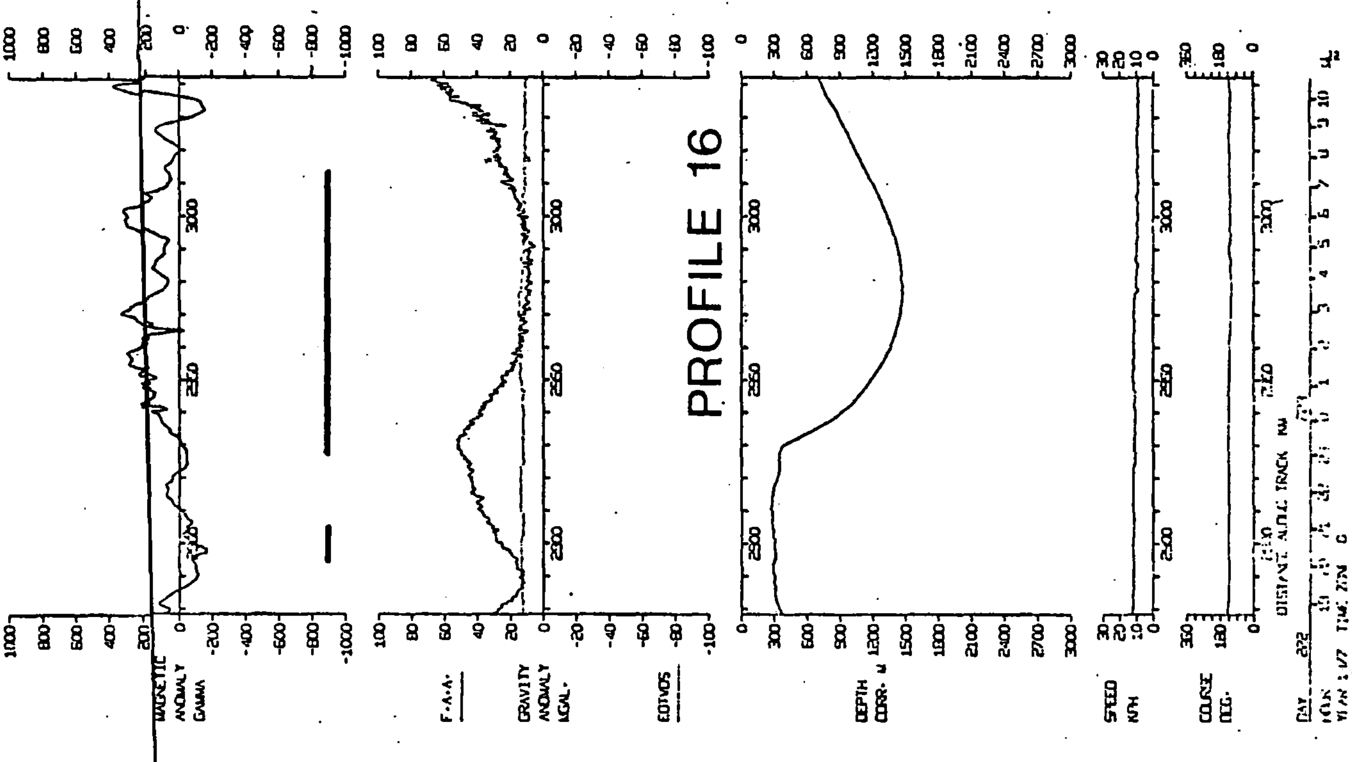
PROFILE 16
MAGNETIC ANOMALY GAMMA
F.A.A.
GRAVITY ANOMALY MGAL.
EOTVOS
DEPTH CORR. M
SPEED KPH
COURSE DEG.
DISTANCE ALONG TRACK KM

APPENDIX B

COMPUTER PROGRAMS

The two computer programs presented in this appendix have been designed primarily for interactive use on a VDU terminal. Extensive comments have been incorporated into both program listings. During execution, each program will prompt the user with questions relating to various input parameters and any input formats are specified at this time also. Computer programs, MERCAT and SPECTRAL, are stored on the magnetic tape QGK2Ø2 (see Appendix A).

(1) Program: MERCAT

Purpose: To calculate distance along ship's track in kilometres for marine data from geodetic latitudes and longitudes. The program may be used to project the navigational data on to a loxodrome of specified heading or the best fitting rhumbline, in the least squares sense, may be fitted through the data.

Program execution:

```
ØRUN *FTNX SCARDS = MERCAT    SPUNCH = -temp
ØRUN -temp  2 = input file    4 = output file
            5 = *SOURCE*      6 = *SINK*
```

I/O Data transfer:

The input file attached to logical unit 2 is assumed to be in edited Merged-Merged Format 3 (Appendix A and Table A.1). Beginning of profile markers and the integer number of 2-minute data values along the profile are used by the program to locate each profile within the data set. The program reads the following parameters from unit 2:

ITIME(J)	time (hours/tenths of minutes)
RLAT(J)	geodetic latitude (decimal degrees)
RLON(J)	longitude (decimal degrees)
IDEP(J)	corrected depth (metres)
IMAG(J)	magnetic anomaly (gamma)
IGRAV(J)	free air gravity anomaly (tenths of mgals).

After program execution, these data are written onto the output file attached to logical unit 4 in exactly the same format, with the addition of calculated distance, DIST(J) along the projected loxodrome inserted between RLON(J) and IDEP(J) in the format: 3X, F7.2, 5X. Each profile listing in the output file is terminated by summary information including:

heading of projected profile (degrees)
average velocity along projected profile (km hr^{-1})
average sample spacing (km)
RMS error in sample spacing (km).

```
C
C
C     PROGRAM NAME:     MERCAT
C
C     AUTHOR:   TOM ARMSTRONG        JULY,1979
C
C     ABSTRACT:
C                 THIS PROGRAM CALCULATES DISTANCE ALONG SHIP'S TRACK IN
C     KILOMETRES FOR MARINE DATA FROM GEODETIC LATITUDES AND LONGITUDES.
C     IT MAY BE USED TO PROJECT THE DATA ONTO A LOXODROME OF SPECIFIED
C     HEADING OR THE BEST FITTING RHUMBLINE IN THE LEAST SQUARES SENSE
C     MAY BE FITTED TO THE DATA
C
C     REFERENCES:
C                    (1) RICHARDUS,P. AND ADLER,R.K.(1972),MAP PROJECTIONS
C                        FOR GEODICISTS,CARTOGRAPHERS AND GEOGRAPHERS.
C                        NORTH-HOLLAND PUBL.CO.,AMSTERDAM-LONDON,1972.
C                    (2) BOMFORD,G.(1962),GEODESY,
C                        OXFORD UNIVERSITY PRESS,OXFORD,SECOND EDITION,1962.
C                    (3) EWING,C.E.AND MITCHELL,M.M.(1970),INTRODUCTION TO
C                        GEODESY,AMERICAN ELSEVIER PUBL.CO.,INC.,NEW YORK,
C                        1970.
C
C
C
C
C     DATA INPUT SECTION:  DESIGNED FOR INTERACTIVE USE
C                          UNITS SPECIFIED:
C                                                2=INPUT FILE
C                                                4=OUTPUT FILE
C
C     DEFINITIONS:
C                  A=EQUATORIAL RADIUS OF THE EARTH,KM.
C                  F=FLATTENING OF THE EARTH,(A-B)/A
C                  RTD=RADIANS TO DEGREES CONVERSION FACTOR
C                  SCALE=SCALING FACTOR FOR MERCATOR PROJECTION
C                  QUAD=INTEGER FLAG TO DENOTE QUADRANT IN WHICH VALUE
C                       OF HEADING LIES
C                  NPROF=INTEGER PROFILE IDENTIFICATION NO.
C
      REAL*8 DLAT,DLON,F,DARG
      DIMENSION RLAT(1000),RLON(1000),DIST(1000),IDEP(1000)
      DIMENSION IGRAV(1000),ITIME(1000),DLAT(1000),DLON(1000)
      DIMENSION IMAG(1000),X(1000),Y(1000)
      INTEGER QUAD
      PI=3.14159265
      A=6378.16
      F=1.0/298.25
      RTD=180.0/PI
      ISAMP=2
      QUAD=0
      SCALE=A/100.0
      WRITE(6,200)
  200 FORMAT('ENTER START AND END LEG NUMBERS',/,'FORMAT: 2I3')
      READ(5,100) ISTART,IEND
  100 FORMAT(2I3)
      WRITE(6,201)
  201 FORMAT('IF DATA IS TO BE PROJECTED ON TO GIVEN HEADING',/,
     1'ENTER HEADING IN DEGREES; FORMAT: I5',/,'IF LEAST SQUARES LINE TO
     2 BE FITTED THROUGH PROFILE DATA, ENTER A VALUE >360')
```

```
      READ(5,101) IHEAD
  101 FORMAT(I5)
      DO 90 I=ISTART,IEND
    5 READ(2,101) NPROF
      IF(NPROF.NE.I) GO TO 5
      READ(2,101) NUM
      BACKSPACE 2
      BACKSPACE 2
      DO 10 J=1,NUM
      READ(2,105) ITIME(J),RLAT(J),RLON(J),IDEP(J),IMAG(J),IGRAV(J)
  105 FORMAT(20X,I5,F8.4,F9.4,15X,I5,8X,I5,I5)
C
C     CHANGE INPUT LATITUDE AND LONGITUDE INTO RADIANS AND CONVERT
C     GEODETIC LATITUDE TO REDUCED LATITUDE(SEE REFERENCE (3),
C     PAGES 23-24)
C
      DLAT(J)=RLAT(J)/RTD
      DARG=DSQRT(1.0-2.0*F+F**2)*DSIN(DLAT(J))/DCOS(DLAT(J))
      DLAT(J)=DATAN(DARG)
      DLON(J)=RLON(J)/RTD
C
C     TRANSFORM REDUCED LATITUDE AND LONGITUDE ON MAJOR SPHERE OF
C     ELLIPSOID TO THE X AND Y COORDINATES OF THE MERCATOR PROJECTION.
C     THE TRANSFORMATION FORMULAE FOR A SPHERICAL EARTH ARE USED
C     SINCE THE DATA HAVE BEEN PROJECTED ONTO THE MAJOR SPHERE OF
C     THE ELLIPSOID.
C
      X(J)=SCALE*DLON(J)
      THETA=0.5*(DLAT(J)+PI/2.0)
      Y(J)=SCALE*ALOG(SIN(THETA)/COS(THETA))
   10 CONTINUE
C
C     IF THE BEST FITTING LEAST SQUARES LOXODROME IS TO BE FITTED
C     THROUGH THE DATA,CALL THE LEAST SQUARES SUBROUTINE.
C
      IF(IHEAD.GT.360) CALL LEASQU(X,Y,NUM,GRAD,CONST,ERROR)
      IF(IHEAD.GT.360) GO TO 15
C
C     IF DATA TO BE PROJECTED ONTO A LOXODROME OF SPECIFIED AZIMUTH
C     CALCULATE THE SLOPE OF THE STRAIGHT LINE ON THE X-Y PLANE
C     EQUIVALENT TO THE GIVEN HEADING,IHEAD AND THE CONSTANT IN THE
C     EQUATION Y=SLOPE*X+C.
C
      THETA=FLOAT(IHEAD)/RTD
      IF(THETA.LE.PI) THETA=0.5*PI-THETA
      IF(THETA.GT.PI) THETA=1.5*PI-THETA
      GRAD=SIN(THETA)/COS(THETA)
      CONST=Y(1)-GRAD*X(1)
C
C     PROJECT THE DATA ONTO THE CHOSEN LOXODROME AND CALCULATE
C     THE NEW X AND Y COORDINATES.
C
   15 CALL COORDS(X,Y,NUM,GRAD,CONST)
C
C     INVERT THE NEW X AND Y COORDINATES ALONG THE LOXODROME
C     TO THEIR EQUIVALENT REDUCED LATITUDES AND LONGITUDES.
C
      CALL INVERT(X,Y,NUM,DLAT,DLON,SCALE)
C
C     CONVERT THE NEW REDUCED LATITUDES TO GEODETIC LATITUDES
```

```
C      AND CHANGE THE ANGULAR VALUES FROM RADIANS TO DEGREES FOR
C      OUTPUT PURPOSES: STORED IN ARRAYS RLAT(J) AND RLON(J).
C
       DO 20 J=1,NUM
       DARG=DSIN(DLAT(J))/(DCOS(DLAT(J))*DSQRT(1.0-2.0*F+F**2))
       DLAT(J)=DATAN(DARG)
       RLAT(J)=SNGL(DLAT(J)*RTD)
       RLON(J)=SNGL(DLON(J)*RTD)
    20 CONTINUE
C
C      HAVING DETERMINED THE QUADRANT IN WHICH THE AZIMUTH
C      OF THE LOXODROME LIES, CONVERT THE SLOPE OF THE STRAIGHT
C      LINE TO THE EQUIVALENT HEADING IN DEGREES FROM NORTH
C      (CLOCKWISE).
C
       IF(IHEAD.LE.360) GO TO 50
       IF(RLAT(NUM).GE.RLAT(1).AND.RLON(NUM).GE.RLON(1)) QUAD=1
       IF(RLAT(NUM).LT.RLAT(1).AND.RLON(NUM).GE.RLON(1)) QUAD=2
       IF(RLAT(NUM).LT.RLAT(1).AND.RLON(NUM).LT.RLON(1)) QUAD=3
       IF(RLAT(NUM).GE.RLAT(1).AND.RLON(NUM).LT.RLON(1)) QUAD=4
       GO TO (30,30,40,40),QUAD
    30 BEAR=0.5*PI-ATAN(GRAD)
       GO TO 50
    40 BEAR=1.5*PI-ATAN(GRAD)
    50 IF(IHEAD.LE.360) HEAD=FLOAT(IHEAD)
       IF(IHEAD.GT.360) HEAD=BEAR*RTD
       IF(IHEAD.GT.360) ERROR=ATAN(ERROR)*RTD
C
C      CALCULATE DISTANCE ALONG THE LOXODROME ONTO WHICH
C      THE GEOPHYSICAL DATA HAS BEEN PROJECTED.
C
       CALL DISTAN(DLAT,DLON,NUM,DIST,A,F,HEAD)
C
C      CALCULATE THE MEAN AND STANDARD DEVIATION OF THE
C      SAMPLING INTERVAL ALONG THE LOXODROME PROFILE.
C
       CALL STDDEV(NUM,DIST,XMEAN,RMS)
C
C      CALCULATE THE AVERAGE VELOCITY ALONG THE NEW SHIP'S
C      TRACK PROJECTED ONTO THE LOXODROME
C      ISAMP=THE SAMPLING INTERVAL IN TIME(MINUTES)
C
       AVEL=60.0*(DIST(NUM)-DIST(1))/FLOAT(ISAMP*(NUM-1))
C
C      DATA OUTPUT SECTION:
C                                  THE NEW DATA ARE OUTPUT IN THE SAME
C      FORMAT AS THE DATA ARE INPUT. THE GEODETIC LATITUDES AND
C      LONGITUDES ALONG THE LOXODROME ARE GIVEN IN DEGREES; THE
C      DISTANCE ALONG SHIP'S TRACK IN KILOMETRES.
C
       WRITE(4,209) I,ITIME(1),RLAT(1),RLON(1),DIST(1),IDEP(1),IMAG(1),
      1IGRAV(1)
       WRITE(4,209) NUM,ITIME(2),RLAT(2),RLON(2),DIST(2),IDEP(2),IMAG(2)
      1,IGRAV(2)
   209 FORMAT(I5,15X,I5,F8.4,F9.4,3X,F7.2,5X,I5,8X,I5,I5)
       DO 60 J=3,NUM
       WRITE(4,210) ITIME(J),RLAT(J),RLON(J),DIST(J),IDEP(J),IMAG(J),
      1IGRAV(J)
   210 FORMAT(20X,I5,F8.4,F9.4,3X,F7.2,5X,I5,8X,I5,I5)
    60 CONTINUE
```

```
      WRITE(4,220) HEAD,AVEL,XMEAN,RMS
  220 FORMAT(/,'HEADING OF PROJECTED PROFILE(DEGREES)=',F7.2,/,'AVERAGE
     1VELOCITY ALONG PROJECTED PROFILE(KM/HR)=',F7.2,/,'AVERAGE SAMPLE S
     2PACING(KM)=',F7.2,/,'RMS ERROR IN SAMPLE SPACING(KM)=',F7.2)
      IF(IHEAD.GT.360) WRITE(4,221) ERROR
  221 FORMAT('STANDARD ERROR IN AZIMUTH OF PROFILE(DEGREES)=',F7.2)
   90 CONTINUE
      STOP
      END
C
C
C     SUBROUTINE LEASQU
C
C     THIS SUBROUTINE CALCULATES THE BEST FITTING STRAIGHT LINE
C     OF THE FORM Y=SLOPE*X+Y0 IN THE LEAST SQUARES SENSE TO LX
C     PAIRS OF X,Y COORDINATES AND RETURNS THE VALUES OF THE
C     GRADIENT AND THE CONSTANT IN THE VARIABLES SLOPE AND Y0
C     RESPECTIVELY.
C
      SUBROUTINE LEASQU(X,Y,LX,SLOPE,Y0,ERROR)
      DIMENSION X(1000),Y(1000)
      REAL*8 SUMX,SUMY,SUMXY,SUMX2
      SUMX=0.0
      SUMY=0.0
      SUMXY=0.0
      SUMX2=0.0
      DO 10 I=1,LX
      SUMX=SUMX+X(I)
      SUMY=SUMY+Y(I)
   10 CONTINUE
      XMEAN=SUMX/FLOAT(LX)
      YMEAN=SUMY/FLOAT(LX)
      DO 20 I=1,LX
      SUMXY=SUMXY+(X(I)-XMEAN)*Y(I)
      SUMX2=SUMX2+(X(I)-XMEAN)**2
   20 CONTINUE
      SLOPE=SUMXY/SUMX2
      Y0=YMEAN-SLOPE*XMEAN
      SUMX=0.0
      DO 30 I=1,LX
      SUMX=SUMX+(Y(I)-SLOPE*X(I)-Y0)**2
   30 CONTINUE
      ERROR=SNGL(DSQRT(SUMX/(SUMX2*FLOAT(LX-2))))
      RETURN
      END
C
C
C     SUBROUTINE COORDS
C
C     THIS SUBROUTINE PROJECTS POINTS AT X,Y COORDINATES IN THE
C     X-Y PLANE ONTO A SPECIFIED STRAIGHT LINE OF GRADIENT=SLOPE
C     AND CONSTANT=Y0. THE NEW X,Y COORDINATES ALONG THE LINE
C     ARE CALCULATED AND RETURNED VIA THE X,Y ARRAYS, SO OVER-
C     WRITING THE ORIGINAL DATA.
C
      SUBROUTINE COORDS(X,Y,LX,SLOPE,Y0)
      DIMENSION X(1000),Y(1000)
      DO 10 I=1,LX
      C0=Y(I)+X(I)/SLOPE
      X(I)=SLOPE*(C0-Y0)/(1.0+SLOPE**2)
```

```
      Y(I)=Y0+SLOPE*X(I)
   10 CONTINUE
      RETURN
      END
C
C
C     SUBROUTINE INVERT
C
C     THIS SUBROUTINE INVERTS THE X AND Y COORDINATES OF THE
C     MERCATOR PROJECTION BACK INTO REDUCED LATITUDE AND LONGITUDE.
C
      SUBROUTINE INVERT(X,Y,LX,FY,RLAM,SCALE)
      REAL*8 FY,RLAM,TOP,BOT,THETA
      DIMENSION X(1000),Y(1000),FY(1000),RLAM(1000)
      DO 10 I=1,LX
      RLAM(I)=X(I)/SCALE
      THETA=Y(I)/SCALE
      TOP=DEXP(THETA)-1.0
      BOT=DEXP(THETA)+1.0
      FY(I)=2.0*DATAN(TOP/BOT)
   10 CONTINUE
      RETURN
      END
C
C
C     SUBROUTINE DISTAN
C
C     THIS SUBROUTINE CALCULATES DISTANCE ALONG SHIP'S TRACK FROM
C     INPUT LATITUDE AND LONGITUDE ALONG A LOXODROME OF SPECIFIED
C     HEADING. A GREAT CIRCLE, BEING THE SHORTEST DISTANCE BETWEEN
C     TWO POINTS ON A SPHERE, IS PROJECTED BETWEEN EACH PAIR OF
C     ADJACENT POINTS AND THE DISTANCE ALONG THE ARC IS CALCULATED
C     USING A SUITABLY CALCULATED VALUE OF THE RADIUS OF CURVATURE
C     OF THE ELLIPSOID AT THAT LATITUDE.
C
      SUBROUTINE DISTAN(FY,RLAM,LX,X,A,F,HEAD)
      REAL*8 DLAM,SDUM,CDUM,SB,CB,CS,SS
      REAL*8 FY,RLAM,R,F,THETA,AZIM,DEN,RR,RN
      DIMENSION FY(1000),RLAM(1000),X(1000)
      PI=3.14159265
      DTR=PI/180.0
      AZIM=HEAD*DTR
      MSTART=1
      MEND=LX
      JJ=1
      X(1)=0.0
      K=1
      IF(FY(1).GT.FY(LX)) JJ=-1
      IF(JJ.GT.0) MSTART=2
      IF(JJ.LT.0) MEND=LX-1
      DO 10 J=MSTART,MEND
      K=K+1
C
C     CALCULATE THE RADIUS OF CURVATURE ALONG THE AZIMUTH OF THE
C     LOXODROME FROM EULER'S THEOREM(SEE REFERENCE (3),PAGES 17-21)
C     AT THE MEAN LATITUDE,THETA OF THE TWO ADJACENT POINTS.
C     RR=RADIUS OF CURVATURE IN THE PLANE OF THE MERIDIAN
C     RN=RADIUS OF CURVATURE IN THE PLANE OF THE PRIME VERTICAL
C     R=RADIUS OF CURVATURE ALONG THE LOXODROME AT LATITUDE THETA.
C
```

```
      THETA=0.5*(FY(J)+FY(J-JJ))
      DEN=DSQRT(1.0-(2.0*F-F**2)*DSIN(THETA)**2)
      RR=A*(1.0-2.0*F+F**2)/DEN**3
      RN=A/DEN
      R=RR*RN/(RR*DSIN(AZIM)**2+RN*DCOS(AZIM)**2)
C
C     CALCULATE DIFFERENCE IN LONGITUDE,DLAM AND CORRECT THIS
C     SMALL CIRCLE ANGLE TO THE EQUIVALENT GREAT CIRCLE ANGLE.
C
      DLAM=DABS(RLAM(J)-RLAM(J-JJ))
      CDUM=DSIN(FY(J-JJ))**2+DCOS(DLAM)*(DCOS(FY(J-JJ))**2)
      SDUM=DSQRT(1.0-CDUM**2)
C
C     USING SPHERICAL TRIGONOMETRY, CALCULATE ANGULAR DISTANCE
C     IN RADIANS BETWEEN ADJACENT POINTS ALONG THE LOXODROME.
C
      SB=DSIN(0.5*PI-FY(J-JJ))*DSIN(DLAM)/SDUM
C
C     CHECK SB IS NOT GREATER THAN ZERO,SINCE IF ANGLE IS CLOSE
C     TO 90 DEGREES, THIS CONDITION MAY ARISE DUE TO INHERENT
C     LACK OF PRECISION IN VALUE OF CALCULATED SINE VALUE.
C
      IF(SB.GT.1.0) SB=1.0
      CB=DSQRT(1.0-SB**2)
      THETA=DABS(FY(J)-FY(J-JJ))
      CS=DCOS(THETA)*CDUM+DSIN(THETA)*SDUM*CB
      SS=DSQRT(1.0-CS**2)
C
C     CALCULATE INCREMENTAL DISTANCE,S ALONG LOXODROME AND
C     THEN ACCUMULATIVE DISTANCE,X(K).
C
      S=DATAN(SS/CS)*R
      X(K)=X(K-1)+S
   10 CONTINUE
      RETURN
      END
C
C
      SUBROUTINE STDDEV(LX,X,AMEAN,RMS)
C
C     SUBROUTINE STDDEV CALCULATES THE MEAN AND ROOT MEAN SQUARE DEVIATION
C     OF THE DATA FROM THE MEAN FOR A ONE DIMENSIONAL ARRAY, WHICH IN THIS
C     APPLICATION IS THE SPATIAL INCREMENT,XSTEP(I), BETWEEN ANOMALY VALUES
C
      DIMENSION X(1000),XSTEP(1000)
      LSTEP=LX-1
      SUM=0.0
      DO 10 I=1,LSTEP
      XSTEP(I)=X(I+1)-X(I)
      SUM=SUM+XSTEP(I)
   10 CONTINUE
      AMEAN=SUM/FLOAT(LSTEP)
      SUM=0.0
      DO 20 I=1,LSTEP
      SUM=SUM+(XSTEP(I)-AMEAN)**2
   20 CONTINUE
      VAR=SUM/FLOAT(LSTEP-1)
      RMS=SQRT(VAR)
      RETURN
      END
```

Program: SPECTRAL

Purpose: To calculate the power spectral density estimate of magnetic anomaly data using the maximum entropy method (the Burg algorithm; Claerbout, 1976), and subsequently, to estimate the depth to the causative buried magnetic body by calculating the slope of the natural logarithm of the normalised power spectral density estimate plotted against wavenumber.

Program execution:

```
$RUN *FTNX    SCARDS = SPECTRAL    SPUNCH = -temp
$RUN - temp + *GHOST + *NAG    2 = input file    4 = output file
5 = *SOURCE*    6 = *SINK*    9 = plot file
$RUN  *DURPLOT    1 = plot file
```

I/O Data transfer:

The program is designed to operate on a two-pass basis:

Pass 1: At this stage, a plot of the natural log of the normalised maximum entropy spectral density estimate versus wavenumber is produced. Furthermore, a plot of the final prediction error (Akaike, 1970) versus wavenumber is also produced for the Akaike criterion option if only one spectral estimate is made from the data set (that is, if the segment of data chosen for spectral estimation is equal to the data set length itself). The plot file is assigned to logical unit 9. A typical plot is shown in Figure B.1.

Pass 2: A straight line least squares regression is performed between specified wavenumber limits (chosen from the log spectrum plot produced in Pass 1) for each spectral density curve generated from the segments of magnetic anomaly data and the depth to the causative body is estimated from the slope of each straight line (see Section 3.2.4). The depth estimates and associated statistics for each segment of data are written on to the output file assigned to logical unit 4 (see Figure B.2).

The basic input data file for the program operating in pass 1 or pass 2 mode is either of edited Merged-Merged Format 3 (Appendix A)

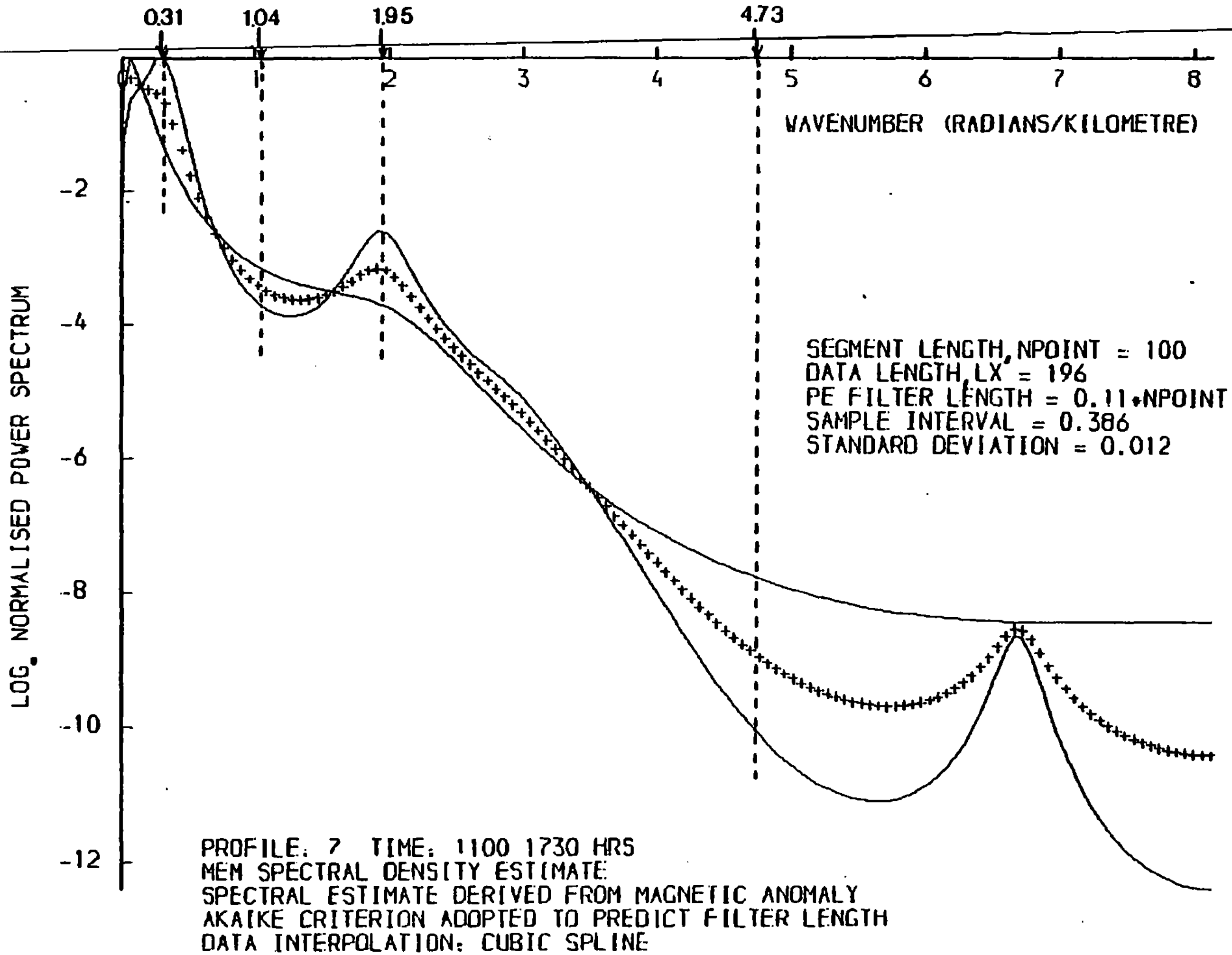

Figure B.1 Typical example of the natural logarithm, normalised MEM spectral density estimate drawn by the plotter after execution of Pass 1 of the computer program, SPECTRAL.

```
MARINE PROFILE NO.  7
START = 11000     IEND = 17300


OPERATOR LENGTH CHOSEN BY AKAIKE CRITERION
```

SEGMENT XSTART (KM)	XEND (KM)	LINE NUMBER	DEPTH (KM)	ERROR +/-(KM)	COEFFICIENT OF CORRELATION	LOW-CUT WAVENUMBER	HIGH-CUT WAVENUMBER	LPEF AKAIKE
2.61	40.82	1	1.23	0.07	-0.9821	0.31	1.04	5
2.61	40.82	2	0.78	0.01	-0.9924	1.95	4.73	5
2.61	40.82	3	0.69	0.01	-0.9920	0.31	4.73	5
21.91	60.12	1	2.74	0.17	-0.9812	0.31	1.04	11
21.91	60.12	2	1.33	0.02	-0.9972	1.95	4.73	11
21.91	60.12	3	0.89	0.04	-0.9391	0.31	4.73	11

```
MEAN STATISTICS FOR LINE NO. 1
AVERAGE DEPTH =     1.98
STANDARD ERROR IN DEPTH =     0.12
CORRELATION COEFFICIENT =-0.9819
LENGTH OF BERRYMAN OPERATOR = 38

MEAN STATISTICS FOR LINE NO. 2
AVERAGE DEPTH =     1.05
STANDARD ERROR IN DEPTH =     0.00
CORRELATION COEFFICIENT =-0.9997
LENGTH OF BERRYMAN OPERATOR = 38

MEAN STATISTICS FOR LINE NO. 3
AVERAGE DEPTH =     0.79
STANDARD ERROR IN DEPTH =     0.02
CORRELATION COEFFICIENT =-0.9703
LENGTH OF BERRYMAN OPERATOR = 38
```

Figure B.2 Depth estimates and associated statistics for each segment of data written on the output file assigned to logical unit 4 after execution of Pass 2 of the computer program, SPECTRAL.

type (for example, the output file format from program MERCAT) or it may be in the format of the output file from the magnetic anomaly generating program, MAGN, available in the Department of Geological Sciences, University of Durham. If alternative input formats are required, it is suggested that the FORMAT statement contained in line 132 of the program listing is modified rather than alter the marine data input format option.

The parameters read by the program from the input data file are the distance, X(I) along the profile and the magnetic anomaly, ANOM(I). In addition, for the marine data input option, the time is read from the input file since time is used to define the start and end of the data set length. The start and end times specified must be even multiples of 2-minute values in order to match the geophysical data 2-minute values listed in the input data file. It is important to note that when used for analysis of marine magnetic data, the program searches through the input data file to find the beginning of the specified profile. Therefore, the input data file must have start-of-profile markers present as indicated in Appendix A.

```
C
C      PROGRAM NAME:   SPECTRAL
C
C      AUTHOR:   TOM ARMSTRONG     AUGUST,1979
C
C      ABSTRACT:
C               THIS PROGRAM USES THE MAXIMUM ENTROPY METHOD(MEM) TO
C      CALCULATE THE POWER SPECTRAL DENSITY ESTIMATE.
C
C         THE BURG ALGORITHM IS USED TO CALCULATE THE COEFFICIENTS OF A
C      PREDICTION ERROR FILTER WHICH, OPERATING ON THE INPUT SIGNAL, WILL
C      PRODUCE A WHITE SPECTRUM. FROM WIENER OPTIMUM FILTER THEORY, THE
C      DESIRED INPUT SPECTRUM IS OBTAINED AS THE INVERSE OF THE SQUARED
C      RESPONSE OF THE PREDICTION ERROR FILTER.
C         THE FINAL PREDICTION ERROR CRITERION DUE TO AKAIKE(1970) IS
C      ADOPTED TO PREDICT THE OPTIMUM PREDICTION ERROR FILTER LENGTH IN
C      THE INEVITABLE TRADE-OFF BETWEEN STATISTICAL VARIANCE AND RESOLUTION.
C         AN EMPIRICAL CRITERION PROPOSED BY BERRYMAN(1978) IS ALSO
C      AVAILABLE AS AN OPTION TO CALCULATE AN UPPER BOUND ON THE
C      NUMBER OF COEFFICIENTS IN THE PREDICTION ERROR OPERATOR.
C
C         *NOTE*: THE INTEGRATED MEM SPECTRUM AMPLITUDE VALUE IS PROPORTIONAL
C      TO THE ACTUAL POWER IN A GIVEN FREQUENCY. THE SPECTRAL DENSITY ESTIMATE
C      IS PROPORTIONAL TO POWER**2.
C
C      REFERENCES:
C                (1) CLAERHOUT,J.F.(1976) FUNDAMENTALS OF GEOPHYSICAL
C                 DATA PROCESSING,MCGRAW-HILL,NEW YORK.
C
C                (2) KANASEWICH,E.R.(1975) TIME SEQUENCE ANALYSIS IN
C                 GEOPHYSICS,UNIVERSITY OF ALBERTA PRESS,EDMONTON,CANADA.
C
C                (3) LACOSS,R.T.(1971) DATA ADAPTIVE SPECTRAL ANALYSIS
C                 METHODS,GEOPHYSICS,36,661-675.
C
C                (4) BERRYMAN,J.G.(1978) CHOICE OF OPERATOR LENGTH FOR
C                 MAXIMUM ENTROPY SPECTRAL ANALYSIS,
C                 GEOPHYSICS,43,1384-1391.
C
       REAL*8 XDUM(1024),YDUM(1024),POINT,VALUE,WORK1(50),WORK2(50)
       DIMENSION S(256),G(1024),X(1024),ANOM(1024),W(256),FPE(256)
       DIMENSION SS(256),ANEW(1024),XNEW(1024),TITLE(8)
       DIMENSION STORE(50,256),BCUT(10),TCUT(10)
C
C
C      *******************************************************************
C
C
C      DATA INPUT SECTION: DESIGNED FOR INTERACTIVE USE
C                          UNITS SPECIFIED:
C                                          2=DATA FILE
C                                          4=OUTPUT FILE
C                                          5=*SOURCE*
C                                          6=*SINK*
C                                          9=PLOT FILE
C
C
C
C      THIS PROGRAM IS DESIGNED ON A TWO PASS SYSTEM;
C
```

```
C           PASS 1:
C                   THE MEM SPECTRAL DENSITY ESTIMATE IS CALCULATED
C                   FOR THE CHOSEN OPERATOR LENGTH AND A PLOT IS PRODUCED
C                   OF THE LOG SPECTRUM VERSUS WAVENUMBER.FOR THE AKAIKE
C                   CRITERION,IF THE NOS. OF POINTS IN THE SEGMENT IS
C                   EQUAL TO THE NOS. OF POINTS IN THE PROFILE, A FURTHER
C                   PLOT OF FINAL PREDICTION ERROR IS PRODUCED.
C
C           PASS 2:
C                   WAVENUMBER LIMITS ARE GIVEN BETWEEN WHICH A STRAIGHT
C                   LINE LEAST SQUARES REGRESSION IS PERFORMED ON THE LOG
C                   SPECTRUM VS. WAVENUMBER PLOT. THE RESULTS ARE OUTPUT
C                   TO THE FILE ON UNIT 4.
C
C
C       ***************************************************************
        PI=3.14159265
        WRITE(6,206)
    206 FORMAT('IS THIS THE FIRST PASS? YES=0  NO=1',/,'FORMAT: I2')
        READ(5,105) IPASS
    105 FORMAT(I2)
        IF(IPASS.EQ.0) GO TO 3
        WRITE(6,207)
    207 FORMAT('ENTER NOS.OF STRAIGHT LINE SEGMENTS TO BE FITTED',/,
       1'FORMAT: I2')
        READ(5,105) NLINE
        DO 6 I=1,NLINE
        WRITE(6,208) I
    208 FORMAT('ENTER WAVENUMBER LIMITS OF LINE',I2,/,'FORMAT: 2F5.2')
        READ(5,108) BCUT(I),TCUT(I)
    108 FORMAT(2F5.2)
      6 CONTINUE
      3 WRITE(6,205)
    205 FORMAT('ENTER NOS. OF POINTS IN EACH PROFILE SEGMENT',/,
       1'FORMAT: I3')
        READ(5,102) NPOINT
    102 FORMAT(I3)
        WRITE(6,209)
    209 FORMAT('CHOSE CRITERION FOR LPEF',/,'AKAIKE=0  BERRYMAN=1'
       1,/,'ALGEBRAIC SUM OF SPECTRA CALCULATED BETWEEN THESE',/,
       2'CRITERIA=2',/,'SPECIFIC VALUE OF OPERATOR=3',/,'FORMAT:  I2')
        READ(5,105) IFILT
        IF(IFILT.LT.3) GO TO 1
        WRITE(6,204)
    204 FORMAT('ENTER LENGTH OF OPERATOR AS % OF SEGMENT LENGTH',/,
       1'FORMAT: I2')
        READ(5,105) LPEF
        LPEF=IFIX(0.5+FLOAT(LPEF*NPOINT)/100.0)
      1 WRITE(6,215)
    215 FORMAT('CHOOSE METHOD OF SPECTRAL ESTIMATION:',/,
       1'SPECTRAL ESTIMATE FROM MAGNETIC ANOMALY=0',/,
       2'SPECTRAL ESTIMATE FROM HORIZONTAL DERIVATIVE OF ANOMALY=1'
       3,/,'FORMAT: I2')
        READ(5,105) IFLAG
        WRITE(6,200)
    200 FORMAT('DATA INTERPOLATION=0',/,'EVENLY SPACED DATA=1',/,
       1'UNEVENLY SPACE DATA=2',/,'FORMAT: I2')
        READ(5,105) INPOL
        WRITE(6,201)
    201 FORMAT('CHOOSE MODE OF DATA INPUT',/,'MARINE=1',/,
```

```
     1'MAGN=0',/,'FORMAT: I2')
      READ(5,105) ISIG
      IF(ISIG.EQ.1) GO TO 4
      WRITE(6,220)
  220 FORMAT('ENTER TITLE TO APPEAR ON GRAPH',/,'FORMAT: 8A4')
      READ(5,110) TITLE
  110 FORMAT(8A4)
      READ(2,100) LX
  100 FORMAT(I5)
      DO 2 I=1,LX
      READ(2,150) X(I),ANOM(I)
  150 FORMAT(2X,F8.1,12X,F10.1)
    2 CONTINUE
      GO TO 16
    4 WRITE(6,240)
  240 FORMAT('ENTER PROFILE NUMBER',/,'FORMAT: I2')
      READ(5,105) NPROF
      WRITE(6,245)
  245 FORMAT('ENTER START AND END TIMES IN HRS/MINS',/,
     1'FORMAT:  2I5')
      READ(5,106) ISTART,IEND
  106 FORMAT(2I5)
      ISTART=ISTART*10
      IEND=IEND*10
      J=0
      WRITE(6,250)
  250 FORMAT('ARE START AND END TIMES AMBIGUOUS?',/,'NO=0  YES=1',/,
     1'FORMAT: I2')
      READ(5,105) IAMB
      IF(IAMB.EQ.0) GO TO 5
      WRITE(6,256)
  256 FORMAT('ENTER NENTH OCCURRENCE REQUIRED',/,'FORMAT: I2')
      READ(5,105) IAMB
    5 READ(2,100) N
      IF(N.NE.NPROF) GO TO 5
      BACKSPACE 2
      LX=1
   10 READ(2,115) ITIME
  115 FORMAT(20X,I5)
      IF(ITIME.NE.ISTART) GO TO 10
      J=J+1
      IF(IAMB.GT.0.AND.IAMB.NE.J) GO TO 10
      BACKSPACE 2
   15 READ(2,120) ITIME,X(LX),IMAG
  120 FORMAT(20X,I5,20X,F7.2,18X,I5)
      ANOM(LX)=FLOAT(IMAG)
      IF(ITIME.EQ.IEND) GO TO 16
      LX=LX+1
      GO TO 15
C
C
   16 IF(IPASS.EQ.0) GO TO 23
C
C     PREPARE OUTPUT FILE ON UNIT 4 WITH TITLE,OPERATOR LENGTH
C     CRITERION AND DATA HEADINGS
C
      IF(ISIG.EQ.0) WRITE(4,211) TITLE
      IF(ISIG.EQ.1) WRITE(4,212) NPROF,ISTART,IEND
  211 FORMAT(//,3X,8A4,//)
  212 FORMAT(//,3X,'MARINE PROFILE NO.',I3,/,3X,'START =',I6,3X,
```

```
     1'IEND =',I6,//)
      IF(IFILT.EQ.0) WRITE(4,213)
      IF(IFILT.EQ.1) WRITE(4,214)
      IF(IFILT.FQ.2) WRITE(4,216)
  213 FORMAT(3X,'OPERATOR LENGTH CHOSEN BY AKAIKE CRITERION',/)
  214 FORMAT(3X,'OPERATOR LENGTH CHOSEN BY BERRYMAN CRITERION',/)
  216 FORMAT(3X,'ALGEBRAIC SUM OF SPECTRA GENERATED BY LPEF"S',
     1/,3X,'BETWEEN AKAIKE AND BERRYMAN CRITERIA',/)
      WRITE(4,255)
  255 FORMAT(12X,'SEGMENT',/,8X,'XSTART',5X,'XEND',6X,'LINE',5X,
     1'DEPTH',5X,'ERROR',5X,'COEFFICIENT',7X,'LOW-CUT',7X,'HIGH-CUT',
     28X,'LPEF',/,9X,'(KM)',6X,'(KM)',4X,'NUMBER',5X,'(KM)',5X,
     3'+/-(KM)',3X,'OF CORRELATION',2(4X,'WAVENUMBER'),6X,'AKAIKE',/)
C
C     CALCULATE MEAN VALUE,DELX, OF SAMPLING INTERVAL AND ROOT MEAN
C     SQUARE ERROR OF THE DATA FROM THE MEAN
C
   23 CALL STDDEV(LX,X,DELX,RMS)
C
C     CALCULATE LENGTH OF BERRYMAN OPERATOR
C
      TOP=FLOAT(2*NPOINT)
      BOT=ALOG(TOP)
      LOPER=IFIX(0.5+TOP/BOT)
      IF(INPOL.NE.0) GO TO 26
C
C     INTERPOLATION OF DATA SAMPLED AT IRREGULAR INTERVALS USING A
C     CUBIC SPLINE TECHNIQUE
C
      I=1
      XEND=X(LX)
      XNEW(1)=X(1)
   17 I=I+1
      XNEW(I)=XNEW(I-1)+DELX
      IF(XNEW(I).GT.XEND) GO TO 18
      GO TO 17
   18 NNEW=I-1
      I=1
      DO 19 J=1,NNEW
   20 IF(XNEW(J).LE.X(I+1).AND.XNEW(J).GE.X(I)) GO TO 21
      I=I+1
      GO TO 20
   21 N1=I-5
      N2=I+5
      IF(N1.LE.0) N1=1
      IF(N1.EQ.1) N2=N1+10
      IF(N2.GT.LX) N2=LX
      IF(N2.EQ.LX) N1=N2-10
      M=0
      DO 22 K=N1,N2
      M=M+1
      XDUM(M)=X(K)
      YDUM(M)=ANOM(K)
   22 CONTINUE
      POINT=XNEW(J)
      IG=M+1
C
C     *NAG:E01ADF
C     SUBROUTINE FOR INTERPOLATION OF UNEQUALLY SPACED DATA
C     REFERENCES:
```

```
C                       (1) HAYES,J.G.(ED) NUMERICAL APPROXIMATIONS TO FUNCTIONS
C                        AND DATA,ATHLONE PRESS,1970.
C
C                       (2) HANDSCOMB,D.C.(ED) METHODS OF NUMERICAL APPROXIMATION,
C                        PERGAMON PRESS,1966.
C
      CALL E01ADF(M,POINT,XDUM,YDUM,WORK1,WORK2,IG,VALUE)
      ANEW(J)=SNGL(VALUE)
   19 CONTINUE
      DO 25 I=1,NNEW
      ANOM(I)=ANEW(I)
      X(I)=XNEW(I)
   25 CONTINUE
      LX=NNEW
C
C     SET INTEGER VALUE OF N TO DETERMINE ULTIMATE RESOLVING POWER OF
C     SPECTRAL DENSITY ESTIMATE CALCULATED BY BURG ALGORITHM
C
   26 N=256
      DO 24 I=1,N
      SS(I)=0.0
   24 CONTINUE
C
C     CALCULATE NOS.OF SEGMENTS OF PROFILE FOR WHICH SPECTRAL
C     DENSITY ESTIMATE TO BE CARRIED OUT
C
      NSEG=(2*LX/NPOINT)-1
      NSTART=1
      NEND=NPOINT
      IF(IFILT.EQ.1) LPEF=LOPER
C
C     APPLY BURG ALGORITHM TO EACH SEGMENT OF PROFILE DATA
C
      DO 44 J=1,NSEG
      IF(IFILT.EQ.0.OR.IFILT.EQ.2) LPEF=0
      KK=0
      DO 29 K=NSTART,NEND
      KK=KK+1
      ANEW(KK)=ANOM(K)
   29 CONTINUE
      IF(IFLAG.EQ.0) GO TO 28
C
C     CALCULATE HORIZONTAL DERIVATIVE OF MAGNETIC ANOMALY
C
      CALL DERIV(NPOINT,5,X,ANEW,G)
      DO 27 I=1,NPOINT
      ANEW(I)=G(I)
   27 CONTINUE
C
C     REMOVE LINEAR TREND FROM INPUT DATA BEFORE APPLICATION OF
C     SPECTRAL ANALYSIS TECHNIQUES
C
   28 CALL TREND(X,ANEW,NPOINT)
C
C     CALCULATE SPECTRAL DENSITY ESTIMATE OF INPUT DATA USING THE
C     BURG ALGORITHM
C
      CALL BURG(NPOINT,ANEW,N,LPEF,DELX,S,W,FPE,NUM)
      IF(IFILT.NE.2) GO TO 30
C
```

```
C     CALCULATE MEAN VALUE OF POWER SPECTRAL DENSITY ESTIMATE
C     BETWEEN AKAIKE AND BERRYMAN OPERATOR LENGTHS FOR EACH
C     SEGMENT OF DATA
C
      CALL SIGMA(NPOINT,ANEW,N,LOPER,LPEF,DELX,S,W,FPE,NUM)
C
C     CALCULATE LENGTH OF PREDICTION ERROR FILTER AS PROPORTION OF INPUT
C     DATA WINDOW LENGTH
C
   30 SC=FLOAT(LPEF)/FLOAT(NPOINT)
      BERRY=FLOAT(LOPER)/FLOAT(NPOINT)
      MID=1+N/2
C
C     DOUBLE THE VALUE OF POWER AT EACH WAVENUMBER EXCEPT FOR
C     ZERO WAVENUMBER TERM, SINCE POWER IN NEGATIVE WAVENUMBERS
C     HAS NO PHYSICAL MEANING FOR PROFILE DATA
C
   35 DO 39 I=2,MID
      S(I)=2.0*S(I)
   39 CONTINUE
C
C     CALCULATE NATURAL LOGARITHM OF POWER SPECTRAL DENSITY
C     ESTIMATE NORMALISED TO MAXIMUM POWER TERM
C
      CALL MAXMIN(MID,S,SMAX,SMIN)
      DO 40 I=1,MID
      S(I)=ALOG(S(I)/SMAX)
      STORE(J,I)=S(I)
C
C     CALCULATE AVERAGE SPECTRAL DENSITY ESTIMATE OF ALL SEGMENTS
C
      SS(I)=SS(I)+S(I)/FLOAT(NSEG)
   40 CONTINUE
      CALL MAXMIN(MID,S,SMAX,SMIN)
      IF(J.GT.1) GO TO 41
      YMAX=(SMAX+SMIN)/2.0
      YMIN=YMAX
   41 IF(SMAX.GT.YMAX) YMAX=SMAX
      IF(SMIN.LT.YMIN) YMIN=SMIN
      IF(IPASS.EQ.0) GO TO 42
C
C     CALCULATE DEPTHS TO CAUSATIVE BODIES BY FITTING LEAST
C     SQUARES LINE OF REGRESSION TO SPECTRAL ESTIMATE BETWEEN
C     SPECIFIED WAVENUMBER LIMITS
C
      CALL DEPTH(W,S,MID,LX,BCUT,TCUT,NLINE,X,NSTART,NEND,LPEF,LOPER)
   42 NSTART=NSTART+NPOINT/2
      NEND=NEND+NPOINT/2
   44 CONTINUE
C
C     CALCULATE AVERAGE DEPTH ALONG PROFILE FROM AVERAGE
C     SPECTRAL DENSITY ESTIMATE
C
      IF(IPASS.EQ.1) CALL DEPTH(W,SS,MID,LX,BCUT,TCUT,NLINE,X,
     1NSTART,NEND,LPEF,LOPER)
      IF(IPASS.EQ.1) GO TO 70
C     ************************************************************
C
C
C     OUTPUT SECTION: *GHOST PLOTTING SUBROUTINES
```

```
C
C
C     ******************************************************************
      CALL MAXMIN(MID,W,XMAX,XMIN)
      CALL PAPER(1)
      CALL CTRMAG(12)
      CALL CSPACE(0.0,2.0,0.0,1.0)
      CALL PSPACE(0.1,0.9,0.25,0.85)
      CALL MAP(XMIN,XMAX,YMIN,YMAX)
      CALL AXES
      CALL PTPLOT(W,SS,1,MID,43)
      DO 47 J=1,NSEG
      DO 46 I=1,MID
      S(I)=STORE(J,I)
   46 CONTINUE
      CALL PTPLOT(W,S,1,MID,-2)
   47 CONTINUE
      CALL CTRORI(1.0)
      CALL PLACE(38,2)
      CALL TYPECS('LOG',3)
      CALL SUFFIX
      CALL CTRSET(2)
      CALL TYPENC(15)
      CALL NORMAL
      CALL CTRSET(1)
      CALL TYPECS(' NORMALISED POWER SPECTRUM',26)
      CALL CTRORI(0.0)
      CALL PLACE(20,1)
      IF(ISIG.EQ.0) GO TO 45
      ISTART=ISTART/10
      IEND=IEND/10
      CALL TYPECS('PROFILE:',8)
      CALL TYPENI(NPROF)
      CALL SPACE(2)
      CALL TYPECS('TIME:',5)
      CALL TYPENI(ISTART)
      CALL TYPENI(IEND)
      CALL TYPECS(' HRS',4)
   45 IF(ISIG.EQ.0) CALL TYPECS(TITLE,32)
      CALL PLACE(20,2)
      CALL TYPECS('MEM SPECTRAL DENSITY ESTIMATE',29)
      CALL PLACE(20,3)
      IF(IFLAG.EQ.0) CALL TYPECS('SPECTRAL ESTIMATE DERIVED FROM MAGNETI
     1C ANOMALY',47)
      IF(IFLAG.EQ.1) CALL TYPECS('SPECTRAL ESTIMATE DERIVED FROM HORIZON
     1TAL GRADIENT',50)
      CALL PLACE(20,4)
      IF(IFILT.EQ.0) CALL TYPECS('AKAIKE CRITERION ADOPTED TO PREDICT FI
     1LTER LENGTH',49)
      IF(IFILT.EQ.1) CALL TYPECS('OPERATOR LENGTH CHOSEN BY BERRYMAN CRI
     1TERION',44)
      IF(IFILT.EQ.2) CALL TYPECS('SPECTRA CALCULATED FOR ALL LPEF VALUES
     1 BETWEEN AKAIKE AND BERRYMAN CRITERIA',75)
      IF(IFILT.EQ.3) CALL TYPECS('OPERATOR LENGTH CHOSEN ARBITRARILY',
     134)
      CALL PLACE(20,5)
      IF(INPOL.EQ.0) CALL TYPECS('DATA INTERPOLATION: CUBIC SPLINE',32)
      IF(INPOL.EQ.1) CALL TYPECS('EVENLY SPACED DATA',18)
      IF(INPOL.EQ.2) CALL TYPECS('UNEVENLY SPACED DATA',20)
      CALL PLACE(95,32)
```

```
      CALL TYPECS('SEGMENT LENGTH,NPOINT =',23)
      CALL TYPENI(NPOINT)
      CALL PLACE(95,33)
      CALL TYPECS('DATA LENGTH,LX =',16)
      CALL TYPENI(LX)
      CALL PLACE(95,34)
      CALL TYPECS('PE FILTER LENGTH =',18)
      CALL TYPENF(SC,2)
      CALL TYPECS('*NPOINT',7)
      CALL PLACE(95,35)
      CALL TYPECS('SAMPLE INTERVAL =',17)
      CALL TYPENF(DELX,3)
      CALL PLACE(95,36)
      CALL TYPECS('STANDARD DEVIATION =',20)
      CALL TYPENF(RMS,3)
      FACT=-(YMAX-YMIN)/12.0
      CALL PCSEND(XMAX,FACT,'WAVENUMBER (RADIANS/KILOMETRE)',30)
      IF(IFILT.NE.0.OR.NPOINT.NE.LX) GO TO 60
      DO 50 I=1,NUM
      X(I)=FLOAT(I)/FLOAT(NPOINT)
   50 CONTINUE
      CALL MAXMIN(NUM,X,XMAX,XMIN)
      CALL MAXMIN(NUM,FPE,YMAX,YMIN)
      CALL FRAME
      CALL CTRMAG(12)
      CALL CSPACE(0.0,2.0,0.0,1.0)
      CALL PSPACE(0.1,0.9,0.3,0.9)
      CALL MAP(XMIN,XMAX,YMIN,YMAX)
      CALL AXES
      CALL PTPLOT(X,FPE,1,NUM,-2)
      CALL CTRORI(1.0)
      CALL PLACE(38,2)
      CALL TYPECS('LOG',3)
      CALL SUFFIX
      CALL TYPECS('10',2)
      CALL NORMAL
      CALL TYPECS(' NORMALISED FINAL PREDICTION ERROR',34)
      CALL CTRORI(0.0)
      CALL PLACE(20,1)
      IF(ISIG.EQ.0) GO TO 55
      CALL TYPECS('PROFILE:',8)
      CALL TYPENI(NPROF)
      CALL SPACE(2)
      CALL TYPECS('TIME:',5)
      CALL TYPENI(ISTART)
      CALL TYPENI(IEND)
      CALL TYPECS(' HRS',4)
   55 IF(ISIG.EQ.0) CALL TYPECS(TITLE,32)
      FACT=(YMAX-YMIN)*0.04
      CALL PCSEND(XMAX,FACT,'LENGTH OF PREDICTION ERROR FILTER AS PROPOR
     1TION OF INPUT DATA WINDOW LENGTH',75)
   60 CALL GREND
   70 STOP
      END
C
C
      SUBROUTINE BURG(LX,ANOM,N,LC,DELX,P,W,FPE,NUM)
C
C     SUBROUTINE BURG CALCULATES THE MEM POWER SPECTRAL DENSITY ESTIMATE
C     USING THE BURG ALGORITHM,ADAPTED FROM CLAERBOUT(1976).
```

```
C           THE SUBROUTINE ALSO CALCULATES THE FINAL PREDICTION ERROR FOR
C       EACH FILTER AS ITS LENGTH IS INCREMENTED IN THE SUBROUTINE.
C           IF PARAMETER LC.GT.0, THE FILTER LENGTH SPECIFIED IN THE MAIN
C       PROGRAM IS ADOPTED.
C           IF PARAMETER LC=0, THE AKAIKE FINAL PREDICTION ERROR CRITERION
C       IS ADOPTED TO PREDICT THE OPTIMUM FILTER LENGTH IN THE INEVITABLE
C       TRADE-OFF BETWEEN VARIANCE AND RESOLUTION. FOLLOWING ULRYCH AND
C       BISHOP(1975), A LIMIT ON THE MAXIMUM LENGTH OF THE PREDICTION
C       ERROR FILTER OF HALF OF THE DATA LENGTH IS IMPOSED.
C
C       REFERENCES:
C                  (1) ULRYCH,T.J. AND BISHOP,T.N.(1975) MAXIMUM ENTROPY
C                   SPECTRAL ANALYSIS AND AUTOREGRESSIVE DECOMPOSITION,
C                   REV.GEOPHYSICS AND SPACE PHYSICS,13,183-200
C
C                  (2) AKAIKE,H.(1970) STATISTICAL PREDICTOR IDENTIFICATION,
C                   ANN.INST.STATIST.MATH.,22,203-217
C
C
        DIMENSION ANOM(1024),P(1024),FPE(1024),W(1024)
        COMPLEX S(1024),CX(1024),A(1024),EP(1024),EM(1024)
        COMPLEX CP(1024),SMIN(1024),TOP,BOT,C(1024),EPI
        PI=3.14159265
        NN=1+N/2
        WL=PI/(FLOAT(N/2)*DELX)
        CP(1)=CMPLX(0.0,0.0)
        A(1)=CMPLX(1.0,0.0)
        DUMMY=0.0
        MIN=0
        NUM=0
        IFLAG=0
        IF(LC.EQ.0) IFLAG=1
        IF(LC.EQ.0) LC=LX/2
        DO 10 I=1,N
        S(I)=CMPLX(0.0,0.0)
        SMIN(I)=CMPLX(0.0,0.0)
        P(I)=0.0
        IF(I.LE.NN) W(I)=WL*FLOAT(I-1)
        IF(I.GT.NN) W(I)=WL*FLOAT(I-N-1)
     10 CONTINUE
        DO 20 I=1,LX
        CX(I)=CMPLX(ANOM(I),0.0)
        CP(1)=CP(1)+CX(I)*CONJG(CX(I))
        EM(I)=CX(I)
        EP(I)=CX(I)
     20 CONTINUE
        CP(1)=CP(1)/FLOAT(LX)
        FPE(1)=FLOAT(LX+2)*CABS(CP(1))/FLOAT(LX-2)
        FTEMP=FPE(1)
        FPE(1)=0.0
        DO 60 J=2,LC
        TOP=CMPLX(0.0,0.0)
        BOT=CMPLX(0.0,0.0)
        DO 30 I=J,LX
        BOT=BOT+EP(I)*CONJG(EP(I))+EM(I-J+1)*CONJG(EM(I-J+1))
        TOP=TOP+EP(I)*CONJG(EM(I-J+1))
     30 CONTINUE
        C(J)=CMPLX(2.0,0.0)*TOP/BOT
        DO 40 I=J,LX
        EPI=EP(I)
```

```
      EP(I)=EP(I)-C(J)*EM(I-J+1)
      EM(I-J+1)=EM(I-J+1)-CONJG(C(J))*EPI
   40 CONTINUE
      A(J)=CMPLX(0.0,0.0)
      DO 50 I=1,J
      S(I)=A(I)-C(J)*CONJG(A(J-I+1))
   50 CONTINUE
C
C     CALCULATION OF FINAL PREDICTION ERROR FOR FILTER OF LENGTH,J
C     THE SCALING FACTOR,(LX+J+1)/(LX-J-1), IS CHOSEN BECAUSE THE MEAN
C     HAS BEEN REMOVED FROM THE 'PROCESS' PRIOR TO CALCULATION OF THE
C     FILTER COEFFICIENTS (SEE ULRYCH AND BISHOP,1975)
C
      CP(J)=CP(J-1)*(1.0-S(J)**2)
      IF(IFLAG.EQ.0) GO TO 55
      FPE(J)=FLOAT(LX+J+1)*CABS(CP(J))/FLOAT(LX-J-1)
      FPE(J)=FPE(J)/FTEMP
      FPE(J)=ALOG10(FPE(J))
      IF(FPE(J).GT.DUMMY) GO TO 55
      DUMMY=FPE(J)
      MIN=J
      DO 54 I=1,J
      SMIN(I)=S(I)
   54 CONTINUE
   55 DO 60 I=1,J
      A(I)=S(I)
   60 CONTINUE
      IF(MIN.NE.0) GO TO 65
      DO 63 I=1,LC
      SMIN(I)=S(I)
   63 CONTINUE
      GO TO 70
   65 NUM=LC
      LC=MIN
C
C     TAKE FOURIER TRANSFORM OF PREDICTION ERROR FILTER COEFFICIENTS
C
   70 CALL FASFOR(N,SMIN,+1)
C
C     CALCULATE POWER SPECTRAL DENSITY ESTIMATE OF INPUT DATA FROM THE
C     INVERSE OF THE SQUARED RESPONSE OF THE PREDICTION ERROR FILTER
C
      DO 80 I=1,N
      P(I)=CABS(CP(LC))*DELX/(SMIN(I)*CONJG(SMIN(I)))
   80 CONTINUE
      RETURN
      END
C
C
      SUBROUTINE FASFOR(LX,CX,ISIGN)
C
C     SUBROUTINE FASFOR PERFORMS FAST FOURIER TRANSFORM
C     BY THE COOLEY AND TUKEY ALGORITHM(1965),MODIFIED
C     FROM BRENNER. THE SUBROUTINE IS ADAPTED FROM
C     CLAERBOUT(1976).
C
C     REFERENCE:CLAERBOUT,J.F.(1976),FUNDAMENTALS OF
C     GEOPHYSICAL DATA PROCESSING,MCGRAW HILL,NEW YORK
C
C     DIGITAL FOURIER TRANSFORM GIVEN BY:
```

```
C                    LX
C     CX(K)=SQRT(I/LX)SUM(CX(J)*EXP(2*PI*ISIGN*I*(J-1)*(K-1)/LX))
C                    J=1
C         FOR K=1,2.............(LX=2**INTEGER)
C
C     *NOTE*: ISIGN=+1     FORWARD TRANSFORM
C             ISIGN=-1     INVERSE TRANSFORM
C
      REAL*8 PI,SC,ARG
      COMPLEX CX(1024),CTEMP,CARG*16,CW*16
      PI=3.14159265
      J=1
      ARG=1.0/FLOAT(LX)
      SC=DSQRT(ARG)
      DO 30 I=1,LX
      IF(I.GT.J) GO TO 10
      CTEMP=CX(J)*SC
      CX(J)=CX(I)*SC
      CX(I)=CTEMP
   10 M=LX/2
   20 IF(J.LE.M) GO TO 30
      J=J-M
      M=M/2
      IF(M.GE.1) GO TO 20
   30 J=J+M
      L=1
   40 ISTEP=2*L
      DO 50 M=1,L
      CARG=(0.0,1.0)*(PI*FLOAT(ISIGN*(M-1))/FLOAT(L))
      CW=CDEXP(CARG)
      DO 50 I=M,LX,ISTEP
      CTEMP=CW*CX(I+L)
      CX(I+L)=CX(I)-CTEMP
      CX(I)=CX(I)+CTEMP
   50 CONTINUE
      L=ISTEP
      IF(L.LT.LX) GO TO 40
      RETURN
      END
C
C
      SUBROUTINE TREND(X,Y,NUM)
C
C     SUBROUTINE TREND CALCULATES THE BEST FITTING STRAIGHT LINE OF THE
C     FORM Y=M*X+C BY A LEAST SQUARES PROCEDURE AND THEN REMOVES THAT
C     LINEAR TREND FROM THE INPUT DATA ORDINATE ARRAY, Y(I),OVERWRITING
C     THE ORIGINAL VALUES SO THAT THE INPUT DATA ORDINATE VALUES ARE
C     LOST.
C
      DIMENSION X(1024),Y(1024)
      REAL*8 SUMX,SUMY,SUMXY,SUMX2,A,B
      SUMX=0.00000000
      SUMY=0.00000000
      SUMXY=0.00000000
      SUMX2=0.00000000
      DO 10 I=1,NUM
      SUMX=SUMX+X(I)
      SUMY=SUMY+Y(I)
      SUMXY=SUMXY+X(I)*Y(I)
      SUMX2=SUMX2+X(I)**2
```

```
   10 CONTINUE
      DEN=FLOAT(NUM)*SUMX2-SUMX**2
      A=(FLOAT(NUM)*SUMXY-SUMX*SUMY)/DEN
      B=(SUMY*SUMX2-SUMX*SUMXY)/DEN
      DO 20 I=1,NUM
      Y(I)=Y(I)-A*X(I)-B
   20 CONTINUE
      RETURN
      END
C
C
      SUBROUTINE MAXMIN(N,DUMMY,AMAX,AMIN)
C
C     SUBROUTINE MAXMIN SEARCHES AN ARRAY,DUMMY(I),TO EXTRACT THE MAXIMUM
C     AND MINIMUM VALUES RESPECTIVELY
C
      DIMENSION DUMMY(1024)
      AMAX=DUMMY(1)
      AMIN=DUMMY(1)
      DO 300 I=2,N
      IF(AMAX.LT.DUMMY(I)) AMAX=DUMMY(I)
      IF(AMIN.GT.DUMMY(I)) AMIN=DUMMY(I)
  300 CONTINUE
      RETURN
      END
C
C
      SUBROUTINE DERIV(NUM,NP,X,Y,GRAD)
C
C     SUBROUTINE DERIV CALCULATES THE HORIZONTAL DERIVATIVE
C     OF A FUNCTION,Y WHICH VARIES WITH X BY A LEAST SQUARES
C     FITTING PROCEDURE OF THE POLYNOMIAL Y=A*X**2+B*X+C
C     OVER A WINDOW OF CHOSEN LENGTH OF THE OBSERVED DATA.
C     THE FIRST DERIVATIVE IS THEN CALCULATED AT THE CENTRE
C     OF THE WINDOW SAMPLE,THAT IS,
C                           DY/DX=2*A*X+B
C
C     NUM=NUMBER OF POINTS IN THE COMPLETE DATA SET,Y(I)
C     NP=NUMBER OF POINTS DEFINING LENGTH OF SAMPLE WINDOW
C     X(I)=ABSCISSA VARIABLE
C     Y(I)=ORDINATE VARIABLE
C     GRAD(I)=HORIZONTAL FIRST DERIVATIVE CALCULATED FROM
C             Y(I) VERSUS X(I)
C
C
      DIMENSION X(1024),Y(1024),GRAD(1024)
      REAL*8 SUMX4,SUMX3,SUMX2,SUMXY,SUMX2Y,SUMX,SUMY
      REAL*8 C1,C2,C3,C4,C5,C6,A,B,DEN
      INTEGER UL
      MP=(NP+1)/2
      NN=NUM-MP+1
      DO 30 I=MP,NN
      LL=I-MP+1
      UL=I+MP-1
      SUMX4=0.000000000000
      SUMX3=0.000000000000
      SUMX2=0.000000000000
      SUMX=0.000000000000
      SUMY=0.000000000000
      SUMXY=0.000000000000
```

```
      SUMX2Y=0.000000000000
      DO 10 J=LL,UL
      XX=X(J)-X(LL)
      SUMX4=SUMX4+XX**4
      SUMX3=SUMX3+XX**3
      SUMX2=SUMX2+XX**2
      SUMX=SUMX+XX
      SUMY=SUMY+Y(J)
      SUMXY=SUMXY+XX*Y(J)
      SUMX2Y=SUMX2Y+Y(J)*XX**2
   10 CONTINUE
      C1=FLOAT(NP)*SUMX3-SUMX2*SUMX
      C2=FLOAT(NP)*SUMX2-SUMX**2
      C3=SUMX*SUMY-SUMXY*FLOAT(NP)
      C4=SUMX4*SUMX-SUMX3*SUMX2
      C5=SUMX3*SUMX-SUMX2**2
      C6=SUMX2*SUMXY-SUMX*SUMX2Y
      DEN=C1*C5-C4*C2
      A=(C6*C2-C3*C5)/DEN
      B=(C3*C4-C1*C6)/DEN
      GRAD(I)=2.0*A*(X(I)-X(LL))+B
      IF(I.GT.MP.AND.I.LT.NN) GO TO 30
      ISIGN=1
      IF(I.EQ.MP) ISIGN=-ISIGN
      IDUM=MP-1
      DO 25 L=1,IDUM
      LP=ISIGN*L
      GRAD(I+LP)=2.0*A*(X(I+LP)-X(LL))+B
   25 CONTINUE
   30 CONTINUE
      RETURN
      END
C
C
      SUBROUTINE STDDEV(LX,X,AMEAN,RMS)
C
C     SUBROUTINE STDDEV CALCULATES THE MEAN AND ROOT MEAN SQUARE DEVIATION
C     OF THE DATA FROM THE MEAN FOR A ONE DIMENSIONAL ARRAY, WHICH IN THIS
C     APPLICATION IS THE SPATIAL INCREMENT,XSTEP(I), BETWEEN ANOMALY VALUES
C
      DIMENSION X(1024),XSTEP(1024)
      LSTEP=LX-1
      SUM=0.0
      DO 10 I=1,LSTEP
      XSTEP(I)=X(I+1)-X(I)
      SUM=SUM+XSTEP(I)
   10 CONTINUE
      AMEAN=SUM/FLOAT(LSTEP)
      SUM=0.0
      DO 20 I=1,LSTEP
      SUM=SUM+(XSTEP(I)-AMEAN)**2
   20 CONTINUE
      VAR=SUM/FLOAT(LSTEP-1)
      RMS=SQRT(VAR)
      RETURN
      END
C
C
      SUBROUTINE LEASQU(X,Y,LX,SLOPE,ERROR,CORR)
C
```

```
C     SUBROUTINE LEASQU FITS A LEAST SQUARES LINE OF REGRESSION
C     THROUGH LX PAIRS OF COORDINATE POINTS,X AND Y. IT RETURNS
C     THE VALUE OF THE SLOPE,THE STANDARD ERROR IN THE SLOPE AND
C     THE COEFFICIENT OF CORRELATION
C
      DIMENSION X(1024),Y(1024)
      REAL*8 SUMX,SUMY,SUMXY,SUMX2,DD,TOP,BOT
      SUMX=0.0
      SUMY=0.0
      SUMXY=0.0
      DO 10 I=1,LX
      SUMX=SUMX+X(I)
      SUMY=SUMY+Y(I)
   10 CONTINUE
      XMEAN=SUMX/FLOAT(LX)
      YMEAN=SUMY/FLOAT(LX)
      SUMX=0.0
      SUMY=0.0
      DO 20 I=1,LX
      SUMX=SUMX+(X(I)-XMEAN)**2
      SUMY=SUMY+(Y(I)-YMEAN)**2
      SUMXY=SUMXY+(X(I)-XMEAN)*(Y(I)-YMEAN)
   20 CONTINUE
      CORR=SUMXY/DSQRT(SUMX*SUMY)
      SLOPE=SUMXY/SUMX
      Y0=YMEAN-SLOPE*XMEAN
      SUMX=0.0
      SUMX2=0.0
      DD=0.0
      DO 30 I=1,LX
      DD=DD+(Y(I)-SLOPE*X(I)-Y0)**2
      SUMX2=SUMX2+X(I)**2
      SUMX=SUMX+X(I)
   30 CONTINUE
      TOP=DD/FLOAT(LX-2)
      BOT=FLOAT(LX)*SUMX2-SUMX**2
      ERROR=SNGL(DSQRT(TOP*FLOAT(LX)/BOT))
      RETURN
      END
C
C
      SUBROUTINE DEPTH(X,Y,MID,LX,BCUT,TCUT,NLINE,XX,NSTART,NEND,LP,LQ)
C
C     SUBROUTINE DEPTH CALCULATES THE DEPTH(BETWEEN SPECIFIED
C     WAVENUMBER LIMITS) FROM THE LEAST SQUARES LINE OF REGRESSION
C     RETURNED BY SUBROUTINE LEASQU AND OUTPUTS THE DEPTH,STANDARD
C     ERROR IN THE DEPTH,CORRELATION COEFFICIENT AND WAVENUMBER
C     LIMITS FOR EACH SEGMENT OF THE PROFILE TO THE FILE ATTACHED
C     TO UNIT 4.
C
      DIMENSION XDUM(256),YDUM(256),XX(1024),BCUT(10),TCUT(10)
      DIMENSION X(256),Y(256)
      DO 30 K=1,NLINE
      KK=0
      DO 10 I=1,MID
      IF(X(I).LT.BCUT(K).OR.X(I).GT.TCUT(K)) GO TO 10
      KK=KK+1
      XDUM(KK)=X(I)
      YDUM(KK)=Y(I)
   10 CONTINUE
```

```
      CALL LEASQU(XDUM,YDUM,KK,SLOPE,ERROR,CORR)
      DEP=-0.5*SLOPE
      ERROR=0.5*ERROR
      IF(NEND.LE.LX) GO TO 20
      WRITE(4,210) K,DEP,ERROR,CORR,LO
  210 FORMAT(/,3X,'MEAN STATISTICS FOR LINE NO.',I2,/,3X,'AVERAGE DEPTH
     1=',F7.2,/,3X,'STANDARD ERROR IN DEPTH =',F7.2,/,3X,'CORRELATION CO
     2EFFICIENT =',F7.4,/,3X,'LENGTH OF BERRYMAN OPERATOR =',I3)
      GO TO 30
   20 WRITE(4,200) XX(NSTART),XX(NEND),K,DEP,ERROR,CORR,BCUT(K),
     1TCUT(K),LP
  200 FORMAT(3X,2F10.2,I9,1X,2F10.2,F15.4,F13.2,F14.2,I13)
   30 CONTINUE
      RETURN
      END
C
C
      SUBROUTINE SIGMA(LX,Y,N,LOPER,LPEF,DELX,SS,W,FPE,NUM)
C
C     SUBROUTINE SIGMA CALCULATES THE AVERAGE SPECTRAL DENSITY
C     ESTIMATE FOR OPERATOR LENGTHS BETWEEN THAT SPECIFIED BY
C     THE AKAIKE CRITERION(MINIMUM) AND THAT GIVEN BY THE BERRYMAN
C     CRITERION(MAXIMUM).
C
      DIMENSION Y(1024),S(1024),W(1024),SS(1024),FPE(1024)
      IF(LOPER.EQ.LX/2) LOPER=LOPER+1
      IF(LOPER.LT.LPEF) WRITE(6,200) LOPER,LPEF
  200 FORMAT(/,'ERROR: BERRYMAN OPERATOR LENGTH<LPEF OF AKAIKE'
     1,/,'LOPER =',I5,/,'LPEF =',I5)
      DO 10 I=1,N
      SS(I)=0.0
   10 CONTINUE
      IDIFF=LOPER-LPEF+1
      DO 30 LEN=LPEF,LOPER
      CALL BURG(LX,Y,N,LEN,DELX,S,W,FPE,NUM)
      DO 20 I=1,N
      SS(I)=SS(I)+S(I)/FLOAT(IDIFF)
   20 CONTINUE
   30 CONTINUE
      RETURN
      END
END OF FILE
```

APPENDIX C

DERIVATION OF FORMULA FOR MAGNETIC ANOMALY DUE TO A FINITE MAGNETISED STEP, TAKING INTO ACCOUNT REMANENT MAGNETISATION

The derivation of Equation 3.10 follows, the form of the equation being made compatible with that of Nabighian (1972) and the derivation influenced by the approach of Hood (1964). The symbols used are defined in Figures C.1 and C.2.

Further definitions are as follows:

h = the depth to the upper surface of the finite step
t = the thickness of the finite step
i and a are the inclination and declination of the resultant magnetisation, $\underline{J}$ relative to the axes shown in Figure C.2
I and A_F are the inclination and declination of the Earth's field, $\underline{F}$ relative to the axes shown in Figure C.2
I_R and A_R are the inclination and declination of the remanent magnetisation, $\underline{R}$ relative to the axes shown in Figure C.2

$$\left.\begin{array}{l}\lambda\\ \omega\\ \psi\end{array}\right\}\ \text{resolved direction of}\ \left\{\begin{array}{l}\text{induced, } kF_r\\ \text{remanent, } R_r\\ \text{resultant, } J_r\end{array}\right\}\ \begin{array}{l}\text{components of}\\ \text{magnetisation in}\\ \text{the xz plane}\end{array}$$

k = the magnetic susceptibility contrast of the finite step.

The formulae for the vertical and horizontal components of the total field magnetic anomaly in the x-z plane due to a two-dimensional finite step with sloping face are well established (for example, Heiland, 1940). In the following derivation, the volume distribution of magnetic poles is assumed to be replaced by a surface distribution of magnetisation. A constant, uniform magnetisation is assumed. From the basic definition of magnetic potential and the application of Gauss' theorem (Grant and West, 1965; Telford <u>et al</u>, 1976), the general formulae for the vertical and horizontal components of the total field magnetic anomaly (perpendicular to strike) may be calculated:

$$\Delta z = \frac{\mu_o\, \underline{J}.\hat{\underline{n}}}{2\pi}\left[\sin i.\ln\left(\frac{r_1}{r_2}\right) + \cos i.(\theta_2-\theta_1)\right]$$

$$\Delta H_x = \frac{\mu_o\, \underline{J}.\hat{\underline{n}}}{2\pi}\left[\cos i.\ln\left(\frac{r_1}{r_2}\right) - \sin i.(\theta_2-\theta_1)\right]$$

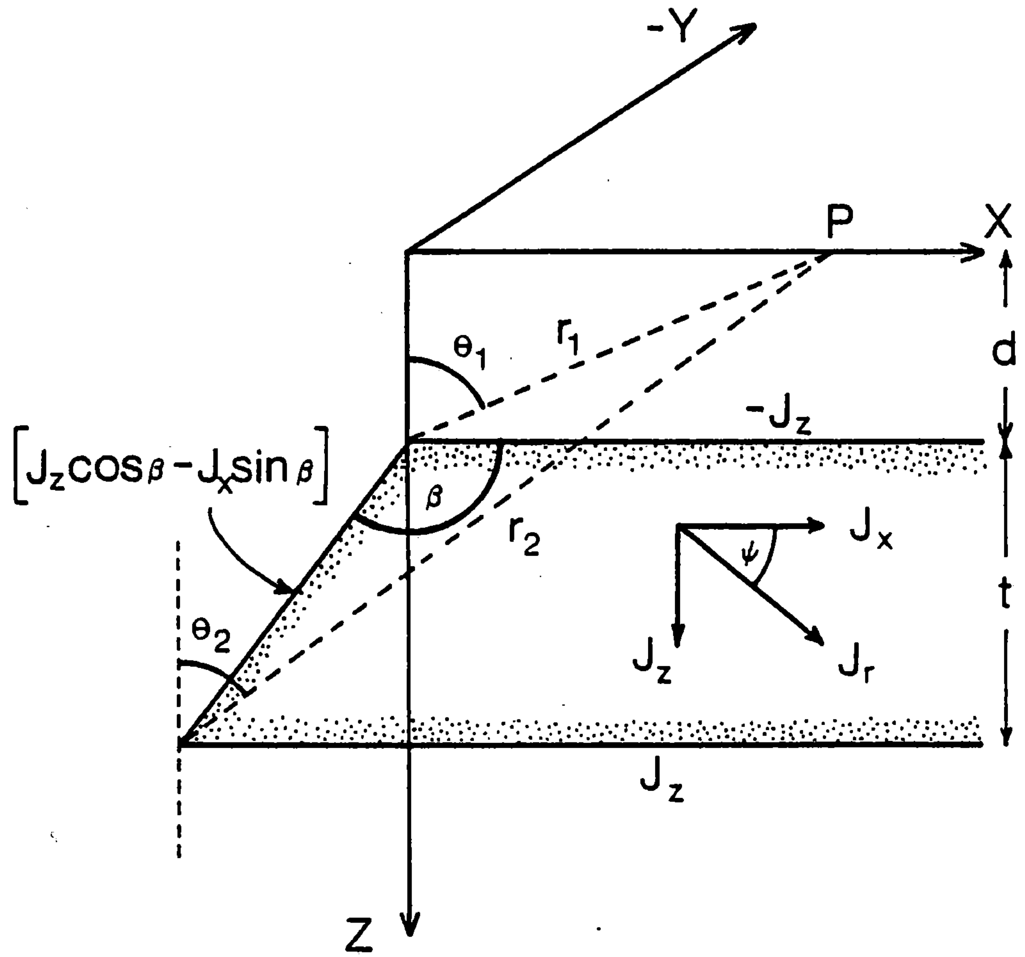

$$b = \left[1 - \cos^2 i \ \sin^2 a\right]^{1/2}$$

$$c = \left[1 - \cos^2 I \ \sin^2 A_F\right]^{1/2}$$

$$\phi = \lambda + \psi - \beta - 90^\circ$$

Figure C.1 Definition of symbols for derivation of the total field magnetic anomaly for a buried magnetised finite step model taking into account remanent magnetisation.

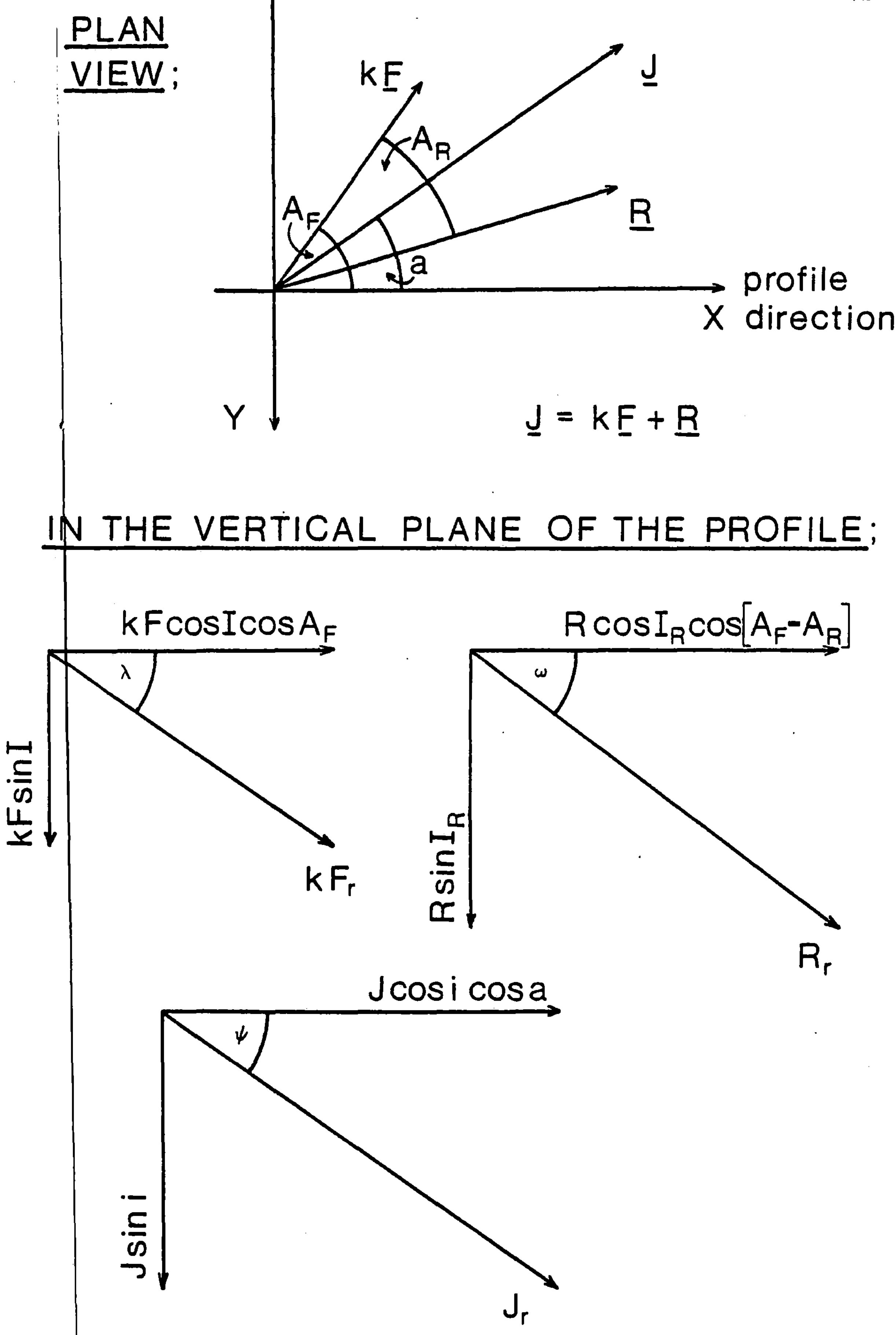

Figure C.2 Definition of parameters relating to magnetic field vector components for derivation of Equation 3.10.

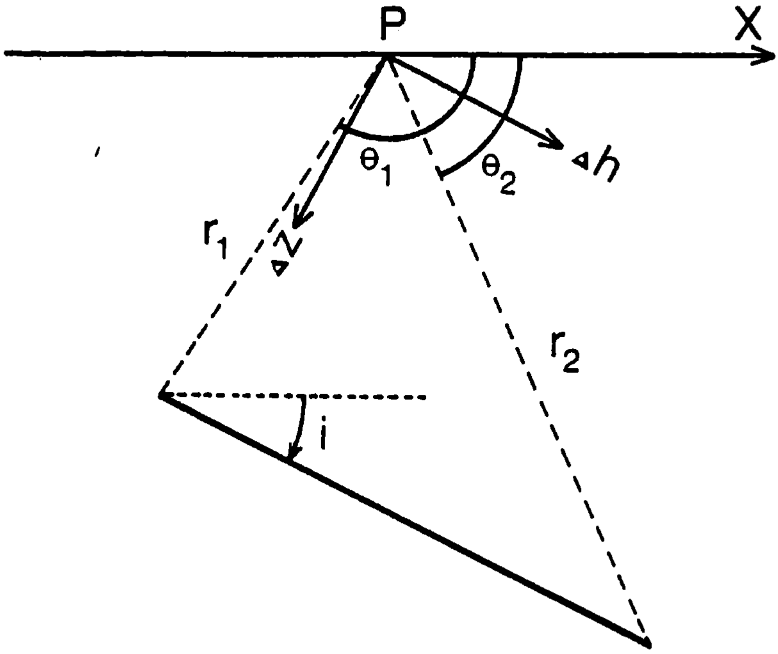

$$\Delta Z = \Delta h \sin i + \Delta z \cos i$$

$$\Delta H_x = \Delta h \cos i - \Delta z \sin i$$

$$\Delta z = \frac{\mu_0 \underline{J} \cdot \hat{\underline{n}}}{2\pi} \left[\theta_2 - \theta_1\right]$$

$$\Delta h = \frac{\mu_0 \underline{J} \cdot \hat{\underline{n}}}{2\pi} \ln\left[r_1/r_2\right]$$

$\hat{\underline{n}}$ = outward normal to body

Figure C.3 Definition of parameters relating to the vertical and horizontal components of the magnetic anomaly due to an inclined, two-dimensional thin sheet.

where $\hat{\underline{n}}$ = the unit vector along the outward normal of the surface of the causative body.

The other symbols are defined in Figure C.3.

Using these equations, the derivation of Equation 3.10 is as follows:

Vertical anomaly:

$$\Delta z = \frac{\mu_o}{2\pi}\left\{- J_z(-\frac{\pi}{2} - \theta_1) + J_z(-\frac{\pi}{2} - \theta_2) + \right.$$

$$\left. + (J_z \cos\beta - J_x \sin\beta) \cdot \left[\sin\beta \ln\frac{r_1}{r_2} + \cos\beta\ (\theta_2 - \theta_1)\right]\right\}$$

$$= \frac{\mu_o}{2\pi}\left\{- J_z\left[\sin^2\beta\ (\theta_2 - \theta_1) - \cos\beta \sin\beta \ln\frac{r_1}{r_2}\right] - \right.$$

$$\left. - J_x\left[\sin^2\beta \ \ln\frac{r_1}{r_2} + \sin\beta\cos\beta\ (\theta_2 - \theta_1)\right]\right\}$$

Now $\underline{J}$ = resultant magnetisation

and $J_x = J \cos i \cos a \qquad Jz = J \sin i.$

By substitution for J_x and J_z, and rearranging:

$$\Delta z = \frac{\mu_o J}{2\pi}\left\{- A(\theta_2 - \theta_1) + B \ln\frac{r_1}{r_2}\right\} \qquad \text{C.1}$$

where $A = \sin\beta\ (\sin i \sin\beta + \cos i \cos a \cos\beta)$

$B = \sin\beta\ (\sin i \cos\beta - \cos i \cos a \sin\beta).$

Horizontal anomaly:

$$\Delta H_x = \frac{\mu_o}{2\pi}\left\{- J_z \ln\frac{r_1}{r_\infty} + J_z \ln\frac{r_2}{r_\infty} + \right.$$

$$\left. + \left[J_z \cos\beta - J_x \sin\beta\right] \cdot \left[\cos\beta \ln\frac{r_1}{r_2} - \sin\beta\ (\theta_2 - \theta_1)\right]\right\}$$

$$= \frac{\mu_o}{2\pi}\left\{- J_z \left[\sin^2 \beta \ln \frac{r_1}{r_2} + \cos \beta \sin \beta \ (\theta_2 - \theta_1)\right] + \right.$$

$$\left. + J_x\left[\sin^2 \beta \ (\theta_2 - \theta_1) - \sin \beta \cos \beta \ln \frac{r_1}{r_2}\right]\right\}$$

Since $J_x = J \cos i \cos a$ and $J_z = J \sin i$, by substitution for J_x and J_z, and rearranging:

$$\Delta H_x = \frac{\mu_o J}{2\pi}\left\{- B \ (\theta_2 - \theta_1) - A \ln \frac{r_1}{r_2}\right\} \qquad \text{C.2}$$

where $A = \sin \beta \ (\sin i \sin \beta + \cos i \cos a \cos \beta)$
$B = \sin \beta \ (\sin i \cos \beta - \cos i \cos a \sin \beta)$.

If ΔT = the amplitude of the total field magnetic anomaly, then:

$$\Delta T = \Delta z \sin I + \Delta H_x \cos I \cos A_F \qquad \text{C.3}$$

By substitution for Δz and ΔH_x from Equations C.1 and C.2 respectively, Equation C.3 yields the result:

$$\Delta T = \frac{\mu_o J}{2\pi}\left[C \ (\theta_1 - \theta_2) + D \ln \frac{r_1}{r_2}\right] \qquad \text{C.4}$$

where $C = A \sin I + B \cos I \cos A_F$
$D = B \sin I - A \cos I \cos A_F$.

Following the approach of Hood (1964):

$$\tan \lambda = \frac{\tan I}{\cos A_F} \qquad \tan \omega = \frac{\tan I_R}{\cos (A_F - A_R)} \qquad \tan \psi = \frac{\tan i}{\cos a}$$

By definition,

$$JA = \sin \beta \ (J \sin i \sin \beta + J \cos i \cos a \cos \beta)$$

$$= J_r \sin \beta \ (\sin \psi \sin \beta + \cos \psi \cos \beta)$$

Hence:

$$A = \frac{J_r}{J} \sin \beta \; (\cos \psi \cos \beta + \sin \psi \sin \beta)$$

$$= \frac{J_r}{J} \sin \beta \cos (\psi - \beta) \qquad \text{C.5}$$

Similarly, by definition,

$$JB = \sin \beta \; (J \sin i \cos \beta - J \cos i \cos a \sin \beta)$$

$$= J_r \sin \beta \; (\sin \psi \cos \beta - \cos \psi \sin \beta)$$

Therefore,

$$B = \frac{J_r}{J} \sin \beta \sin (\psi - \beta) \qquad \text{C.6}$$

Also, using the fact that $\sin^2 \psi + \cos^2 \psi = 1$ and the relationships of Figure C.2:

$$J_r^{\;2} = J_r^{\;2} \sin^2 \psi + J_r^{\;2} \cos^2 \psi$$

$$= J^2 \sin^2 i + J^2 \cos^2 i \cos^2 a$$

$$\therefore \; \frac{J_r}{J} = (\sin^2 i + \cos^2 i \cos^2 a)^{\frac{1}{2}}$$

$$\frac{J_r}{J} = (1 - \cos^2 i \sin^2 a)^{\frac{1}{2}} \qquad \text{C.7}$$

Also, $J_r \sin \psi = J \sin i$ (Figure C.2)

$$\therefore \; \frac{J_r}{J} = \frac{\sin i}{\sin \psi} \qquad \text{C.8}$$

Combining Equations C.7 and C.8, then:

$$b = \frac{J_r}{J} = \frac{\sin i}{\sin \psi} = (1 - \cos^2 i \sin^2 a)^{\frac{1}{2}} \qquad \text{C.9}$$

By an analogous approach:

$$(kF_r)^2 = (kF_r)^2 \sin^2 \lambda + (kF_r)^2 \cos^2 \lambda$$

$$= (kF)^2 \sin^2 I + (kF)^2 \cos^2 I \cos^2 A_F$$

Hence:

$$\frac{kF_r}{kF} = (\sin^2 I + \cos^2 I \cos^2 A_F)^{\frac{1}{2}}$$

$$= (1 - \cos^2 I \sin^2 A_F)^{\frac{1}{2}}$$

Also, $kF_r \sin \lambda = kF \sin I$ (Figure C.2). Therefore:

$$c = \frac{kF_r}{kF} = \frac{\sin I}{\sin \lambda} = (1 - \cos^2 I \sin^2 A_F)^{\frac{1}{2}} \qquad \text{C.10}$$

Since $b = J_r/J$, from Equations C.5 and C.6:

$$A = b \sin \beta \cos (\psi - \beta)$$

$$B = b \sin \beta \sin (\psi - \beta) \qquad \text{C.11}$$

From the definitions of parameters C and D in Equation C.4 and by substitution for A and B from Equation C.11, it follows that:

$$kFC = kF \sin I\, b \sin \beta \cos (\psi-\beta) + kF \cos I \cos A_F\, b \sin \beta \sin (\psi-\beta)$$

$$= b \sin \beta\, (kF_r \sin \lambda \cos (\psi-\beta) + kF_r \cos \lambda \sin (\psi-\beta))$$

$$= kF_r b \sin \beta \sin (\lambda+\psi-\beta)$$

But $kF_r = kFc$ (from Equation C.10)

$$\therefore \quad C = bc \sin \beta \sin (\lambda + \psi - \beta) \qquad \text{C.12}$$

Similarly,

$$kFD = kF \sin I\, b \sin \beta \sin (\psi-\beta) - kF \cos I \cos A_F\, b \sin \beta \cos (\psi-\beta)$$

$$= b \sin \beta\, (kF_r \sin \lambda \sin (\psi-\beta) - kF_r \cos \lambda \cos (\lambda-\beta))$$

$$kFD = - kF_r b \sin \beta \cos (\lambda + \psi - \beta)$$

$$\therefore \quad D = - bc \sin \beta \cos (\lambda + \psi - \beta) \qquad C.13$$

By substitution of the values of C and D from Equations C.12 and C.13, the general expression for the total field magnetic anomaly, ΔT given in Equation C.4 becomes:

$$\Delta T = \frac{\mu_o}{2\pi} Jbc \sin \beta \left[\sin (\lambda + \psi - \beta) \; (\theta_1 - \theta_2) - \cos (\lambda + \psi - \beta) \; \ln \frac{r_1}{r_2} \right]$$

Let $\gamma = \lambda + \psi - \beta$. Hence:

$$\Delta T = \frac{\mu_o}{2\pi} Jbc \sin \beta \left[(\theta_1 - \theta_2) \cdot \sin \gamma - \ln \left(\frac{r_1}{r_2} \right) \cdot \cos \gamma \right] \qquad C.14$$

Now $\sin \gamma = \cos (\frac{\pi}{2} - \gamma) = \cos (\gamma - \frac{\pi}{2})$

$\cos \gamma = \sin (\frac{\pi}{2} - \gamma) = - \sin (\gamma - \frac{\pi}{2})$

By using the above relationships for $\sin \gamma$ and $\cos \gamma$, Equation C.14 becomes:

$$\Delta T = \frac{\mu_o}{2\pi} Jbc \sin \beta \left[(\theta_1 - \theta_2) \cdot \cos (\gamma - \frac{\pi}{2}) + \ln \left(\frac{r_1}{r_2} \right) \cdot \sin (\gamma - \frac{\pi}{2}) \right]$$

Now, let $\phi = \gamma - \frac{\pi}{2}$, so that:

$$\Delta T = \frac{\mu_o}{2\pi} Jbc \sin \beta \left[(\theta_1 - \theta_2) \cos \phi + \ln \left(\frac{r_1}{r_2} \right) \sin \phi \right] \qquad C.15$$

where $\phi = \lambda + \psi - d - \frac{\pi}{2}$.

Equation C.15 represents the final result, identical to Equation 3.10. This form of the equation is identical to that given by Nabighian (1972) for the case of induced magnetisation only. The new equation, derived in a similar manner to that for the dipping dyke of Hood (1964), includes both remanent and induced magnetic components for the case of the finite magnetised step.

SF 10045

DURHAM UNIVERSITY E. GREENLAND MARGIN	
Line F	Shot Points 0 to 3588
CDP STACK	Section A

BP

Geophysical Division London

RECORDING

12 ← TRACE → 1

Instruments	DAS50/10 system, SEG A format filters; low cut out high cut out 6 s records at 4 ms sampling interval
Spread	1200 m cable, 12 groups, active section length 50 m passive section length 50 m, quoted offset 229 m cable depth 12 m
Source	Airgun array (3 X 160 cu.in. + 1 X 300 cu. in.) at a depth of 6.5 m pop interval 50 m
Coverage	12 fold, 12 trace
Field polarity	compression = negative number
Crew	Durham University (vessel: R.R.S. Shackleton)
Date	August 1977

PROCESSING

1. Amplitude recovery — formula for curve = te^0.21; static correction for multiplexer delay
2. Trace editing
3. Deconvolution — operator 0.15 s, prewhitening 3%; gate: near trace Δ0 + 0.1 s – 4.0 s; far trace Δ0 + 0.8 s – 4.0 s
4. Normal moveout correction
5. Dynamic offset dependent trace weighting to enhance multiple attenuation
6. First break mutes
7. 11 fold common depth point stack
8. FK velocity filtering — reject zone of ±33 ms/trace
9. 3 fold weighted trace mix — weighting 1 : 2 : 1
10. Static correction for gun and cable depth 0.012 s
11. Deconvolution — operator 0.53 s, prewhitening 3%; gate WB + 0.1 s – 4.0 s
12. Time and space variant bandpass filter (length 0.3 s)

TIME			FREQUENCY
SP 0 – 1737	SP 2427	SP 3367	
0 – 1.0 s	0 – 2.2 s	0 – 1.0 s	12.16 – 50.60 Hz
1.0 s	2.6 s	1.4 s	8.12 – 40.55 Hz
1.5 – 4.0 s	3.0 – 4.0 s	1.5 – 4.0 s	5.10 – 40.50 Hz

13. Dynamic equalisation — initial time WB + 0.1 s; initial gate 0.1 s; final gate 1.0 s

DISPLAY

Derived shot points annotated at centre of gun array	
Display polarity	positive number = black peak
Overall polarity	compression = white trough
Scale velocity	20,000 m/s
Date	Jan 1979 — 20 1633

5 km.

VELOCITY FN 2

TIME MS	STACK VEL M/S	INT VEL M/S
748	1500	
950	1680	2223
1150	1950	2908
4000	4000	4574

VELOCITY FN 3

TIME MS	STACK VEL M/S	INT VEL M/S
724	1500	
950	1700	2222
1200	2000	2866
1600	2490	3577
4000	4000	4746

VELOCITY FN 4

TIME MS	STACK VEL M/S	INT VEL M/S
748	1500	
900	1600	2021
975	1650	2161
1125	2000	3507
1650	2600	3560
4000	4000	4742

VELOCITY FN 5

TIME MS	STACK VEL M/S	INT VEL M/S
688	1500	
950	1770	2334
1125	1950	2727
1475	2400	3471
4000	4000	4688

VELOCITY FN 6

TIME MS	STACK VEL M/S	INT VEL M/S
450	1500	
600	1600	1868
650	1700	2617
800	1900	2100
900	2100	3718
1400	2400	3414
4000	4000	4480

VELOCITY FN 7

TIME MS	STACK VEL M/S	INT VEL M/S
596	1500	
725	1620	1963
875	1770	2364
1035	1920	2587
1400	2400	3414
4000	3750	4305

VELOCITY FN 8

TIME MS	STACK VEL M/S	INT VEL M/S
950	1500	
1304	1590	1888
1496	1650	2010
1640	1800	2395
1920	1900	2791
2168	2130	3880
2336	2340	4193
4900	3500	4564

VELOCITY FN 9

TIME MS	STACK VEL M/S	INT VEL M/S
1500	1500	
1952	1580	1857
2096	1680	2620
2208	1800	2792
2752	2610	4968
4000	3400	4928

VELOCITY FN 10

TIME MS	STACK VEL M/S	INT VEL M/S
1796	1500	
2236	1650	2189
2332	1680	2269
2508	1770	2728
2716	1920	3176
3124	2350	4212
4000	3250	7341

VELOCITY FN 11

TIME MS	STACK VEL M/S	INT VEL M/S
1856	1500	
2376	1598	1984
2684	1740	2673
3080	2070	3775
3380	2370	4898
4000	3000	5173

VELOCITY FN 12

TIME MS	STACK VEL M/S	INT VEL M/S
1800	1500	
2000	1550	1942
2150	1680	2158
2275	1650	2348
2425	1750	2866
4000	3000	4259

VELOCITY FN 13

TIME MS	STACK VEL M/S	INT VEL M/S
1700	1500	
1900	1650	2016
2092	1550	1688
2380	1770	2743
2650	2300	4929
4000	3500	5090

VELOCITY FN 14

TIME MS	STACK VEL M/S	INT VEL M/S
1452	1500	
1784	1560	1813
2364	1680	2368
2600	2700	6917
4000	3750	5161

VELOCITY FN 15

TIME MS	STACK VEL M/S	INT VEL M/S
1144	1500	
1456	1620	1999
2008	1830	2297
2508	2700	4834
4000	4000	5524

VELOCITY FN 16

TIME MS	STACK VEL M/S	INT VEL M/S
930	1500	
1050	1550	1700
1100	1600	2422
1552	2300	3846
1500	2600	5870
4000	4000	4641

VELOCITY FN 17

TIME MS	STACK VEL M/S	INT VEL M/S
388	1500	
470	1700	2804
900	1950	2258
1100	2225	3934
1600	3375	4573
2500	4150	5171
4000	4000	3711

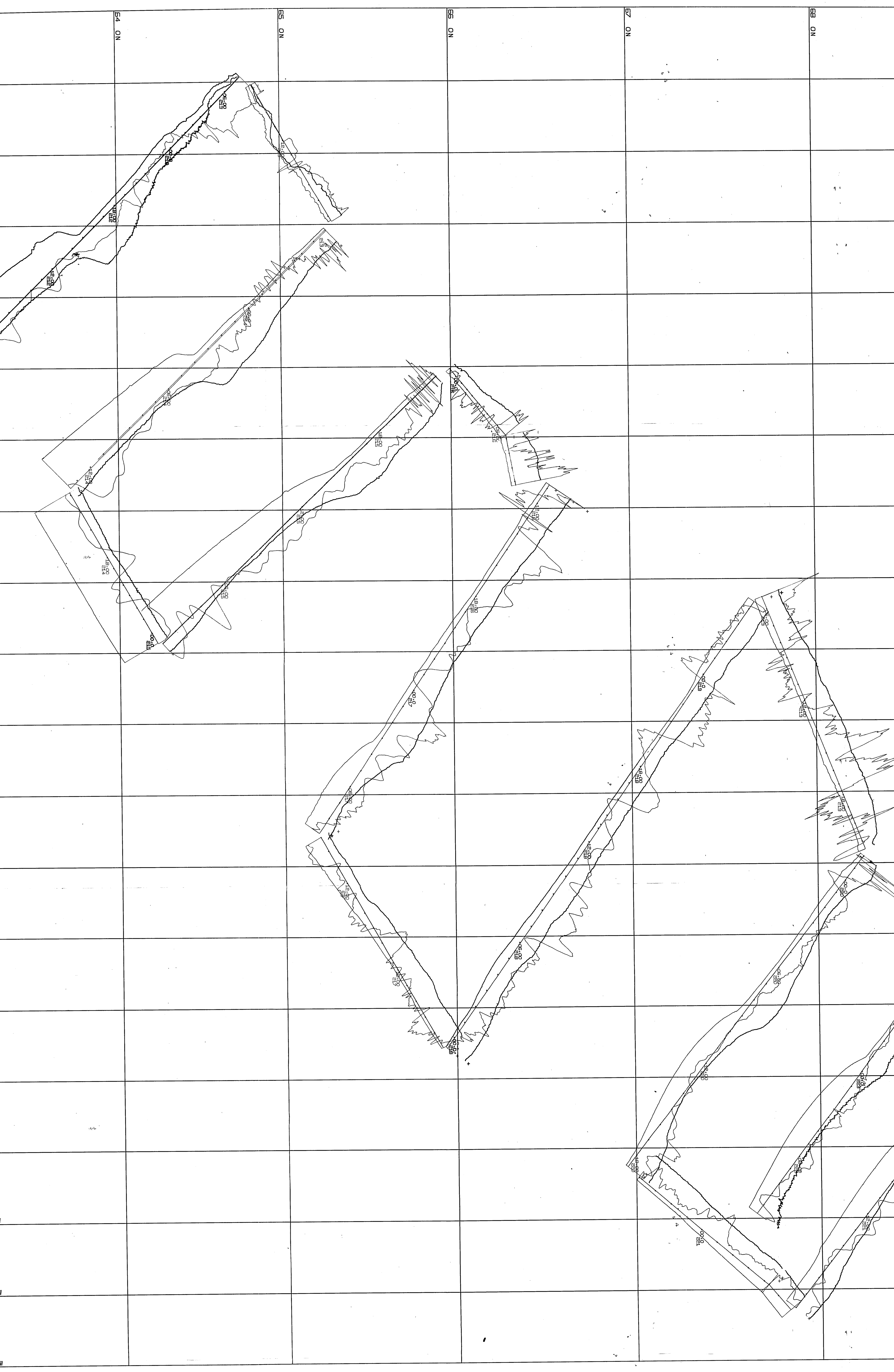
64 0N
65 0N
66 0N
67 0N
68 0N

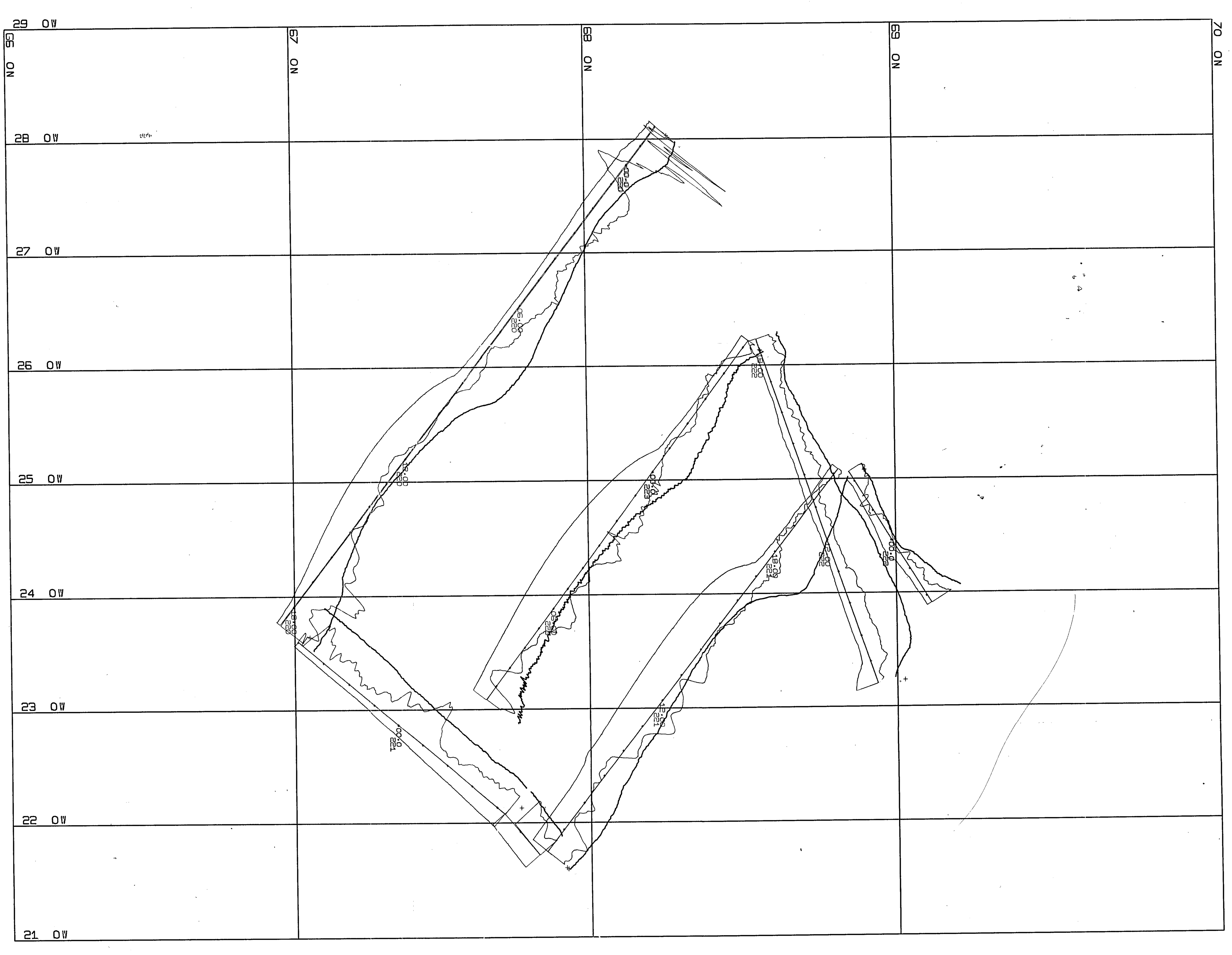
29 0W
28 0W
27 0W
26 0W
25 0W
24 0W
23 0W
22 0W
21 0W
66 0N
67 0N
68 0N
69 0N
70 0N